The Mechanism of Action of External Protons on hERG Potassium Channels

by

Yu Patrick Shi

B.Sc., Simon Fraser University, 2011

Thesis Submitted in Partial Fulfillment of the
Requirements for the Degree of
Doctor of Philosophy

in the
Department of Biomedical Physiology and Kinesiology
Faculty of Science

SIMON FRASER UNIVERSITY
Fall 2018

Approval

Name:	**Yu Patrick Shi**
Degree:	**Doctor of Philosophy**
Title:	**The Mechanism of External Protons on hERG Potassium Channels**
Examining Committee:	**Chair:** William Cupples Professor
	Thomas Claydon Senior Supervisor Associate Professor
	Peter Ruben Supervisor Professor
	Edgar Young Supervisor Associate Professor
	Damon Poburko Internal Examiner Associate Professor
	Gea-Ny Tseng External Examiner Professor
Date Defended/Approved:	November 19th, 2018

Ethics Statement

The author, whose name appears on the title page of this work, has obtained, for the research described in this work, either:

a. human research ethics approval from the Simon Fraser University Office of Research Ethics

or

b. advance approval of the animal care protocol from the University Animal Care Committee of Simon Fraser University

or has conducted the research

c. as a co-investigator, collaborator, or research assistant in a research project approved in advance.

A copy of the approval letter has been filed with the Theses Office of the University Library at the time of submission of this thesis or project.

The original application for approval and letter of approval are filed with the relevant offices. Inquiries may be directed to those authorities.

Simon Fraser University Library
Burnaby, British Columbia, Canada

Update Spring 2016

Abstract

Myocardial ischemia occurs when there is a reduction of blood flow to the heart due to blockage of an artery, causing inefficient delivery of oxygen and nutrients to the heart muscle. Acidosis is one of the major consequences during myocardial ischemia and affects a wide array of ion channels in the heart that may predispose individuals to cardiac arrhythmia. The human *ether-à-go-go* (hERG) related gene encodes the potassium channel that conducts the I_{Kr} current, which is responsible for the repolarization phase of the cardiac action potential and is particularly sensitive to external acidosis. External acidosis had been well observed to reduce hERG channel overall conductance, right-shift the voltage-dependence of activation, and accelerate deactivation rate, all of which lead to a loss-of-function effect on the hERG channels. We hypothesized that this can prolong action potential duration, increase susceptibility of individuals to long QT syndrome and reduce the protective current against premature ectopic beat. My first study aimed to determine the site and mechanism for the right-shift in the voltage-dependence of activation. I found that external protons disrupt stable interactions formed by the cation binding pocket, compose of three acidic residues: D456, D460 in S2, and D509 in S3, with positive charges in S4 to destabilize the activated voltage sensor. My second study aims to determine the site and mechanism for the acceleration of deactivation induced by external protons. Using voltage-clamp fluorimetry and gating current measurement with long duration protocols to measure voltage sensor mode-shift, we determined that external protons reduced the voltage sensor mode-shift by right shifting the voltage-dependence of deactivation suggesting that the relaxed conformation of the voltage sensor is destabilized and that D509 is a critical protonation site. In my last study, I used zebrafish heart as a translational model, with the optical mapping technique to investigate the effect of external protons on the overall cardiac action potential. We discovered that at low pH, the cardiac action potential is significantly prolonged, triangulation is increased, and the electrical restitution curve is flattened, which are all predictors for arrhythmogenicity.

Keywords: hERG; pH; Acidosis; Relaxation; Zebrafish; optical mapping;

Dedication

To My Family and Grandmother.

Acknowledgements

My PhD journey was a roller coaster ride of a lifetime that I never regretted getting on. Despite the ups and downs, this was an unforgettable experience. A lot of this was because of all the people who have crossed path and helped me along the way. I would like to thank them and show my appreciation.

I want to first show my appreciation and gratitude to my senior supervisor, Dr. Tom Claydon, for all his dedicated supervision, and guidance. Without his trust in me during my undergraduate co-op term with him, I would have never had the opportunity to partake on this journey. The support, and encouragement I received from him during my PhD was extremely motivating and is a big factor that drive my passion for scientific research. He always encourages and challenge students and from this, I have developed and grown under his leadership to be more well-rounded person. Here, I would also like to thank Dr. Peter Ruben, and Dr. Edgar Young, on my supervisory committee, for their insightful comments, and advices to help me become a better thinker.

Next, I would like to thank all my previous and current lab members from the Claydon lab. Many have come and gone whom have greatly impacted my life. Dr. Yen May Cheng have really taught me what it is to do research the right way, her meticulous attention to detail and organization is contagious and inspiring. A big thank you to Dr. Samrat Thouta and Danielle Jeong for the countless scientific discussions and afterhours heartfelt talks. Ji Qi, whom was a technician and a lab “mom”, for making all the DNA and RNA for us, taking care of us, and giving life advices. Christina Hull, whom can lighten up any conversation, make the lab environment fun, but also contribute to great scientific discussion as well.

I cannot thank the members from Dr. Glen Tibbits lab and Dr. Glen Tibbits enough for their patient guidance in teaching me how to operate the optical mapping system. Dr. Glen Tibbits for his fatherly support and graciously included me as one of his own lab member. Dr. Eric Lin for the wealth of support on the optical mapping rig, and his patience with me when troubleshooting the rig. Huge thanks to Sanam Shafaattalab, Marvin Gunawan, Alison Li, Sabi Sangha, Kaveh Rayani, Barun Kim for their friendship and support over the years, and all the past and present friends and colleagues of the Molecular Cardiac Physiology Group (MCPG) and BPK department.

Lastly, I would like to thank my parents, and Grace Song for being on this ride with me all these years. They have shared my frustration and celebrated my success, unconditionally, and I can never have completed this journey without their support. Finally, I would like to thank my grandmother, who passed away from cancer, for inspiring and motivating me to walk the path of scientific research.

Table of Contents

Approval ii
Ethics Statement iii
Abstract iv
Dedication v
Acknowledgements vi
Table of Contents viii
List of Tables xii
List of Figures xiii
List of Acronyms xiv
Glossary xvii

Chapter 1. Introduction 1
1.1 Voltage-gated K^+ channel diversity 1
1.2 HERG potassium channels 3
1.2.1 Physiological role of hERG channels 3
1.2.2 Features of the hERG channel architecture 9
1.2.3 Unique hERG channel gating 14
1.2.3.1 Molecular basis of hERG activation 16
1.2.3.2 Molecular basis of hERG inactivation 17
1.2.3.3 Molecular basis of hERG deactivation 19
1.2.3.4 Molecular basis of hERG mode-shift 20
1.3 Myocardial ischemia 21
1.3.1 Background 22
1.3.2 Major ion concentration changes during myocardial ischemia 23
1.3.2.1 Increase in $[K^+]_o$ 23
1.3.2.2 Accumulation of $[Na^+]_i$ 24
1.3.2.3 Changes in $[Ca^{2+}]_i$ distribution 25
1.3.2.4 Changes to extracellular and intracellular $[H^+]$ 26
1.4 Effect of acidosis on major ion channels 27
1.5 Effects of external acidosis on hERG channels 31
1.5.1 External protons reduce the maximum conductance of hERG channels by directly blocking the pore 32
1.5.2 External protons right-shift the voltage-dependence of activation and slow activation kinetics 33
1.5.3 External protons accelerate hERG channel deactivation 33
1.5.4 Effects of divalent cations on hERG channel gating mimic those of external protons 35
1.5.5 External protons impair the protective nature of hERG channels 37
1.6 Zebrafish *Danio rerio* as a translational heart model 38
1.6.1 Zebrafish heart anatomy and electrophysiology 40
1.6.2 Zebrafish ether-à-go-go related gene (zERG) 43
1.7 Overview and objectives 44

Chapter 2. Materials and Methods....46
2.1 Molecular biology - mutagenesis 46
2.2 Expression system 47
2.2.1 Oocyte preparation 48
2.2.2 Oocyte injection 49
2.3 Electrophysiology 50
2.3.1 Two-Electrode Voltage-Clamp (TEVC) 50
2.3.2 Voltage-Clamp Fluorimetry (VCF) 51
2.3.3 Cut-Open Vaseline Gap Voltage-Clamp (COVG) 54
2.4 Voltage protocols 56
2.4.1 Voltage-dependence of activation 56
2.4.2 Voltage-dependence of deactivation 56
2.4.3 Deactivation kinetics 57
2.5 Data analysis 57
2.5.1 Voltage-dependence relationship 57
2.5.2 Deactivation time course 58
2.6 Zebrafish optical mapping 58
2.6.1 Dye and labeling 61
2.6.2 Solutions 61
2.6.3 Zebrafish heart isolation procedure 61
2.6.4 Data collection and analysis 62

Chapter 3. External Protons Destabilize The Activated Voltage Sensor in hERG Channels. 65
3.1 Overview 65
3.2 Introduction 65
3.3 Material and Methods 68
3.3.1 Molecular Biology 68
3.3.2 Solutions 68
3.3.3 Electrophysiology and Data Analysis 69
3.3.4 Voltage-Clamp Fluorimetry (VCF) 70
3.4 Results 71
3.4.1 Effects of Proton and Cd^{2+} on hERG Activation and Deactivation. 71
3.4.2 Role of Individual Acidic Residues In The S2/S3 Cation Binding Pocket 76
3.4.3 Role of Double and Triple Neutralization of the Metal Cation Binding Pocket 78
3.4.4 External Protons Destabilize the Activated Voltage Sensor 80
3.5 Discussion 82
3.5.1 Protonation Site for Modulation of Activation Gating 82
3.5.2 Competition Between Protons and Cd^{2+} Within Cation Binding Pocket 83
3.5.3 The Mechanism of Action of Protons on Activation Gating 84
3.5.4 Other Protonation Sites Affecting hERG Gating 84

Chapter 4. External Protons Destabilize the Relaxed Conformation of the Voltage Sensor 86

4.1 Overview 86
4.2 Introduction 87
4.3 Materials and Methods 90
4.3.1 Molecular Biology 90
4.3.2 Oocyte preparation and injection 90
4.3.3 Electrophysiology 91
4.3.4 Cut-Open Voltage Clamp 91
4.3.5 Voltage-Clamp Fluorimetry 92
4.3.6 Data Analysis 92
4.3.7 Supplementary Material 93
4.4 Results 93
4.4.1 Acidic pH reduces mode-shift behaviour in hERG channels 93
4.4.2 Acidic pH destabilizes the relaxed state of the voltage sensor 98
4.4.3 Destabilization of voltage sensor relaxation by protons is mediated by an extracellular acidic site, D509 103
4.4.4 Voltage sensor relaxation contributes to the hERG protective current conducted in the early refractory period of the action potential 107
4.5 Discussion 111
4.5.1 The effects of acidic pH support a correlation between mode-shift and deactivation kinetics 112
4.5.2 External protons destabilize the relaxed voltage sensor 112
4.5.3 Site and mechanism of action of external protons 116
4.5.4 The stability of the relaxed state modulates deactivation kinetics in hERG channels 119
4.5.5 Destabilization of the relaxed state by external protons compromises hERG protective currents in response to premature stimulations 120
4.5.6 An activator compound that slows deactivation kinetics rescues hERG protective currents 120
4.6 Supplementary Material 122

Chapter 5. Acidosis delays repolarization in optically mapped adult zebrafish whole hearts as a result of hERG channel inhibition 124
5.1 Overview 124
5.2 Introduction 125
5.3 Material and Methods 128
5.3.1 Zebrafish husbandry 128
5.3.2 Heart Isolation and reagents 128
5.3.3 Optical Mapping 129
5.3.3.1 Data Analysis 130
5.4 Results 131
5.4.1 External acidosis prolonged the action potential duration in adult zebrafish hearts. 131
5.4.2 The effect of acidosis on the ventricular APD is acute and extracellular 133
5.4.3 The presence of dofetilide greatly reduced the prolongation of the ventricular APD by external acidosis. 137

5.4.4 External acidosis flattened the slope of the electrical restitution curve 140
5.5 Discussion 142
5.5.1 Prolongation of the ventricular action potential by acute external acidosis is an extracellular effect. 142
5.5.2 External acidosis increased AP triangulation, which is a strong predictor for Torsade de Pointes. 144
5.5.3 Dofetilide and external acidosis compete for block of I_{Kr} current. 145
5.5.4 The slope of the electrical restitution curve as a predictor of arrhythmia. 146
5.5.5 Limitations 147

Chapter 6. General Discussion and Future Directions 149
6.1 hERG activation gating 149
6.1.1 Modulation of hERG activation by external protons 149
6.1.2 Extracellular protons altered the voltage-dependence of hERG activation by protonating D456, D460, and D509. 150
6.2 hERG deactivation gating 153
6.2.1 Modulation of slow hERG deactivation 153
6.2.2 Slow hERG deactivation as a result of voltage sensor relaxation 155
6.3 Using a translational model to assess arrhythmogenicity 156
6.4 Final summary and future directions 158

References 161

List of Tables

Table 1-1: Kv channel classification 2

Table 4-1: Activation and deactivation G-V Boltzmann fit parameters recorded with physiological durations. 110

Table 4-2: pH-dependence of steady-state activation and deactivation G-V Boltzmann fit parameters. 110

Table 4-3: Charge-voltage and fluorescence-voltage relationship Boltzmann fit parameters for activation and deactivation. 110

Table 4-4: Rates and factors for the Markov model 111

List of Figures

Figure 1.1 - Ventricular cardiomyocyte action potential with major underlying ionic currents. 5
Figure 1.2 - The transient hERG current in response to premature stimuli 8
Figure 1.3 - hERG channel architecture 13
Figure 1.4 - hERG channel gating 15
Figure 1.5 - Zebrafish heart anatomy and the ionic currents underlying the ventricular AP. 42
Figure 2.1 – Schematic of Voltage-Clamp Fluorimetry Apparatus 53
Figure 2.2 – Schematic of Cut-Open Voltage Clamp (COVG) Apparatus 55
Figure 2.3 – Schematics of the optical mapping setup 60
Figure 2.4 - Zebrafish heart cannulation 62
Figure 2.5 - Optical mapping example recordings 64
Figure 3.1 - Competitive effects of Cd^{2+} and protons on hERG activation, but not deactivation. 75
Figure 3.2 - Role of individual acidic residues in the S2/S3 metal ion binding pocket on the pH sensitivity of activation. 77
Figure 3.3 - Three acidic residues mediate the pH dependence of activation. 79
Figure 3.4 - External protons destabilize the activated voltage sensor. 81
Figure 4.1 – hERG mode-shift is reduced by acidic pH. 95
Figure 4.2 - The pH-sensitivity of mode-shift behaviour is similar to that of deactivation kinetics. 97
Figure 4.3 - Voltage sensor mode-shift. 100
Figure 4.4 - Voltage sensor mode-shift is reduced by acidic pH. 102
Figure 4.5 - Neutralization of D509 mimics the effect of protons on voltage sensor mode-shift. 104
Figure 4.6 - Mode-shift is greatly diminished and is pH-independent in D509A mutant channels. 106
Figure 4.7 - The small molecule RPR260243 enhances hERG protective current. 109
Figure 4.8 - Model of hERG voltage sensor relaxation. 115
Figure 5.1 - External acidosis prolonged the ventricular AP. 132
Figure 5.2 - External acidosis acts extracellularly to prolong the ventricular AP. 135
Figure 5.3 - Acidosis increases triangulation of the ventricular AP. 136
Figure 5.4 – Dofetilide block of I_{Kr} attenuates the effect of external acidosis in the ventricular APD. 139
Figure 5.5 - External acidosis flattened the electrical restitution curve (ERC) and is pro-arrhythmogenic. 141
Figure 6.1 - Cartoon representation of the resting to activated state of the hERG voltage sensor. 152

List of Acronyms

AP	Action Potential
APD	Action Potential Duration
Cav	Voltage-gated Calcium Channel
CICR	Calcium-Induced Calcium Release
CNBHD	Cyclic Nucleotide Binding Homology Domain
COVG	Cut-open Vaseline Gap
DAD	Delay-after Depolarization
DRLP	Long Pass Dichoic Mirror
EAD	Early-after Depolarization
FV	Fluorescence-Voltage Relationship
GV	Conductance-Voltage Relationship
HCN	Hyperpolarization-activated Cyclic Nucleotide Gated Channel
hERG	Human-*ether-à-go-go*
hIPSC-CM	Cardiomyocytes derived from Human Induced Pluripotent Stem Cell
HR	Heart Rate

Ig	Gating current
I_{kr}	Rapidly delayed rectifier potassium current
I_{ks}	Slow delayed rectifier potassium current
K_v	Voltage-gated Potassium Channel
LP	Long-Pass Filter
LQTS	Long QT syndrome
$MgOR_2$	Magnesium Oocytes Ringer solution
Nav	Voltage-gated Sodium Channel
NCX	Sodium-Calcium Exchanger
ND96	Extracellular recording solution
PAS	Per-Arnt-Sim
PCR	Polymerase Chain Reaction
PD	Pore Domain
PMT	Photomultiplier Tube
QV	Gating Charge-Voltage Relationship
RH 237	*N*-(4-Sulfobutyl)-4-(6-(4-(Dibutylamino)phenyl)hexatrienyl)Pyridinium

SEM	Standard Error Mean
SOS	Standard Oocyte Solution
SR	Sarcoplasmic Reticulum
TEVC	Two-electrode Voltage-Clamp
TMRM	Tetramethylrhodamine-5-Maleimide
VCF	Voltage-Clamp Fluorimetry
VSD	Voltage-Sensing Domain
WT	Wild Type
ZF	Zebrafish

Glossary

Activation	The opening of the channel following depolarization of membrane voltage
Deactivation	The closing of the channel following repolarization of membrane voltage
Depolarization	A change in membrane potential to voltages more positive than the resting membrane potential
Gating Current	Currents produced by movement of charged residues across the membrane
Hyperpolarization	A change in membrane potential to more negative voltages than resting membrane potential
Ionic Current	Currents induced by ions flowing through the pore of the channel
Mode-Shift	The separation in the voltage-dependence of activation and deactivation
Repolarization	A return of membrane potential toward the resting membrane potential after depolarization

Chapter 1. Introduction

1.1 Voltage-gated K^+ channel diversity

Potassium ion channels are transmembrane proteins that form K^+-selective pores, which conduct potassium ions across the membrane down their electrochemical gradient. The potassium-selective channels are the largest and most diverse group of ion channels. The voltage-gated K^+ channels (K_v) form the largest sub-family with over 40 genes cloned from humans (Gutman *et al.*, 2005). K_v channels transition through open, closed, or inactivated (non-conducting) states, termed gating, in response to changes in membrane voltage to regulate the conduction of K^+. Because of this, K_v channels play a critical role in the regulation of electrical activity in excitable cells within the body, which includes resetting the cells back to resting state, regulating firing rate and duration of neuronal and cardiac action potentials (Hille, 2001; Korn & Trapani, 2005).

K_v channels are broadly classified into 12 families (K_v1 to K_v12), which includes *Shaker*-related (K_v1), *Shab*-related (K_v2), *Shaw*-related (K_v3), *Shal*-related (K_v4), *eag* (K_v10), *erg* (K_v11), and *elk* (K_v12) sub-families (See Table 1-1). There are also four additional sub-families, K_v5, K_v6, K_v8, and K_v9, which encode “modifier” subunits that do not form functional channels on their own, but form heterotetramers with K_v2 subunits and modify their behaviour. One factor that contributes to the diversity of the K_v channel family is heteromultimerization. Each of the K_v genes encode a single subunit, and four subunits are required to form a functional channel. K_v channels can form homotetramers, but can also form heterotetramers within the same sub-family and this can have diverse biophysical functional consequences (Gutman *et al.*, 2005). Another factor that increases the diversity are accessory such as β subunits for K_v1 and K_v2, KCHIP1 for K_v4, calmodulin for K_v10 and minK (K_v11), which modify channel properties. In addition, many K_v channels can be post-translationally modified by phosphorylation (Ismailov & Benos, 1995), N-linked glycosylation (Gong *et al.*, 2002; Watanabe *et al.*, 2004) and ubiquitinylation (Henke *et al.*, 2004). In this thesis, I am interested in the *KCNH2* gene in the $K_v11.1$ family that encodes the pore-forming subunit of the *human-ether-à-go-go related gene* (hERG) potassium channel in the heart.

Table 1-1: Kv channel classification

α-subunit	*Gene Name* / Protein Name	Category
$K_v1.1$	*KCNA1* / KCNA1	*Shaker*-related family
$K_v1.2$	*KCNA2* / KCNA2	
$K_v1.3$	*KCNA3* / KCNA3	
$K_v1.4$	*KCNA4* / KCNA4	
$K_v1.5$	*KCNA5* / KCNA5	
$K_v1.6$	*KCNA6* / KCNA6	
$K_v1.7$	*KCNA7* / KCNA7	
$K_v1.8$	*KCNA10* / KCNA10	
$K_v2.1$	*KCNB1* / KCNB1	*Shab*-related family
$K_v2.2$	*KCNB2* / KCNB2	
$K_v3.1$	*KCNC1* / KCNC1	*Shaw*-related family
$K_v3.2$	*KCNC2* / KCNC2	
$K_v3.3$	*KCNC3* / KCNC3	
$K_v3.4$	*KCNC4* / KCNC4	
$K_v4.1$	*KCND1* / KCND1	*Shal*-related family
$K_v4.2$	*KCND2* / KCND2	
$K_v4.3$	*KCND3* / KCND3	
$K_v5.1$	*KCNF1* / KCNF1	Modifier
$K_v6.1$	*KCNG1* / KCNG1	Modifiers
$K_v6.2$	*KCNG2* / KCNG2	
$K_v6.3$	*KCNG3* / KCNG3	
$K_v6.4$	*KCNG4* / KCNG4	
$K_v7.1$	*KCNQ1* / KCNQ1	*KVLQT* *KQT2*
$K_v7.2$	*KCNQ2* / KCNQ2	
$K_v7.3$	*KCNQ3* / KCNQ3	
$K_v7.4$	*KCNQ4* / KCNQ4	
$K_v7.5$	*KCNQ5* / KCNQ5	
$K_v8.1$	*KCNV1* / KCNV1	Modifiers
$K_v8.2$	*KCNV2* / KCNV2	
$K_v9.1$	*KCNS1* / KCNS1	Modifiers
$K_v9.1$	*KCNS2* / KCNS2	
$K_v9.1$	*KCNS3* / KCNS3	
$K_v10.1$	*KCNH1* / KCNH1	*eag1*
$K_v10.2$	*KCNH5* / KCNH5	*eag2*
$K_v11.1$	*KCNH2* / KCNH2 (hERG)	*erg1*
$K_v11.2$	*KCNH6* / KCNH6	*erg2*
$K_v11.3$	*KCNH7* / KCNH7	*erg3*
$K_v12.1$	*KCNH8* / KCNH8	*elk1, elk3*
$K_v12.2$	*KCNH3* / KCNH3	*elk2*
$K_v12.3$	*KCNH4* / KCNH4	*elk1*

1.2 HERG potassium channels

The "*ether-à-go-go"* family was first discovered and named by Kaplan and Trout in 1969 from the observation that the *Drosophila melanogaster* fruit fly exhibits leg shakes, following ether anesthesia, which resembles go go dancers (Kaplan & Trout, 1969). The *KCNH2* gene that encodes the hERG potassium channel was then cloned in 1994 by Warmke and Ganetzky through screening the human hippocampal cDNA with a mouse homolog of the *ether-à-go-go* gene (Warmke & Ganetzky, 1994). The *KCNH2* gene was shown to be located on chromosome 7, and mutations in the *KCNH2* gene had been identified as the basis of chromosome 7-associated long QT syndrome (LQT syndrome type 2) (Curran *et al.*, 1995). An early study discovered that there were two kinetically distinct components of the delayed rectifier K^+ currents in ventricular cardiac myocytes: A slow activating component, I_{ks}, and a rapid component, I_{kr} (Noble & Tsien, 1969). In 1990, Sanguinetti and Jurkiewiecz showed that the rapid component, I_{kr}, can be blocked by using class III antiarrhythmic drug, E4031, to which I_{ks} was resistant (Sanguinetti & Jurkiewicz, 1990). Subsequent characterization of hERG channel function revealed it to be the molecular correlate of I_{kr} and that reduction in hERG current by inherited mutations or drug block is associated with LQT syndrome and increased susceptibility to cardiac arrhythmia (Curran *et al.*, 1995; Sanguinetti *et al.*, 1995; Trudeau *et al.*, 1995). Due to this, an interest has emerged to better understand the molecular and structural basis underlying the gating machinery, drug interactions, small-molecule activator interactions, and assessment of arrhythmogenicity of hERG channels, which can assist clinical interventions for both inherited and acquired LQTS type 2.

1.2.1 Physiological role of hERG channels

hERG channels are expressed in numerous tissues including the brain, tumour cells, and the heart. The role of hERG channels is especially well characterized in the heart where they have been shown to play a crucial role in the cardiac action potential (Sanguinetti & Tristani-Firouzi, 2006). The cardiac action potential morphology and duration arises as a result of the balance of a collection of ion channels. The ventricular cardiac action potential, for example, can be divided into five phases (0-4). Phase 0 is the upstroke that reflects the influx of Na^+ through the fast activating $Na_v1.5$ channels, which produce I_{Na} that rapidly depolarize the cell. Phase 1 occurs with the activation of $K_v4.3$

transient outward K^+ channels, which produces I_{to} that quickly repolarizes the cell to produce a signature “spike and dome” phenotype, particularly in the epicardial regions, which shows a rapid repolarization immediately following depolarization. Phase 2 is the plateau phase where a balance of depolarizing and repolarizing currents are activated to keep the cell depolarized long enough for Ca^{2+} to facilitate muscle contraction. Membrane depolarization activates $Ca_v1.2$, L-type Ca^{2+} channels, that produce I_{CaL} and allows Ca^{2+} influx to facilitate calcium-induced calcium release (CICR) from the sarcoplasmic reticulum, which is the mechanism that drives the increase in cytoplasmic Ca^{2+} required for muscle contraction. Also, during this phase, the sodium-calcium exchanger (NCX) operates in the forward mode, driven by the flow of Na^+ down the concentration gradient into the cell, while extruding cytoplasmic Ca^{2+}. NCX exchanges three Na^+ ions for every Ca^{2+} ion, thus producing a net depolarizing current. Membrane depolarization during phase 2 also activates the delayed rectifying potassium channel, $K_v7.1$, which produces the I_{ks} repolarizing current that is crucial in maintaining a balance during this plateau phase. Phase 3 is the repolarization phase where the I_{ks}, conducted by $K_v7.1$ channels and the resurgent I_{kr} current, conducted by hERG channels, repolarize the cell back to the resting potential. Phase 4 is the resting phase where mostly the $K_{ir}2.1$ channel, that produce the I_{k1} current, is responsible for maintaining the resting membrane potential until the next firing of an action potential (Figure 1.1).

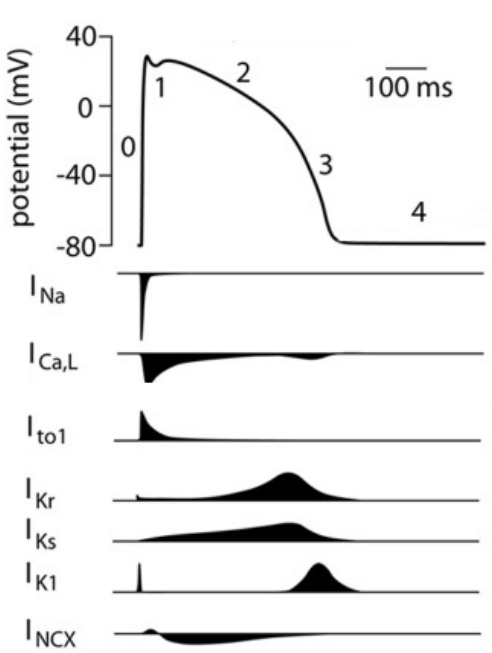

Figure 1.1 - Ventricular cardiomyocyte action potential with major underlying ionic currents.

Schematic representation of a single human ventricular action potential with the major underlying ionic currents. Permission from (Hoekstra *et al.*, 2012). Currents below the line represents depolarizing current, and currents above the line represents repolarizing current.

The physiological importance of hERG channels is underscored by loss-of-function mutations or drug block that reduce the hERG I_{kr} current and lead to long QT syndrome (LQTS). LQTS is a cardiac repolarization disorder that predisposes the individual to potentially lethal arrhythmia and sudden cardiac death (Sanguinetti & Tristani-Firouzi, 2006). In the electrocardiogram (ECG), the QT interval represents the time required for repolarization of the ventricles during each cardiac cycle. LQTS manifests as a prolongation of the QT interval as a result of an increase in the action potential duration due to delay repolarization. LQTS can develop into a type of ventricular arrhythmia called *Torsade de Pointe* (TdP), which means “twisting of the points”, and can lead to ventricular fibrillation and sudden cardiac death (Curran *et al.*, 1995; Sanguinetti *et al.*, 1996). LQTS can be congenital (inherited) or acquired, and there are at least 16 genes that have been identified to be associated with LQT syndrome. The most common types (LQT1, LQT2 and LQT3) account for approximately 75% of all genotype-positive cases (Schwartz *et al.*, 2012, 2013). More than 500 LQT-associated mutations have been identified within the hERG channel, which result in long QT syndrome type 2 (LQT2) and account for approximately 40% of all LQTS cases (Perry *et al.*, 2016). The most prevalent are missense mutations that lead to mis-folding of the channel protein that impairs trafficking of the channel to the membrane. Other mutations can reduce hERG current by altering normal gating mechanisms. For example, R56Q is a LQT syndrome type 2 causing mutation that dramatically accelerates deactivation kinetics (Chen *et al.*, 1999; Sanguinetti & Tristani-Firouzi, 2006). Acquired LQT syndrome can be drug- or environment-induced and results from an inhibition of the hERG current. hERG channels are highly sensitive to drug blockade and are blocked by a diverse range of drugs (Mitcheson *et al.*, 2000), leading to the need for new drugs to be screened routinely against hERG channels. Mutagenesis studies have identified a high-affinity binding site for drugs in the inner central cavity below the selectivity filter. Identification of the location of the pore gate supports the idea that the inner cavity of the hERG channel is large and may be a contributing factor to its high propensity to drug interactions (Thouta *et al.*, 2014). Furthermore, recent cryo-EM structures of the open state of the hERG channel have revealed hydrophobic pockets and a focused electronegative region within the central cavity that is unique to hERG channels, which may aid its high susceptibility to drug block (Wang & MacKinnon, 2017).

While there is strong evidence that hERG channels play a crucial role in the repolarization phase and therefore in the modulation of the action potential duration, hERG

channels may also act to protect against unwanted depolarization, that interrupt phases 2, 3, or 4 of the cardiac action potentials, such as early afterdepolarizations (EADs) or delayed afterdepolarizations (DADs) (Weiss *et al.*, 2010; Antzelevitch & Burashnikov, 2011). The underlying ionic contribution to the development of EADs and DADs are distinct and different. EADs develop between phases 2 and 3 of the cardiac action potential and are usually due to an impaired balance of several different ionic currents, such as an increased influx of Ca^{2+} current through L-type Ca^{2+} channels, impaired I_{ks} and I_{kr} repolarization currents, or persistent slow non-inactivating Na^{+} current (Weiss *et al.*, 2010). DADs develop during phase 4 of the cardiac action potential and is driven mainly by the activity of the NCX (Antzelevitch & Burashnikov, 2011). Elevated concentration of cytoplasmic Ca^{2+} drives NCX to extrude Ca^{2+} in exchange for Na^{+} leading to an overall depolarizing Na^{+} current that occurs following the termination of the action potential (Blaustein & Lederer, 1999). EADs and DADs can develop even in healthy individuals; however only large afterdepolarizations may lead to a triggered activity, which is defined as an ectopic firing of an action potential. Sustain triggered activity can degenerate into ventricular fibrillation (Antzelevitch & Burashnikov, 2011). In action potential clamp experiments using Chinese hamster ovary (CHO) cells, hERG channels pass a robust transient current when subjected to premature depolarization pulses (Figure 1.2), which mimic the occurrence of EADs or DADs (Yu Lu *et al.*, 2001). With varying interpulse intervals, the transient hERG currents produced a biphasic profile with an increase in current amplitude followed by a gradual decrease, which coincide, kinetically, with recovery from inactivation and slow deactivation, respectively (Figure 1.2) (Yu Lu *et al.*, 2001). This outward repolarizing hERG current, which peaks around the termination of the action potential and remains robust long into the refractory period has been suggested to protect against afterdepolarization-induced triggered activities, although this remains to be tested.

These observations show that hERG channels play a critical physiological role. This role is due to their unique gating kinetics and voltage-dependence which I will address in the next sections.

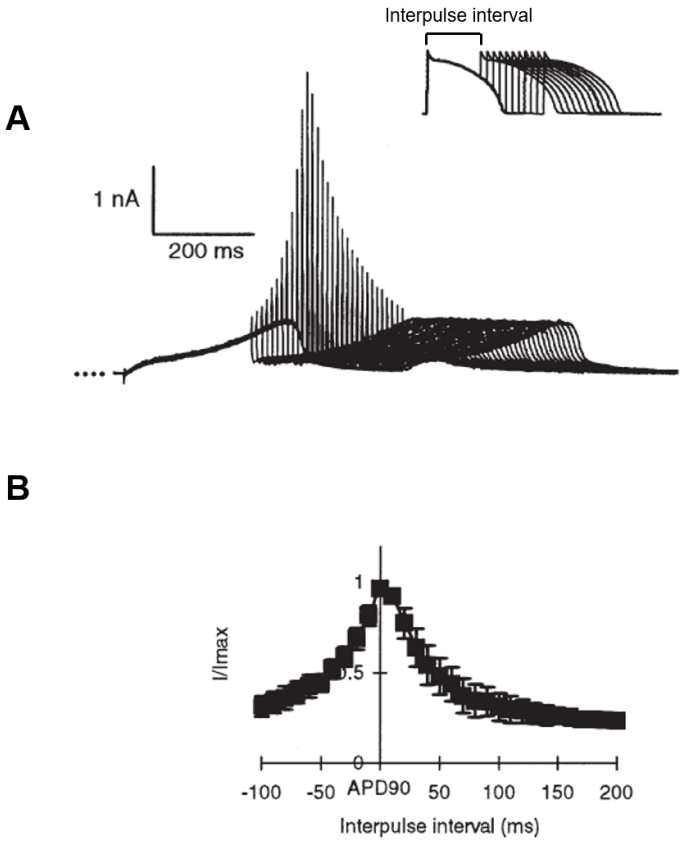

Figure 1.2 - The transient hERG current in response to premature stimuli

A. Typical examples of family of currents recorded in CHO cells in response to premature stimuli in a paired action potential clamp protocol shown in the *inset*. The second action potential is introduced at times corresponding to APD_{90} - 100 ms to APD_{90} + 200 ms and and the normalized peak transient current is plotted in **B.** Permission from (Yu Lu *et al.*, 2001).

1.2.2 Features of the hERG channel architecture

The features of the hERG channel architecture dictate its physiological function. The *Streptomyces lividans* (KcsA) prokaryotic K^+ channel was the first atomic resolution structure of an ion channel determined by X-ray crystallography. With a resolution of 3.2 angstroms the structure gave the first glimpse of a K^+ channel structure with four identical subunits assembled in a teepee, or cone, and a 12-angstrom long selectivity filter at the outer end of the pore (Doyle *et al.*, 1998). Subsequent effort led to crystallization of voltage-gated potassium channels: $K_v1.2$ (Long, 2005; Long *et al.*, 2005), and the $K_v1.2/K_v2.1$ chimera (Long *et al.*, 2007). Recent advancement in cryo-EM technology led to the structural determinant of the *eag1* channel bound to calmodulin with a 3.78 angstrom resolution (Whicher & MacKinnon, 2016) and in the following year the hERG cryo-EM structure in the open state at 3.8 angstrom resolution (Wang & MacKinnon, 2017). These structures not only provide valuable insights to the normal gating properties of the channels, but also act as models to predict structural changes under physiological and pathophysiological conditions that will further the understanding of the role these potassium channels play *in vivo*.

The *KCNH2* gene encodes the pore-forming subunit of the hERG potassium channel (Figure 1.3). Like other K_v channels, each subunit consists of six membrane-spanning domains (S1-S6), and large cytoplasmic N- and C- terminus domains. The S1-S4 confers the voltage sensing domain (VSD). Most importantly, the S4 transmembrane segment contains six positive residues (Arg or Lys): K525, R528, R531, R534, R537, and K538 that moves in responds to change in membrane voltage, acting as a primary voltage sensor. There are also six negative residues within the voltage sensing domain: D411 in S1, D456, D460, and D466 in S2, D501 and D509 in the S3. These negative residues have been suggested to play an important role in forming stabilizing interactions with the basic residues in the voltage sensor that dramatically alter the channel gating (See section 1.2.3.1 for more details) (Liu *et al.*, 2003).

The pore domain (PD) is formed by the S5-S6 transmembrane segments and are joined by the S5-S6 linker containing a re-entrant pore helix, or P-loop (Figure 1.3). The functional channel is a tetramer with the pore domains from four subunits aligned to form the central ion-conducting pathway. The X-ray crystal structure of the closed state bacterial K^+ channel, KcsA, revealed a highly conserved region, consisting of five residues

with the consensus sequence (T/S-V/I/L-G-F/Y-G), within the P-loop called the selectivity filter (Vandenberg *et al.*, 2012). The carbonyl backbone of the oxygen atoms in these amino acids align towards the central ion conducting pore to form a hydration shell around K^+ ions and coordinates the movement of K^+ ions in and out of the cell. The hERG channel has a high selectivity for K^+ over Na^+ (p_K: p_{Na} > 100:1) (Sanguinetti *et al.*, 1995). Interestingly, the hERG potassium channel selectivity filter is constructed by the residues SVGFG, which is slightly different to that in other K_v channels such as *Shaker* or K_v1.2, where TVGYG forms the filter (Labro & Snyders, 2012). The recent hERG cryo-EM structure shows that the selectivity filter exhibits a slightly different conformation compared to the closely related eag1 channel (Wang & MacKinnon, 2017), which may contribute to the unique gating process of hERG potassium channels.

An important component in the coupling between the voltage sensor domain (S1-S4) and the pore domain (S5-S6) is the S4-S5 linker. Numerous studies have been done to understand how the VSD can translate to the movement of the PD during channel gating (Sanguinetti & Xu, 1999; Long *et al.*, 2005; Van Slyke *et al.*, 2010; Blunck & Batulan, 2012; Tan *et al.*, 2012; de la Peña *et al.*, 2013; Hull *et al.*, 2014). The VSD and the PD are joined by the S4-S5 linker (Figure 1.3). It is a short amphipathic α-helical linker that runs parallel to the intracellular side of the membrane, with the hydrophobic side facing the lipid membrane, and the hydrophilic side exposed to the cytoplasm (Wang & MacKinnon, 2017). The recent hERG cryo-EM structure suggests this linker interacts with its own S5 segment (non-domain swapped) (Wang & MacKinnon, 2017), contrary to that seen in Shaker, where the linker interacts with the neighbouring S5 segment (domain swapped). It is proposed that the energy driving the opening of the pore is generated by the voltage sensor upon changes in the membrane voltage. The transferring of this electrical energy from the voltage sensor to the pore domain, triggering the mechanical opening of the pore, is termed the electromechanical coupling (Blunck & Batulan, 2012). The S4-S5 linker acts as a covalent link between the VSD and PD to facilitate this electromechanical coupling. The first mutagenic study on the functional role of S4-S5 linker in hERG was done in 1999. In this study they examined the functional consequences of mutating the two acidic residues in the S4-S5 linker to neutral (alanine) or basic residues (lysine): D540A, D540K, E544A and E544K. Neutralization mutations accelerated the activation kinetics while the charge reversal mutations did the opposite (Sanguinetti & Xu, 1999). All mutant channels accelerated the deactivation kinetics but had no effect on inactivation parameters

(Sanguinetti & Xu, 1999). Subsequent studies found that position G546 is crucial in stabilizing the closed-state of the hERG channel, and differentially modulates deactivation rate depending on which residue is substituted (Van Slyke 2012). Follow-up studies suggest that the flexibility of the linker is important in the hERG channel activation (Hull *et al.*, 2014). Other studies suggest that the S4-S5 linker interacts with the N-terminus and C-terminus to facilitate the deactivation of the hERG channel (de la Peña *et al.*, 2011, 2015, 2018). Furthermore, another study created a split channel construct where two halves of the hERG channel are created, one half is the VSD, and the other is the PD, disconnected within the S4-S5 linker by introducing a stop codon. They then co-expressed these two halves in *Xenopus* oocytes. Their study illustrated that the S4-S5 linker does not need to be covalently linked to form a functional conducting channel, but activation and deactivation gating processes are dramatically altered, suggesting the importance of the S4-S5 linker in regulating normal hERG channel gating (de la Peña *et al.*, 2018). This observation, combined with the short non-domain swapped S4-S5 linker (Wang & MacKinnon, 2017), suggests that there may a different coupling mechanism between the VSD and PD in hERG compared with other K_v channels. Overall these studies solidify the importance of this unique feature of the S4-S5 linker as a crucial regulator of the gating machinery in the hERG channel.

Apart from the S4-S5 linker, the large cytoplasmic N-terminus of the hERG channel plays a critical role in gating of the channel and is structurally well conserved amongst the closely related family channels such as *drosophila* elk and mouse eag channels (Adaixo *et al.*, 2013). The N-terminus can be divided into distal and proximal domains, where the distal N-terminus consists of the Per-Arnt-Sim (PAS) domain (residues 1-136), and the proximal region makes up the remainder of the N-terminus up to the first transmembrane helix (residues 136-397) (de la Peña *et al.*, 2013). Crystal structures of the PAS domain revealed a hydrophobic patch, which is important in interaction with the PAS domain from the neighbouring subunit. However, the N-terminus also participates in non-PAS domain interactions that are functionally important, such as with the S4-S5 linker and the C-terminus (Fernández-Trillo *et al.*, 2011; Adaixo *et al.*, 2013; de la Peña *et al.*, 2015, 2018)

The main feature of the C-terminus in hERG channels is the well conserved cyclic nucleotide binding homology domain (cNBHD) within the EAG family, which share similarities to cyclic nucleotide gated (cNG) and hyperpolarization-activated cyclic nucleotide-gated (HCN) channels. However, in hERG channels the cNBHD lacks the

critical arginine residue that binds to the phosphate head group of cAMP and does not appear to be directly regulated by binding of cyclic nucleotides (Brelidze *et al.*, 2012, 2013; Marques-Carvalho *et al.*, 2012). X-ray crystallography revealed a region similar to the binding pocket of cyclic nucleotide binding domains (Haitin *et al.*, 2013) that is occupied by an “intrinsic ligand” comprising of side chains that loop back to occupy the binding site in hERG channels (Brelidze *et al.*, 2012, 2013; Marques-Carvalho *et al.*, 2012; Zhao *et al.*, 2017). Mutation analysis suggests that the intrinsic ligand is important in stabilizing the open pore and the fully activated conformation of the voltage sensor (Zhao *et al.*, 2017). Deletion of the cNBHD in hERG channel produces an increase in the slope (k) of the activation G-V curve and an accelerated deactivation suggesting that the intact cNBHD is important in the regulation of gating transitions during activation and deactivation, and interaction with the N-terminus is suggested to be important for shaping the voltage-dependence of activation and deactivation. The cNBHD is also connected to the S6 transmembrane helix via the C-linker, which has been shown to serve a functional role by directly interacting with the PAS domain (Gustina & Trudeau, 2011). Despite numerous studies on the complex interplay between cytoplasmic PAS domain, S4-S5 linker, and cNBHD, the exact interactions involved in the coupling between the movement of the S4 voltage sensor and the pore, during activation and deactivation, are still poorly understood.

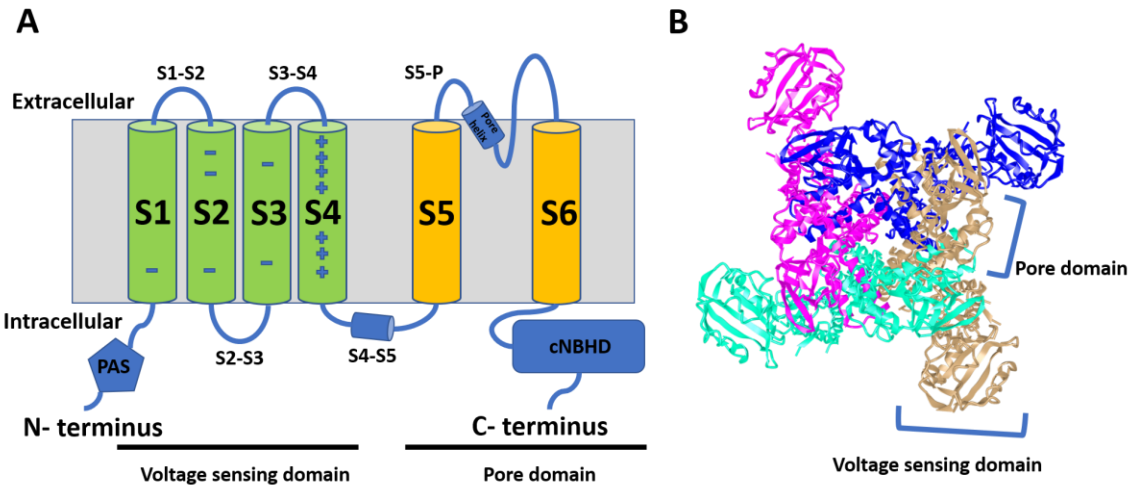

Figure 1.3 - hERG channel architecture

A. Schematic of a single α-subunit of the hERG channel comprising the voltage sensing domain (S1-S4) and the pore domain (S5-S6). Key features of the hERG channel consist of the PAS and cNBHD, short S4-S5 linker, the pore helix, six acidic residues between S1-S3, and six basic residues in the S4. **B.** Top down view of the ribbon diagram of the cryo-EM structure of the hERG channel assembled as a tetramer with the central conducting pore formed by the pore domains from all four subunits. Each subunit is highlighted by a different colour with permission from (Wang & MacKinnon, 2017).

1.2.3 Unique hERG channel gating

hERG channel gating processes are unique and unusual. Upon depolarization the channel activates slowly from the closed to the open state and quickly inactivates, which limits hERG channel current during the early phases of the cardiac action potential. Following repolarization, the hERG channel quickly recovers from inactivation and slowly deactivates leading to a large resurgent current that contributes to the repolarization of the cardiac action potential (Figure 1.4). The voltage-dependence and kinetics of activation, deactivation and inactivation were measured experimentally in *Xenopus* oocytes and used as constraints to construct a five state linear Markov model of hERG channel gating. hERG channel gating behaviour is best described by a model with three closed states, one open state and one inactivated state (*Scheme 1*, with permission from Wang et al 1997) (Wang *et al.*, 1997). α, β represent voltage-dependent forward and reverse rates, respectively, and k_f and k_b are voltage-independent forward and reverse rates, respectively.

$$C_0 \underset{\beta_{a0}}{\overset{\alpha_{a0}}{\rightleftharpoons}} C_1 \underset{k_b}{\overset{k_f}{\rightleftharpoons}} C_2 \underset{\beta_{a1}}{\overset{\alpha_{a1}}{\rightleftharpoons}} O \underset{\beta_i}{\overset{\alpha_i}{\rightleftharpoons}} I$$

Scheme 1

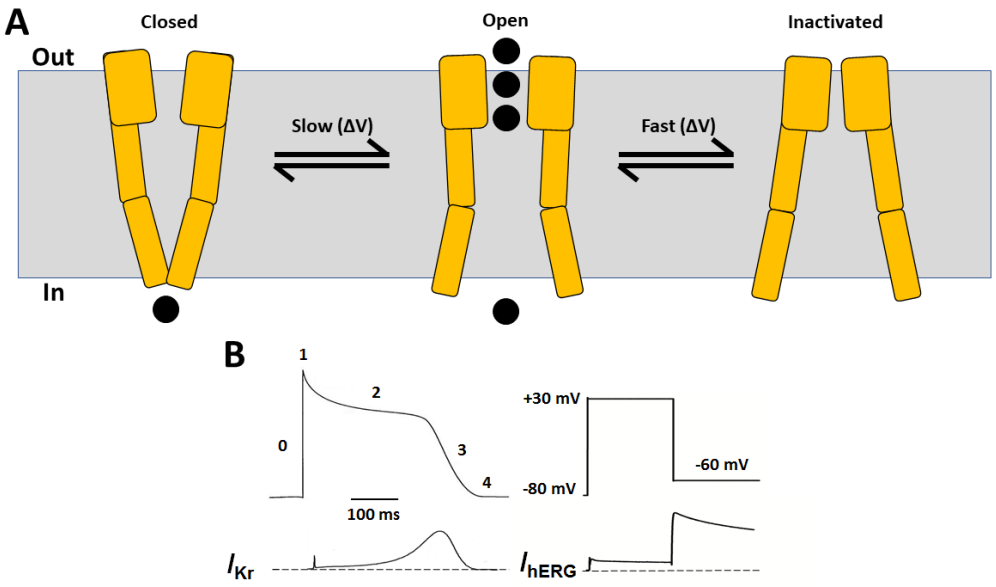

Figure 1.4 - hERG channel gating

A. Cartoon representation of the state transitions during hERG channel gating. Upon membrane voltage change, the channel transitions between closed and open states more slowly than between open and inactivated states. The result from this unusual gating is a small hERG current during early phases of the cardiac action potential, but a large resurgent current during the repolarization phase (phase 3) (**B**). Experimentally, a square depolarization pulse to +30 mV showed little hERG current, however, repolarization to -60 mV recovers the channels from inactivation, producing a large hERG current that decays slowly.

1.2.3.1 Molecular basis of hERG activation

The hERG channel has unusually slow activation following depolarization, with a time course of ~50 ms at +60 mV (Tan *et al.*, 2012) compared to < 2 ms in *Shaker* channels (Hoshi *et al.*, 1994). To measure the kinetics of hERG activation, an envelope of tails protocol is developed where the cell is initially held at -80 mV and stepped to a constant depolarized potential to activate the channel for varying durations, then stepped to a hyperpolarized potential to recover the channels from inactivation and allow deactivation. The peak tail current elicited by the hyperpolarization step is used to assess the relative open probability of the preceding depolarizing step and is plotted against duration and fitted to a single exponential function to yield the Tau of activation for each depolarized potential tested. At very short durations, and at voltages near the activation threshold, the tail currents measured showed a lag phase, which lead to sigmoidicity in the voltage-dependence of activation, suggesting that the channels transitioned through multiple closed states before opening. The three closed states in the five state linear model describe this sigmoidicity during the activation process, and four closed states did not further improve the model (Wang *et al.*, 1997). Activation kinetics of hERG channels are strongly voltage-dependent with a Tau of activation of ~420 ms at 0 mV, which decreases with depolarized potentials to reach an asymptotic value of 37.3 ms at +120 mV (Van Slyke *et al.*, 2010), instead of reaching 0 ms. This suggests that a voltage-insensitive step becomes the rate limiting step at depolarized potentials (Wang *et al.*, 1997; Van Slyke *et al.*, 2010). The physiological importance of slow activation is to reduce the repolarizing current by lowering the availability of hERG channels during the early phases of the cardiac action potential. Several studies using gating currents and/or fluorescence reports of VSD movement suggest that the unusually slow activation is a result of slow voltage sensor movement that is the rate limiting step (Smith & Yellen, 2002; Piper *et al.*, 2003, 2005; Van Slyke *et al.*, 2010). In *Shaker* channels activation kinetics are rapid and opening of the activation gate is the rate limiting step (Cha & Bezanilla, 1997). This suggests that the mechanisms that underlie the hERG channel slow activation are different compared to those in *Shaker*; however the mechanism underlying the regulation of slow activation in hERG channels remains poorly understood.

Like other K_v channels, the hERG channel contains a series of basic residues in the S4 voltage sensor that has been shown to traverse the electric field upon changes in membrane voltage (Bezanilla *et al.*, 1991; Starace & Bezanilla, 2004; Ahern & Horn, 2005)

and induce conformational changes to the voltage sensor leading to opening of the channel pore (Lu *et al.*, 2002; Long *et al.*, 2005). Like mentioned above, the hERG channels comprise a series of regularly spaced basic residues, (from top of S4 to bottom): K525, R528, R531, R534, R537, and K538. Mutational analysis of these basic residues revealed their critical involvement in both hERG activation and deactivation. Replacing each of the positively charged residues in the S4 with glutamine have significant impact on the voltage-dependence of activation of the channel. In particular, the K525Q mutation caused a hyperpolarizing shift in the voltage-dependence of activation suggesting the equilibrium is shifted towards the open state compared to WT (Liu *et al.*, 2003). Interestingly, in most Kv channels this outermost S4 basic charge is arginine and not lysine (K525), and charge conserving mutation (K525R) did not restore WT-like phenotype, suggesting that the lysine side chain at this position may be more important than charge alone (Subbiah *et al.*, 2004). Conversely, R528Q, R531Q, R534Q, and R537Q mutants all exhibited a depolarizing shift in the voltage-dependence of activation indicating these mutations altered the equilibrium towards the closed state (Zhang *et al.*, 2004).

Following these observations, cysteine and alanine mutation scans revealed that the outer three positive charges in the S4 reduced the gating charges transferred during activation, suggesting that the majority of the charge associated with activation is due to the movement of K525, R528, and R531. This was supported through the state-dependent accessibility assay of the three basic residues to a membrane-impermeable thiol-modifying reagent (MTSET) during activation (Zhang *et al.*, 2004). In contrast, S4 accessibility to MTSET in *Shaker* channels showed the translocation of four outermost arginines, consistent with the movement of ~12-14 elemental gating charges (e_o) across the electric field (Aggarwal & MacKinnon, 1996; Seoh *et al.*, 1996). The limited movement of the S4 segment in hERG channel is consistent with the measurement of a lower number of elemental gating charges moved during activation (~8 e_o) (Zhang *et al.*, 2004). The cryo-EM structure of the open state hERG channel structure aligns with these functional studies (Wang & MacKinnon, 2017).

1.2.3.2 Molecular basis of hERG inactivation

Slow activation of hERG channels is followed by an unusual fast inactivation process that occurs more rapidly than activation and is voltage-dependent. Studies in K_v channels have shown two distinct types of inactivation: N-type and C-type inactivation

(Rasmusson *et al.*, 1998). N-type inactivation, such as that seen in *Shaker* channels, occurs in the order of milliseconds and involves the N-terminus tethering to the intracellular mouth of the pore, blocking the conduction pathway (Hoshi *et al.*, 1990). This is also termed the ball-and-chain mechanism (Hoshi *et al.*, 1990; Zagotta *et al.*, 1990). Deletion of the N-terminus abolished this N-type inactivation and revealed a slower inactivation called C-type inactivation (Hoshi *et al.*, 1991). C-type inactivation occurs as a result of conformational rearrangements on the outer mouth of the pore that blocks the conduction pathway (Hoshi & Armstrong, 2013). Mutation in this outer region of the pore mouth, such as T449 in *Shaker* channels, altered the C-type inactivation process (López-Barneo *et al.*, 1993). External application of tetraethylammonium (TEA) has also been shown to slow C-type inactivation (MacKinnon & Yellen, 1990) leading to the suggestion that the process involves a collapse of the outer pore.

It has been shown that hERG channel inactivation lacks an N-type inactivation process and is more similar to C-type inactivation observed in *Shaker* channels. First of all, hERG channel inactivation is slowed with the external application of TEA, similar to that seen in *Shaker* channels, and is unaffected by deletion of N-terminus (Schönherr & Heinemann, 1996). Second, hERG channel inactivation is sensitive to ion occupancy of the selectivity filter like that in C-type inactivation in *Shaker* channels. Both of these are hallmark characteristics of C-type inactivation (Schönherr & Heinemann, 1996). These studies suggest that inactivation of hERG channels involves a collapse of the selectivity filter (Smith *et al.*, 1996). Consistent with this, mutation of the pore residue, S631, into alanine greatly shifted the inactivation of hERG channels, just as mutation of the residue at the equivalent site in *Shaker,* Thr449, greatly reduces C-type inactivation (López-Barneo *et al.*, 1993). What is unusual about inactivation in hERG channels is the fast rate and voltage-dependence. C-type inactivation in other channels is slow and voltage-independent. Inactivation in hERG channels appears to be complex and many components of the channel influence inactivation such as the selectivity filter, S4, S4-S5 linker, and/or pore helix. The exact mechanism that regulates hERG channel inactivation remains unclear. One proposed mechanism of the inactivation process is analogous to a Japanese puzzle box model, where a set of precise sequence of moves, that involves interconnected but separate components, is required to open and close this mechanism (Wang *et al.*, 2011). The importance of this inactivation process is highlighted by the characterization of two novel LQTS type 2 causing mutations A614V and V630L (located

at the outer mouth of the pore). Both mutations reduced hERG channel current by causing a hyperpolarizing shift in the voltage-dependence of inactivation, which enhances inactivation (Nakajima *et al.*, 1998). The authors suggest that the enhanced inactivation reduced the channel availability during phase 3 of the action potential resulting in arrhythmia and sudden death in these individuals (Nakajima *et al.*, 1998). On the contrary, drugs or agonists that reduce hERG inactivation have been investigated due to their potential to rescue loss-of-function due to inherited mutations, however they often enhance repolarizing current so much that they induce short QT syndrome, which is also proarrhythmogenic (Lu *et al.*, 2008). The intricate regulation of the hERG inactivation process appears to be critical in maintaining a normal cardiac action potential duration.

1.2.3.3 Molecular basis of hERG deactivation

Another hallmark feature of hERG channel gating is slow deactivation. Inherited LQTS type 2 mutations, such as R56Q, that accelerate hERG channel deactivation rate, without greatly affecting other gating processes, underline the importance of slow deactivation in hERG channels (Chen *et al.*, 1999). hERG deactivation kinetics are best described by a double exponential fit that yields a fast and slow component. Interestingly, at hyperpolarized potentials, the fast component dominates the majority of deactivation, while at more depolarized potential the slow component is more dominant. These two components can be individually altered by mutations. For example the G546L mutation within the S4-S5 linker produces deactivation kinetics that can be well described by a single exponential function at all potentials, suggesting that the two components may be mediated by separate mechanisms (Van Slyke *et al.*, 2010). It is currently unclear what is the mechanism underlying the two components. Regulation of the slow deactivation in hERG channels is complex, and it can be modulated by multiple regions of the channel. The distal N-terminus, termed the Cap domain, consisting of residues 1-26, has been shown to be critical in regulating slow deactivation. The Cap domain contains a positively charged surface and mutations within the Cap domain accelerated deactivation suggesting that this domain is essential for normal hERG deactivation gating (Cabral *et al.*, 1998; Wang *et al.*, 1998; Gustina & Trudeau, 2009; Ng *et al.*, 2011; Muskett *et al.*, 2011). FRET experiments have shown that the Cap domain, along with the N-terminus is in close proximity to the C-linker/cNBH domain suggesting interactions between N- and C- terminus are important in regulating normal slow deactivation (Fernández-Trillo *et al.*, 2011; de la Peña *et al.*, 2015). Charge surface analysis on a homology model of the cNBH

domain revealed a patch of negatively charged residues that could be a docking site for the Cap domain in the N-terminus (Muskett *et al.*, 2011). Other studies suggest that the Cap domain may interact with the C-terminus via the S4-S5 linker, and mutations within the S4-S5 linker also showed accelerated deactivation kinetics (Van Slyke *et al.*, 2010; Fernández-Trillo *et al.*, 2011; Hull *et al.*, 2014; de la Peña *et al.*, 2015). Additionally, slow deactivation has also been shown to be affected by the six negative residues in the S1-S3 transmembrane segments (mentioned earlier). A functional study revealed that while mutation of each residue had distinct effects on channel function, such as activation or inactivation, all mutations produced a faster deactivation rate. This led to the proposal that there is a “master-switch” in hERG channels that maintains a slow deactivation, and that all the negative residues need to be present to keep the master-switch in the ON position (Liu *et al.*, 2003). Mutations or conditions that turn OFF this master-switch will set the channel in a fast deactivation mode. A potential candidate for this master-switch has been suggested to be the PAS domain in the N-terminus (Liu *et al.*, 2003). More recent studies suggest that another contributor to slow deactivation is relaxation of the voltage sensor, where prolonged depolarization stabilizes the voltage sensor from the activated state to a relaxed, more stable, conformation. In doing so, more energy is required to return the voltage sensor, thus inducing a left-shift in the voltage-dependence of deactivation compared to that for activation (mode-shift), and a slowing of the deactivation kinetics. Mutations that accelerate deactivation may exhibit reduced voltage sensor mode-shift (Thouta *et al.*, 2017).

1.2.3.4 Molecular basis of hERG mode-shift

The term mode-shift, in the context of ion channel studies, was first coined in HCN channel studies where holding the channel at depolarized potentials shifts the voltage-dependence of activation to more negative voltages, such that channels remain closed at voltages that would normally open channels. Conversely, holding the channel at more negative voltages shifted the voltage dependence of activation to more positive voltages facilitating the activation of HCN channels. This shifting in the mode of activation is critical for the function of HCN channels in generating and regulating rhythmic cardiac pacing pattern. Mode-shift behaviour has also been observed in other channels, such as *Shaker* (Lacroix *et al.*, 2011; Haddad & Blunck, 2011; Labro *et al.*, 2012; Priest *et al.*, 2013), Kv1.2 (Labro *et al.*, 2012), NaChBac (Kuzmenkin *et al.*, 2004), HCN (Elinder *et al.*, 2006; Xiao *et al.*, 2010), L-type calcium (Brum *et al.*, 1987, 1988), Hv1 (Villalba-Galea, 2014).

Observation of mode-shift in the voltage-sensor related protein, Ci-VSP, which lacks a pore domain (Villalba-Galea *et al.*, 2008)**,** provides strong evidence that mode-shift behaviour is an intrinsic property of the voltage sensor. In each of these cases, mode-shift requires prolonged depolarization that shifts the channels into a more stable relaxed state as suggested by studies in *Shaker* and Ci-VSP (Villalba-Galea *et al.*, 2008; Labro *et al.*, 2012; Priest *et al.*, 2013). Due to this, more energy is required to return the voltage sensor to rest leading to a separation of the voltage-dependence of activation and deactivation.

We, and others, have reported mode-shift in hERG channels (Piper *et al.*, 2003; Tan *et al.*, 2012; Goodchild & Fedida, 2014; Hull *et al.*, 2014; Thouta *et al.*, 2017), interestingly, the mode-shift occurs in response to depolarizations in the time course of hundreds of milliseconds (in contrast to *Shaker* channels that occurs in the seconds), which is physiologically relevant in duration. This suggests that mode-shift may play a role in the slow deactivation of hERG channels that is critical to the physiological function of the channel. Recent characterization of hERG mode-shift showed that short depolarization durations recruited fewer channels into the relaxed state and produced a relatively fast deactivation (Goodchild *et al.*, 2015; Thouta *et al.*, 2017). However, increasing depolarization durations recruited more channels into the relaxed state, thus slowing the deactivation kinetics. A plot of depolarization durations against deactivation kinetics showed a bi-exponential slowing of deactivation with one component of slowing occurring with a time constant of 93 ms and the second component with a time constant of 4.3 s at +60 mV. Such bi-exponential slowing is consistent with that seen in *Shaker* channels and has been suggested to reflect stabilization of the activated voltage sensor by the open pore gate (fast component), and relaxation of the voltage sensor (slow component) (Thouta *et al.*, 2017). When measuring the onset of relaxation of the voltage sensor from gating currents, a similar bi-exponential slowing of charge return was observed, suggesting that the relaxation process is intrinsic to the voltage sensor and that slow voltage sensor return may play a role in the slow deactivation of the hERG channel (Thouta *et al.*, 2017).

1.3 Myocardial ischemia

Apart from inherited and drug-induced inhibition of hERG channel gating, the hERG channel can also be influenced by metabolic changes that may increase the risk for arrhythmia. In my thesis, I study the effect of acidosis, which is a major consequence

during myocardial ischemia, on hERG channel gating. In this section I will provide background to myocardial ischemia and the major ionic concentration changes that are associated with myocardial ischemia.

1.3.1 Background

Myocardial ischemia is characterized by a reduction in blood flow to the heart due to a partial or complete blockage of an artery, for example due to atherosclerosis, leading to reduction in oxygen (hypoxia) delivery to the cardiac muscle. The low oxygen supply, coupled with reduced waste removal, can result in deterioration of electrical profile, failure of contraction, and eventual cell death of the cardiac muscle. Severe or prolonged myocardial ischemia can cause cardiac dysfunction, arrhythmias, and myocardial infarction (Carmeliet *et al.*, 1999).

Clinically, the classical diagnosis for myocardial infarction is a ST-segment elevation in the electrocardiogram (ECG) during exercise or pharmacological stress test. The link between the ST-segment changes during ischemia and the high incidence of lethal arrhythmias leads to closer investigation of the electrophysiological mechanism that underlies these changes in the ECG. Several studies have suggested that the ST-segment elevation arises from a combination of increased extracellular potassium, which depolarizes the resting membrane potential, a shortening of the APD, and myocyte inexcitability (Kléber, 2000). However, the onset of these effects, that reflect on the ECG, are only apparent several minutes after ischemia and not instantaneous. Interestingly, in animal studies, the APD is prolonged during the initial onset of ischemia (< 1 min), and then shortens with further prolonged ischemia. This biphasic change raises the possibility that the initial prolongation of the APD may manifest during early ischemia, which is then follow by ST-segment elevation, and that this APD prolongation may be an important initiator for triggered activity that may increase the risk of arrhythmia. Indeed, in a clinical study, occlusion of blood flow by balloon inflation, through an elective percutaneous coronary balloon angioplasty procedure, produced a prolongation in the corrected QT (QTc) interval on the ECG within 1 min in all 74 patients with atherosclerosis. This robust observation supports the idea that prolongation of the APD may underlie the initial QTc prolongation, which occurs during the initial onset of ischemia, and be important in early arrhythmia generation (Kenigsberg *et al.*, 2007). An important contributing factor to this biphasic change in the cardiac APD is due to the ionic concentration changes in the

intracellular and extracellular space, which affects normal ion channel function. In the next section, I will outline some of the major ion concentration changes and how these changes may affect the changes to APD and arrhythmogenicity.

1.3.2 Major ion concentration changes during myocardial ischemia

Myocardial ischemia induces changes to concentrations of $[K^+]$, $[Na^+]$, $[Ca^{2+}]$, $[Mg^{2+}]$, and $[H^+]$, intracellular phosphate $[PO_4]_i$, neurotransmitters, and hormones. The complex interplay of the changes in the distribution of these ions disrupt the equilibrium of a whole array of ion channels, carriers, transporters, and hormones that ultimately increases the susceptibility to development of lethal arrhythmias during both acute and prolonged ischemic events (Carmeliet *et al.*, 1999).

1.3.2.1 *Increase in $[K^+]_o$*

One of the major changes following ischemia is an increase in extracellular $[K^+]$. In normal conditions, intracellular $[K^+]$ is around 155 mM, while extracellular $[K^+]$ is around 3 mM. Generally, this equilibrium is regulated by the passive efflux of K^+ and active influx of K^+ via the Na^+/K^+ pump. The increase in $[K^+]_o$, following ischemia, occurs in three phases: an initial increase, then a plateau within 3-10 minutes, followed by another slower increase after 15-30 minutes. The reason for this increase is due to an increase in K^+ efflux and a decrease in the active K^+ influx. The decrease in the active K^+ influx is due to the fall of [ATP] and increase of [ADP] + $[P_i]$ that inhibits the Na^+-K^+ pump by raising the reversal potential of the pump from -180 mV to -60 mV, which is similar to the membrane potential of the cells, thus reducing its function leading to an increase in $[K^+]_o$ (Glitsch & Tappe, 1995). Another mechanism is an increase in K^+ efflux via K_{ATP} channels which are normally inhibited by ATP. During ischemic conditions, depletion of ATP level leads to activation of the K_{ATP} channel. Since the single channel conductance for K_{ATP} is very high, only a small proportional of the channels need to activate to generate a large K^+ current (Nichols *et al.*, 1991). Sodium-activated potassium channels (K_{Na}), and arachidonic acid-activated potassium channels (K_{AA}) have also been suggested to contribute to the increase in $[K^+]_o$ during ischemia. For example, the increase in $[Na^+]_i$ as a result of ischemia can activate I_{KNa}, and the open probability of the K_{AA} channels is also enhanced by acidosis (Kameyama *et al.*, 1984).

The electrophysiological consequence of an increase in $[K^+]_o$, is depolarization of the membrane potential, reduction in the amplitude of the AP, and shortening of the APD. The depolarization of the cell and subsequent inactivation of the Na^+ current is responsible for the reduced AP amplitude, and the enhanced conductance of several K^+ currents are the main drivers for a shortening of the APD. The increase in these K^+ currents can also contribute to a reduction in excitability, which leads to a longer relative refractory period, which can cause conduction velocity to reduce. These changes in excitability, refractoriness, and conduction suggest an increase in susceptibility to the occurrence of reentry arrhythmias. These changes, which require time for intracellular ATP levels to fall, likely contribute to the shortening of the APD observed with more prolonged ischemia.

1.3.2.2 *Accumulation of $[Na^+]_i$*

The approximate distribution of $[Na^+]$ across a mammalian cardiomyocyte membrane is ~135-145 mM extracellularly, while intracellular sodium can vary between 5-20 mM (Baartscheer *et al.*, 1997). This low intracellular concentration of Na^+ is maintained by the active pump, Na^+/K^+ -ATPase also known as the Na^+/K^+ pump, which hydrolyzes ATP to export three sodium ions and import two potassium ions. The pump is electrogenic and produces a net positive charge. Another important player in the regulation of Na^+ is NCX. The activity of the NCX depends heavily on both the Na^+ and Ca^{2+} gradient and can act to operate in forward (Ca^{2+} efflux) or reverse (Ca^{2+} influx) mode. NCX exchanges three sodium ions for every calcium ion, therefore is also electrogenic and produces a net positive charge per exchange. In physiological conditions, NCX mostly operates in forward mode, driven by the large extracellular Na^+ gradient that facilitates Ca^{2+} efflux (Bers & Despa, 2009). Lastly, there is the Na^+/H^+ exchanger (NHE), which primarily functions to extrude intracellular protons. In mammalian cells the intracellular pH is slightly more acidic (pH 7.2) compared to the extracellular pH (pH 7.4), so there is a consistent electrochemical gradient for the exchanger to extrude protons (Karmazyn *et al.*, 1999). The exchanger exports one proton for one sodium making this process electroneutral (Karmazyn *et al.*, 1999).

Accumulation of intracellular $[Na^+]_i$ during myocardial ischemia is a result of reduced active efflux and an increase in inward leak. The reduction in the active efflux is the result of the drop in the [ATP] during ischemia that results in the inhibition of the Na^+/K^+ pump. This is the main driver for the accumulation of $[Na^+]_i$. The inward leak of Na^+ is

driven, in part by the Na^+/H^+ exchanger that brings in Na^+ in order to extrude H^+. Blockage of Na^+/H^+ exchanger function dramatically reduced the accumulation of $[Na^+]_i$ during ischemia (Anderson *et al.*, 1991). External acidification during myocardial ischemia also increases late persistent I_{Na} which contributes to the accumulation of intracellular Na^+. Increasing in $[Na^+]_i$ can depolarize the resting membrane potential, and contribute to reduce excitability and conduction. Increase in $[Na^+]_i$ can also activate I_{KNa}, like mentioned earlier, which can contribute to a shortening of the APD.

1.3.2.3 *Changes in $[Ca^{2+}]_i$ distribution*

The $[Ca^{2+}]$ differs in the cytosol, sarcoplasmic reticulum (SR), and extracellular space. The Ca^{2+} in the cytosol modulates myofilaments, ion channels, and exchangers such as NCX. The SR acts as a Ca^{2+} storage and modulates the contraction and relaxation of the myocytes. Cytoplasmic $[Ca^{2+}]$ is approximately 100 nM during diastole and can fluctuate to 500-1000 nM or even higher during systole depending on the Ca^{2+} load in the SR through a process called calcium-induced calcium release (CICR) (Bers, 2002). CICR occurs when L-type calcium channels on the plasma membrane are activated by cell depolarization that brings in Ca^{2+} into the cytosol. The elevated cytosolic Ca^{2+} activates the ryanodine receptors located on the membrane surface of the SR to release Ca^{2+} from the store that facilitates the contraction of the cardiac muscle (Bers, 2002). The SR has been estimated to store 700 µM of free $[Ca^{2+}]$ (Bers, 2002), which, compared to 500-1000 nM during systole in the cytosol, provides an enormous gradient. This gradient facilitates the huge efflux of Ca^{2+} into the cytosol for contraction during the depolarization phase of the action potential.

During ischemia cytoplasmic $[Ca^{2+}]$ is increased, although this occurs after a delayed onset. This increase is due to the inefficient removal of cytoplasmic Ca^{2+} by NCX and reduced Ca^{2+} uptake by the SR. The NCX plays a major role in Ca^{2+} extrusion, and is less efficient during ischemia due to an increase in $[Na^+]_i$ that reduces the Na^+ gradient across the membrane (Carmeliet *et al.*, 1999). Gradual increase in $[H^+]_i$ during ischemia will further reduce the efficiency of NCX, and displace calcium from intracellular binding sites, thus keeping the cytoplasmic $[Ca^{2+}]$ high. A major regulator of cytoplasmic Ca^{2+} is the Ca^{2+} uptake by the SR. During ischemic conditions, the drop in [ATP] reduces the Ca^{2+}-ATPase (SERCA) activity, which in turn reduces the uptake of cytoplasmic Ca^{2+} by the SR, further increasing the cytoplasmic $[Ca^{2+}]$ (Kaplan *et al.*, 1992). A pronounced

increase in cytoplasmic Ca^{2+} can enhance NCX activity that generates a depolarizing Na^+ current that increases the susceptibility to development of DADs. Increase in cytoplasmic Ca^{2+}, coupled with increased $[Na^+]_i$, during ischemia, will keep a depolarized membrane potential that can increase the occurrence of DADs that may trigger premature firing of an action potential that can generate lethal arrhythmia. In addition, increased cytoplasmic Ca^{2+} during ischemic conditions have been shown to reduce muscle contractility, and increase cardiac muscle damage (Carmeliet *et al.*, 1999).

1.3.2.4 *Changes to extracellular and intracellular [H^+]*

In normal aerobic condition, the intracellular pH (pH_i = 7.2) of the cardiac myocytes is slightly more acidic than extracellular (pH_o = 7.4), owing to a combination of metabolic and respiratory processes that produce H^+ as by-products. The major metabolic processes that produce H^+ are the breakdown of glucose during glycolysis, and ATP hydrolysis. The major respiratory process that produce H^+ is the excessive CO_2 from cellular respiration, which can diffuse through the cell membrane and combine with H_2O to form carbonic acid (H_2CO_3) that dissociates into H^+ and HCO^{3-}. Intracellular protons are extremely reactive and a decrease in pH_i can alter calcium homeostasis by inhibiting Ca^{2+} uptake by SERCA, promote cellular apoptosis, and reduce cardiac contractility (Vaughan-Jones *et al.*, 2009). Therefore, the constant production of H^+ requires a continuous elimination of intracellular H^+. Two important mechanisms are at work to resist the accumulation of intracellular protons. First is the Na^+/H^+ exchanger (NHE), which is activated by intracellular protons and exchanges protons to the extracellular side using the large Na^+ gradient. Second is the electrogenic Na^+/HCO_3^- co-transporter (NBC), which transports 1 Na^+ for every 2 HCO_3^- into the cell. The HCO_3^- couples with protons to form carbonic acid (H_2CO_3), which dissociates into CO_2 and H_2O. CO_2 then readily diffuses across the cell membrane. At pH_i of 7.2 both NHE and NBC extrude about the same amount of H^+ (Leem *et al.*, 1999). In addition to H^+ extrusion by NHE and NBC, modest intracellular acidification can activate gap junction channels that encourages passive spreading and dissipation of H^+ to neighbouring cells thus largely increasing the buffering capacity for intracellular H^+ and further resisting the changes to pH_i (Vaughan-Jones *et al.*, 2009).

One of the major consequences of myocardial ischemia is a decrease in both pH_i and pH_o due to increased production of H^+ and insufficient removal. The increase of protons in the intracellular and extracellular environment are, however, not equal. During

the early phases of ischemia, the low local perfusion rate allows for rapid accumulation of extracellular H^+ as intracellular H^+ are being extruded by NHE and NBC. In ischemic rat hearts, it was observed that the extracellular pH changes rapidly, within minutes, from pH 7.4 to as low as pH 6.0 (Clarke *et al.*, 1993). The rapid accumulation of extracellular protons then inhibits the activities of NHE and NBC leading to a more delayed increase in intracellular protons. The cell can still resist this increase in intracellular protons by activating gap junction channels (Firek & Weingart, 1995). However, when intracellular protons continue to rise, the gap junction channels are then inhibited to prevent spreading of intracellular protons to neighbouring cells. Studies in blood-perfused papillary muscles of the rabbit heart subjected to ischemia showed that after 18 minutes of ischemia, the external pH changes rapidly from 7.4 down to as low as 6.1, while intracellular pH is more resistant to acidification (Yan & Kléber, 1992), leading to a reversal of the pH_o/pH_i ratio. The changes in the extracellular and intracellular pH have numerous effects on different ion channels and may underlie changes in the cardiac action potential. In the next section I will outline the changes that protons have on ion channels.

1.4 Effect of acidosis on major ion channels

The changes to both extracellular and intracellular pH, during myocardial ischemia reduce the current conducted by a wide array of ion channels in the cardiac myocyte. Some currents are inhibited by extracellular acidosis (e.g. I_{Na}, I_{CaL}, I_{To}, I_{Ks}, I_{Kr}), while others are inhibited by intracellular acidosis (e.g. I_{KNa}, I_{K1}) (Prod'hom *et al.*, 1989; Zhang & Siegelbaum, 1991; Ito *et al.*, 1992; Stengl *et al.*, 1998; Carmeliet *et al.*, 1999). The overall result on the cardiac action potential is a depolarization of the resting potential, reduction in upstroke velocity, oscillations at the plateau level, and prolonged refractoriness that lead to altered cardiac rhythm in the heart that increases the susceptibility for cardiac arrhythmia (Carmeliet *et al.*, 1999). In this section I will outline the differential modulation of protons on the major sodium, calcium, and potassium channels in the cardiac action potential that contributes to the development of arrhythmia during myocardial ischemia.

Surface Charge Screening

Before discussing the modulation of each of the major ion channels by protons, a common observation in voltage-gated channels, exposed to external acidic pH, is a depolarized shift in the voltage-dependence parameters. Previously, this observation was

thought to be due to a charge screening effect under the Gouy-Chapman theory (Gilbert & Ehrenstein, 1969). The theory states that there are static surface charges on the membrane in which positive ions can bind and alter the local extracellular membrane potential. According to the theory, any curve describing a voltage-dependent property of the channel (e.g. activation, deactivation or inactivation) should shift along the voltage axis with a change in cation concentration with no change in the shape of the curve. Furthermore, the theory predicts that for a given channel and at a given cation concentration, the voltage shifts will be the same for all voltage-dependent parameters (Ehrenstein, 2001). The first experiment supporting such a theory was the observation by Frankenhaeuser and Hodgkin in 1957 that the potassium conductance-voltage relationship shifted along the voltage axis as the external calcium ion concentration is varied, with no change in the slope, suggesting that the calcium ions are occupying or modifying the surface charges and changing the membrane field in which the channels are embedded (Frankenhaeuser & Hodgkin, 1957). However, over time studies on many different voltage-gated channels such as $Na_v1.5$, L-type calcium channels, *Shaker*, $K_v1.2$, $K_v1.4$, and hERG revealed that the effects of external protons are inconsistent with the surface charge screening theory and are more consistent with protonation of specific locations on the channel that differentially affect channel gating (Jo *et al.*, 1999; Jiang *et al.*, 1999; Vereecke & Carmeliet, 2000; Bett & Rasmusson, 2003; Starkus *et al.*, 2003; Van Slyke *et al.*, 2012). One such evidence from *Shaker* channels showed that extracellular acidification caused a depolarized shift in the voltage-dependence of activation. If this was due to a charge screening effect, then tail currents measured at a constant tail voltage would result in an apparently greater hyperpolarization and therefore in a faster deactivation (Starkus *et al.*, 2003). Intracellular acidification would be expected to cause the opposite effect: a hyperpolarized shift in the voltage-dependence of activation and slower deactivation. However in excised patch experiments, in which the intracellular pH was changed, intracellular acidification also showed an acceleration of deactivation that cannot be explained by the charge screening effect (Starkus *et al.*, 2003). Other evidence is seen in hERG channels for example, where the *pKa* for current suppression and rate of activation (*pKa* = 5.5) is substantially lower than that of rate of deactivation (*pKa* = 6.8) induced by low external pH (Bett & Rasmusson, 2003), suggesting that the two processes are mediated by two potentially different sites. In addition, previous studies showed that, at the pH ranges where activation and deactivation are affected, there is no effect of external protons on the voltage-dependence of inactivation (Anumonwo *et al.*,

1999; Jo *et al.*, 1999; Vereecke & Carmeliet, 2000; Van Slyke *et al.*, 2012). Overall, there is more evidence supporting a direct effect on channel gating by that may involve protonation of specific residues exposed to the extracellular surface of the channel.

Effects of external acidosis on I_{Na}

Since the 1960s, the inhibitory effects of extracellular protons on sodium currents has been observed in nerve, and muscle cells (Hille 1968). The main observations are that extracellular protons induced a depolarizing shift in the voltage-dependence of activation and a reduction in the maximum sodium conductance. The same observations were seen in the cardiac sodium channel, $Na_v1.5$, which conducts I_{Na}, in which low external pH reduced the peak sodium current, likely as a result of reduction in the single channel conductance from channel block, and caused a depolarized shift in the voltage-dependence of activation (Zhang & Siegelbaum, 1991; Jones *et al.*, 2011). The rapid onset and reversibility suggests an external effect. Another major modification is destabilization of fast-inactivation of $Na_v1.5$ where pH 6.0 induced a significant slowing of the kinetics of fast-inactivation, and also accelerated the recovery from fast-inactivation. Both of these effects would be expected to increase the probability of channels reopening during the AP plateau and may contribute to the development of EADs and triggered activity (Jones *et al.*, 2011). Lastly, external protons slow the kinetics of the onset of slow inactivation and accelerate the recovery from slow inactivation. This would also contribute to an increase in I_{Na} during the cardiac action potential. AP modeling of a ventricular myocyte, combining all the observed effects of external protons on $Na_v1.5$ channels, revealed that pH 6.0 caused a 60% reduction in the upstroke velocity, due to the reduction in $Na_v1.5$ conductance, and a prolongation of the ventricular APD, likely due to the increase in persistent late I_{Na} current (Jones *et al.*, 2011).

Effects of external acidosis on I_{CaL}

The cardiac L-type calcium channel, which conducts the I_{CaL} current, is also inhibited by external protons. Similar to $Na_v1.5$ channels, external protons inhibit the maximum conductance with a complete block at pH 4.8 or lower (Krafte & Kass, 1988). Inside-out patch recordings of single L-type calcium channels revealed that the channels are only modulated by changes in pH_o and not changes in pH_i suggesting that extracellular protonation sites are responsible for the effect (Prod'hom *et al.*, 1989). Several proposed mechanistic explanations include the protonation of a H^+ binding site far away from the

pore that induces an allosteric change, which reduces the conductance (Prod'hom *et al.*, 1989). On the contrary, Root and Mackinnon argued that protonation of glutamate residues within the channel pore produced pore block (Root & MacKinnon, 1994). This was further supported by site-directed mutagenesis and single channel recordings, where mutation of glutamates within each of the four P-loops of the L-type Ca^{2+} channels to glutamines produced differential effects in the pH_o-induced reduction of the single channel conductance. This suggests that the conserved glutamates within the P-loop regions act in concert to conduct Ca^{2+} ions and that protonation of these glutamates blocked the permeation pathway (Chen *et al.*, 1996). In addition, external protons also right-shift the activation conductance-voltage relationship and inactivation-voltage relationship to a similar degree, -9 mV and -13 mV respectively, and titration of extracellular sites has been suggested to be responsible (Krafte & Kass, 1988). Overall, a decrease in I_{Ca} during external acidification would be expected to shorten the APD and may cause a reduced calcium-induced calcium release (CICR) process that ultimately reduces the available Ca^{2+} to facilitate cardiac contraction.

Effects of external acidosis on K_V channels

The inhibitory effects of external protons of K_V channels are different amongst the sub-families with specific mechanisms that are inconsistent with charge screening effect. In the *Shaker* channels, external protons reduced the peak current and induced a depolarized shift in the voltage-dependence of activation that was similar to the shift of the voltage-dependence of inactivation with a *pKa* of 4.7-5.0. The similarity in the *pKa* between the effects on activation and inactivation suggest that these two processes may be linked and modulated by the side chain of an aspartate or glutamate residue as a proton sensor (Pérez-Cornejo, 1999). This is in contrast to $K_v1.4$ channels, where external protons enhanced the C-type inactivation of $K_v1.4$ channels via protonation of two extracellular residues H508 and K532. Mutation of H508 to glutamine or cysteine abolished the pH-induced enhancement of C-type inactivation, and mutation of K532 to glutamine and cysteine also showed reduced pH-sensitivity, suggesting that either protonation of H508 allosterically affects K532 near the pore, or that both residues may be acting independently (Claydon *et al.*, 2000, 2002). Striking similarities in the mechanism of action by external protons is also seen in $K_v1.5$ channels, which mediate the ultra rapid potassium current (I_{Kur}) that augments the late cardiac action potential repolarization in the atrial myocytes. External protons enhanced $K_v1.5$ C-type inactivation,

which may contribute to a prolongation of the action potential duration and be pro-arrhythmogenic during myocardial ischemia (Steidl & Yool, 1999), although these channels are mostly expressed in atrial rather than ventricular tissue. It was discovered that mutation of a histidine residue in the S5-pore loop linker region (H452) to glutamine abolished the enhanced C-type inactivation at pH 6.3, suggesting that the histidine residue is the proton sensor (Steidl & Yool, 1999). The I_{Ks} current in the heart, encoded by KCNQ1 (Kv7.1) and KCNE1, is also sensitive to external protons (Peretz *et al.*, 2002). External protons reduced the maximum conductance and caused a depolarizing shift of the voltage-dependence of KCNQ1 channel activation like many other potassium channels, however the onset of inactivation is slowed at pH_o 5.5, as are activation and deactivation. The slowed activation and deactivation kinetics at pH 5.5 is particularly interesting and paradoxical because a slowed activation would be expected to be coupled with an accelerated deactivation. Interestingly, it was shown that deletion of five residues (39-43) in the N-terminus of KCNE1, and subsequent co-expression of the Δ39-43 KCNE1 mutant construct with KCNQ1 abolished the pH-induced slowing of deactivation without affecting the slowing of activation and reduction in maximum conductance. The two negatively charged residues, D39 and E43, have been proposed to interact with KCNQ1 intracellularly to allosterically modify the external conformation of KCNQ1 for the pH-induced slowing of deactivation (Peretz *et al.*, 2002). Overall the inhibition of potassium channels in the heart by external protons has been suggested to modify repolarization, alter action potential duration, and increase susceptibility to arrhythmia.

1.5 Effects of external acidosis on hERG channels

The main focus of my thesis is to investigate the site and mechanisms for the effects of external protons on hERG channels. External protons rapidly inhibit hERG channel function and, as discussed earlier, the loss-of-function of hERG channel reduces the repolarization current during the phase 3 of the cardiac action potential and contributes to a prolongation of the cardiac AP. During myocardial ischemia, the APD is rapidly prolonged during the initial onset of ischemia followed by a shortening (see section 1.3.1), and the QT interval is prolonged in a clinical study (Kenigsberg *et al.*, 2007). The extracellular acidification coincides well with the early onset of prolongation of the cardiac AP during ischemia, and I hypothesize that the underlining mechanism is due to an inhibition of hERG channels by external protons (Carmeliet *et al.*, 1999; Kenigsberg *et al.*,

2007). The first description of the effects of external protons on the hERG channel was reported in 1999 in *Xenopus laevis* oocytes (Jo *et al.*, 1999). External protons reduced the maximum conductance, induced a depolarized shift of the voltage-dependence of activation, slowed activation, and accelerated deactivation. In the same year, a separate group observed the same effects of external protons in L929 mammalian cells stably transfected with hERG channels at physiological temperature (35 ºC), corroborating and confirming the gating modifications by low pH (Anumonwo *et al.*, 1999).

1.5.1 External protons reduce the maximum conductance of hERG channels by directly blocking the pore

The mechanism underlying the proton-induced reduction in the maximum conductance in other channels, such as Na^+ (Khan *et al.*, 2006), L-type Ca^{2+} (Chen *et al.*, 1996) , and *Shaker* (Starkus *et al.*, 2003), has been suggested to be due to a block of the pore. Consistent with this, external protons have been shown to reduce hERG channel conductance in a voltage- and time-dependent manner (Jo *et al.*, 1999). The maximum conductance of hERG channels was reduced with a *pKa* of 5.1 (Van Slyke *et al.*, 2012), consistent with a previous report of current suppression at low pH with a *pKa* of 5.5 (Bett & Rasmusson, 2003), suggesting that protonation of histidine side chain (*pKa* of 6.5) may not be a mechanism in contrast to that seen in $K_v1.4$ (Claydon *et al.*, 2000). Indeed, site-directed mutagenesis mutating the five native extracellular histidine residues to glutamine all had no effect on the pH-dependent inhibition of maximum conductance confirming that the native histidine residues are not the proton sensor. Since low pH have no effect on the voltage-dependence of inactivation, the reduction in the maximum conductance is also not likely due to stabilization of the inactivated state of the channel. Indeed, a rapid reduction in single channel current amplitude at pH 5.5 was preserved in inactivation removed (S620T) channels (Van Slyke *et al.*, 2012). Instead, several lines of evidence strongly support that external protons inhibit hERG channel conductance via block of the pore. Firstly, protons caused a rapid block of hERG single channel current amplitude (Van Slyke *et al.*, 2012) that is consistent with H^+ block observed in L-type Ca^{2+} channels (Chen *et al.*, 1996). Secondly, the proton-induced inhibition of hERG conductance is hindered by the presence of increasing extracellular Na^+, which occupies the outer pore of the channel. Lastly, introduction of a glutamate residue, that can be protonated, at H587 in the outer mouth of the channel pore, altered the voltage-dependence of pore block by protons

further supporting the notion that block of the pore by protons reduces the maximum conductance of the hERG channels (Van Slyke *et al.*, 2012).

1.5.2 External protons right-shift the voltage-dependence of activation and slow activation kinetics

External protons have two effects on activation parameters. External protons induced a depolarizing shift in the voltage-dependence of activation and a slowing of activation kinetics. The slowing of activation kinetics has been proposed to be due to an effect of external protons modifying the voltage-insensitive step described by the five state linear model. As discussed, (see section 1.2.2.1), the activation time course of hERG channels is strongly voltage-dependent but reaches an asymptote at depolarized potentials of +80 mV and above, where a voltage-insensitive step becomes rate-limiting. At pH 6.0 the asymptote, extrapolated from +80 mV was ~50 ms compared to that of ~25 ms at pH 7.4 suggesting that external protons modified the voltage-insensitive step and slowed activation kinetics (Zhou & Bett, 2010). The asymptote was plotted against a range of pH values tested (from 5.5 to 8.0) and yielded a *pKa* = 6.4 which would suggest a histidine side group may mediate this effect. Modifying the voltage-insensitive step in the five state linear model produced comparable currents to the experimental data which supports the notion that external protons slowed the activation kinetics by modifying the voltage-insensitive step (Zhou & Bett, 2010).

The depolarizing shift in the voltage-dependence of activation has been suggested to be the result of surface charge screening effect, but the lack of a parallel shift induced by external protons in the voltage-dependence of inactivation suggests that the effect on activation is likely due to a specific mechanism on the channel. However, the site and mechanism for this depolarizing shift is unknown in hERG channels and is the focus of Chapter 3 of this thesis.

1.5.3 External protons accelerate hERG channel deactivation

Another distinctive effect of external protons on hERG channel gating, that was well observed in numerous studies, is an acceleration of the deactivation rate (Anumonwo *et al.*, 1999; Bérubé *et al.*, 1999; Jiang *et al.*, 1999; Terai *et al.*, 2000; Bett & Rasmusson, 2003; Du *et al.*, 2010, 2011*a*; Zhou & Bett, 2010; Van Slyke *et al.*, 2012; Shi *et al.*, 2014).

Changing pH within the physiological range (7.5 to 6.5) was observed to dramatically accelerate both the fast and the slow components of deactivation with little effect on the maximum conductance, the voltage-dependence of activation, or the kinetics of activation or inactivation (Jiang *et al.*, 1999). This observation was further supported by characterization of the pH-induced reduction of maximum conductance, which had a *pKa* close to 5.5, and the pH-induced acceleration of deactivation, which had a *pKa* close to 6.8 (Bett & Rasmusson, 2003). The differing *pKa* values between the pH-induced pore block and acceleration of deactivation suggests that there is the possibility of two distinct protonation sites on the channel that mediates these effects separately (Bett & Rasmusson, 2003). Furthermore, within the physiological and pathophysiological range of pH_o, the dominant effect will overwhelmingly be on the deactivation kinetics of hERG. Jiang et al 1999 tested a series of hypotheses to elucidate the mechanism underlying the pH-induced acceleration of deactivation. The *pKa* of 6.8 strongly implicates histidine residues as proton sensors mediating the effect on deactivation. However, mutation of the two extracellular histidine residues in the S5-P loop of hERG channels (H578E/H587E), did not abolish the proton-induced acceleration of deactivation, implying that these histidine residues are not responsible (Jiang *et al.*, 1999). Another possibility may be that external protons destabilize the C-type inactivated state of the channel and expedite the transition of channels to the open state and consequently accelerates closing of the channel (Jiang *et al.*, 1999). However, C-type inactivation-removed mutations (G628C/S631C) still show an acceleration of deactivation going from pH 7.5 to 6.5 that is comparable to that in WT channels, therefore, external protons may not be binding near the outer mouth of the pore to accelerate deactivation kinetics (Jiang *et al.*, 1999). In addition, an N-terminus deleted channel, which dramatically accelerated deactivation kinetics, showed further acceleration of deactivation at pH 6.5 rejecting the idea that external protons may allosterically affect an intracellular regulatory mechanism involving the N-terminus. These data suggest that the pH-induced acceleration of deactivation is likely a result of protonation of the extracellular region of the channel (Jiang *et al.*, 1999). Indeed, this was supported by experiments using diethylpyrocarbonate (DEPC) to modify extracellular exposed side chains and subsequent observation of the pH sensitivity of the channel. DEPC is a membrane impermeable hydrophilic reagent that covalently modifies histidine side chains, as well as side chains of cysteine, tyrosine, serine, lysine, arginine, and tryptophan at high concentrations > 2 mM (Jiang *et al.*, 1999). DEPC treatment of WT hERG channels showed a drastic acceleration of deactivation rate and abolished further

acceleration of deactivation at pH 6.5, implying that extracellular residues that are exposed to the extracellular milieu are responsible for the pH-induced acceleration of deactivation (Jiang *et al.*, 1999). However, the specific residue(s) and the mechanism by which external protons accelerate deactivation remains unknown. This will be the focus of Chapter 4 in my thesis.

1.5.4 Effects of divalent cations on hERG channel gating mimic those of external protons

Interestingly, many pH-induced changes in hERG channel gating, which are outlined above, exhibit striking similarities with the effect of divalent cations (Paquette *et al.*, 1998; Ho *et al.*, 1998; Anumonwo *et al.*, 1999; Johnson *et al.*, 1999*b*, 2001; Silverman *et al.*, 2000; Fernandez *et al.*, 2005; Abbruzzese *et al.*, 2010; Kazmierczak *et al.*, 2013). hERG channel gating is differentially modulated by a wide array of different divalent cations. It was observed that both Ca^{2+} and Mg^{2+} cause a depolarized shift in the voltage-dependence of activation, and an acceleration of the deactivation rate without affecting inactivation parameters (Paquette *et al.*, 1998; Ho *et al.*, 1998; Johnson *et al.*, 1999*b*). One study observed the effects of various divalent cations (Cd^{2+}, Ni^{2+}, Co^{2+}, Mn^{2+}, and Zn^{2+}) on hERG channels in rabbit ventricular myocytes (Paquette *et al.*, 1998). Each of the divalent cations tested caused a depolarized shift in the voltage-dependence of activation. Several cations such as Cd^{2+}, Ni^{2+}, Co^{2+}, and Mn^{2+} increased the maximum conductance and this is likely due to a depolarized shift in the voltage-dependence of inactivation. Indeed, further study using a double point mutation (G628C/S631C) that removes hERG inactivation showed this mutant channel is insensitive to the Cd^{2+}-induced increase in conductance. This supports the idea that Cd^{2+} destabilizes the inactivated state and thus reduces the apparent rectification and increasing the hERG current (Johnson *et al.*, 1999*b*). Zn^{2+} and Ca^{2+} have been reported to block hERG channels (Paquette *et al.*, 1998; Ho *et al.*, 1998). However, there are several discrepancies in the effects of Zn^{2+} and Ca^{2+} that makes interpretation of their mechanism difficult. A study in *Xenopus* oocytes showed that Zn^{2+} and Ca^{2+} both caused a depolarized shift in the voltage-dependence of activation and blocked the hERG channel in a voltage-dependent manner (Ho *et al.*, 1998). In contrast, Ca^{2+} did not block the hERG channel in a voltage or time-dependent manner in CHO cells (Johnson *et al.*, 1999*b*), and in rabbit ventricular myocytes, Zn^{2+} blocked hERG channels with minimal effect on the voltage-dependence of activation (Paquette *et al.*, 1998).

Regardless of the uncertainties around the action of Zn^{2+} and Ca^{2+} on activation, the differential modulation of different hERG channel gating processes by divalent cations supports the idea of specific interactions with the channel, rather than a surface charge screening effect. Indeed, numerous reports suggest that divalent cations coordinate with acidic residues in the S2 and S3 transmembrane domains of voltage-gated potassium channels (Silverman *et al.*, 2000, 2003; Fernandez *et al.*, 2005; Zhang *et al.*, 2009; Abbruzzese *et al.*, 2010; Kazmierczak *et al.*, 2013). Within the EAG superfamily (eag, elk, erg), which includes hERG, these acidic residues are well conserved and locate within the voltage sensing domain, and divalent cation coordination with these acidic residues could conceivably alter channel gating. In eag channels, there are five aspartate residues, three in S2 (D274, D278, and D284), and two in S3 (D319, and D327) that correspond to D456, D460, D466 in S2, and D501, and D509 in S3 of hERG channels. In eag channels, Mg^{2+} dramatically slows the activation kinetics and was found to coordinate with D278 (in S2) and D327 (in S3) to exert the effect. Neutralization of either of these two residues abolished the Mg^{2+} sensitivity whereas neutralization of the other three acidic residues preserved the Mg^{2+}-induced slowing of activation kinetics (Silverman *et al.*, 2000). Further study in hERG channels using Mg^{2+} and a mutagenic approach revealed that neutralization of D456, D460, and D509 to alanine had differential effects on Mg^{2+} modulation of activation and deactivation gating (Lin & Papazian, 2007). Abolition of Mg^{2+}-induced acceleration of deactivation required double mutations containing D456A, while each of the single aspartate mutants abolished the Mg^{2+}-induced slowing of activation. This not only suggests that divalent cations modulate activation and deactivation via D456, D460, and D509 by separate mechanisms in hERG channels, but also that there are likely subtle structural differences between S2, S3 and S4 transmembrane segments in eag and hERG channels (Liu *et al.*, 2003; Lin & Papazian, 2007). These findings corroborated an earlier study, where the non-physiological ion, Cd^{2+}, which induced a depolarized shift in activation, was used to probe the coordination site for divalent cations (Fernandez *et al.*, 2005). Using site-directed mutagenesis, it was found that a single neutralization mutation to alanine at D456, D460, or D509 reduced the Cd^{2+}-induced shift in the voltage-dependence of activation. The Cd^{2+}-induced shift in the double mutation of D456A/D509A was equivalent to the sum of the shifts induced by individual mutations, which suggests that the effects of D456A and D509A are independent and that efficient coordination of Cd^{2+} requires these two residues to induce the shift in the voltage-dependence of activation (Fernandez *et al.*, 2005). Furthermore, the triple mutation,

D456A/D460A/D509A, showed an extremely depolarized activation and completely abolished the Cd^{2+}-induced shift. These data strongly suggest that the three acidic residues within S2-S3 coordinate Cd^{2+} to modulate the depolarized shift in the voltage-dependence of activation (Fernandez *et al.*, 2005; Abbruzzese *et al.*, 2010).

Overall, divalent cations provide a valuable tool to probe the understanding of normal hERG channel gating, but also provide clues to the potential mechanism by which external protons modulate hERG channel gating. These will be explored more in Chapter 3.

1.5.5 External protons impair the protective nature of hERG channels

As discussed earlier (see section 1.2.3), the normal slow deactivation gating process in hERG channels plays an important role in phase 3 repolarization of the cardiac action potential, but it also been suggested to protect against premature depolarizations in the form of EADs or DADs (Yu Lu *et al.*, 2001). Such afterdepolarizations would otherwise increase the susceptibility to the initiation of a premature action potential that could lead to lethal arrhythmia. Given the dramatic inhibition of hERG channel function by external protons, it is conceivable that protons may not only prolong the action potential duration, but also inhibit the protective role of hERG channels against EADs or DADs. A previous study using a ventricular action potential voltage clamp waveform in CHO cells, expressing hERG channels, observed that external application of pH 6.3 solution reduced the peak resurgent current during the action potential by 31%, and the current decline was also faster compared to pH 7.4 (Du *et al.*, 2010). In addition, the transient peak protective current elicited by premature stimuli was also dramatically decreased at pH 6.3, refer to Figure 1.2 (Du *et al.*, 2010). Both observations would suggest a prolongation of the APD and an increased susceptibility to initiation of a premature action potential. Indeed, computer simulation (using the five state linear Markov model), of an action potential clamp experiment showed that the peak resurgent current was reduced at pH 6.3, and the APD_{90} (action potential duration at 90% repolarization from the peak) was prolonged slightly from 301 ms to 310 ms. Although the prolongation for the APD_{90} is modest, pH 6.3 increased the susceptibility to initiation of a premature action potential when subjected to a set of premature stimuli (Du *et al.*, 2010). In these simulations, a suprathreshold depolarization stimulus was elicited to ensure successful firing of a normal action potential, and this was followed by a second subthreshold depolarization stimulus to simulate a

DAD. At pH 7.4, this second subthreshold depolarization stimulus did not initiate an action potential, but the same subthreshold stimulus was able to initiate an action potential at pH 6.3 (Du *et al.*, 2010). These *in silico* results highlight a potential role of hERG current in the protection against premature stimuli and suggest inhibition of normal hERG channel gating by external protons may be pro-arrhythmogenic by reducing the protective hERG current. This idea is further explored in Chapter 4.

1.6 Zebrafish *Danio rerio* as a translational heart model

The observed effects of external protons on hERG channels expressed in heterologous expression systems, such as *Xenopus* oocytes, and CHO cells, suggest that external protons may be pro-arrhythmogenic during early ischemia by inhibiting normal hERG function. *In silico* simulations using human ventricular models also suggest that external protons reduce hERG channel current and increase the susceptibility to a premature initiation of an action potential elicited by afterdepolarizations, in the form of EADs and DADs, which could lead to lethal arrhythmia. However, experimental assessment of the pro-arrhythmogenic effects of external protons on hERG channels in a whole heart model has not been done. The drawbacks of heterologous expression systems is that the channel of interest is not normally expressed in the expression system and is observed in isolation. This means that regulatory subunits, intracellular milieu, and post-translational modifications of the channels are different or absent in the expression system of choice. In contrast, observing channel function in a whole organ model would give insight to how the channels function within their native intracellular milieu surrounded by endogenous regulatory components. Moreover, fundamental biophysical knowledge gained from heterologous expression system studies can be translated to a whole heart model to further advance potential therapeutic treatments.

In the last decade, zebrafish *Danio rerio,* a tropical freshwater teleost fish species, has been gaining recognition as an excellent translational model system to study cardiac diseases (Nemtsas *et al.*, 2010; Poon & Brand, 2013; Vornanen & Hassinen, 2016). Although most studies conducted on zebrafish hearts concern cardiac development diseases (Bakkers, 2011), advancement in *ex vivo* ECG and optical mapping techniques using Ca^{2+} and voltage-sensitive fluorescence dyes have opened the opportunity to perform high-throughput studies of cardiac electrophysiology and diseases as well as drug screening. Zebrafish present several major advantages as a cardiac model: 1) the

zebrafish heart rate at 28 ºC (the temperature of their native environment) is between 120-180 beats per minute (bpm), which is significantly closer to the human heart rate of 60-100 bpm compared to that of mouse at 300-600 bpm (Leong *et al.*, 2010*a*); 2) at 28 ºC, the Q-T interval of zebrafish is around 200-290 ms, which is similar to that of human (300-450 ms), and in contrast to that of mouse (83-96 ms) (Leong *et al.*, 2010*a*; Poon & Brand, 2013; Lin *et al.*, 2014); 3) the major current that facilitates repolarization are expressed after just 72 hours post-fertilization. The major repolarizing current is I_{Kr}, which makes zebrafish an ideal model to study the changes to I_{Kr} in *ex vivo* experiments; 4) *in vivo* examination of the gene of interest in zebrafish is relatively easy to perform. One popular method is the use of morpholino antisense oligonucleotides (MO) to knock-out specific genes. MO are DNA analogues with an altered backbone which replaces the ribose backbone in DNA with a morpholine backbone. MO can be injected directly into the one to four-cell stage of zebrafish embryos and can be designed to target binding of ribosomes to a defined location (Heasman, 2002); 5) Another emerging method is the creation of transgenic zebrafish using CRISPR genome editing technology to introduce precise specific knock-ins or knock-outs of genomic DNA. The transparent morphology of the zebrafish, during development, allows easy screening of successfully incorporated genes by using fluorescent markers such as yellow fluorescence eye marker (Hwang *et al.*, 2013); 6) electrophysiology studies on MO knockout or CRISPR-modified zebrafish can be performed via the optical mapping technique. Optical mapping has emerged as a popular technique that allows rapid imaging of Ca^{2+} and voltage responses in zebrafish whole heart when subjected to different extracellular conditions such as application of drugs, small molecules, and pH change; 7) lastly, zebrafish are relatively cheap, easy to maintain, and fast to reproduce and develop.

Despite these attractive advantages, the zebrafish translational model is not without its limitations. Zebrafish are a phylogenetically distant species from human, and therefore the two-chambered heart of the zebrafish presents fundamental differences compared to the four-chambered human heart, which can make direct comparisons in cardiac development challenging. Zebrafish have also gone through multiple whole genome duplication events that may give rise to multiple orthologs in the zebrafish genome for a given human gene, and several thousand unique zebrafish genes without an ortholog (Woods *et al.*, 2000). Orthologs are corresponding genes in different species, in which the genes arise from a common ancestor in the lineage of the two species. For

example, using RT-PCR to quantify transcript expression in the zebrafish, four erg gene products have been described (*Kcnh6*, *Kcnh2a*, *Kcnh2b*, and *Kcnh7*) (Vornanen & Hassinen, 2016), although unpublished data from our lab indicate that there are *Kcnh6a*, *Kcnh6b*, and that *Kcnh6a* is by far the most prevalent transcript in the zebrafish heart. At 28 ºC *Kcnh6a* channels exhibit human *KCNH2*-like gating properties and pharmacology. Due to this complication, careful designing of experiments and interpretation of results is needed to draw the most appropriate conclusion from the zebrafish model to the human. Since zebrafish are ectothermic, their body temperature varies drastically based on their surrounding environment and the tolerable range is between 6.2 to 41.7 ºC (Vornanen & Hassinen, 2016). Therefore, their cardiac AP durations and heart rate changes dependent on their body temperature. At 28 ºC the measured ventricular APD_{50} and heart rate is between 143 and 250 ms and 120-145 bpm, respectively, whereas at 36 ºC the APD_{50} and heart rate is 66 ms and 301 bpm, respectively, which is quite different from that of humans (Vornanen & Hassinen, 2016).

1.6.1 Zebrafish heart anatomy and electrophysiology

The zebrafish has a two-chambered heart with an atrium and a ventricle (Figure 1.5). The heart functions to pump deoxygenated blood to the gills first before circulating to the body, therefore one fundamental difference with humans is the lack of a pulmonary circulation (Leong *et al.*, 2010*a*). In the mammalian heart, the pulmonary circulation acts to pump deoxygenated blood away from the right ventricle of the heart to the lungs and return oxygenated blood to the left atrium and ventricle. In human, filling occurs passively upon atrial relaxation. However, in zebrafish, the filling of the atrium is an active process where the atrium must contract for filling to occur then ventricular contraction pumps the blood to the gills via the bulbus arteriosus. The bulbus arteriosus is a tubular structure composed of smooth muscle cells and elastic tissues that act to maintain blood pressure to allow continuous blood flow into the gills (Hu *et al.*, 2001; Leong *et al.*, 2010*a*). These fundamental differences between zebrafish and mammalian heart can make direct comparison of cardiac development a challenge.

Although the zebrafish cardiac anatomy is different compared to that of mammalian species, representing a more simplistic structure, the electrophysiology of the zebrafish is surprisingly similar to that of human. The conduction system starts at the sinoatrial node and propagates to the ventricle via the atrio-ventricular canal (AV node)

(Leong *et al.*, 2010*a*). Ventricular contraction starts at the apex and ends at the base (Figure 1.5) like that in the human heart. Measurement of the action potential in whole zebrafish hearts at 28 ºC reveal that the ventricular zebrafish AP closely resembles that of the human ventricular AP (Figure 1.5) with a rapid upstroke phase, plateau phase, repolarization phase, and resting phase (Nemtsas *et al.*, 2010; Lin *et al.*, 2014). Patch clamp recordings of isolated zebrafish cardiomyocytes using selective ion channel blockers have been performed to examine the underlying ionic contributions. The rapid upstroke of the zebrafish AP is dominated by a TTX (tetrodotoxin)-sensitive I_{Na} current due to sodium channels (TTX is a specific sodium channel blocker). The application of 100 nM of TTX reduced the upstroke velocity by 25% in the atria and 19% in the ventricle (Nemtsas *et al.*, 2010). The plateau phase is dominated by the I_{Ca} current from L-type Ca^{2+} channels in adult zebrafish (T-type Ca^{2+} channels dominate in fetal hearts). Application of 10 µM of the L-type Ca^{2+} channel specific blocker, nifedipine, greatly shortened the action potential duration of the plateau phase (APD_{20}). Lastly, the I_{Kr} specific blocker, E4031, profoundly prolonged both the atrial and ventricular action potential duration indicating that the zebrafish ERG channel is the main driver behind the I_{Kr} current (Nemtsas *et al.*, 2010). The use of HMR 1556, a I_{Ks} specific blocker, did not prolong the action potential duration indicating that repolarization in zebrafish is conducted by the I_{Kr} current (Nemtsas *et al.*, 2010). One noticeable difference is the lack of the signature “spike and dome” phenotype in the zebrafish AP compared to that of the human epicardial AP, which is conducted by the I_{to} current. Since the zebrafish AP exhibits no “spike and dome” phenotype, there is likely very little I_{to} present in zebrafish, which likely, therefore reflects a human endocardial ventricular AP that also exhibits little I_{to} expression. Using quantitative real-time PCR (qPCR), it was shown that there are six $K_{ir}2$ genes that may conduct the I_{K1} current in zebrafish heart. The four most abundant ($drK_{ir}2.1a$, $drK_{ir}2.2a$, $drK_{ir}2.2b$, and $drK_{ir}2.4$), show strong inward rectification at potentials above -80 mV (close to the reversal potential for K^+), and are completely blocked by application of external Ba^{2+}, which has been shown to block I_{K1} current (Hassinen *et al.*, 2015).

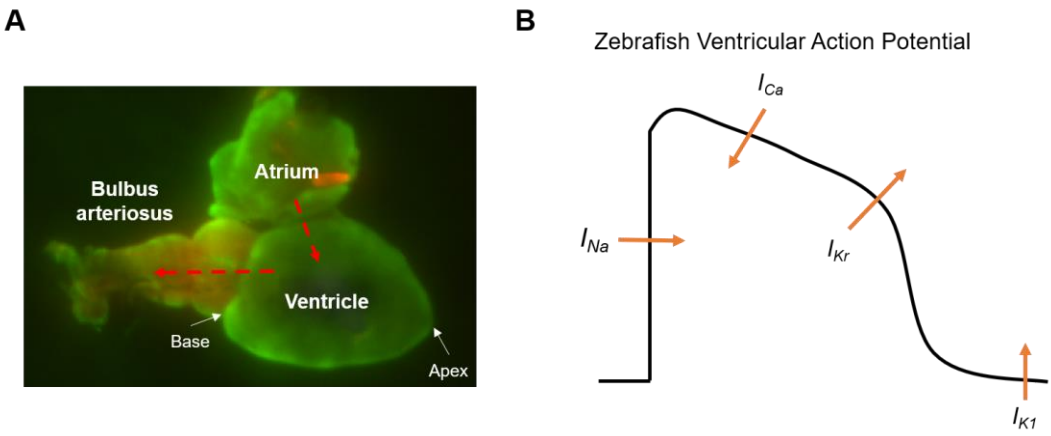

Figure 1.5 - Zebrafish heart anatomy and the ionic currents underlying the ventricular AP.

A. Optical mapping image of an adult zebrafish heart with the atrium and ventricle attached and the bulbus arteriosus attached to the ventricle. The structure of the zebrafish atrium is highly variable between fish: some adapt a more orderly structure, while others are more fibrous like. In contrast the structure of the ventricle is highly ordered and changes very little between fish to fish. Red dashed arrows indicate the flow of blood. **B.** A schematic representation of a zebrafish ventricular AP. Known currents are indicated with the arrow showing the direction of ionic flow.

1.6.2 Zebrafish ether-à-go-go related gene (zERG)

The I_{Kr} current has been shown to be the predominant current during the repolarization phase of both the atrial and ventricular action potential of the zebrafish heart and is conducted by the zebrafish erg channel (zerg) channel. A bioinformatic approach was used to determine the genes involved in the expression of the zerg channel. The amino acid sequence of human *KCNH2* gene was queried against the zebrafish genome using a BLAST (basic local alignment search tool) algorithm and revealed at least two orthologues located on chromosome 2 (*Zerg-2,* orthologue of *KCNH2* in human), 3 (*Zerg-3*, orthologue of *KCNH6* in human), and 24 (*Zerg-24*), which is thought to be a paralog of *Zerg-2* (Leong *et al.*, 2010*b*). Paralogs are genes that arise from genome duplication events. q-PCR was used to quantify the tissue expression profile of these genes and found that z*erg-2* is mostly expressed in the muscle, brain, kidney and gills with very low expression level in the heart. Interestingly, close to 99% of the gene expressed in the atrium and ventricle of the zebrafish heart is in fact *zerg-3* (Leong *et al.*, 2010*b*; Vornanen & Hassinen, 2016). However, in human, the *KCNH6* gene (orthologue to *zerg-3*) encodes for the hERG2 channel that is expressed mainly in the brain rather than the heart. This has made comparing the correct orthologues between zebrafish and human confusing. For example, previous characterizations of zERG channels have been mostly done on *zerg-2,* instead *zerg-3* (Milan *et al.*, 2003; Arnaout *et al.*, 2007; Hassel *et al.*, 2008; Scholz *et al.*, 2009). This can be a major problem when comparing results from heterologous expression systems with that from zebrafish whole heart system, since the gene products being compared may not be equivalent. Nevertheless, one study examined the effect of QT-prolonging drugs on zebrafish embryo and used the ratio of heart rate changes between atrium and ventricle as a measure for induction of arrhythmia in *zerg-3*. It was found that all the QT-prolonging drugs induced a 2:1 atrioventricular block (the ventricular rate dropped by 50% compared to that of atrium) and knockdown of *zerg-3* by MO also show a 2:1 atrioventricular block, suggesting that the QT-prolonging drugs are blocking *zerg-3* (Langheinrich *et al.*, 2003). This shows that the zebrafish is an excellent model for studying cardiac electrophysiology with known caveats to consider. In my thesis, I will use zebrafish hearts as the model to assess the arrhythmogenicity during acute application of external protons to better understand the mechanism by which external protons may contribute to arrhythmogenesis during early myocardial ischemia.

1.7 Overview and objectives

There have been numerous studies observing the effects of external protons on hERG channels and some have elucidated potential mechanisms underlying these effects (Anumonwo *et al.*, 1999; Bérubé *et al.*, 1999; Jo *et al.*, 1999; Jiang *et al.*, 1999; Terai *et al.*, 2000; Vereecke & Carmeliet, 2000; Bett & Rasmusson, 2003; Du *et al.*, 2010; Zhou & Bett, 2010; Van Slyke *et al.*, 2012). The main effects of external protons are a reduction in the maximum conductance, slowed activation kinetics, a depolarized-shift in the voltage-dependence of activation, and an acceleration of deactivation. While these main effects of external protons are similar to the effects produced by divalent cations and may share a similar mechanism, the exact sites and mechanisms for the individual effects is unknown. Recently, Aaron Van Slyke, a former master's student in the lab, determined that the proton-induced reduction in the maximum conductance is due to block of the hERG channel pore (Van Slyke *et al.*, 2012), and the slowed activation rate has been shown to be due to modulation of the voltage-insensitive step during the activation pathway (Zhou & Bett, 2010). This leaves the determination of the remaining two effects to be discovered: the proton-induced change in the voltage-dependence of activation, and the acceleration of deactivation. I believe that understanding how external protons modulate hERG channel function gives insight in two main ways. The first is that there is a need to understand the normal gating processes in hERG channels, which are critical to cardiac repolarization that are not yet fully understood. For example, the regulation of slow deactivation in hERG channels involves a complex interaction between S4-S5 linker, C-terminus, and N-terminus at the intracellular side, but also can be regulated by acidic and basic residues within the voltage sensing domain and S4. How do these components all interact to regulate deactivation? The second purpose is to provide insights into potential therapeutic targets to rescue or compensate for the inhibition of hERG channel function by protons that may restore the protective function of hERG channels against electrical abnormalities in the cardiac action potential.

The goal of my thesis is to use mutagenesis, and a combination of electrophysiology techniques (TEVC, VCF, and COVG) to first determine the site and mechanism for the proton-induced change in hERG activation and deactivation. Then I will use this biophysical knowledge from a heterologous expression system and translate

that to the zebrafish whole heart model to assess the arrhythmogenicity of external protons using the optical mapping technique. The objectives of my research are the following:

1. To determine the site and mechanism for the depolarized-shift in the voltage-dependence of activation induced by external protons (Chapter 3). My hypothesis is that external protons protonate the cation binding pocket to destabilize the activated voltage sensor, similar to that of divalent cations.

2. To determine the site and mechanism for the acceleration of deactivation induced by external protons and also provide insights to the normal regulation of slow deactivation (Chapter 4). My hypothesis is that external protons accelerate the deactivation rate by destabilizing the relaxed state of the voltage sensor, through protonation of the acidic residue, D509, as a mechanism.

3. To use the high-throughput optical mapping technique on zebrafish whole hearts to assess the arrhythmogenicity of external protons (Chapter 5). My hypothesis is that acute external acidification prolonged the ventricular AP duration of zebrafish and increase arrhythmogenicity as a result of an inhibition of I_{kr} current during early ischemia.

Chapter 2. Materials and Methods

2.1 Molecular biology - mutagenesis

The hERG potassium cDNA sequence was subcloned into the pBluescript II SK(-) bacterial expression vector using EcoRI restriction sites. Site-directed mutagenesis was performed by overlap extension polymerase chain reaction (PCR). The overlap extension PCR involves two PCR steps to introduce a mutation at the site of interest using high fidelity *PfuTurbo* DNA polymerase. The first step requires designing a set of outer primers and a set of mutagenic primers to create two PCR fragments. The outer primers contain restriction sites that allows easy insertion of the PCR fragment into the vector. The first step involves amplifying two PCR fragments: one spans from the forward outer primer to the reverse mutagenic primer, and the second spans from the forward mutagenic primer to the reverse outer primer. The second step uses the two fragments, created in the first step, as template and the same set of outer primers to amplify a single, larger, fragment with the mutation of interest in the centre. This fragment was then subcloned back into the hERG full sequence in the pBluescript II SK(-) expression vector using the restriction sites within the outer primers. All primer synthesis was done by Sigma Genosys (Oakville, ON).

A particular challenge of creating mutations within the hERG channel sequence is due to its guanine-cytosine (GC) rich content at 65.9% (Sroubek *et al.*, 2013). The GC pair is formed by three hydrogen bonds that provide more thermal stability through base stacking interactions than that of adenine-thymine (AT) pair (Yakovchuk *et al.*, 2006), thus requiring a much higher melting temperature to separate the DNA strands during the PCR reaction. In addition, GC pairs can also form stable hairpin structures in the DNA that create roadblocks for DNA polymerase. Lastly, GC rich primers can also hybridize with each other to form primer dimers which will further decrease the amplification success. Overlap extension method amplifies smaller fragments which results in lower melting temperatures, lower chances of hairpin formation in the template DNA, higher amplification efficiency, and shorter primers which reduces the chance of primer dimers formation. As a co-op student in my undergraduate career, I troubleshoot and streamlined the overlap extension method and achieved high efficiency in producing a library of mutated hERG channel constructs.

The plasmid, containing the mutated hERG construct, was then transformed into DH5α competent cells (Thermo Fisher Scientific, Massachusetts, US) and incubated for 16 hours at 37 ºC followed by DNA extraction with a Qiagen miniprep kit. Mutant constructs were sequenced by Eurofins MWG Operon (Huntsville, AL) to ensure successful incorporation of the mutation with no off-target mutations. Once the mutation was confirmed, the plasmid was linearized with the *Xbal* restriction endonuclease, and a mMessagemMachine T7 Ultra cRNA transcription kit (Ambion, Austin, TX) was used for *in vitro* mRNA transcription using the T7 promoter. The kit also includes the process of adding a modified cap analog to the 5' end (ARCA) and a poly(A) tail on the 3' end. The ARCA is a modified cap analog that creates a functional orientation in which the mRNA is 100% translatable thus increases the translation of the protein, and the poly(A) tails provides stability to the mRNA within the cell. In combination, these modifications increase the transitional efficiency, improving surface expression of the protein.

2.2 Expression system

There are several well established heterologous expression systems widely used for studying ion channel function such as Chinese Hamster Ovary (CHO) cell lines, Human Embryonic Kidney (HEK293) cell lines, and *Xenopus laevis* oocytes. Also, the recent emergence of cardiomyocytes derived from human induced pluripotent stem cell (HiPSC-CM) have been used as an ion channel expression system (Jones *et al.*, 2014). In this dissertation, I have used *Xenopus* oocytes extensively as a heterologous expression system for all electrophysiology experiments. *Xenopus* oocytes present several advantages that make it the most appropriate system for my studies: 1) One major advantage of oocytes is that they express very few endogenous ion channels and receptors, which reduces the endogenous currents that may contaminate the exogenous expressed channel of interest (Goldin, 1991); 2) The large cell size (1.0 mm in diameter) allows for easy injection of RNA, and manipulation during recording with the two-electrode voltage-clamp technique; 3) The cells are also robust so that they not only can last for days without dying, but can also be subjected to many rigorous recording conditions for paired experiments; 4) A large number of good quality cells can easily be harvested; 5) RNA expression level can be predicted and controlled by the concentration of RNA injected. This is particularly important in voltage-clamp fluorimetry (VCF) and cut-open Vaseline gap voltage-clamp (COVG) recordings where a high expression of protein is

required to measure high resolution fluorescence deflections and gating currents, respectively.

Xenopus oocytes do have some disadvantages as an ion channel expression system: 1) Although oocytes express few endogenous channels, when left to express for 5-6 days (in the case of voltage-clamp fluorimetry and cut-open voltage clamp experiments), the endogenous channels can be large enough to potentially contaminate the exogenously expressed channel. One such channel is the calcium-activated chloride channels. To reduce the activation of the chloride channels, we used low calcium recording solution (0.5 mM $CaCl_2$) to reduce activation of chloride channels; 2) The large sized cell can act as a double-edged sword where large, high resolution, macroscopic currents may be easy to record, but also produce large membrane capacitance current during changes in voltage that may mask fast channel kinetics. This is a result from the large time constant for charging the membrane of the cell and since oocytes have a high surface area, this ultimately leads to a large membrane capacitance. To reduce contamination by capacitance currents, we used a high-gain amplifier and low resistance electrodes to maximize clamp speed to within 1 ms to quickly discharge the membrane so that fast channel kinetics can be resolved; 3) Another disadvantage of oocytes is that drug efficacy is often different in oocytes compared to other expression systems. The difference in efficacy can be attributed to the thick and dense cytoplasm of the oocytes, which can alter the mobility of the drug and also interfere with the accessibility of the drug to the channel (Goldin, 1991).

2.2.1 Oocyte preparation

In agreement with the policies and procedures of the Simon Fraser University Animal Care Committee and the Canadian Council of Animal Care, *Xenopus laevis* frogs were terminally anaesthetized by immersion in 2 g L^{-1} tricaine solution for 15 min before placing on an iced surface on the bench top for surgery. The oocytes were surgically removed by making two small incisions on the side of the lower abdominal regions, then carefully removing the oocytes while cutting off any connective tissues attached to the cells. 5 ml of the removed oocytes were then treated with collagenase (1 mg ml^{-1} collagenase type 1A) in $MgOR_2$ (magnesium oocyte ringer) solution (in mM: 96 NaCl, 2 KCl, 20 $MgCl_2$, 5 HEPES, titrated to pH 7.4 with NaOH) for 1 h. Oocytes were then transferred to SOS+ media (in mM: 96 NaCl, 2 KCl, 1.8 $CaCl_2$, 1 $MgCl_2$, 5 HEPES, 5 %

horse serum, 2.5 sodium pyruvate, 100 mg L^{-1} gentamicin sulfate, titrated to pH 7.4 with NaOH). Stage V-VI oocytes with uniform coloured animal, and vegetal poles, and a distinct band across the equator of the cell were selected from the batch for manual defolliculation. Defolliculation is necessary because the follicular layer also contain endogenous channels that may contaminate the current recordings. In additions, folliculated cells are harder to pierce which will make injection of RNA, and impaling for voltage-clamp experiments difficult.

2.2.2 Oocyte injection

Injection pipettes were made from borosilicate glass pulled using a P-87 Flaming/Brown Micropipette Puller (Sutter Instrument Co), and the tip was manually crafted with forceps. The injection pipette was backfilled with mineral oil and mounted on the plunger of a manual oocyte microinjection pipette (Drummond Scientific Company). A drop of mineral oil was then dispensed onto a parafilm surface, and subsequently 1 uL of cRNA was pipetted onto the mineral oil droplet. The RNA droplet was then filled from the tip of the injection pipette using the micro-dispenser. In general, 50 nL (5-15 ng) of cRNA was injected into each oocyte. Higher concentrations of cRNA were injected for slow expressing mutants or when higher expression of the protein was needed. Injected oocytes were stored and incubated in SOS+ media at 19 °C for 1-3 days before recording. For VCF and COVG recordings, incubation time was increased to 4-5 days to ensure higher expression. Oocytes were incubated with fresh SOS+ daily to maximize survival.

In some cases, the Nanoject II Auto-Nanoliter injector (Drummond Scientific Company) was used to inject the oocytes. Here, the plunger for the autoinjector is controlled automatically with an automated microprocessor. The automated microprocessor can be programmed to inject a fixed amount each time. This gives the advantage of delivering nanolitre of cRNA with precision thus reducing human errors. This is especially important for expression level studies where a precise and known amount of RNA is required for accurate comparison between constructs.

2.3 Electrophysiology

2.3.1 Two-Electrode Voltage-Clamp (TEVC)

Ionic current experiments recorded in this thesis were performed with the TEVC setup and technique. This setup requires two intracellular recording microelectrodes. When the cell is clamped, the first microelectrode acts as a voltage electrode, which continuously measures the membrane voltage of the cell relative to the reference electrode, which is fixed in the bath chamber. The second is a current electrode that injects an electrical current into the cell that is proportional and opposite in polarity to the flow of ions (in our study, mostly K^+ ions) across the membrane to ensure that the command voltage (membrane voltage that the user specify in the computer) and membrane voltage of the cell are held equal. This electrical current recorded is the ionic current. In this way TEVC allows the user to control the membrane voltage of the cell and observe the ionic current flowing through the channel. The system does this through a series of feedback amplifiers: The membrane voltage, measured by the voltage electrode with a high input impedance amplifier, is fed into a high gain feedback amplifier and compared with the command voltage protocols programmed using the pCLAMP 10.2 Electrophysiology Data Acquisition and Analysis Software (Axon Instruments, Foster City, CA). The high gain feedback amplifier detects any difference between the command voltage and membrane voltage and sends an output to the current electrode to inject current to bring the difference to zero. Therefore, the current that is required to be injected into the cell to bring the membrane voltage to the command voltage is equal and opposite in polarity to the ionic current conducted by ion flow. All signals were digitized using a digidata 1440 A/D converter.

TEVC recordings were performed at room temperature (20-22 ºC), and oocytes were bathed and recorded in external ND96 solution (in mM: 96 NaCl, 3 KCl, 0.5 CaCl, 1 $MgCl_2$, and 5 HEPES, titrated to pH 7.4 with NaOH). For pH solutions below pH 6.5, HEPES was replaced with MES to buffer the solution to ensure no changes in pH while recording. All recordings were collected under constant perfusion at a flow rate of 1 ml/min. All current signals were acquired at a sampling rate of 10 kHz with a 4 kHz low-pass Bessel filter.

Ag/AgCl Electrodes

The Ag/AgCl electrodes were made from thin-walled borosilicate glass pulled with a P1000 puller to a resistance of 0.2 – 2.0 MΩ when backfilled with a 3 M KCl. The Ag/AgCl electrodes are commonly used in electrophysiology recordings to transform ionic current to electrical current and vice versa. This is achieved by the redox reaction:

$$Ag + Cl^{-} \leftrightarrows AgCl + e^{-} \qquad (1.1)$$

The Ag/AgCl electrode is non-polarized under high Cl^- solution. In order words, the transfer of current from electrical to ionic relies on the concentration of Cl^-. When the Ag/AgCl is filled with saturated 3 M KCl solution, the current transferred by Cl^- is at a constant potential. This makes the Ag/AgCl electrode suitable for DC current measurement. Another added benefit of using a high saturating concentration filling solution such as 3 M NaCl or KCl is to maintain a large but stable liquid to liquid junction potential between the intracellular cytoplasm of the cell to the electrode tip so that the junction potential can be offset by applying a voltage in the opposite polarity against the junction potential.

2.3.2 Voltage-Clamp Fluorimetry (VCF)

Ion channel gating processes are complex and many details of the mechanism of how ion channels function are not yet fully understood. With advancement in fluorescence microscopy, VCF has emerged to be a powerful tool that allows dynamic visualization of conformational changes within the channel during gating in real time thus providing valuable information on channel function. VCF takes advantage of a unique property of a class of molecules that absorb light at a given wavelength and emit at another that can be detected and captured. These molecules are called fluorophores, and they can be tethered to cysteine residues through covalent sulfhydryl bonds, allowing site-specific visualization of fluorescence reports at region of interest on a channel. During the gating processes, conformational changes within the channel induce environmental change around the fluorophore that may quench or de-quench the emitted light. The VCF setup detects, captures and records changes in emitted fluorescence light intensity, while simultaneously measuring the ionic current with TEVC in parallel. Here, we used a membrane impermeable thiol-reactive fluorescence probe, tetramethylrhodamine-5-maleimide (TMRM), as our fluorophore. (Mannuzzu *et al.*, 1996; Cha & Bezanilla, 1998;

Es-Salah-Lamoureux *et al.*, 2010; Shi *et al.*, 2014). TMRM was covalently linked to a cysteine residue engineered at L520, which is located at the top of the S4 voltage sensor. In addition, we also substituted two native cysteines within the S1-S2 linker of the channel with valine (C445V, C449V) to reduce any off-target labeling that may contaminate the fluorescence signal at L520C (Es-Salah-Lamoureux *et al.*, 2010). Prior to recording, oocytes were incubated in depolarizing solution (in mM: 99 KCl, 1 $MgCl_2$, 2 $CaCl_2$, 5 HEPES, titrated to pH 7.4 with NaOH) containing 5 µM TMRM for 30 mins at 10 ºC in the dark, then washed with and kept in ND96.

For the VCF recordings (Figure 2.1), TMRM-labeled oocytes were excited by a 100W metal halide lamp filtered by a 525 nm band-pass (45 nm) excitation filter (Omega Optical, Brattleboro, VT), then reflected by a 560 nm long-pass dichroic mirror through a 20x objective lens, with a 0.75 numerical aperture (NA). The emitted rhodamine signal passed through the dichroic mirror and was filtered by a 565 nm long-pass emission filter before being detected by a Hamamatsu photomultiplier tube (PMT) module (Carin Research, Kent, UK). The signal-to-noise ratio for the fluorescence signal was improved by averaging multiple sweeps. To compensate for photobleaching, we recorded a control fluorescence report at -120 mV, where channels are not open, following every protocol, and subtracted this signal from experimental fluorescence recording. All fluorescence signals were acquired at a sampling frequency of 10 kHz with a 4 kHz low-pass Bessel filter. Although signals were often filtered further offline. The TEVC setup (Fig 2.1F) in parallel with the VCF apparatus allowed us to simultaneously measure the ionic current and fluorescence signal.

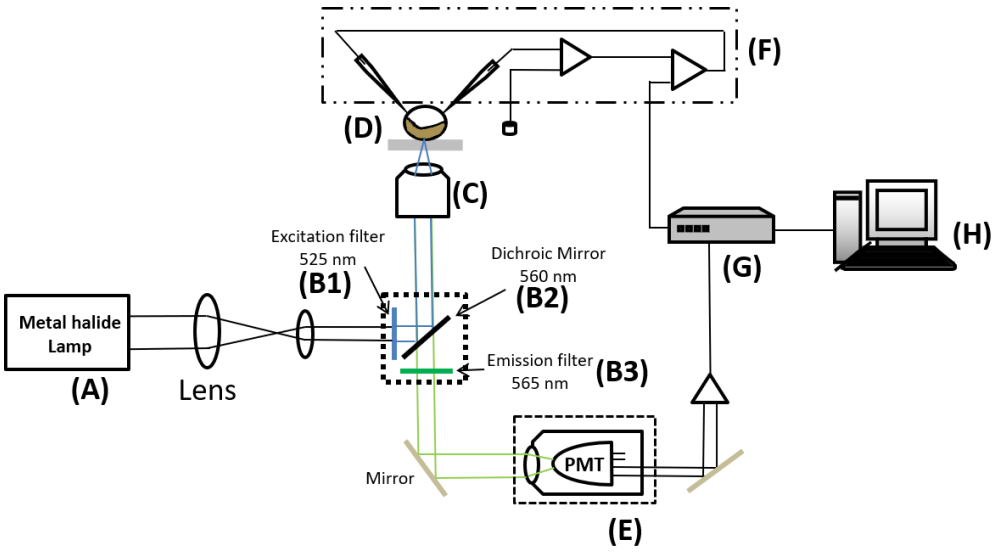

Figure 2.1 – Schematic of Voltage-Clamp Fluorimetry Apparatus

Fluorescence emitted from the fluorophore is recorded from individual oocytes by using a Nikon TE2000 inverted microscope with an Epi-Fluorescence attachment and PMT module. The fluorophore is excited by light from a 100 W metal halide lamp **(A)** that is filtered through a band-pass excitation filter (B1), and reflected by a long-pass dichroic mirror (B2) through a 20x objective with 0.75 NA. **(C)** on to the oocyte in the chamber **(D)**. Fluorescence emission from the fluorophore is passed through the 20x objective and filtered through the emission filter **(B3)**. The signal is then detected and amplified by the PMT module **(E)**, and digitized using an Axon Digidata 1440A A/D Converter **(G)**. Fluorescence emission intensity and ionic current is measured by a computer using the software pClamp 10 **(H)**. Simultaneously, the voltage-clamp of the oocyte is achieved using the two-electrode voltage clamp technique with an Axoclamp 900A amplifier **(F)**.

2.3.3 Cut-Open Vaseline Gap Voltage-Clamp (COVG)

Gating currents were measured using the cut-open oocyte Vaseline gap voltage clamp technique using a CA-1B amplifier (Dagan, Minneapolis, MN). The COVG technique involves mounting the *Xenopus* oocyte within three electrically isolated chambers. Six agar bridges, and one intracellular electrode (filled with 3 M NaCl) are assembled to complete the voltage clamp circuit (Figure 2.2). The three chambers, from top to bottom, are referred to as recording, guard shield, and lower chamber, respectively. The recording chamber accommodates the domus of the oocyte, in which the gating currents were recorded from using the intracellular electrode. The guard shield chamber acts to electrically shield the top and bottom chamber. There is a Vaseline-lined hole (~0.6 mm) at the top and guard chamber, that electrically isolates the chambers while accommodating the oocyte. The portion of the oocyte, immersed in the bottom chamber, was permeabilized by 0.1% saponin for 30-60 s so that the cytoplasm of the oocyte is electrically connected to the internal solution in the bottom chamber. In contrast, the recording and guard shield chambers were filled with external solution. The six agar bridges provide electrical connections between the chambers and were made from glass capillary tubes containing an internal platinum wire to increase the capacity to pass high-frequency currents. Each recording and guard shield chambers were voltage clamped by two agar bridges to the inverse of the command voltage. A third voltage clamp involves injecting current to the bottom chamber to ensure the interior of the oocyte is at ground with reference to the intracellular electrode in the top chamber. This allows measurement of the membrane potential relative to the command voltage.

The external solution in the top and guard chamber contained (in mM): 120 tetraethylammonium hydroxide (TEA-OH), 120 2-(N-Morpholino) ethane sulfonic acid (MES), 10 HEPES, and 0.5 $Ca(OH)_2$ titrated to pH 7.4 or pH 6.5 with MES. Internal solution contained (in mM): 120 TEA-OH, 120 MES, 10 HEPES, and 2 EGTA, titrated to pH 7.4 using MES. In addition, 20 µM of the hERG blocker, terfenadine, was added to both external and internal solutions to inhibit ionic current. Terfenadine is an open channel hERG blocker that binds to the inner pore cavity in the open state, and when the channel closes, terfenadine is trapped in the closed pore. 0.1 % saponin was perfused to the bottom chamber for 30-60 s to permeabilize the oocyte membrane, and subsequently replaced with internal solution. Prior to gating current measurements, the membrane was held at -10 mV for 30 minutes to ensure depletion of endogenous K^+ ions from the cytosol

of the oocytes to further minimize ionic current during recording. Microelectrodes were pulled from borosilicate glass and had a resistance of 0.25-0.5 MΩ when filled with 3 M CsCl. All acquired COVG signals were filtered at 10 kHz with a low-pass filter, digitized at 50 kHz, and acquired using Patchmaster software (HEKA electronics) at ~20 ºC. Capacitive currents were subtracted using the analog circuitry of the amplifier, and linear leak subtraction was performed online with a P/-8 protocol.

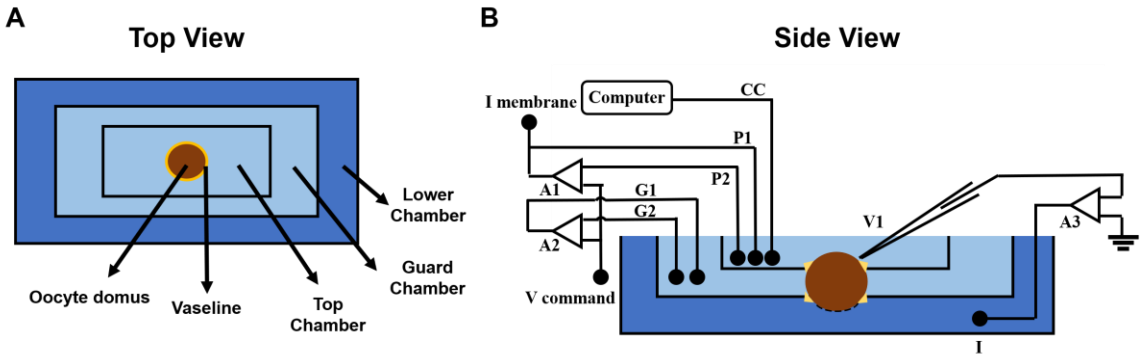

Figure 2.2 – Schematic of Cut-Open Voltage Clamp (COVG) Apparatus

A. Top view of the COVG setup with the Vaseline-lined domus of the oocyte in the top chamber, followed by the guard and lower chamber. **B.** Side view of the cut-open voltage clamp setup with voltage clamp circuitry. The oocyte is mounted between the top, guard and lower chamber, which are electrically separated by Vaseline rings (yellow), and part of the ocoyte in the lower chamber was permeabilized with 0.1% saponin. The six agar bridges (P1, P2, G1, G2, CC, and I) and the intracellular electrode V1, was assembled around the oocyte with three operating amplifiers, A1, A2, and A3.

2.4 Voltage protocols

This section outlines the voltage protocols used to record ionic currents. It is important to note that some parameters such as pulse durations and voltages were modified to better capture the channel states at different experimental conditions. Voltage protocols are annotated as *insets* in corresponding figures.

2.4.1 Voltage-dependence of activation

To determine the voltage-dependence of activation, oocytes were held at -80 mV and subjected to 2 s depolarizing steps to +60 mV in 10 mV increments (P1) to activate and inactivate the channel. This is followed by a repolarizing step to -60 mV current (P2) to recover the channel from inactivation. Peak tail currents elicited by the -60 mV pulse were measured and plotted against voltage and the data were fitted with a Boltzmann equation to yield the $V_{1/2}$ and the slope factor. To measure voltage-dependence of activation using physiological durations, a 250 ms P1 pulse duration was used. To measure the steady-state voltage-dependence of activation, an 8 s P1 pulse duration was used to ensure full activation of the channel.

2.4.2 Voltage-dependence of deactivation

Voltage-dependence of deactivation was measured by holding the oocytes at -80 mV then depolarize to +60 mV for 500 ms (P1) to collect the channels into the open state. This is followed by a series of 8 s repolarizing steps from -110 mV to +40 mV in 10 mV increments (P2), allowing the channels to deactivate. Lastly, this is followed by a short hyperpolarizing pulse to -110 mV for 100 ms (P3) as a test pulse to assess the extent of deactivation in P2. The peak tail currents measured at P3 indicates the proportion of channels that remained open during P2, thus providing an indirect measurement of channel deactivation. A Boltzmann equation was used to describe the peak tail current against voltage relationship to yield the $V_{1/2}$ of deactivation and slope factor. For voltage-dependence of deactivation measured at physiological durations, the P1 pulse duration used was 250 ms, followed by a P2 pulse duration of 750 ms. For steady-state measurements, a 15 s depolarization pulse was used to ensure the channels were fully activated, inactivated and relaxed, followed by a P2 pulse of 8 s to ensure steady-state deactivation is achieved.

2.4.3 Deactivation kinetics

To determine the kinetics of deactivation, oocytes were held at -80 mV and depolarized to +60 mV for 500 ms to activate and inactivate the channels. This is followed by 8 s P2 steps from -110 mV to +40 mV in 10 mV increments to recover the channel from inactivation and subsequently deactivate the channel. The current decay during the P2 was fitted with a double exponential function. Analysis of the kinetics of deactivation is described in section 2.5.2.

2.5 Data analysis

Data were analyzed using Clampfit 10.3 (Axon Instruments), SigmaPlot 13.0 (Systat Software, San Jose, CA), and IGOR Pro (Wavemetrics, Lake Oswego, OR) software. Data were presented as mean ± SEM, and n represents the sample numbers of cell recorded. Statistical analysis was performed using a Student's *t*-test or two-way analysis of variance (ANOVA) where appropriate using JMP statistical software. A p-value of < 0.05 represents statistical significance.

2.5.1 Voltage-dependence relationship

Conductance voltage (GV) relationships was obtained by measuring the peak tail currents at the P2 pulse for activation and P3 pulse for deactivation as outlined above. Data points were normalized to their maximum and plotted against voltage. Fluorescence voltage (FV) relationships was obtained by measuring the fluorescence deflection at the end of the P1 pulse, normalized to their maximum deflection, against voltage. Charge voltage (QV) relationships was obtained by integrating the off gating (Q_{off}) currents for activation, and on gating (Q_{on}) currents for deactivation. The calculated integrals were normalized to the maximum and plotted against test voltages. All GV, FV, and QV voltage-dependence relationships were fitted with the Boltzmann equation:

$$y = \frac{1}{(1 + exp^{(\frac{(V_{1/2} - V)}{k})})}$$

Where y is conductance (G/G_{max}), fluorescence signal (F/F_{max}), or gating charge (Q/Q_{max}) normalized to the maximum. $V_{1/2}$ is half activation or deactivation voltage. V is the test

voltage, and k is the slope factor which equals to RT/zF, where z is the apparent number of gating charges, R is the universal gas constant, T is absolute temperature and F is Faraday's constant.

2.5.2 Deactivation time course

Deactivation kinetics were quantified by fitting the decaying portion of the tail current (P2) during the test pulse to a bi-exponential function:

$$f(t) = A_{slow} exp^{(\frac{-t}{\tau_{slow}})} + A_{fast} exp^{(\frac{-t}{\tau_{fast}})} + C$$

where A_{slow} and A_{fast} are the relative amplitudes of the slow and fast components, τ_{slow} and τ_{fast} are the time constants for slow and fast component respectively, and C is a constant. For ease of comparison, a weighted time constant for deactivation ($\tau_{weighted}$) was calculated:

$$\tau_{weighted} = \frac{(A_{slow}\tau_{slow} + A_{fast}\tau_{fast})}{(A_{slow} + A_{fast})}$$

The $\tau_{weighted}$ is a sum of the contribution from the slow and fast components of deactivation. This simplifies the comparison of deactivation kinetics between different mutations and experimental conditions.

2.6 Zebrafish optical mapping

Optical mapping is a powerful technique that enables the measurement of membrane voltage changes in an isolated intact heart to observe changes in the cardiac action potential under various experimental conditions (Figure 2.3). This technique takes advantage of a potentiometric dye, *N*-(4Sulfobutyl)-4-(6-(4-(Dibutylamino)phenyl)hexatrieneyl)Pyridinium, (RH 237), where depolarization of the membrane voltage causes a corresponding blue shift in the emission signal, that leads to the decrease in the fluorescence signal acquired through the 700-nm long-pass filter. Using this potentiometric dye, we can capture the cardiac action potential of the zebrafish heart.

After the fish was euthanized in an ice bath, the intact heart was isolated from the zebrafish, as outlined in section 2.6.3, and cannulated. The heart was then labeled with 10 µM of RH 237 for 30 mins and subsequently labeled with 10 µM of blebbistatin for 1 h to arrest contraction while maintaining normal excitation. Blebbistatin is a myosin II inhibitor that lowers the myosin II affinity to actin. It has now been commonly used in optical mapping technique to reduce motion artefact induced by heart contraction (Swift *et al.*, 2012). The labeled heart was lowered into the imaging chamber containing 10 µM blebbistatin in calcium Tyrode solution to prevent photo-released of blebbistatin during long protocols. The aluminum top-loading imaging chamber has two ports: injection and electrode port. The injection port allows rapid change of extracellular environment by using a syringe to introduce drugs, compounds, or low pH solution, which is one of the major advantages of this technique. The electrode port on each side of the chamber fits a positive and negative electrode made out of 1.0 mm diameter Tungston electrode to ensure that the entire size of the Zebrafish heart lies within the field stimulation between the two electrodes. These electrodes serve to electrically stimulate the heart at any commanding heart rates and voltages, which opens the opportunity for introducing premature stimulus of various voltages and timing to access arrhythmogenicity under various experimental conditions. The imaging chamber is temperature controlled by the PID (proportional-integral-derivative) controller element where the command temperature is read and compared to the chamber temperature that is monitored by the thermocouple, and a DC current is injected into the Peltier element to reach the desire temperature. The Peltier element is a device that heats or cools two conducting material via electrical current (Peltier effect). This device has two conductor plates, as DC current is passed through the device the heat is directed from one side to the other, leading to one side gradually heating up and another cooling. In my study, all the data were collected at 28 ºC.

To excite the RH 237 on the labeled zebrafish heart, a 350 mW 530 nm LED module was used to excite the dye via a 630 nm long pass dichroic mirror, and the emission signal was filtered through a 700 nm long-pass filter (700ALP, Omega, Optical) and acquired by a GE680 CCD (charged-coupled device) camera (Allied Vision Technologies).

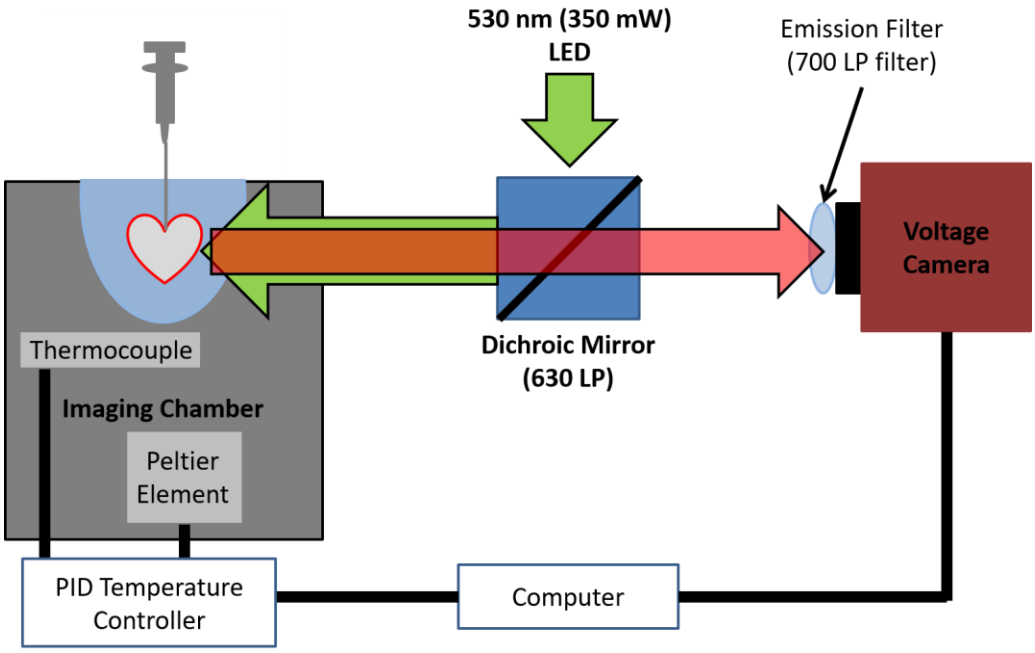

Figure 2.3 – Schematics of the optical mapping setup

The illumination system is a 530 nm (350 mW) LED module (Thorlabs M530L3). The isolated and cannulated heart, labeled with blebbistatin and RH 237. The voltage-sensitive dye, RH 237, is excitable by a 530 nm light and the emission signal is collected by a 700 nm long-pass filter via a 630 nm dichroic mirror. A peltier element ensures the imaging chamber temperature is maintained at 28 °C for all experiments (Lin *et al.*, 2015).

2.6.1 Dye and labeling

Blebbistatin and RH 237 were diluted with calcium Tyrode solution to a working concentration of 20 µM and 10 µM, respectively, in all studies. Blebbistatin suppresses heart contraction in a concentration and time-dependent manner. However, the effect of blebbistatin can be negated by long and/or LED exposure (Lin *et al.*, 2015). This is especially important in premature simulation and variable rate stimulation protocols where series of LED firing in successions may reduce the effect of blebbistatin, via a process call photo-release, leading to a restoration in the contraction of the heart. For this reason, 20 µM of blebbistain was also added in the external solution of the imaging chamber (Lin *et al.*, 2015).

RH 237 was easily retained by the zebrafish cardiomyocytes and was therefore, loaded first for 30 mins. The loading level was confirmed by fluorescence imaging, and if insufficient, the heart can be reloaded in short increments to increase signal intensity. Overloading of RH 237 can saturate the camera sensor. RH 237 is susceptible to photobleaching from sustained LED exposure, and therefore protocols were designed to restrict exposure time to < 10 s using a programmed shutter that is coupled to the firing of acquisition cameras.

2.6.2 Solutions

Calcium Tyrode solution was used in all Zebrafish optical mapping procedure as a physiological solution. The solution contains (in mM): 117 NaCl, 5.7 KCl, 4.4 $NaHCO_3$, 1.5 NaH_2PO_4, 1.7 $MgCl_2$, 10 Na-HEPES, 5 glucose, 5 creatine, 5 Na-pyruvic acid, and 1.8 $CaCl_2$, titrated to pH 7.3. Stock concentration of 10 mM (-)-blebbistatin (Sigma-Aldrich, St Louis, MO), and 5 mM RH 237 (Molecular Probes, Eugene, OR) was made by dissolving the compound in 100% DMSO, then aliquoted to reduce freeze thaw, and kept in -20 ºC. A final concentration of 20 µM for blebbistatin and 10 µM RH 237 was used in all experiments (Lin *et al.*, 2015).

2.6.3 Zebrafish heart isolation procedure

Adult zebrafish were purchased from Noah's Pet Ark, and kept at 28 ºC, in accordance with the principles established by the Canadian Council on Animal Care, and

the experimental protocols approved by the Simon Fraser University Animal Care Committee. First, the fish were euthanized in an ice bath, then a razor blade was used to decapitate the head by cutting at the base of the gills, followed by another cut at the base of the pectoral fin to create a tissue wedge. The tissue wedge was then transferred to a 100 mm petri dish filled with calcium Tyrode solution. A pair of surgical forceps were used to carefully open the pericardial cavity, in which the heart lies, and to extract the heart. The heart has three defining structural features, a bulbus, the atrial and the ventricle. For cannulation, the isolated heart was mounted through a 1 ml syringe with a 34-gauge ultrafine cannula (World Precision Instruments, Sarasota, FL). The cannula was inserted through the bulbus and into the lumen of the ventricle, and secured with a surgical knot (Figure 2.4) (Lin *et al.*, 2015).

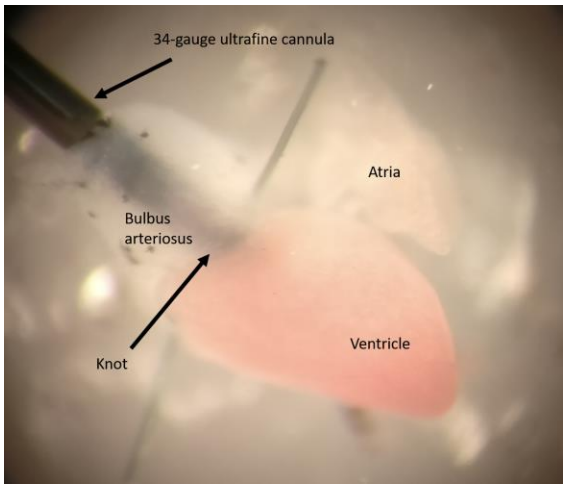

Figure 2.4 - Zebrafish heart cannulation

The extracted heart is cannulated on a 34-gauge ultrafine cannula by penetrating the bulbus arteriosus through to the apex of the ventricle and secured with a surgical knot. A small amount of calcium-Tyrode's solution is pumped into the heart

2.6.4 Data collection and analysis

Data were collected and analyzed using a custom-built software in the IDL environment (Exelis Visual Information Solutions, McLean, VA), built by Dr. Eric Lin (Lin *et al.*, 2015). Opening of the shutter commands the firing of the LED module and triggers the voltage camera. Image acquisition were captured at 2000 frames at a frame rate per second (FPS) of 205. Region of interest (ROI) were manually drawn outlining the ventricle and atria for each image. Following ROI selection, the raw output of the ensemble of AP cycles, within the captured frames, is shown in panel A in Figure 2.5. The fluorescence

signal is normalized to max. Membrane depolarization cause a blue-shift in the RH 237 emission spectra resulting in a reduction in the fluorescence intensity. The ensemble of AP cycles was averaged spatially and temporally to create an averaged, representative AP shown in panel B in Figure 2.5. Spatial averaging involves taking the average of all the pixels within area of the ROI per recordings. Large area of ROI allows spatial averaging of large number of pixels, yielding a smoother and less noisy AP signal. Temporal averaging involves first detecting the peak of each individual AP within an ensemble, then aligning all the peaks, follow by averaging the voltage signal of all the individual AP to 1 (Lin *et al.*, 2014). To reduce noise in the averaged, representative AP, a recorded ensemble of at least 5-10 individual AP cycles is recommended. Occasionally, when the intrinsic heart rate is low, the capture frames is increased to 4000 in order to acquire enough AP cycles to generate a smooth, representative AP with high signal-to-noise ratio. APD is estimated from detection of the AP peak (at 0% repolarization of APD_0), down to the desire repolarization percentage, e.g. APD_{50}, APD_{75} or APD_{95}, which correspond to repolarization to 50%, 75%, and 95% from the AP peak, respectively.

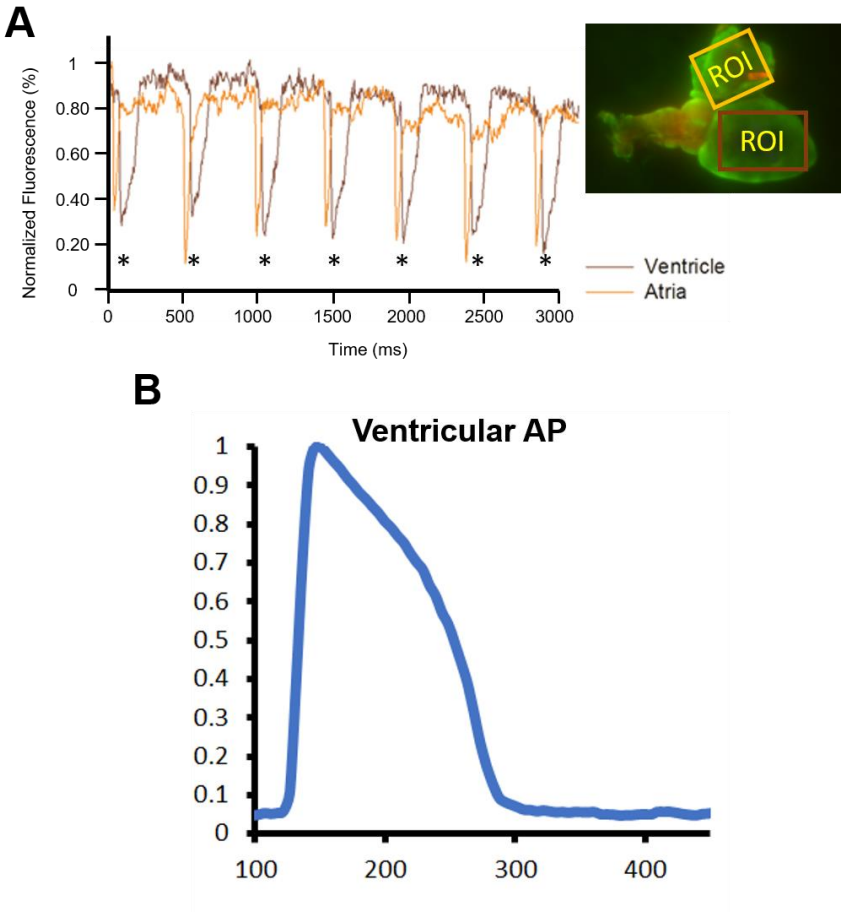

Figure 2.5 - Optical mapping example recordings

Typical raw optical mapping recording of the ventricle and atria action potential representing the normal intrinsic heart rate (**A**) with the region of interest (ROI) selected for the ventricle and atria. Fluorescence intensity is normalized to max. Astrix (*) represent APD_0, or the AP peak. **B.** An average of the action potential cycles to produce a low noise, and high resolution ventricular action potential.

Chapter 3. External Protons Destabilize The Activated Voltage Sensor in hERG Channels.

3.1 Overview

As discussed in Section 1.5.2, one of the major effects of extracellular acidosis on the hERG potassium channel is a depolarizing shift in the voltage-dependence of activation, however the mechanism underlying this effect is unclear. Interestingly, external divalent cations e.g. Ca^{2+} and Cd^{2+} also cause a depolarized shift in the voltage-dependence of activation that mimics that of external protons (Paquette *et al.*, 1998; Ho *et al.*, 1998; Silverman *et al.*, 2000; Fernandez *et al.*, 2005; Kazmierczak *et al.*, 2013). Charge screening theory cannot fully explain the mechanism underlying the proton-induced depolarized shift in the voltage-dependence of activation as external proton do not alter the voltage-dependence of inactivation (Van Slyke *et al.*, 2012). This suggests that external protons may exert this effect via a specific site(s) on the channel. Molecular mapping of Cd^{2+}-induced modification on hERG revealed that Cd^{2+} coordinates, in part, by a metal ion binding pocket composing of three acidic residues in hERG: D456, and D460 in S2, and D509 in S3. Neutralization of these three acidic residues reduced the Ca^{2+}, Mg^{2+}, and Cd^{2+}-induced depolarized shift in the voltage-dependence of activation without altering inactivation (Fernandez *et al.*, 2005). From this observation, we hypothesize that a common mechanism may underlie the divalent cation and proton-induced shift in the voltage-dependence of activation. My aim in this chapter is to use mutagenic study in combination with two-electrode voltage clamp and voltage-clamp fluorimetry to investigate the site and mechanism for the depolarizing shift of the voltage-dependence of activation induced by extracellular protons on the hERG channel.

3.2 Introduction

The Kv11.1 or ether-à-go-go related gene (hERG) potassium channel is a member of the ether-à-go-go (EAG) superfamily of K^+ channels. hERG channels underlie the rapidly activating delayed rectifier current, I_{Kr}, in the heart (Sanguinetti & Jurkiewicz, 1990; Warmke & Ganetzky, 1994; Sanguinetti *et al.*, 1995; Trudeau *et al.*, 1995) and are thus critically important in termination of the cardiac action potential (Sanguinetti & Jurkiewicz, 1990; Sanguinetti & Tristani-Firouzi, 2006). The importance of understanding hERG

channel function is underscored by the link between loss-of-function caused by mutations or drug block and long QT syndrome, a cardiac arrhythmia that can result in sudden death (Sanguinetti & Tristani-Firouzi, 2006).

The activity of hERG, like that of many other ion channels, can be affected by extracellular acidosis, such as that which occurs during myocardial ischemia (Vandenberg *et al.*, 2012). Low external pH has been found to reduce I_{Kr} in cardiac myocytes (Vereecke & Carmeliet, 2000; Cheng *et al.*, 2009), which may predispose to long QT syndrome 2 and arrhythmia (Lin *et al.*, 2005*a*; Du *et al.*, 2010). Extracellular acidosis has also been shown to affect the ability of some anti-arrhythmic drugs to bind to hERG channels (Dong *et al.*, 2004; Lin *et al.*, 2005*a*, 2005*b*; Du *et al.*, 2011*b*). While there have been some discrepancies between studies on hERG channels in heterologous expression systems, the major effects of extracellular protons can be summarised as: i) a depolarizing shift of the conductance-voltage (G-V) relationship (Anumonwo *et al.*, 1999; Jo *et al.*, 1999; Terai *et al.*, 2000; Bett & Rasmusson, 2003; Van Slyke *et al.*, 2012); ii) a decrease in maximal conductance (Anumonwo *et al.*, 1999; Bérubé *et al.*, 1999; Jo *et al.*, 1999; Terai *et al.*, 2000; Bett & Rasmusson, 2003; Van Slyke *et al.*, 2012); iii) a slowing of activation (Anumonwo *et al.*, 1999; Terai *et al.*, 2000; Zhou & Bett, 2010) and; iv) an acceleration of deactivation (Anumonwo *et al.*, 1999; Bérubé *et al.*, 1999; Jo *et al.*, 1999; Jiang *et al.*, 1999; Terai *et al.*, 2000; Bett & Rasmusson, 2003; Liu *et al.*, 2003; Van Slyke *et al.*, 2010). We have previously shown that the reduction of conductance is likely due to block of the pore by protons (Van Slyke *et al.*, 2012). In addition, there are reports that the effects on activation and deactivation also have different pH sensitivities (Anumonwo *et al.*, 1999; Bett & Rasmusson, 2003), which suggests that there may be multiple binding protonation sites. A recent study revealed that acidic residues in the metal ion binding pocket of EAG family channels are required for the pH-sensitivity of activation (Kazmierczak *et al.*, 2013); however, the mechanism of action of protons on the steady-state and kinetic properties of activation and the site and mechanism of action on deactivation remain poorly defined.

The effects of external protons on hERG channel gating are very similar to those of divalent cations including, but not limited to, Ca^{2+} and Cd^{2+} (Johnson *et al.*, 1999*a*, 1999*b*; Jo *et al.*, 1999; Fernandez *et al.*, 2005; Lin & Papazian, 2007). While the similarity has previously led to the suggestion that charge screening effects are accountable for the effects of protons on hERG channels, charge screening does not account for the observed proton-induced shifts of the G-V relationship that occur without effect on the voltage-

dependence of inactivation (Jo *et al.*, 1999; Terai *et al.*, 2000). More recently, evidence suggests that di- and trivalent cations modify voltage-dependent gating via interactions with specific channel sites on S2 and S3 (Fernandez *et al.*, 2005; Hoshi & Armstrong, 2012) and that in hERG and EAG family channels, conserved acidic residues mediate the majority of the observed proton-induced activation gating shift (Kazmierczak *et al.*, 2013). This leads to the intriguing possibility that protons may share common cation binding sites. This hypothesis is supported by reports that the ability of protons to affect hERG channels is reduced by external Ca^{2+} ions (Jo *et al.*, 1999; Kazmierczak *et al.*, 2013). Ca^{2+}, as well as Mg^{2+} and Cd^{2+}, ions have been shown to co-ordinate within an externally accessible metal ion binding pocket that is found in hERG and EAG-family channels; in hERG, this pocket is comprised of three conserved acidic residues within the voltage-sensing domain: D456 and D460 in the S2 segment and D509 in the S3 segment (Silverman *et al.*, 2000; Fernandez *et al.*, 2005; Lin & Papazian, 2007; Abbruzzese *et al.*, 2010; Kazmierczak *et al.*, 2013). Cd^{2+} bound within this pocket has been shown to directly affect voltage sensor movement and, consequently, channel activation and it is proposed that this occurs by impeding the formation of transient, stabilizing interactions between the acidic residues and basic S4 gating charges (Fernandez *et al.*, 2005; Abbruzzese *et al.*, 2010). This comprehensive description of the site and mechanism of action of Cd^{2+} binding in hERG channels that involves specific co-ordination with three acidic residues within the metal ion binding pocket (Fernandez *et al.*, 2005; Abbruzzese *et al.*, 2010) makes Cd^{2+} competition an ideal tool to probe for the site and mechanism of action of protons on hERG channel gating.

Here, we have taken advantage of the specific nature of Cd^{2+} co-ordination within the metal ion binding pocket to investigate the proton binding site in hERG channels. Using two-electrode voltage clamp of *Xenopus* oocytes we first present data showing that Cd^{2+} inhibits the depolarizing shift of hERG activation caused by extracellular protons, as has previously been shown by other divalent cations, e.g. Ca^{2+} (Jo *et al.*, 1999; Kazmierczak *et al.*, 2013). Interestingly, the pH-dependence of deactivation gating was preserved in concentrations of Cd^{2+} that greatly attenuated the effects of protons on activation supporting independent sites/mechanisms of action. Using a mutagenesis approach, we then confirm that the effect of low pH is largely reduced by neutralization of D509 (Jo *et al.*, 1999; Kazmierczak *et al.*, 2013), and extend this to show that the effect of protons is completely attenuated by the additional neutralization of both D456 and D460. Finally, we

present results from voltage-clamp fluorimetry experiments showing that voltage-sensor activation is right-shifted and deactivation is accelerated in the presence of external protons. Together, our findings show that D509 acting alone, and D456 and D460 acting in concert, comprise the site of action of external protons on hERG channel activation. Furthermore our data point to a mechanism of action by which protons alter channel activation: that protons interacting with the metal ion binding site destabilize the activated configuration of the voltage sensor.

3.3 Material and Methods

3.3.1 Molecular Biology

For expression in *Xenopus laevis* oocytes, hERG1a channel cDNA was subcloned into a pBluescript SKII expression vector; mutant constructs were generated by conventional overlap extension PCR. Mutagenic primers were synthesized by Sigma-Genosys (Oakville, ON, Canada). All mutations were confirmed by sequencing using Eurofins MWG Operon (Huntsville, AL). *XbaI* restriction enzyme was used to linearize channel constructs for subsequent synthesis of cRNA with the mMessage mMachine T7 Ultra cRNA Transcription Kit (Ambion, Austin, TX).

3.3.2 Solutions

During voltage-clamp experiments, oocytes were bathed in ND96 solution containing (in mM): 96 NaCl, 3 KCl, 0.5 $CaCl_2$, 1 $MgCl_2$, and 5 HEPES. For solutions at pH 7.4 or 6.5, the desired pH was achieved by titration with NaOH. For solutions pH 6.0 and below, the HEPES was replaced with 5 mM MES. Where applicable, $CdCl_2$ (0.05 – 10 mM) was added to ND96 solution without compensation for changes in osmolarity. All reagents were purchased from Sigma-Aldrich (Oakville, ON, Canada). Experiments were performed under constant perfusion (1 mL min^{-1}). New solutions were perfused for 5 min before recording to ensure a complete exchange of the bath solution (working volume ≈1 ml).

3.3.3 Electrophysiology and Data Analysis

Ionic current recordings were performed at room temperature (22-24 °C) using conventional two electrode voltage-clamp with either an Axoclamp 900A amplifier (Axon Instruments, Foster City, CA) or a Warner Instruments OC-725C amplifier (Harvard Apparatus, St. Laurent, QC, Canada) coupled to a Digidata 1440 interface (Axon Instruments). Data acquisition and analysis were performed using pClamp 10.2 software (Axon Instruments). Glass microelectrodes were made with thin-walled borosilicate glass (World Precision Instruments, Sarasota, FL) and when filled with 3 M KCl had a tip resistance of 0.2-0.8 MΩ. All current signals were acquired at a 10 kHz sampling frequency and low-pass filtered at 4 kHz (−3 dB, 8 pole Bessel filter).

In all experiments, the holding potential was −80 mV. The G-V relationship was determined using standard analysis of normalized peak tail currents recorded at −60 mV following 2 s conditioning pulses ranging from −80 mV to +80 mV in 10 mV increments. Voltage protocols were adjusted accordingly for mutant channels exhibiting right-shifted voltage-dependencies. Activation parameters were obtained from fits of the G-V relationship to the Boltzmann function

To measure deactivation, a 500 ms depolarizing pulse to +60 mV was applied to activate channels, followed by a 4 s test pulse at voltages ranging from −110 mV to +40 mV in 10 mV increments. Deactivation kinetics were quantified by fitting the decaying portion of the tail current during the test pulse to a bi-exponential function: $I = A_{fast}\exp(t/\tau_{fast}) + A_{slow}\exp(t/\tau_{slow}) + C$; where A_{fast} and A_{slow} are the relative amplitudes of the fast and slow components, τ_{fast} and τ_{slow} are the time constants for fast and slow component respectively, and C is a constant. For ease of comparison, a weighted average time constant for deactivation (τ_{deact}) was calculated: $\tau_{deact} = (A_{fast}\,\tau_{fast} + A_{slow}\,\tau_{slow})/(A_{fast} + A_{slow})$. Data for individual fast and slow components show that this weighted tau approach represents an accurate, yet simpler, description of the effects of protons in the absence and presence of Cd^{2+}.

The Hill equation was used to describe the concentration-dependence for the effects of H^+ on either the voltage-dependence of activation or the time course of deactivation: $y = \text{base} + (\text{max} - \text{base})/(1 + (Kd/[X^+])^n)$, where y is either the change in the $V_{1/2}$ ($\Delta V_{1/2}$) relative to control (pH 7.4) or τ_{deact}, base and max are the minimum and

maximum values of $\Delta V_{1/2}$ or τ_{deact}, respectively, Kd is the equilibrium dissociation constant and is expressed as *pKa*, $[X^+]$ is the concentration of H^+, and n is the Hill co-efficient.

Extracellular protons shifted the voltage-dependence of activation to more depolarized potentials and changed the chemical potential difference between the closed and open states at 0 mV ($\Delta G0 = zFV_{1/2}$). Due to this effect, the electrochemical driving force for deactivation varies at each pH and it is therefore difficult to make simple comparisons of the rate of deactivation at a given test voltage. Therefore, deactivation kinetics were plotted against the electrochemical potential energy for deactivation (i.e., $-(\Delta G0 - zFV)$), which describes the total energy, both electrical and chemical, driving deactivation. By selecting similar electrochemical potentials, deactivation kinetics at each pH can be compared in the face of similar total driving forces that account for the observed changes to $\Delta G0$.

Curve fitting was performed in pClamp10.2 or SigmaPlot 11.0 (Systat Software, Inc, San Jose, CA). Unless otherwise noted, data are shown as mean ± S.E.M.; n represents the number of oocytes tested.

3.3.4 Voltage-Clamp Fluorimetry (VCF)

The L520C mutation at the external face of the S4 segment was incorporated for the site-directed labeling of hERG channels with tetramethylrhodamine-5-maleimide (TMRM; Invitrogen Life Technologies, Burlington, ON, Canada). Oocytes were labeled in the dark with 5 µM TMRM in depolarizing solution (in mM: 98 KCl, 1 $MgCl_2$, 2 $CaCl_2$, and 5 HEPES, titrated to pH 7.4 with NaOH) for 30 min at 10 °C, then washed with ND96 solution. Two-electrode voltage-clamp fluorimetry was performed with a Nikon TE2000S inverted microscope (Nikon Canada, Mississauga, ON, Canada) with an epifluorescence attachment and photomultiplier tube detection module (Cairn Research, Kent, UK) as described previously in Chapter 2.3.2.

3.4 Results

3.4.1 Effects of Proton and Cd^{2+} on hERG Activation and Deactivation.

Figure 3.1 firstly summarizes the effects of external pH changes on voltage dependent activation and deactivation gating of hERG channels heterologously expressed in *Xenopus* oocytes and then displays the effects of Cd^{2+} on the pH-dependence of these processes. Typical families of current traces recorded in response to depolarizing voltage steps under control conditions (pH 7.4) and following application of solution with pH 5.5 are shown in Figure 3.1A. From data such as these, the normalized peak tail current amplitude, as an indicator of relative channel conductance, was plotted against membrane voltage and fitted with a Boltzmann function (see Methods). We have previously shown that low pH reduces peak tail current amplitude as a result of reduced single channel conductance due to direct proton block of the pore (Van Slyke *et al.*, 2012). Therefore, to compare the effects of protons on the voltage-dependence of channel activation, peak tail currents were normalized to the maximum tail current amplitude recorded at each proton concentration. The effects of a range of external pH values on the G-V relationship of hERG channels are shown in Figure 3.1B. Protons shifted the voltage-dependence of activation to more depolarized potentials. The concentration-response curve plotted in the inset shows that the *pKa* for the effect of external protons was 5.6 (n = 7). These effects on the voltage-dependence of activation are consistent with previous reports of the effects of protons on hERG channels expressed in *Xenopus* oocytes and mammalian cells (Anumonwo *et al.*, 1999; Jo *et al.*, 1999; Terai *et al.*, 2000; Bett & Rasmusson, 2003; Van Slyke *et al.*, 2012) and are similar to the reported effects of Cd^{2+} on activation (Johnson *et al.*, 1999*a*; Fernandez *et al.*, 2005).

Figure 3.1C shows typical families of current traces recorded in response to a voltage protocol designed to investigate deactivation properties in hERG channels at pH 7.4 or 5.5. In Figure 3.1D the effects of protons on the time constant for deactivation (τ_{deact}) is plotted. Since protons shift the voltage-dependence of activation, τ_{deact} is plotted against electrochemical potential energy so as to assess the effect of pH or Cd^{2+} concentration at an equivalent driving force for deactivation (see Methods). It is clear that protons markedly accelerated deactivation even with the depolarizing shift of activation taken into account. The pH-dependence of τ_{deact} is described in the inset to Figure 3.1D and shows that the

pKa for the effect of protons was 6.7 (n = 3). The effects on the time course of deactivation shown in Figures 3.1C and D are consistent with previous reports of the effects of protons on hERG channels (Anumonwo *et al.*, 1999; Bérubé *et al.*, 1999; Jo *et al.*, 1999; Jiang *et al.*, 1999; Terai *et al.*, 2000; Bett & Rasmusson, 2003; Liu *et al.*, 2003; Van Slyke *et al.*, 2012). Taken together, the data show that protons cause a relative destabilization of the hERG channel open state, by depolarizing the voltage-dependence of activation and accelerating deactivation. Interestingly, the acceleration of deactivation with low pH occurred over and above the shift of activation and exhibited a different pH-dependence, which is indicative of separable sites of action of protons on activation and deactivation (see also Bett and Rasmusson 2003).

Given the similar effects of protons (outlined in Figure 3.1) and Cd^{2+} (Johnson *et al.*, 1999*a*; Fernandez *et al.*, 2005) on activation and deactivation, we reasoned that they may act on hERG channels via a common site and/or mechanism. To test this, we performed experiments to determine the ability of Cd^{2+} to impede the actions of protons by quantifying the pH-dependence of hERG channels in the presence of different concentrations of Cd^{2+}. Cd^{2+} is a useful tool in the investigation of a protonation site, since its binding site and mechanism of action have been comprehensively described (Fernandez *et al.*, 2005; Abbruzzese *et al.*, 2010). Figures 3.1E-H show the effects of different pH solutions on the voltage-dependence of activation and the time course of deactivation in the presence of Cd^{2+}. The G-V relations in Figure 3.1E show that the presence of 0.1 mM Cd^{2+} largely abolished the effects of protons on the voltage-dependence of activation (compared to Figure 3.1B). A plot of the $[H^+]$-dependent shift of the $V_{1/2}$ of activation in the presence of a range of Cd^{2+} concentrations (Figure 3.1G) strongly suggests that protons compete with Cd^{2+}. Although we could not fit the data to a competitive binding model (see Discussion), because the loss of channel conductance at very low pH prevented measurements at saturating proton concentrations, it is clear that the pH-sensitivity of the voltage-dependence of activation was reduced by Cd^{2+} in a concentration-dependent manner. By contrast, the pH-dependence of the deactivation time course was considerably less sensitive to Cd^{2+} (Figures 3.1F and H). In the presence of 0.1 mM Cd^{2+}, which almost completely abolished the pH-dependency of activation, the pH-sensitivity of deactivation was relatively unchanged (compare to Figure 3.1D), and higher concentrations (e.g. 1 mM) only moderately altered the pH-dependence (Figure 1H). These data show that the effect of protons on the voltage-dependence of activation

is largely abolished in the presence of Cd^{2+}, but that the effect on deactivation was much less sensitive to Cd^{2+} and supports the conclusion that activation and deactivation are modulated by protons at separable sites.

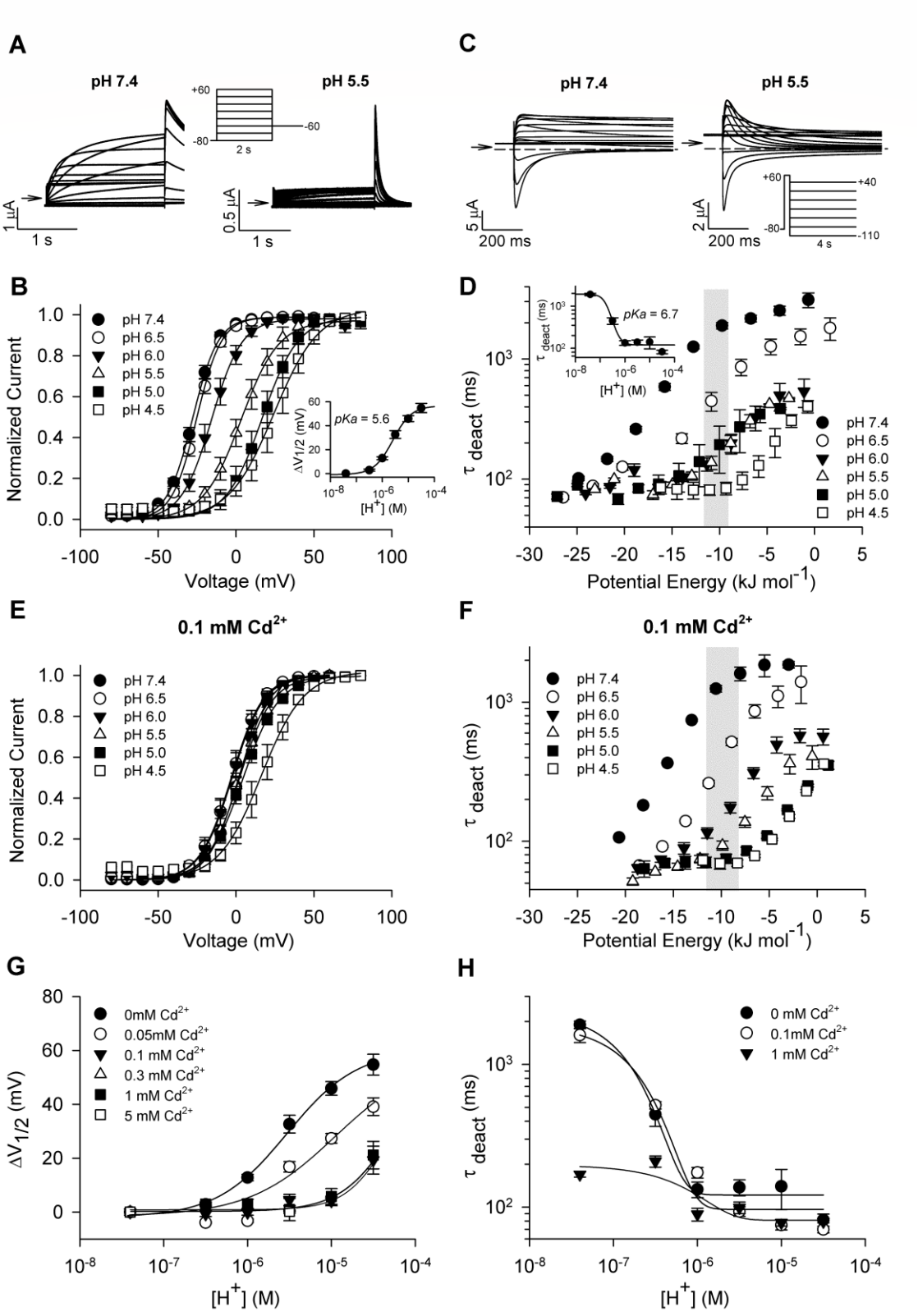
A
pH 7.4
pH 5.5
+60
-80
-60
2 s
1 µA
1 s
0.5 µA
1 s
C
pH 7.4
pH 5.5
5 µA
200 ms
2 µA
200 ms
+60
-80
+40
-110
4 s
B
Normalized Current
pH 7.4
pH 6.5
pH 6.0
pH 5.5
pH 5.0
pH 4.5
pKa = 5.6
ΔV1/2 (mV)
[H+] (M)
Voltage (mV)
D
τ deact (ms)
pKa = 6.7
[H+] (M)
Potential Energy (kJ mol-1)
E
0.1 mM Cd2+
Normalized Current
Voltage (mV)
F
0.1 mM Cd2+
τ deact (ms)
Potential Energy (kJ mol-1)
G
ΔV1/2 (mV)
0mM Cd2+
0.05mM Cd2+
0.1 mM Cd2+
0.3 mM Cd2+
1 mM Cd2+
5 mM Cd2+
[H+] (M)
H
τ deact (ms)
0 mM Cd2+
0.1mM Cd2+
1 mM Cd2+
[H+] (M)

Figure 3.1 - Competitive effects of Cd^{2+} and protons on hERG activation, but not deactivation.

***A*,** typical example of current recordings for WT hERG activation under control and low pH conditions. 2 s depolarizing pulses ranging from −80 mV to +80 mV were used; tail currents were measured upon repolarization to −60 mV. Arrows indicate the zero current level. ***B*,** G-V relationships constructed from peak tail current measurements at a range of pH values (n = 5-12). Solid lines represent fits to the Boltzmann function. For pH 7.4, 6.5, 6.0, 5.5, 5.0 and 4.5 the $V_{1/2}$ values were -27.1 ± 1.2, -24.7 ± 1.2, -14.8 ± 3.0, 5.1 ± 4.5, 17.6 ± 4.3, 24.8 ± 4.4 mV, and the corresponding *k* values were 7.5 ± 0.2, 7.5 ± 0.3, 8.9 ± 0.4, 11.3 ± 0.7, 9.6 ± 0.7, 10.9 ± 0.7 mV. *Inset,* plot of $[H^+]$ against the $\Delta V_{1/2}$ of activation, relative to pH 7.4. The solid line represents a fit of the data with a Hill function. Increasing $[H^+]$ right-shifted the G-V relationship with a *pKa* of pH 5.6. ***C*,** typical current recordings of WT hERG deactivation under control and low pH conditions. Channels were activated by a pulse to +60 mV, followed by a 4 s test pulse at voltages ranging from −110 to +40 mV in 10 mV increments. Traces have been truncated for clarity; tail currents following the depolarizing step are shown. ***D*,** deactivating tail currents at different pH were fitted to a bi-exponential function and the weighted average τ_{deact} is plotted against electrochemical potential energy for deactivation (PE; n = 3-4; see Methods). *Inset,* plot of τ_{deact} at an approximately constant PE (see shaded region) against $[H^+]$. Increasing $[H^+]$ accelerated the rate of deactivation with a *pKa* of 6.7. ***E*,** WT hERG G-V relationships constructed from recordings in solutions with a range of pH and in the presence of 0.1 mM Cd^{2+} (n = 4-11). The pH-sensitivity of the voltage-dependence of activation was greatly attenuated by Cd^{2+}. For pH 7.4, 6.5, 6.0, 5.5, 5.0 and 4.5 the $V_{1/2}$ values were -0.4 ± 1.5, -0.4 ± 1.7, -0.2 ± 1.7, 4.5 ± 1.5, 4.0 ± 2.6, 19.5 ± 4.9 mV, and the corresponding *k* values were 9.1 ± 0.2, 9.1 ± 0.3, 9.5 ± 0.2, 10.0 ± 0.2, 11.0 ± 0.6, 12.0 ± 2.0 mV. ***F*,** plots of τ_{deact} against the electrochemical potential energy for deactivation in different pH solutions and in the presence of 0.1 mM (n = 3) Cd^{2+}. ***G*,** summary of the effect of Cd^{2+} on the pH-sensitivity of activation. The absolute $\Delta V_{1/2}$ values observed in the presence of different $[Cd^{2+}]$ are plotted against $[H^+]$. Lines are to guide the eye. Increasing $[Cd^{2+}]$ attenuated the proton-induced shift of activation. ***H*,** summary of the effects of Cd^{2+} on the pH-sensitivity of deactivation. τ_{deact} values at an approximately constant electrochemical potential energy (see shaded area in *F*) and in the presence of different $[Cd^{2+}]$ are plotted against $[H^+]$. Lines are to guide the eye. Compared to its effect on the pH-dependence of activation, increasing the $[Cd^{2+}]$ had only a small effect on the pH-sensitivity of deactivation.

3.4.2 Role of Individual Acidic Residues In The S2/S3 Cation Binding Pocket

Cd^{2+}, as well as other divalent ions, such as Mg^{2+} and Ca^{2+}, have been shown to co-ordinate within a metal ion binding pocket formed in hERG channels by three acidic residues, D456 and D460 in S2, and D509 in S3 (Fernandez *et al.*, 2005; Lin & Papazian, 2007; Kazmierczak *et al.*, 2013). Cd^{2+} binding can be largely reduced by mutation of D509 and essentially eliminated by the triple mutation D456A/D460A/D509A (Fernandez *et al.*, 2005). Given the competition between the effects of protons and Cd^{2+}, we therefore investigated the effects of the D456A, D460A and D509A mutations on the pH-dependence of hERG activation. pH 5.5 closely approximated the *pKa* for WT hERG activation (pH 5.6, Figure 3.1B inset) and was used to probe for changes in pH sensitivity in each mutant. Figure 3.2 shows typical current traces and G-V relations constructed from peak tail currents recorded from each of the mutant channels at pH 7.4 (control) and pH 5.5. Neither D456A nor D460A reduced the effects of pH 5.5 on the voltage-dependence of activation (n = 5-6). In WT hERG the $\Delta V_{1/2}$ caused by switching from pH 7.4 to pH 5.5 was 32.6 ± 3.3 mV, whereas the analogous $\Delta V_{1/2}$ values in D456A and D460A channels were 49.5 ± 1.5 and 34.3 ± 1.1, respectively. However, D509A reduced the $\Delta V_{1/2}$ induced by pH 5.5 by 57 % to 14.0 ± 2.8 mV (n = 7). These data confirm an important role for D509 in the proton-dependence of activation in hERG channels as suggested recently (Kazmierczak *et al.*, 2013).

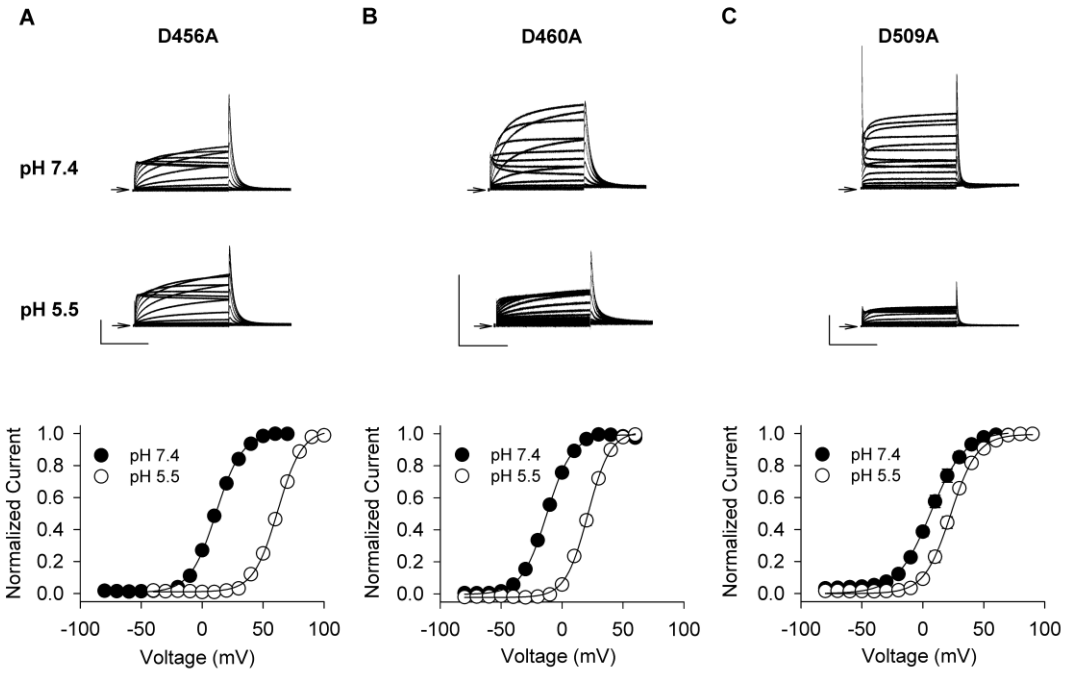

Figure 3.2 - Role of individual acidic residues in the S2/S3 metal ion binding pocket on the pH sensitivity of activation.

A-C*,** typical current trace families at pH 7.4 and 5.5 and G-V relationships recorded from D456A, D460A or D509A mutant channels. Individual D456A (A***) or D460A (***B***) mutations did not reduce the pH-induced shift of activation: the mean $V_{1/2}$ of activation for D456A was +11.7 ± 0.9 mV at pH 7.4 and +61.2 ± 0.8 mV at pH 5.5 (n = 5), and the corresponding values for D460A were −12.8 ± 1.2 mV and +21.5 ± 1.1 mV, respectively (n = 6). ***C*,** D509A reduced the effect of protons on activation by 57 %. The $V_{1/2}$ of activation was +8.9 ± 2.2 mV at pH 7.4 and +22.9 ± 1.6 mV at pH 5.5 (n = 7).

Since a considerable effect of pH on the voltage-dependence of activation remained in the D509A mutant, there must be at least one additional proton interaction site in hERG besides D509. To investigate this possibility further, we first asked whether the remaining pH-sensitivity in D509A channels was sensitive to the presence of Cd^{2+}. In order to do this, we first elicited a near-saturating shift of activation with Cd^{2+} and then probed with pH 5.5 to assess the pH-dependence of channel activation. In D509A the affinity of Cd^{2+} binding within the metal ion pocket is reduced and we therefore used a higher concentration of Cd^{2+}; 10 mM Cd^{2+} has been shown to cause a near-maximal shift of the $V_{1/2}$ of activation in D509A mutant channels (Fernandez *et al.*, 2005). Figure 3.3A shows relevant current traces and G-V relations recorded from D509A channels under pH 7.4, 0 mM Cd^{2+} conditions and in the presence of 10 mM Cd^{2+} at pH 7.4 and 5.5. The data show that in the presence of Cd^{2+}, the 14 mV shift in the activation $V_{1/2}$ induced by pH 5.5 in D509A channels was abolished. This suggests that, in addition to D509 as a key site that mediates the effect of protons on hERG activation, additional proton-mediated effects on activation can be abolished by Cd^{2+} coordination in D509A channels.

3.4.3 Role of Double and Triple Neutralization of the Metal Cation Binding Pocket

Given the Cd^{2+} sensitivity of the D509A pH-dependence, we returned our attention to the other Cd^{2+} coordination sites, D456 and D460, within the metal ion binding pocket. Interestingly, whilst the individual D456A and D460A mutations have been shown to have only limited effects on Cd^{2+} sensitivity, the double mutation D456A/D460A had a dramatic effect (Fernandez *et al.*, 2005), which suggests that Cd^{2+} coordination to both residues is required to shift the voltage-dependence of activation. Therefore, we examined the effect of the D456A/D460A double mutant on the pH-dependence of activation (Figure 3.3B). Surprisingly, the $\Delta V_{1/2}$ induced by pH 5.5 was reduced in the double mutant by 61 %, from 32.6 ± 3.3 mV in WT hERG to 12.8 ± 1.2 mV (n = 5). These data show that D456 and D460 act in concert to contribute to the pH-dependence of activation in hERG channels. As a further test for the role of these residues, we completed experiments using the D456A/D460A/D509A triple mutation (Figure 3.3C). This triple mutation was shown to abolish the effect of Cd^{2+} on hERG channel activation (Fernandez *et al.*, 2005). Consistent with previous reports, the G-V relations depicted in Figure 3.3C show that the voltage-dependence of activation is strongly right-shifted in this mutant. More importantly, it is clear

that removing all three negative charges within the metal ion binding pocket abolished the pH-dependence of activation. Together, the data in Figure 3.3 demonstrate that protons compete with Cd^{2+} to interact with acidic residues D456, D460 and D509 in S2 and S3, which form a metal ion binding site in hERG channels.

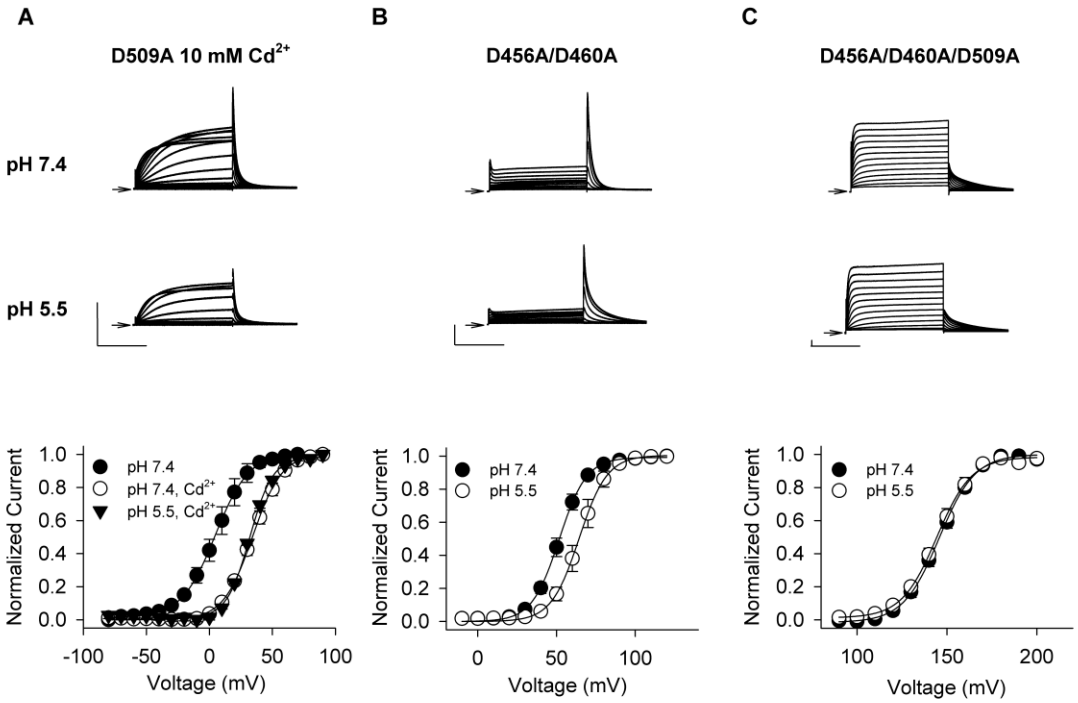

Figure 3.3 - Three acidic residues mediate the pH dependence of activation.

***A*,** typical current traces at pH 7.4 and 5.5 in the presence of Cd^{2+} and a plot of the effect of protons on the G-V relationship in D509A channels shows that the remaining pH-sensitivity in D509A channels is Cd^{2+}-sensitive. At pH 7.4, 10 mM Cd^{2+} shifted the $V_{1/2}$ of activation of D509A channels from +5.0 ± 4.6 mV to +34.6 ± 1.9 mV (n = 4). In the presence of 10 mM Cd^{2+}, the effect of pH 5.5 on the $V_{1/2}$ of activation was abolished: the $V_{1/2}$ was +31.8 ± 0.6 mV (n = 4), which is not different from that at pH 7.4. ***B*,** D456A and D460A combine to play a role in pH-sensitivity. Typical current traces at pH 7.4 and 5.5 and a plot of the G-V relationships from D456A/D460A double mutant channels. The double mutation reduced the pH-induced shift of activation by 61 %: the $V_{1/2}$ was +51.9 ± 1.9 mV at pH 7.4 and +64.7 ± 2.9 mV pH 5.5 (n = 5). ***C*,** the triple mutant D456A/D460A/D509A abolished the pH-sensitivity of activation in hERG channels. The $V_{1/2}$ of activation was +146 ± 1.6 mV at pH 7.4 and +145 ± 2.2 mV at pH 5.5 (n = 5).

3.4.4 External Protons Destabilize the Activated Voltage Sensor

Measurement and analysis of intra-membrane gating current has shown that Cd^{2+} co-ordination within the metal ion binding pocket shifts the voltage-dependence of hERG channel activation by altering voltage sensor movement (Abbruzzese *et al.*, 2010). A mechanism of action was proposed that involves competition between Cd^{2+} and S4 basic charges for interaction with acidic groups in S2 and S3. Such a mechanism can explain the shifted voltage-dependence of activation, and is consistent with the accelerated deactivation time course that is characteristic of the effects of Cd^{2+} (Fernandez *et al.*, 2005).

To investigate whether a similar mechanism may underlie the effect of protons on hERG channel gating, we performed voltage-clamp fluorimetry experiments to provide a report on voltage sensor movement and examined the effects of low external pH. Figure 3.4A shows a typical family of fluorescence traces recorded at pH 7.4 from hERG channels labelled with TMRM at L520C on the external face of S4. As observed previously in hERG (Smith & Yellen, 2002; Es-Salah-Lamoureux *et al.*, 2010; Van Slyke *et al.*, 2010; Ng *et al.*, 2012) and other Kv (Mannuzzu *et al.*, 1996; Cha & Bezanilla, 1998; Claydon & Fedida, 2007) channels, depolarizing voltage steps produced voltage-dependent fluorophore quenching that occurs with a similar time course to movement of the major component of gating charge measured in *Xenopus* oocytes (Piper *et al.*, 2003) and appears to track movement of the voltage sensor. From these data, the steady-state fluorescence amplitude at each membrane voltage was plotted to create a fluorescence-voltage (F-V) relation (Figure 3.4C). Figure 3.4B shows example fluorescence traces recorded at pH 5.5. The F-V relation recorded in pH 5.5 solution is shown in Figure 3.4C. Low pH shifted the voltage-dependence of the report of voltage sensor movement, from −15.2 ± 2.0 mV at pH 7.4 to +11.6 ± 3.9 mV at pH 5.5 (n = 4-7), similar in magnitude to the shift in the voltage-dependence of ionic current activation caused by exposure to pH 5.5 solution. In addition, low pH also accelerated the rate of voltage sensor deactivation. This can be seen by comparing the deactivating fluorescence traces, recorded upon repolarization to -110 mV, in Figure 3.4A and B. The time constant of the fluorescence decay was 111 ± 12 ms at pH 7.4 and this was reduced to 22 ± 1 ms at pH 5.5. This is consistent with the acceleration of charge return observed in the presence of Cd^{2+} (Abbruzzese *et al.*, 2010). The key finding from these data is that low external pH shifts the voltage-dependence of the fluorescence report of voltage sensor activation to more depolarized potentials. These

data are consistent with a mechanism by which protons acting on acidic residues, D456 and D460 in S2 and D509 in S3 that form a metal ion binding pocket, destabilize the activated configuration of the voltage sensor.

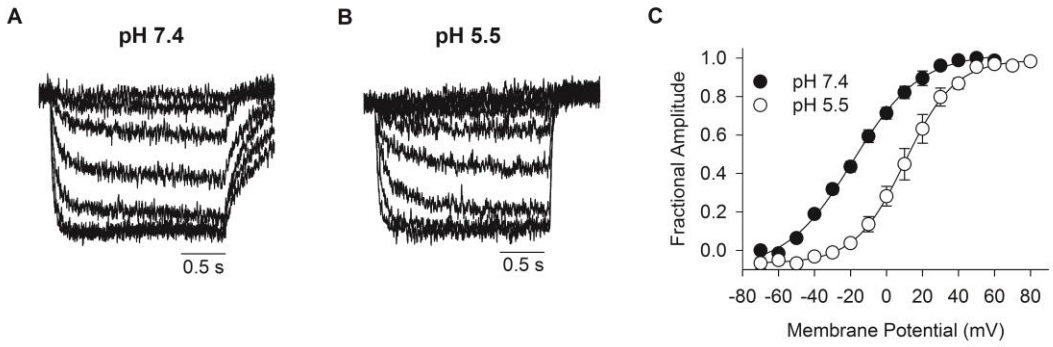

Figure 3.4 - External protons destabilize the activated voltage sensor.

A*, *B, typical fluorescence traces recorded from an oocyte labeled with TMRM at L520C in the extracellular portion of S4 and with the pH of the solution titrated to pH 7.4 (*A*) and 5.5 (*B*). Fluorescence signals were recorded during 2 s depolarizing voltage steps from a holding potential of −80 mV to +60 mV (20 mV increments). ***C*,** fluorescence-voltage (F-V) relationships were constructed using normalized steady-state deflections at pH 7.4 and 5.5 and show that voltage sensor movement is shifted to more depolarized potentials by acidic pH. $V_{1/2}$ values were −15.2 ± 2.0 mV at pH 7.4 (n = 4) and +11.6 ± 3.9 mV at pH 5.5 (n = 5).

3.5 Discussion

3.5.1 Protonation Site for Modulation of Activation Gating

It has previously been reported that the depolarizing shift of activation by protons is diminished by external Ca^{2+} (Jo *et al.*, 1999) and that low concentration of Ca^{2+}, D509 within the metal ion binding pocket in hERG and EAG family channels is required for proton interaction (Kazmierczak *et al.*, 2013). However, these studies could not define the exact identity of the proton interaction site. Here, we took advantage of previous ionic and gating current measurements, which demonstrated that hERG activation can be modulated by Cd^{2+} co-ordination with D456, D460 and D509 alone (Fernandez *et al.*, 2005; Abbruzzese *et al.*, 2010). Our results show that the low pH-induced shift of the hERG G-V relationship is inhibited by the presence of Cd^{2+} (Figure 3.1). We also demonstrate, for the first time, that neutralization of all three acidic residues comprising the metal ion binding pocket completely abolishes the proton-induced shift of activation (Figure 3.3). Together, our results provide strong evidence that the depolarizing shift of hERG activation observed under acidic conditions is due to protonation of D509, as well as D456 and D460 acting in concert, within the metal ion binding pocket. From the present data, we cannot determine the specifics of the co-operative actions of the three charges within the ion binding pocket. That D509 contributes the majority of pH sensitivity and that the double D456A/D460A mutation abolishes the remaining pH-dependence could be interpreted to suggest that D509 acts alone and D456 and D460 act in concert. However, it is also possible that the effect of protons requires cooperative actions of D509 with D456 or D460. Further study is required to resolve this.

We have reported here a *pKa* of 5.6 for the pH-dependent shift of the hERG G-V relationship (Figure 3.1), which is in good agreement with previous observations (Anumonwo *et al.*, 1999; Bett & Rasmusson, 2003). Reducing external Ca^{2+} has been shown to enhance the effect of pH 6.0 solution on the $V_{1/2}$ of hERG activation indicative of a competitive interaction between Ca^{2+} and protons (Kazmierczak *et al.*, 2013). This led to the suggestion that channel activation is more pH-sensitive than previously thought, since most reports of the pH-dependence of activation were from using physiological levels of Ca^{2+}. Since our experimental solutions contain 0.5 mM Ca^{2+}, it is likely that Ca^{2+} impedes protonation and therefore that we have underestimated the true *pKa* (i.e. the *pKa* may be at a less acidic pH) of the proton interaction site. A *pKa* of 5.6, or possibly higher,

differs somewhat from the pKa for the hydroxyl group of aspartic acid in aqueous solution (~pH 4.0). However, the estimated close proximity of the three acidic residues in the metal ion binding pocket may allow for interactions such that the effective *pKa* values are higher (Harris & Turner, 2002; Jasti *et al.*, 2007; Kazmierczak *et al.*, 2013). This may explain how single neutralizations of acidic residues within the metal ion binding pocket reduce pH sensitivity. For example, neutralization of D509 in the S3 segment may result in a reduction of the *pKa* values of D456 and/or D460, and a decrease in the shift of $V_{1/2}$ observed at any given pH. Conversely, neutralization of either D456 or D460 in S2 may have only minimal effect on pH sensitivity because the remaining S2 acidic residue is in close enough proximity with D509 so as to maintain its *pKa* value.

3.5.2 Competition Between Protons and Cd^{2+} Within Cation Binding Pocket

We have shown that protons, like Cd^{2+}, bind to the metal ion binding pocket to modulate the voltage-dependence of hERG channel activation. Intuitively, that Cd^{2+} reduces the low pH-induced shift in the $V_{1/2}$ of activation (Figure 3.1) is suggestive of a competitive interaction. Despite this, our attempts to fit the data presented in Figure 3.1G to competitive binding models, such as the ternary-complex model of interaction used to describe the binding of two ligands to the same receptor (Zhang *et al.*, 2001; Kehl *et al.*, 2002), were unsuccessful. This, however, is most likely due to the technical infeasibility of measuring accurate G-V relationships at saturating concentrations of protons (which also reduce maximal conductance) and Cd^{2+}. A second complication likely arises from the fact that the nature of the interaction with the acidic residues in the metal ion binding pocket is probably different for protons and Cd^{2+} ions. Based on experiments with double mutations, it has been proposed that Cd^{2+} co-ordination in hERG channels is most dependent on D456 and D509 (Fernandez *et al.*, 2005; Abbruzzese *et al.*, 2010). The typical tetrahedral or octahedral co-ordination geometry of Cd^{2+} (Rulíšek & Vondrášek, 1998) suggests that only one ion occupies the metal ion binding pocket and interacts with all three acidic residues. In contrast, we found that the pH-dependent shift of hERG activation was due to protonation of D509 alone, and of D456 and D460 in concert (Figures 3.2 and 3.3). Despite the inability to fit our Cd^{2+} interaction data with a competitive model, our mutagenic analysis strongly suggests that D509 is involved in binding both Cd^{2+} and protons. Furthermore, the ability of Cd^{2+} to inhibit the small proton-induced shift of activation in the

D509A mutation (Figure 3.3A) implies that competition also occurs between Cd^{2+} and protons for the two remaining acidic residues (i.e. D456 and D460) in the metal ion pocket.

3.5.3 The Mechanism of Action of Protons on Activation Gating

Gating current measurements have shown that co-ordination of Cd^{2+}, or Ca^{2+}, within the hERG metal ion binding pocket shifts the voltage-dependence of gating charge activation to more depolarized potentials and accelerates its return upon repolarization (Abbruzzese *et al.*, 2010). It has thus been proposed that the presence of metal ions within the binding pocket prevents the formation of transient, stabilizing interactions between the acidic residues in the pocket and basic S4 gating charges during activation (Fernandez *et al.*, 2005; Abbruzzese *et al.*, 2010). A similar mechanism is proposed for the modulation of activation of EAG family channels by di- and trivalent cations (Silverman *et al.*, 2000; Lin & Papazian, 2007; Zhang *et al.*, 2009). These data suggest that the acidic residues in the binding pocket are key target sites that mediate the modulation of voltage sensor gating by external ions. In this study, we have used voltage-clamp fluorimetry to show that hERG voltage sensor activation is right-shifted and deactivation accelerated by external protons, consistent with a similar interaction of protons with the acidic residues of the metal ion binding pocket that results in modulation of gating (Figure 3.4). The fluorescence data provide novel mechanistic insight: that protons bound within the metal ion binding pocket of the voltage sensing domain shift hERG activation to more depolarized potentials by destabilizing the activated conformation of the voltage sensor and interfering with normal S4 movement.

3.5.4 Other Protonation Sites Affecting hERG Gating

In addition to causing a depolarizing shift of the voltage-dependence, we (Figure 3.1) (see also Van Slyke et al. 2012) and others (Anumonwo *et al.*, 1999; Bérubé *et al.*, 1999; Jo *et al.*, 1999; Jiang *et al.*, 1999; Terai *et al.*, 2000; Bett & Rasmusson, 2003) have shown that external acidosis accelerates the time course of hERG deactivation and that this is accompanied by an accelerated fluorescence report of voltage sensor return (Figure 3.4, see also Van Slyke et al. 2012)). Compared with the pH-dependent shift of activation, we have shown here that the acceleration of deactivation was considerably less sensitive to the presence of external Cd^{2+} ions (Figure 3.1). This, along with the finding that the *pKa* values are an order of magnitude different for the shift in $V_{1/2}$ and τ_{deact} (Figure 3.1) (see

also Bett and Rasmusson 2003), implies that the effects of protons on the voltage-dependence of activation and the deactivation rate are separable and may be due to protonation of different sites in the hERG channel. Our present data do not identify the site responsible for the effects of protons on deactivation, but they may give some indications. The example traces in Figure 3.2 suggest that deactivation is not greatly enhanced by protons in the metal ion binding pocket acidic charge neutralization mutants and this is consistent with previous observations in hERG channels with cysteine substituted for D411, D460, D466, D501 or D509 (Liu *et al.*, 2003). However, these mutations dramatically accelerated deactivation themselves and have been suggested to be part of the deactivation gating machinery (Liu *et al.*, 2003), making interpretation of their role in pH sensing difficult. Interestingly, the pH-dependence of deactivation was reduced somewhat in the presence of higher concentrations of Cd^{2+} (e.g., 1 mM; Figure 3.1H), suggesting that deactivation may be modulated by protons at an alternative, lower affinity Cd^{2+} binding site. It is intriguing to note that hERG channel inactivation is also modulated by Cd^{2+} interacting at an as yet unidentified site (Fernandez *et al.*, 2005). It is possible that this site also regulates deactivation gating, and this will require further investigation.

Chapter 4. External Protons Destabilize the Relaxed Conformation of the Voltage Sensor

4.1 Overview

Now that we identified that external protons cause a depolarizing shift in the voltage-dependence of activation by disrupting ionic interactions between counter charges within the S2 (D456 and D460), and S3 (D509) with that of S4, leading to a destabilization of the activated voltage sensor. The next question is to investigate the site and mechanism for the external proton-induced acceleration of deactivation on the hERG channel. In this chapter, my aim is to determine the site and mechanism for the proton-induced acceleration of deactivation in hERG channels. As discussed in the introduction, hERG channels display unusually slow deactivation gating, which contributes to the resurgent I_{Kr} repolarizing current in cardiomyocytes and may protect against arrhythmia generated by afterdepolarizations. hERG channels exhibit robust mode-shift behaviour, which reflects an energetic separation of the voltage-dependence of activation and deactivation. This separation has been proposed to be due to voltage sensor relaxation, where long depolarization durations further stabilize the activated voltage sensor into a relaxed state, and that more energy is required to deactivate the voltage sensor from this relaxed position, resulting in a slower deactivation kinetics. The mechanism of voltage sensor relaxation is unknown, but it is important in the regulation of slow hERG channel deactivation. We hypothesize that external protons may accelerate deactivation by destabilizing the relaxed state of the voltage sensor. By using a combination of voltage clamp fluorimetry and gating currents measurements at near steady-state durations, we showed that the hERG channel voltage sensor exhibit robust mode-shift and that pH 6.5 reduced this voltage sensor mode-shift by right shifting the voltage-dependence of off-gating charges without affecting the on-gating charges strongly suggesting that the relaxed state is destabilized at pH 6.5. Next, we revealed that neutralization of D509 in S3 also destabilized the relaxed state, mimicking the effects of protons and suggesting that acidic counter-charges of S4 basic residues are involved in stabilizing the relaxed state of the voltage sensor and slowing deactivation kinetics. Finally, we highlight a major consequence of destabilization of the relaxed state by demonstrating that acidosis reduces hERG protective current elicited by premature stimuli applied in the late phase of the action potential and early refractory period. Interestingly, RPR260243, a hERG

activator that slows hERG deactivation gating, restores the protective current highlighting a novel antiarrhythmic therapeutic potential for the compound. Taken together, these findings identify mechanistic determinants of voltage sensor relaxation and demonstrate a functional consequence of slowing deactivation kinetics to produce antiarrhythmic protective hERG currents. We highlight a novel approach for antiarrhythmic hERG activator compounds, describe the long sought-after mechanism by which protons accelerate hERG deactivation.

4.2 Introduction

The human ether-à-go-go-related gene (hERG) encodes a voltage-gated potassium (Kv) channel that underlies the rapid delayed rectifier K^+ channel current (I_{Kr}), which is crucial in the repolarization and termination of the human cardiac action potential (Sanguinetti *et al.*, 1995). The gating kinetics of hERG channels are unique and underlie their physiological importance. Upon depolarization, the hERG channel activates slowly and inactivates rapidly, passing little current during the early phase of the action potential. Upon repolarization, the hERG channel recovers rapidly from inactivation into the open state from which deactivation is slow, permitting a resurgent current that aids repolarization of the cell. It is well established that inherited mutations or drug block that reduce hERG channel function result in compromised resurgent I_{Kr} current and delayed repolarization (Curran *et al.*, 1995; Sanguinetti *et al.*, 1995, 1996), which establishes a substrate for arrhythmogenesis. However, in addition to facilitating phase 3 action potential repolarization, slow deactivation of hERG channels may also maintain refractoriness of cardiac tissue during early diastole and protect against ectopic beats caused by triggered activity (Smith *et al.*, 1996; Yu Lu *et al.*, 2001). This notion has been less explored and highlights the need to understand the mechanisms of slow deactivation and its role in protecting against triggered activity.

hERG channels share structural homology with other Kv channels, with six α-helical transmembrane segments (S1-S6) assembled in a tetrameric configuration with S1-S4 forming the voltage sensing domain and S5-S6 forming the pore domain. Voltage sensitivity arises from the movement of basic S4 helix charges in response to changes in membrane voltage, which result in the translocation of 6-8 *e* per tetramer across the membrane (Zhang *et al.*, 2004). Numerous studies have suggested that S4 charge movement is coupled to opening of the pore gate via the S4-S5 linker (Sanguinetti & Xu,

1999; Ferrer *et al.*, 2006; Van Slyke *et al.*, 2010; Hull *et al.*, 2014); however, this has been challenged recently by observation that the S4-S5 linker is short and not domain-swapped in cryo-EM structures of hERG channels (Wang & MacKinnon, 2017), and that co-expression of hERG channel halves, physically split within the S4-S5 linker, co-assemble to produce wild-type (WT) -like channel activation gating (Lörinczi *et al.*, 2015; de la Peña *et al.*, 2018). Regardless of the mechanism of the coupling between voltage sensing and pore opening, measurement of the energetics of pore opening suggest that the open state of the pore is stable (ΔG_0=-8.4 $kJ\ mol^{-1}$) and that work must be done to close the pore (Hardman *et al.*, 2007; Cheng *et al.*, 2013). This observation indicates deactivation gating as a key regulator of hERG channel open probability, which underscores the need to elucidate the mechanics of slow deactivation gating. Indeed, acceleration of deactivation kinetics is known to be associated with Long QT syndrome type 2 (LQTS2) and sudden cardiac death (Chen *et al.*, 1999).

Several regions within hERG channels have been associated with modulation of deactivation kinetics. Truncation of, or substitutions within, the N-terminus accelerate deactivation kinetics (Spector, 1996; Cabral *et al.*, 1998; Wang *et al.*, 1998, 2000; Chen *et al.*, 1999; Ng *et al.*, 2011; Tan *et al.*, 2012; Adaixo *et al.*, 2013), and several studies using a variety of approaches have suggested that the N-terminus may stabilize the open state of the channel via interactions with the S4-S5 linker, C-linker and the C-terminal cyclic nucleotide binding homology domain (cNBHD) (Al-Owais *et al.*, 2009; Gustina & Trudeau, 2011, 2012, Ng *et al.*, 2012, 2014; Brelidze *et al.*, 2013; de la Peña *et al.*, 2013, 2015). Together, these findings imply that deactivation is influenced by a complex gating machinery involving several cytoplasmic elements (Cabral *et al.*, 1998; Wang *et al.*, 1998; Fernández-Trillo *et al.*, 2011; Ng *et al.*, 2012; de la Peña *et al.*, 2013; Hull *et al.*, 2014). However, numerous mutations throughout the channel transmembrane core also accelerate deactivation (Liu *et al.*, 2003; Subbiah *et al.*, 2004; Zhang *et al.*, 2005; Van Slyke *et al.*, 2010; Shi *et al.*, 2014; Hull *et al.*, 2014). In addition, extracellular ionic manipulations, e.g. increased protons or divalent cations, also accelerate deactivation kinetics (Anumonwo *et al.*, 1999; Johnson *et al.*, 1999*b*; Jiang *et al.*, 1999; Terai *et al.*, 2000; Bett & Rasmusson, 2003; Lin & Papazian, 2007; Abbruzzese *et al.*, 2010; Shi *et al.*, 2014). These observations invoke the need to understand the underlying deactivation regulatory mechanisms.

Recent studies suggest that voltage sensor relaxation contributes to slow deactivation in hERG channels (Tan *et al.*, 2012; Goodchild & Fedida, 2014; Thouta *et al.*, 2017). The mechanistic basis of relaxation is not fully understood, but it describes events following depolarization that further stabilize (relax) the voltage sensor in the activated configuration. Relaxation of the voltage sensor into this more stable state results in more energy being required to return the voltage sensor to its resting state upon repolarization than required to activate it. Thus, voltage sensor relaxation results in an energetic separation of the activation and deactivation pathways, producing a hysteresis, which has been previously described as a mode-shift. Such mode-shift behaviour has been reported in numerous channels, such as *Shaker* (Lacroix *et al.*, 2011; Haddad & Blunck, 2011; Labro *et al.*, 2012; Priest *et al.*, 2013), Kv1.2 (Labro *et al.*, 2012), NaChBac (Kuzmenkin *et al.*, 2004), HCN (Elinder *et al.*, 2006; Xiao *et al.*, 2010), L-type calcium (Brum *et al.*, 1987, 1988), Hv1 (Villalba-Galea, 2014), as well as in the voltage-sensor related protein, *Ci*-VSP (Villalba-Galea *et al.*, 2008), and these observations have led to the suggestion that mode-shift due to relaxation is an intrinsic property of the channel voltage sensor. Importantly however, although in most cases mode-shift required prolonged depolarization, mode-shift in hERG channels occur in response to depolarizations that are of physiologically relevant duration (Goodchild *et al.*, 2015; Thouta *et al.*, 2017). As such, pore closure is slowed by relatively brief occupancy of the open channel state. We recently demonstrated that membrane depolarization stabilizes the hERG voltage sensor in the relaxed state, increasing the energy required for charge return, and that partial return of charge appears to trigger closure of the pore gate (Thouta *et al.*, 2017). Accordingly, we hypothesize that entry of the voltage sensor into a stable relaxed state limits channel closing and that, upon repolarization, transition of an individual subunit voltage sensor back to rest triggers closure of the pore via the S4-S5 linker and other cytoplasmic elements to regulate channel deactivation.

In the current study, we use external acidification as a tool to demonstrate a connection between voltage sensor relaxation and the kinetics of deactivation in hERG channels. Using two methods to track voltage sensor measurement, we show that acidic pH attenuates voltage sensor relaxation, indicating that both approaches are reliable in tracking voltage sensor reconfigurations and that low pH destabilizes the relaxed state of the voltage sensor by lowering the energetic landscape for its return. Furthermore, we identify D509 in S3 as a proton sensor site that resides in a dynamic region of the hERG

cryo-EM structure and is important in mediating the sensitivity of relaxation to external protons. In doing so, we identify a site and mechanism of action of the well-known proton-induced acceleration of hERG channel deactivation gating. These findings provide a description of the molecular mechanism that regulates deactivation gating in hERG channels. In addition, we demonstrate that the consequence of accelerated deactivation by low pH is a dramatically reduced hERG protective current in response to premature stimulations applied in the early refractory period, and highlight the utility of an activator compound, RPR260243, to rescue the protective current in the face of acidosis. These findings suggest that modification of relaxation or its coupling to the pore may present novel approaches for anti-arrhythmic therapies.

4.3 Materials and Methods

4.3.1 Molecular Biology

hERG1a channel cDNA was subcloned into a pBluescript SKII expression vector. The D509A mutation was generated by conventional overlap extension PCR. Mutagenic primers were synthesized by Sigma-Genosys (Oakville, ON, Canada). The mutation was confirmed by sequencing using Eurofins MWG Operon (Huntsville, AL). The *XbaI* restriction enzyme was used to linearize the construct for subsequent synthesis of cRNA with the mMessage mMachine T7 Ultra cRNA Transcription Kit (Ambion, Austin, TX).

4.3.2 Oocyte preparation and injection

In agreement with the policies and procedures of the Simon Fraser University Animal Care Committee and the Canadian Council of Animal Care, *Xenopus laevis* frogs were terminally anaesthetized by immersion in 2 g L^{-1} tricaine solution for 25 min and oocyte lobes were surgically removed. Oocyte lobes were treated with collagenase (1 mg ml^{-1} collagenase type 1A in MgOR2 solution (in mM: 96 NaCl, 2 KCl, 20 $MgCl_2$, 5 HEPES, titrated to pH 7.4 with NaOH) for 1 h prior to manual defolliculation and isolation of stage V-VI oocytes. Defolliculated oocytes were injected with 50 nL of cRNA using a Drummond digital microdispenser and stored in SOS+ media (in mM: 96 NaCl, 2 KCl, 1.8 $CaCl_2$, 1 $MgCl_2$, 5 HEPES, 5 % horse serum, 2.5 sodium pyruvate, 100 mg L^{-1} gentamicin sulfate, titrated to pH 7.4 with NaOH) at 19 °C for 1-3 days before recording.

4.3.3 Electrophysiology

All recordings were performed at 20-22°C. Ionic current recordings were performed using conventional two-electrode voltage-clamp with an OC-725C amplifier (Warner Instruments, Hamden, CT) coupled to a Digidata 1440 interface (Axon Instruments). Oocytes were bathed in ND96 solution containing (in mM): 96 NaCl, 3 KCl, 0.5 $CaCl_2$, 1 $MgCl_2$, and 5 HEPES, titrated to pH 7.4 or 6.5 with NaOH. HEPES was replaced by 2-(N-Morpholino)ethanesulfonic acid (MES) in solutions more acidic than pH 6.5. All reagents were purchased from Sigma-Aldrich (Oakville, ON, Canada). Experiments were performed under constant perfusion (1 mL min^{-1}), and complete exchange of bath solution titrated to different pH was achieved following 5 min perfusion prior to recordings. Glass recording microelectrodes were made with thin-walled borosilicate glass (World Precision Instruments, Sarasota, FL) and when filled with 3 M KCl had a tip resistance of 0.2-0.8 MΩ. All current signals were acquired with a 10 kHz sampling frequency and were low-pass filtered at 4 kHz (−3 dB, 8 pole Bessel filter).

4.3.4 Cut-Open Voltage Clamp

Gating currents were measured using the cut-open Vaseline gap technique with a CA-1B amplifier (Dagan, Minneapolis, MN) and recorded by Patchmaster software (ITC-16 interface; HEKA Electronik, Bellmore, NY). External gating solution consisted of (in mM) 120 tetraethylammonium-hydroxide (TEA-OH), 120 MES, 0.5 Ca-MES, and 10 HEPES (pH titrated to pH 7.4 or pH 6.5 using MES). Internal gating solution consisted of (in mM) 120 tetraethylammonium-hydroxide (TEA-OH), 120 MES, 2 EGTA, and 10 HEPES (titrated to pH 7.4). Oocytes were permeabilized by 30-60 s application of internal gating current solution supplemented by 0.1% saponin. Following permeabilization, but prior to gating current recordings, cells were held at -10 mV for 30 minutes to deplete cytosolic K^+ to minimize ionic currents. The hERG channel blocker, terfenadine (20 μM), was added in both external and internal gating solutions to inhibit residual hERG ionic currents. Glass recording microelectrodes were made from thin-walled borosilicate glass and had a resistance of 250-500 kΩ when filled with 3 M CsCl. Capacitive currents were subtracted using the analog circuitry of the amplifier; linear leak subtraction was performed online using a P/-8 protocol. We were unable to resolve gating currents in oocytes expressing hERG D509A channels. This is likely due to lower expression levels of these mutant channels compared with WT; while we were able to resolve fluorescence

recordings from the L520C reporter site (see below) in D509A channels, signals were consistently smaller than in the absence of the D509A mutation.

4.3.5 Voltage-Clamp Fluorimetry

The L520C mutation was introduced in the N-terminal S4 segment (extracellularly accessible) to engineer a labelling site for tetramethylrhodamine-5-maleimide (TMRM; Invitrogen Life Technologies, Burlington, ON, Canada). Two native cysteines in the S1-S2 extracellular linker (C445 and C449) were also mutated to valine to reduce non-specific labelling. Oocytes were labeled in the dark with depolarizing solution (in mM: 98 KCl, 1 $MgCl_2$, 2 $CaCl_2$, and 5 HEPES, titrated to pH 7.4 with NaOH) supplemented with 5 µM TMRM for 30 min at 10 °C, then washed with ND96 solution. Two-electrode voltage-clamp fluorimetry was performed with a Nikon TE2000S inverted microscope (Nikon Canada, Mississauga, ON, Canada) with an epifluorescence attachment and photomultiplier tube detection module (Cairn Research, Kent, UK) as described previously (Van Slyke *et al.*, 2010).

4.3.6 Data Analysis

Data acquisition and analysis were performed using pClamp 10.2 software (Axon Instruments), SigmaPlot 11 (Systat Software, San Jose, CA), or IGOR Pro 6 (WaveMetrics, Lake Oswego, OR) software. Activation and deactivation conductance-voltage (G-V) relationships were measured from peak tail currents obtained upon repolarization from a series of test voltages. Measurement of charge displacement (Q) vs voltage (Q-V relationships) for activation and deactivation were obtained by integrating the off-gating currents at -100 mV (Ig_{off}) and on-gating currents at 0 mV for 500 ms (Ig_{on}), respectively, elicited by step changes in test voltage. In this way, charge movement during the fixed duration at the standard off- or on-test voltage is used as a measure of the total charges moved in the preceding, variable conditioning pulse, as has been performed previously (Piper *et al.*, 2003; Goodchild & Fedida, 2014; Thouta *et al.*, 2017). Measurements of fluorescence-voltage (F-V) relationships for activation and deactivation were obtained by measuring the fluorescence change at the end of each voltage step. G-V, Q-V and F-V relationships were plotted and fitted to the Boltzmann function: $y = 1/(1+exp((V_{1/2}-V)/k))$; where y is the normalized peak conductance, gating charge or fluorescence change, $V_{1/2}$ is the half-activation potential, V is the variable (test) voltage,

and k is the slope factor. Deactivation kinetics were quantified by fitting the decaying portion of the tail current during the test pulse to a bi-exponential function: $I = A_{fast}exp(t/\tau_{fast}) + A_{slow}exp(t/\tau_{slow}) + C$; where A_{fast} and A_{slow} are the amplitudes of the fast and slow components, τ_{fast} and τ_{slow} are the time constants for fast and slow components, and C is the residual amplitude. All data are expressed as mean ± SEM. Statistical comparisons between means were conducted using a two-tailed Student's t-test, or two-way ANOVA test, as appropriate, with $P < 0.05$ taken as an indicator for statistical significance.

4.3.7 Supplementary Material

Figure S4.1 shows that the use of a hyperpolarized holding potential allows capture of the full F-V relationship from TMRM labelling of L520C. **Figure S4.2** shows ionic current recordings and plots of the voltage-dependence of activation and deactivation from hERG L520C C-less channels. **Table S4-1** shows the effect of holding potential on fluorescence-voltage and conductance-voltage relationship Boltzmann fit parameters.

4.4 Results

4.4.1 Acidic pH reduces mode-shift behaviour in hERG channels

Mode-shift behaviour reflects energetic separation of activation and deactivation gating and becomes pronounced in numerous channels following prolonged depolarization (Piper *et al.*, 2003; Elinder *et al.*, 2006; Bruening-Wright & Larsson, 2007; Villalba-Galea *et al.*, 2008; Lacroix *et al.*, 2011; Haddad & Blunck, 2011; Labro *et al.*, 2012; Villalba-Galea, 2014; Hull *et al.*, 2014; Goodchild *et al.*, 2015; Thouta *et al.*, 2017). In hERG channels, robust mode-shift behaviour is evident following depolarization durations in the normal physiological range (Piper *et al.*, 2003; Goodchild & Fedida, 2014; Thouta *et al.*, 2017). This can be seen in Figure 4.1 (A-B), which shows typical families of hERG channel currents recorded in response to voltage protocols used to measure the voltage-dependence of activation and deactivation gating with physiological durations. We applied 250 ms depolarizing steps to measure activation and 750 ms repolarizing steps (following a 250 ms depolarization) to measure deactivation, so as to mimic durations typical of a basic cardiac cycle. Boltzmann fits of normalized peak tail currents (Figure 4.1B) yielded $V_{1/2}$ values of -12.4 ± 1.1 mV for activation and -66.0 ± 0.9 mV for deactivation (n = 6). These data demonstrate that at physiological durations hERG channels display a robust

mode-shift with a voltage-dependence of channel deactivation that is separated by -53.6 ± 1.8 mV from that of activation gating (See Table 4-1).

We recently showed that the magnitude of mode-shift is strongly dependent on experimental protocol duration, and that the slow kinetics of hERG channel deactivation contribute to the generation of the mode-shift measured using short step durations, such as those in Figure 4.1 (Thouta *et al.*, 2017). To further demonstrate this, we investigated the effect of acidic pH on mode-shift behaviour, since it is well known that external acidification accelerates hERG channel deactivation, albeit via an unknown mechanism (Anumonwo *et al.*, 1999; Bérubé *et al.*, 1999; Terai *et al.*, 2000; Bett & Rasmusson, 2003; Liu *et al.*, 2003; Zhou & Bett, 2010; Shi *et al.*, 2014). Figure 4.1C shows typical current families recorded in response to the voltage protocols shown in Figure 4.1A with the external pH titrated to pH 6.5, which is within the pathophysiological range, (Orchard & Cingolani, 1994), and which accelerated deactivation kinetics. Normalized conductance-voltage relationships for activation and deactivation derived from data such as these are shown in Figure 4.1D. We observed that while the $V_{1/2}$ of activation gating was only minimally affected (-5.9 ± 0.7 mV), the $V_{1/2}$ of deactivation gating (-43.0 ± 0.7 mV) was right shifted by +23 mV. These data suggest that mode-shift behaviour is correlated with deactivation kinetics and prompted us to investigate this relationship further.

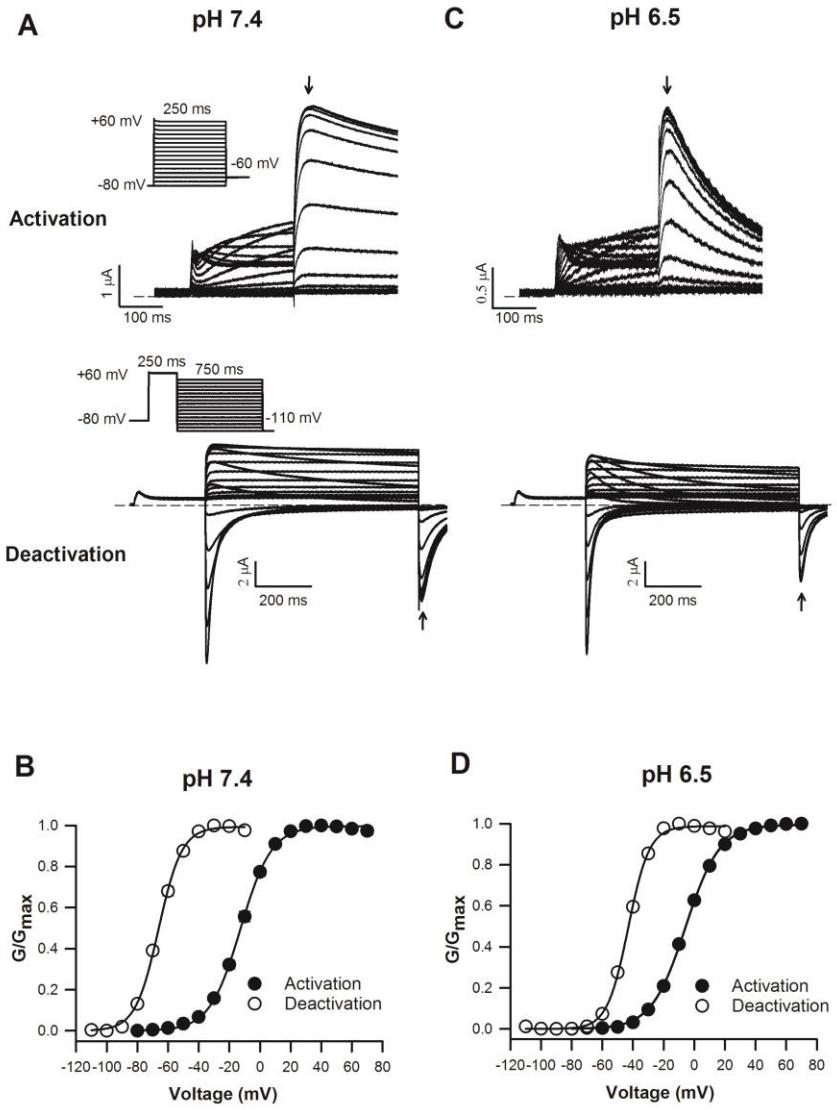

Figure 4.1 – hERG mode-shift is reduced by acidic pH.

A. Typical ionic recordings elicited with activating voltage step durations of 250 ms and deactivating voltage step durations of 750 ms (following depolarization to +60 mV for 250 ms), mimicking physiological durations of a cardiac action potential. Arrows mark where current measurements were made. **B.** Plots of the normalized G-V relationship for activation and deactivation, fitted to a Boltzmann function, yielded $V_{1/2}$ values of -12.4 ± 1.1 mV and -66.0 ± 0.9 mV, respectively. The mean mode-shift was -53.6 ± 1.8 (n = 6). **C.** Typical ionic recordings from the activation and deactivation protocols in panel A at pH 6.5. **D.** Boltzmann fits of the normalized G-V relationship for activation and deactivation yielded $V_{1/2}$ values of -5.9 ± 0.7 mV and -43.0 ± 0.7 mV, respectively, with a mode-shift of -37.1 ± 1.1 mV (n = 6), which was reduced by 31 % compared with that at pH 7.4 (P < 0.0001, calculated from paired two-tailed Student's t-test). Dash lines represent baseline.

The data shown in Figure 4.1 suggest that acidic pH changes in this range alter the energy landscape experienced during deactivation to a greater extent than during activation gating, which is consistent with the observation that low pH markedly accelerates deactivation kinetics. To better understand the relationship between accelerated deactivation kinetics and the reduction in mode-shift at low pH, we measured deactivation kinetics and mode-shift using voltage steps long enough in duration to approximate steady-state activation and deactivation voltage-dependencies over a range of pH values (pH 8.5 to 4.5). Figure 4.2 A-C shows the acceleration of deactivation kinetics with changes in external pH following a 15 s depolarizing step. Tail currents at -110 mV were fitted with a double exponential and the resultant values for τ_{fast} are plotted against pH. A fit of the data with the Hill equation revealed that acidic pH accelerated deactivation kinetics with a *pKa* of pH 6.8 (*n* = 1.9), similar to that reported previously from shorter duration steps (Bett & Rasmusson, 2003). We then measured the pH-dependence of the mode-shift behaviour (Figure 4.2D-F) using long duration steps that allow slow activation and deactivation to reach close to steady-state, as described previously (Thouta *et al.*, 2017). Figure 4.2F plots the pH-dependence of the mode-shift fit to the Hill equation, which yielded a *pKa* of pH 7.0 (*n* = 1.1). The similarity in the pH-dependence of deactivation kinetics (Figure 4.2C) and mode-shift (Figure 4.2F) supports the hypothesis that accelerated deactivation kinetics reduce the measured mode-shift behaviour (Thouta *et al.*, 2017). The Hill coefficient (*n*) values suggest that there may be some cooperativity in the interactions with protons that govern the kinetics of deactivation, which is consistent with the idea that deactivation involves downstream cytoplasmic interactions.

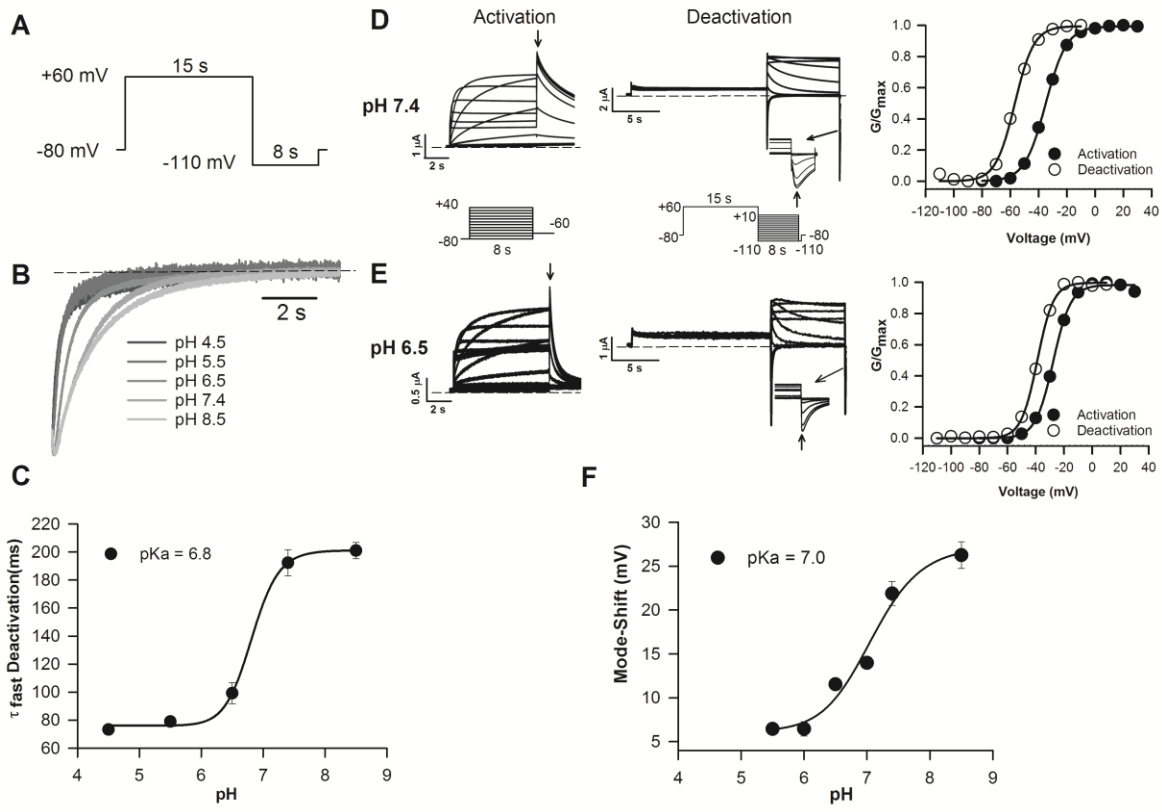

Figure 4.2 - The pH-sensitivity of mode-shift behaviour is similar to that of deactivation kinetics.

A., B. hERG channels were recruited into the relaxed state by applying a 15 s depolarizing step to +60 mV, following which deactivation kinetics were assessed during a repolarizing step to -110 mV. Current decay during repolarization was fitted to exponential function, which yielded values for τ_{fast} of 201 ± 11 ms (pH 8.5, n = 4), 192 ± 20 ms (pH 7.4, n = 5), 99 ± 16 ms (pH 6.5, n = 5), 79 ± 5 ms (pH 5.5, n = 5), and 73 ± 7 ms (pH 4.5, n = 5). **C.** Plot of the pH-dependence of the τ_{fast} of deactivation. Fitting the data with a Hill function yielded a *pKa* of pH 6.8, Hill coefficient, *n* = 1.9. **D**., **E.** Representative traces recorded during the voltage protocols (*insets*) designed to measure the steady-state voltage-dependence of activation and deactivation at pH 7.4 (D) and pH 6.5 (E). Arrows mark where current measurements were made. Plots of the normalized voltage-dependence of activation and deactivation G-V relationships at each pH are shown at right. Boltzmann fits of the data recorded at pH 7.4 yielded $V_{1/2}$ values for activation and deactivation of -34.5 ± 1.3 mV and -56.4 ± 1.2 mV, respectively (n = 12). Corresponding values measured at pH 6.5 were -27.3 ± 0.8 mV and -38.8 ± 1.2 mV (n = 5). The mode-shift calculated from these data was reduced by 74 % from -21.9 ± 1.4 mV at pH 7.4 to -11.5 ± 0.5 mV at pH 6.5. **F.** Plot of the pH-dependence of the mode-shift measured as in Panels D-E. Fitting the data with a Hill function yielded a *pKa* of pH 7.0, Hill coefficient, *n* = 1.1 (see also Table 4-2). Dash lines represent baseline.

4.4.2 Acidic pH destabilizes the relaxed state of the voltage sensor

We next considered the mechanism by which external protons accelerate hERG channel deactivation kinetics. Previous evidence has suggested that acidic pH accelerates return of the voltage sensor domain (Es-Salah-Lamoureux *et al.*, 2010; Van Slyke *et al.*, 2012). In addition, stabilization of the activated voltage sensor in the relaxed state has been shown to slow hERG channel closing (Tan *et al.*, 2012; Goodchild *et al.*, 2015; Thouta *et al.*, 2017). We hypothesized that external protons accelerate deactivation by destabilizing the relaxed state of the voltage sensor. Relaxation is likely an intrinsic property of the voltage sensor, since the relaxation process is abolished following uncoupling of the pore from the voltage sensor domain (Haddad & Blunck, 2011) and in the absence of a pore in the isolated voltage sensor, *Ci*-VSP, (Villalba-Galea *et al.*, 2008). We therefore measured voltage sensor movement in hERG channels to directly investigate the effects of external protons on voltage sensor domain relaxation. Figure 4.3 shows data from two different approaches that we used to report voltage sensor movement. Figure 4.3 (A-C) shows recordings of hERG gating currents, which reflect charge movement, and Figure 4.3 (D-F) displays measurements of fluorescence changes from a TMRM reporter tag attached to L520C at the outer end of the S4 segment, which reports on environmental changes during voltage sensor gating. We used both approaches to track voltage sensor behaviour using long durations that allow near steady-state equilibria of channels between activated and relaxed states. Figure 4.3A shows typical gating current recordings measured in response to the voltage protocol designed to assess activation (holding potential, -100 mV). Boltzmann fits of the data yielded a $V_{1/2}$ value of -48.2 ± 0.5 mV (n = 3) for the Q_{on}-V relationship (see Methods). Figure 4.3B shows typical gating current recordings measured in response to the voltage protocol designed to assess deactivation (holding potential, 0 mV). The fit of the Q_{off}-V relationship yielded a $V_{1/2}$ value of -75.5 ± 2.3 mV (n = 4). From these data recorded using voltage steps long enough in duration to allow measurement of near steady-state equilibria, the mode-shift of the voltage sensor was -27.3 ± 2.4 mV. These data reflect the entry of the hERG voltage sensor into a stable relaxed state upon depolarization.

Voltage clamp fluorimetry reports of voltage sensor movement revealed very similar findings to those of charge movement. We recorded fluorescence reports during hERG channel activation and deactivation using the same near steady-state durations as those used above to record gating currents. We used TMRM as a fluorescence reporter

attached to a cysteine residue engineered at L520 on top of the S4 voltage sensor (with the native C445 and C449 cysteines in the S1-S2 linker mutated to valine). Some question has been raised over the suitability of this site as a reporter of voltage sensor movement, largely due to the observation that the fluorescence-voltage (F-V) relationship overlays the G-V rather than the Q-V; however, introduction of a brief pre-pulse to -120 mV in the voltage protocol ensures complete return of the voltage sensor and the full capture of fluorescence change, yielding an F-V that is consistent with charge movement (Figure S4.1, Table S4-1). Figure 4.3D and E show typical on- and off-fluorescence reports recorded in response to the voltage protocols shown. The $V_{1/2}$ of the F_{on}-V relationship was -44.7 ± 1.0 mV (*n* = 4), and that of the F_{off}-V relationship was -76.1 ± 3.2 mV (*n* = 5). These values are consistent with those measured for charge movement (Figure 4.3C) and report a similar voltage sensor mode-shift of -31.4 ± 3.4 mV. *P*-values were calculated from two-ways ANOVA using Tukey HSD (Honest Significant Difference) post hoc test comparing the means of $V_{1/2}$ of voltage sensor mode-shift between activation and deactivation gating currents and fluorescence report at pH 7.4. These data show that gating charge movement and fluorescence measurements of voltage sensor environmental change both report on the same relaxation-induced stabilization of the activated voltage sensor that results in voltage sensor mode-shift.

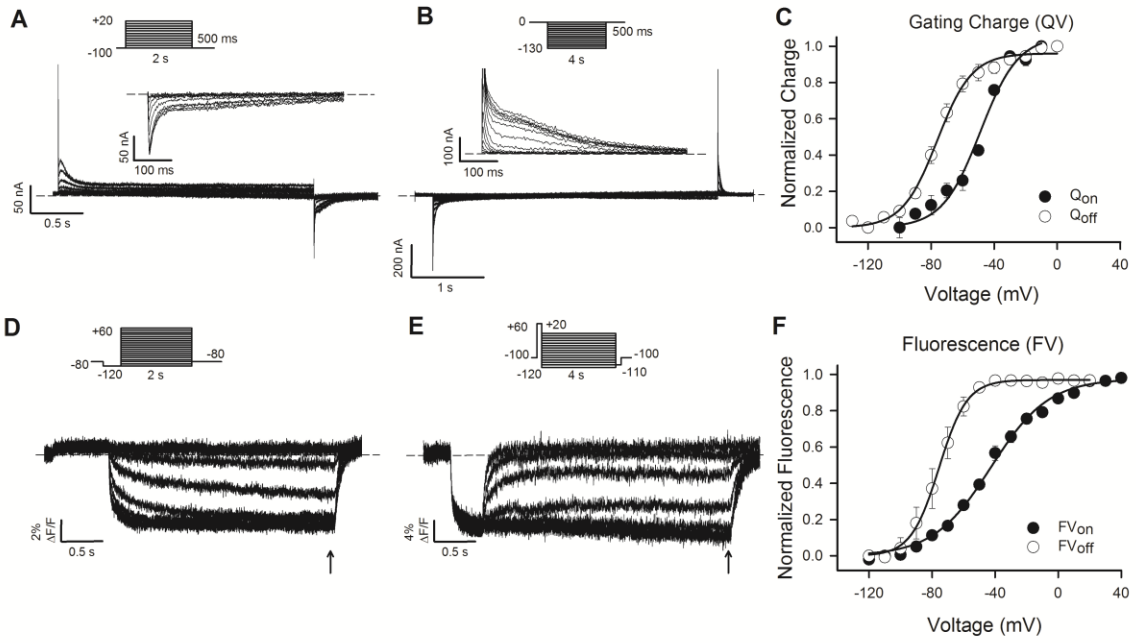

Figure 4.3 - Voltage sensor mode-shift.

A., B. Typical on-gating (Ig_{on}) (A) and off-gating (Ig_{off}) (B) currents recorded at pH 7.4 in response to the voltage protocol shown (*insets*). **C.** Plot of the voltage-dependence of Q_{on} and Q_{off}. The Q_{on}-V relationship was calculated from the integral of the off-gating current measured during a 500 ms step to -100 mV (A, *inset*). The Q_{off}-V relationship was determined from integrals of the on-gating current measured during a 500 ms step to 0 mV (B, *inset*). Data were fitted with a Boltzmann function, which yielded $V_{1/2}$ values for Q_{on} and Q_{off} of -48.2 ± 0.5 mV (n = 3), and -75.5 ± 2.3 mV (n = 4), respectively. The mean gating mode-shift was -27.3 ± 2.4 mV. **D., E**. Typical on-fluorescence (F_{on}) (D) and off-fluorescence (F_{off}) (E) reports from TMRM attached at L520C at pH 7.4 in response to the voltage protocols shown (*insets*). **F**. Plot of the voltage-dependence of normalized F_{on} and F_{off}. The F_{on}-V relationship was constructed by measuring relative fluorescence change at the end of the 2 s depolarizing voltage step. The F_{off}-V relationship was constructed by measuring relative fluorescence change at the end of the 4 s repolarizing voltage step. Data were fitted with a Boltzmann function, which yielded $V_{1/2}$ values for F_{on} and F_{off} of -44.7 ± 1.0 mV (n = 4) and -76.1 ± 3.2 mV (n = 5), respectively. The mean fluorescence mode-shift was -31.4 ± 3.4 mV. The mean $V_{1/2}$ values measured for Q_{on} and F_{on} were not statistically different ($P > 0.17$), neither were the equivalent values for Q_{off} and F_{off} ($P > 0.74$). Dash lines represent baseline.

To test our hypothesis that protons accelerate deactivation gating by destabilizing the relaxed state of the voltage sensor, we measured the effect of acidic pH on voltage sensor mode-shift using gating current recordings and voltage clamp fluorimetry. We used the same voltage protocols as in Figure 4.3 to ensure that recordings were made at near steady-state durations. Typical on- and off-gating current recordings at pH 6.5 are shown in Figure 4.4A-B, and on- and off-fluorescence reports from L520C at pH 6.5 are shown in Figure 4.4D-E. These recordings yielded $V_{1/2}$ values of -44.8 ± 5.0 mV (*n* = 8) and -51.8 ± 3.3 mV (*n* = 5) for Q_{on}-V and Q_{off}-V, respectively (Figure 4.4C), and of -42.8 ± 3.7 mV (*n* = 5) and -57.2 ± 1.9 mV (*n* = 5) for on- and off-fluorescence (Figure 4.4F). Thus, in both measures of voltage sensor gating, while the voltage-dependence of activation gating was not greatly affected at pH 6.5 (see Table 4-3), the voltage-dependence of voltage sensor return was robustly shifted to more depolarized potentials by +23.7 mV (gating currents) and by +18.9 mV (fluorescence report) at pH 6.5. *P*-values were calculated from two-ways ANOVA using Tukey HSD post hoc test comparing the means of $V_{1/2}$ of voltage sensor mode-shift between activation and deactivation gating currents and fluorescence report at pH 6.5. This specific effect of protons on deactivation reduced the voltage sensor mode-shift to -7.0 mV (gating charge) and -14.4 mV (fluorescence). These data show that acidic pH produces a robust reduction in voltage sensor mode-shift by selectively reducing the energy required to return the voltage sensor to its resting configuration, consistent with a proton-induced destabilization of the relaxed configuration of the voltage sensor.

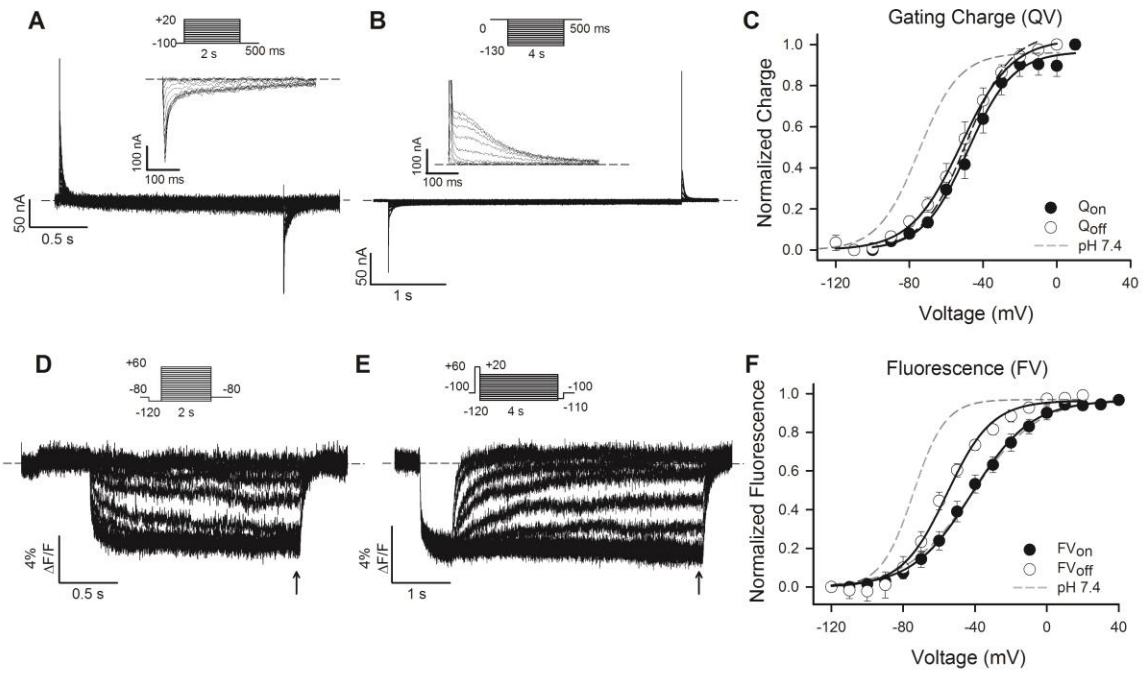

Figure 4.4 - Voltage sensor mode-shift is reduced by acidic pH.

A., B. Typical gating currents recorded at pH 6.5 in response to the voltage protocol shown (*insets*), as in Figure 4.3. **C.** Plot of the voltage-dependence of Q_{on} and Q_{off}. Data were fitted with a Boltzmann function, which yielded $V_{1/2}$ values for Q_{on} and Q_{off} of -44.8 ± 5.0 mV (n = 8; not significantly different from pH 7.4, $P > 0.5$), and -51.8 ± 3.3 mV (n = 5; $P < 0.0007$ compared with pH 7.4), respectively. The mean gating current mode-shift was reduced to -7.0 ± 6.0 mV. Dashed lines show pH 7.4 fits from Figure 4.3C for comparison. **D., E**. Typical on-fluorescence (F_{on}) (D) and off-fluorescence (F_{off}) (E) reports from TMRM attached at L520C at pH 6.5 in response to the voltage protocols shown (*insets*). Arrows mark where fluorescence measurements were made. **F**. Plot of the voltage-dependence of F_{on} and F_{off}. The F_{on}-V relationship was constructed by measuring relative fluorescence change at the end of the 2 s depolarizing voltage step. The F_{off}-V relationship was constructed by measuring relative fluorescence change at the end of the 4 s repolarizing voltage step. Data were fitted with a Boltzmann function, which yielded $V_{1/2}$ values for F_{on} and F_{off} of -42.8 ± 3.7 mV (n = 5; not significantly different from pH 7.5 $P > 0.5$) and -57.2 ± 1.9 mV (n = 5; $P < 0.001$ compared with pH 7.4), respectively. The mean fluorescence mode-shift was reduced to -14.4 ± 4.2 mV. Dash lines represent baseline. Dashed lines show pH 7.4 fits from Figure 4.3F for comparison.

4.4.3 Destabilization of voltage sensor relaxation by protons is mediated by an extracellular acidic site, D509

Having established that external protons destabilize the activated relaxed state of the voltage sensor, we next investigated the interaction site of protons that mediates this effect. The activated position of the voltage sensor is thought to be stabilized by key electrostatic interactions between acidic residues, D456 and D460 in S2 and D509 in S3, with positive residues in S4, such as R531 (Papazian *et al.*, 1995; Liu *et al.*, 2003; Piper *et al.*, 2008). Previous studies have shown that the three acidic residues form a metal cation binding pocket that coordinate cations, such as Ca^{2+}, Mg^{2+}, Cd^{2+}, and is protonated by H^{+}; all of these ions depolarize the voltage-dependence of activation and accelerate the kinetics of deactivation (Ho *et al.*, 1998; Anumonwo *et al.*, 1999; Johnson *et al.*, 1999*a*, 1999*b*; Silverman *et al.*, 2000; Fernandez *et al.*, 2005; Abbruzzese *et al.*, 2010; Kazmierczak *et al.*, 2013; Shi *et al.*, 2014). Neutralization of D509, in particular, shifts the voltage-dependence of activation to more depolarized potentials (Shi *et al.*, 2014), and abolishes the proton-induced acceleration of deactivation (Liu *et al.*, 2003). These observations suggest that D509 is an important site in stabilizing activated channel states (Shi *et al.*, 2014), although this cannot be confirmed structurally since D509 is in a disordered or dynamic region of the latest cryo-EM hERG structures (Wang & MacKinnon, 2017). Despite the structural uncertainty, and driven by the available functional data, we investigated whether protonation of D509 destabilized the relaxed state of the voltage sensor. Although we were not able to resolve gating current recordings from D509A mutant channels, we recorded resolvable fluorescence reports of voltage sensor movement using TMRM labeling at L520C in D509A mutant channels. Figure 4.5A and B shows typical fluorescence reports of voltage sensor movement in D509A channels during the voltage protocols shown, from which on-fluorescence and off-fluorescence voltage relationships were constructed (Figure 4.5C). Figure 4.5D and E shows fluorescence records using the same voltage protocols, but with the external solution titrated to pH 6.5. It is clear that the characteristic separation of the voltage dependencies of voltage sensor activation and deactivation that result from relaxation is largely abolished by neutralization of D509 and that acidic pH has no additional effect on voltage sensor gating in the D509A mutant channel. The reduced separation was, largely, caused by a right-shift of the voltage-dependence of deactivation (F_{off}) in D509A mutant channels (+18.3 mV), with little effect on the F_{on} relationship (Table 4-3). Thus neutralization of D509 mimicked the effect

of pH 6.5, largely abolishing the mode-shift due to voltage sensor relaxation. These data indicate that D509 is a critical site involved in stabilization of the relaxed state.

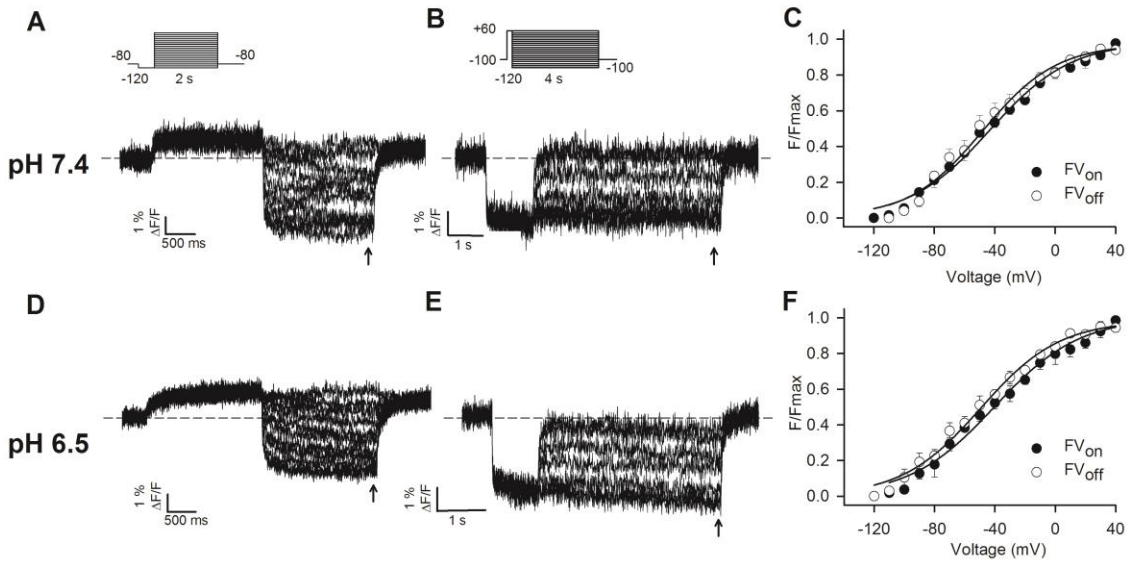

Figure 4.5 - Neutralization of D509 mimics the effect of protons on voltage sensor mode-shift.

A., B., D., E. Typical on-fluorescence (A, D) and off-fluorescence (B, E) changes from TMRM attached at L520C in D509A mutant channels in response to the voltage protocols shown (*insets*) at pH 7.4 (A, B) and pH 6.5 (D, E). Arrows mark where fluorescence measurements were made. **C., F.** Plots of the voltage-dependence of F_{on} and F_{off} at pH 7.4 (C) and pH 6.5 (F). Data were fitted with a Boltzmann function, which yielded $V_{1/2}$ values for F_{on} and F_{off} of -52.2 ± 8.1 mV (n = 4) and -57.8 ± 3.7 (n = 3), respectively, at pH 7.4. The corresponding values at pH 6.5 were -42.7 mV ± 3.5 (n = 3) and -49.6 mV ± 4.4 (n = 4), respectively. The mean voltage sensor mode-shift was -5.6 ± 8.9 mV at pH 7.4 and -6.9 mV ± 2.1 at pH 6.5. Dash lines represent baseline.

If destabilization of the relaxed state of the voltage sensor results in an acceleration of deactivation kinetics as the data in Figures 4.1 and 4.2 suggest, measurement of D509A ionic currents should exhibit fast deactivation. Figure 4.6 shows that this is indeed the case. Typical families of D509A ionic currents recorded at pH 7.4 or pH 6.5 using the voltage protocol shown demonstrate accelerated deactivation kinetics in D509A mutant channels, which were resistant to further acceleration by switching to acidic pH. This is consistent with the conclusion that slow deactivation gating in hERG channels arises from stabilization of the relaxed state of the voltage sensor. Consequently, mode-shift behaviour in D509A channels, measured using physiologically relevant durations, is greatly reduced as a result of the accelerated deactivation kinetics (Figure 4.6G). These findings highlight the physiological significance of entry of the hERG voltage sensor into the stabilized state, that is, destabilization of the relaxed state leads to accelerated deactivation and loss of mode-shift behaviour.

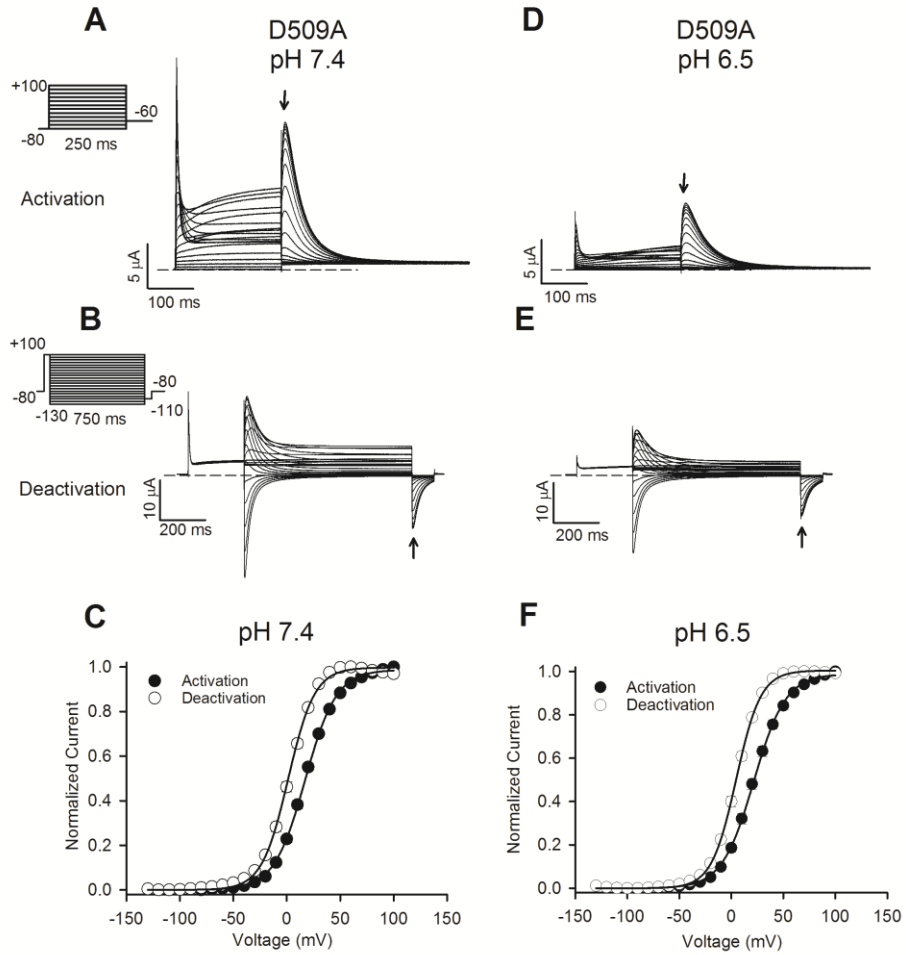

Figure 4.6 - Mode-shift is greatly diminished and is pH-independent in D509A mutant channels.

A., D. Typical ionic current recordings from D509A mutant channels at pH 7.4 (A) or pH 6.5 (D) in response to the voltage protocols shown (*insets*) designed to measure the voltage-dependence of activation. The membrane was held at -80 mV before 250 ms steps were applied up to +100 mV (in 10 mV increments), followed by a repolarizing step to -60 mV. Arrows mark where current measurements were made. **B., E**. Typical ionic current recordings of D509A channel deactivation at pH 7.4 (B) or pH 6.5 (E). The membrane was held at -80 mV, before a 250 ms depolarizing step to +100 mV, followed by 750 ms repolarizing steps down to -130 mV (in 10 mV increments). **C., F.** Plots of the voltage-dependence of activation and deactivation at pH 7.4 (C) and pH 6.5 (F). Data were fitted with a Boltzmann function, which yielded $V_{1/2}$ values for activation and deactivation of +17.1 ± 0.8 mV (n = 5) and +1.6 ± 1.1 mV (n = 5), respectively, at pH 7.4. The corresponding values at pH 6.5 were +21.6 ± 1.5 mV (n = 5) and +4.8 ± 1.2 mV (n = 5), respectively. The mean mode-shift was -15.5 ± 0.1 mV at pH 7.4 and -16.8 mV ± 0.6 at pH 6.5 ($P > 0.3$; not significantly different) (See Table 4-1). *P*-values were calculated from pair-wise mean mode-shift at pH 7.4 and 6.5 using a paired two-tailed Student's t-test. Dash lines represent baseline.

4.4.4 Voltage sensor relaxation contributes to the hERG protective current conducted in the early refractory period of the action potential

Our findings so far suggest that hERG voltage sensor relaxation slows channel deactivation and produces a pronounced mode-shift that is likely to be important in the generation of the resurgent I_{Kr} repolarizing cardiac current. However, relaxation-induced slow deactivation may also be important in contributing to the proposed role for hERG channels in providing repolarizing protective current in response to premature stimulations in early refractory period (Yu Lu *et al.*, 2001; Du *et al.*, 2010). Moreover, accelerated deactivation kinetics induced by acidosis may impair this protective hERG current resulting in a premature action potential (Du *et al.*, 2010). To test this, we measured hERG protective currents in response to premature stimulations in early refractory using a protocol performed previously (Yu Lu *et al.*, 2001). Figure 4.7A shows typical current traces recorded from WT hERG channels in response to the voltage protocol shown. Channels were activated by a step to +30 mV followed by a ramp back to -80 mV to approximate a ventricular action potential. During the repolarization ramp phase, as well as after full repolarization, brief 40 ms depolarizations to 0 mV were applied at increasing coupling intervals to simulate premature stimulations. As observed previously, we saw that hERG channels conduct robust transient currents in response to brief depolarizations applied early in the refractory period (Yu Lu *et al.*, 2001; Du *et al.*, 2010). Transient hERG currents initially increased with coupling interval, but then decreased producing a peak protective current in response to a premature stimulus applied 20 ms after 90 % repolarization ($Repol_{90}$+20) (Figure 4.7A). Interestingly, significant repolarizing force was generated via hERG channels even 300 ms following 90 % repolarization ($Repol_{90}$+300). Figure 4.7A shows the effect of acidic pH on the hERG protective current in response to premature stimulations. At pH 6.5, transient protective currents were smaller in amplitude (reduced to 60 ± 0.02 % of that at pH 7.4, $P < 0.00037$, Student's paired t-test), occurred earlier during repolarization (at $Repol_{90}$+0 ms), compared with $Repol_{90}$+20 ms at pH 7.4) and wane away more rapidly with increasing coupling interval than at pH 7.4, such that there was little protective current at $Repol_{90}$+100. These findings suggest that the acidic pH-induced acceleration of deactivation greatly diminishes the protective current carried by hERG channels during the refractory period and may predispose the myocardium to premature excitation.

RPR260243 is a type I hERG channel activator compound that has been shown to slow deactivation rate in hERG channels (Kang *et al.*, 2005; Perry & Sanguinetti, 2008; Wu *et al.*, 2015). If the loss of protective current in the presence of acidic pH is primarily due to the action of protons on the acceleration of deactivation as a result of destabilization of the relaxed state of the voltage sensor, we hypothesized that RPR260243 could rescue the loss of protective current induced by low pH. Figure 4.7A shows typical recordings of protective hERG ionic currents in the presence of 10 μM RPR260243 at pH 6.5. We observed a significant rescue of the protective current by the activator compound. This is more clearly observed in plots of the peak protective current in Figure 4.7B. These data show that RPR260243 not only increased the peak protective current at pH 6.5 (peak protective current was increased to 79 ± 0.08 % of that at pH 7.4, which is significantly different from that at pH 6.5, $P < 0.03$, t-test), but that the activator also largely restored the robust hERG current that flowed during premature stimulations up to $Repol_{90}$+300. These data suggest that RPR260243 may have therapeutic use as an activator through its enhancement of the protective current carried by hERG channels early in refractory, which would be expected to lower the susceptibility to afterdepolarizations (either early afterdepolarizations, EADs, or delayed afterdepolarizations, DADs) and premature stimulation of an action potential.

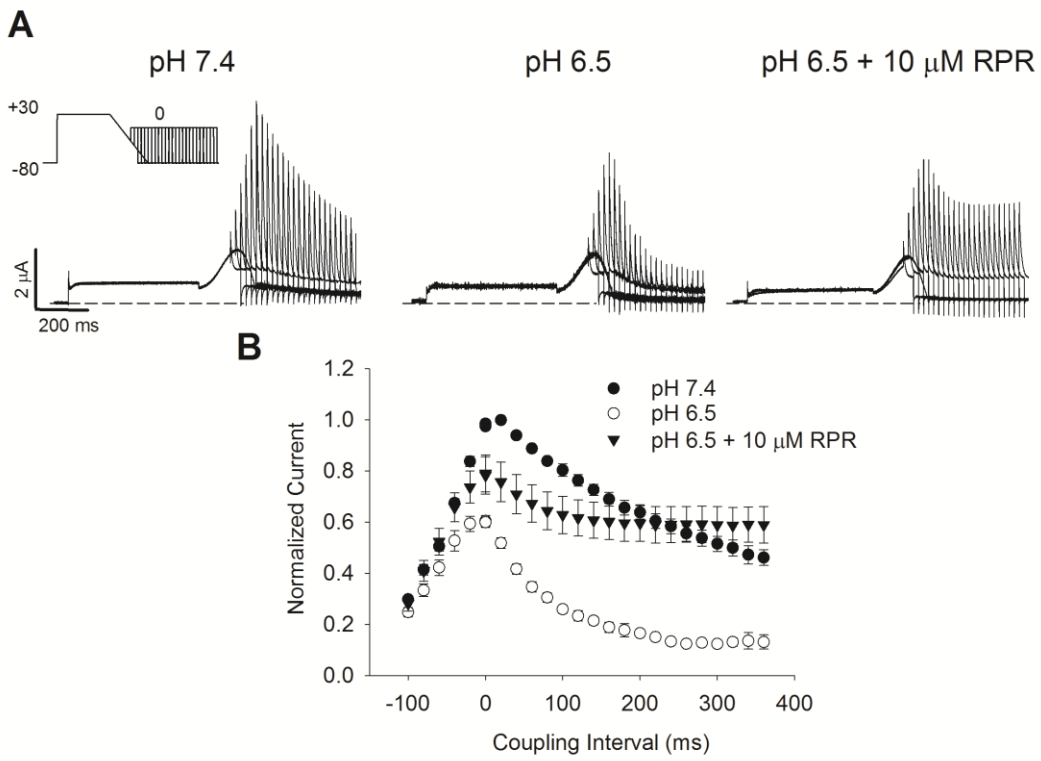

Figure 4.7 - The small molecule RPR260243 enhances hERG protective current.

A. Representative ionic current traces recorded in response to the voltage protocol shown (*inset*) designed to stylize a ventricular cardiac action followed by premature stimuli applied at various coupling intervals. Ionic currents from the same oocyte were recorded at pH 7.4, pH 6.5, and pH 6.5 with 10 μM of RPR260243 (n = 4). Oocytes were depolarized to +30 mV for 500 ms followed by a repolarization ramp to -80 mV over 220 ms. This included a 40 ms premature depolarization step to 0 mV applied at increasing coupling intervals (20 ms increments), from 100 ms prior to 90 % repolarization ($Repol_{90-100}$) to 380 ms after 90 % repolarization ($Repol_{90+380}$), to simulate premature stimulations. **B.** The peak protective current elicited by premature depolarization steps at each condition is plotted against coupling interval. Dash lines represent baseline.

Table 4-1: Activation and deactivation G-V Boltzmann fit parameters recorded with physiological durations.

	Activation G-V $V_{1/2}$ (mV)	*k*	Deactivation G-V $V_{1/2}$ (mV)	*k*	Mode-Shift $V_{1/2}$ (mV)
WT					
pH 7.4	-12.4 ± 1.1 (6)	9.9 ± 0.4	-66.0 ± 0.9 (6)	7.3 ± 0.2	-53.6 ± 1.8
pH 6.5	-5.9 ± 0.7 (6)	11.2 ± 0.3	-43.0 ± 0.7 (6)	6.4 ± 0.1	-37.1 ± 1.1
D509A					
pH 7.4	+17.1 ± 0.8 (5)	14.7 ± 0.4	+1.6 ± 1.1 (5)	12.0 ± 0.4	-15.5 ± 1.4
pH 6.5	+21.6 ± 1.5 (5)	15.1 ± 0.2	+4.8 ± 1.2 (5)	11.6 ± 0.3	-16.8 ± 1.9

Data expressed in mean ± SEM, number of cells in parentheses

Table 4-2: pH-dependence of steady-state activation and deactivation G-V Boltzmann fit parameters.

	Activation G-V $V_{1/2}$ (mV)	*k*	Deactivation G-V $V_{1/2}$ (mV)	*k*	Mode-Shift $V_{1/2}$ (mV)
WT					
pH 8.5	-41.8 ± 0.8 (5)	7.5 ± 0.2	-68.1 ± 1.5 (5)	6.6 ± 0.3	-26.2 ± 1.5
pH 7.4	-34.5 ± 1.3 (12)	7.0 ± 0.3	-56.4 ± 1.2 (12)	6.5 ± 0.3	-21.9 ± 1.4
pH 7.0	-27.4 ± 0.9 (5)	8.1 ± 0.6	-41.4 ± 0.6 (5)	5.4 ± 0.5	-13.9 ± 0.5
pH 6.5	-27.3 ± 0.8 (5)	6.3 ± 0.9	-38.8 ± 1.2 (5)	6.2 ± 1.0	-11.5 ± 0.5
pH 6.0	-22.9 ± 1.8 (5)	7.7 ± 0.5	-29.3 ± 1.2 (5)	6.8 ± 0.7	-6.5 ± 0.8
pH 5.5	-11.5 ± 2.4 (4)	11.9 ± 0.5	-17.9 ± 2.2 (4)	6.9 ± 0.3	-6.4 ± 0.6

Data expressed in mean ± SEM, number of cells in parentheses

Table 4-3: Charge-voltage and fluorescence-voltage relationship Boltzmann fit parameters for activation and deactivation.

	Q_{on}-V $V_{1/2}$ (mV)	*k*	Q_{off}-V $V_{1/2}$ (mV)	*k*	Mode-Shift $V_{1/2}$ (mV)
WT					
pH 7.4	-48.2 ± 0.5 (3)	12.2 ± 2.4	-75.5 ± 2.3 (4)	11.0 ± 0.7	-27.3 ± 2.4
pH 6.5	-44.8 ± 5.0 (8)	12.2 ± 1.0	-51.8 ± 3.3 (5)	13.7 ± 0.5	-7.0 ± 6.0
	F_{on}-V $V_{1/2}$ (mV)	*k*	F_{off}-V $V_{1/2}$ (mV)	*k*	Mode-Shift $V_{1/2}$ (mV)
L520C					
pH 7.4	-44.7 ± 1.0 (4)	21.3 ± 1.9	-76.1 ± 3.2 (5)	8.8 ± 0.5	-31.4 ± 3.4
pH 6.5	-42.8 ± 3.7 (5)	17.3 ± 0.8	-57.2 ± 1.9 (5)	15.5 ± 2.7	-14.4 ± 4.2
D509A/L520C					
pH 7.4	-40.9 ± 8.1 (4)	29.6 ± 2.9	-47.7 ± 3.7 (3)	25.8 ± 5.5	-5.6 ± 8.9
pH 6.5	-42.7 ± 3.5 (3)	27.2 ± 0.6	-49.6 ± 4.4 (3)	26.8 ± 1.3	-6.9 ± 5.6

Data expressed in mean ± SEM, number of cells in parentheses

Table 4-4: Rates and factors for the Markov model

Transition	α_o (s^{-1})	$z\alpha_o$ (s^{-1})	β_o (s^{-1})	$z\beta_o$ (s^{-1})	*c*
S0 - S1	1000	0.2	1500	-0.04	1
S1 - S2	134	0.02	280	-0.05	1.5
S2 - A	2000	2	0.006	-1.7	
A - AR					
pH 7.4	0.5	0	0.001	0	
pH 6.5			10	0	

Parameters for pH 6.5 were the same as pH 7.4 unless indicated. Forward rates were calculated as: $\alpha = \alpha o*\exp(z\alpha*VF/RT)$, and reverse rates were calculated as: $\beta = \beta o*\exp(z\beta*VF/RT)$. *c* reflects the cooperativity factor applied to the independent transitions.

4.5 Discussion

Recent attention has been given to mode-shift behaviour in hERG channels, in part because the pronounced separation of activation and deactivation gating energetics appears to occur in response to physiologically relevant depolarization durations (Figure 1), but also because stabilization of activated states that slows deactivation gating may provide therapeutic strategies for enhancing channel availability. We have previously shown that mode-shift behaviour in hERG channels is caused by both slow activation and, more importantly, slow deactivation gating (Thouta *et al.*, 2017). It is important, therefore, to better understand the mechanism by which slow deactivation gating arises. Several studies have shown that prolonged depolarizations slow hERG voltage sensor return and pore closure (Tan *et al.*, 2012; Goodchild *et al.*, 2015; Thouta *et al.*, 2017), suggesting a role for relaxation in the control of deactivation gating. Consistent with this, hERG channels display robust voltage sensor domain relaxation, such that the voltage-dependence of sensor return is left-shifted from that of pore gate closure (Thouta *et al.*, 2017). This suggests that the energy barrier for exiting the relaxed state is rate-limiting for deactivation. The observation that partial charge return is sufficient to induce pore gate closure (Thouta *et al.*, 2017) is consistent with observations in *Shaker* channels where return of a single voltage sensor is sufficient to close the channel pore (Gagnon & Bezanilla, 2009). Together, the data allow for the generation of a hypothesis that stabilization of activated S4 sensors by relaxation limits hERG pore closure.

4.5.1 The effects of acidic pH support a correlation between mode-shift and deactivation kinetics

In the present study, we have used acidic pH to explore this hypothesis that relaxation limits deactivation, and in doing so, also attempt to understand the mechanistic basis for the pH-induced acceleration of hERG channel gating, which has been the subject of significant previous interest (Bérubé *et al.*, 1999; Jiang *et al.*, 1999; Terai *et al.*, 2000; Bett & Rasmusson, 2003; Liu *et al.*, 2003; Du *et al.*, 2010; Shi *et al.*, 2014). We show that acidic external pH reduces the mode-shift behaviour measured from ionic activation and deactivation gating (Figure 2), and that this is largely due to a specific effect on the voltage-dependence of deactivation gating. These data show that external protons shift the voltage-dependence of deactivation to the right, indicating a reduction in the energetic stability of the activated state and a relative increase in the stability of the closed state of the pore. Interestingly, the pH-dependence of this effect was very similar to that describing the acceleration of deactivation kinetics (compare Figures 4.2C and F), which has been described previously (Bett & Rasmusson, 2003). Such a similarity is consistent with the idea that the kinetics of deactivation gating correlate with the extent of mode-shift behaviour measured from ionic currents (e.g. Figure 4.1).

4.5.2 External protons destabilize the relaxed voltage sensor

To understand the pH-induced acceleration of deactivation gating and reduced energetic stability of the open state, we recorded voltage sensor gating using combined approaches of charge measurement and fluorimetric reports of gating-associated conformational changes sensed at the outer end of S4. Congruence of measurements of fluorescence reports with those of gating charge address uncertainty concerning the interpretation of fluorimetric reports from the hERG voltage sensor. Previous reports of fluorescence changes from TMRM attached at L520C at the top of the voltage sensor displayed a voltage-dependence more similar to that of pore opening than of gating charge movement (Es-Salah-Lamoureux *et al.*, 2010; Van Slyke *et al.*, 2010), suggesting that the reports may track pore gating maneuvers rather than voltage sensing. However, we find close agreement of the voltage-dependence of charge movement and fluorescence signals when a pre-pulse to -120 mV was used to measure the latter (Table S4-1, Figure S1). These data show a fluorescence de-quenching upon hyperpolarization from -80 mV indicating that more hyperpolarized voltages are required to return the voltage sensor to

its resting position. Using a pre-pulse to -120 mV allowed capture of the full fluorescence-voltage relationship, which closely aligned with that of the isochronal charge-voltage relationship. These data demonstrate consistency in the reports of voltage sensor movement from measurement of charge movement and fluorescence changes.

Both approaches reported a profound depolarizing shift in the voltage-dependence of voltage sensor return at pH 6.5 without altering voltage sensor activation (Figures 4.3 and 4.4). This indicates that in the pathophysiologically relevant pH range tested external protons have little effect on the transitions of the voltage sensor into the activated state, but specifically affect interactions that stabilize the voltage sensor in its activated state. Stabilization of the activated voltage sensor, following activation, has been demonstrated in numerous channels and voltage sensor-like proteins and has been attributed to a process termed relaxation (Brum *et al.*, 1987; Elinder *et al.*, 2006; Villalba-Galea *et al.*, 2008; Haddad & Blunck, 2011; Labro *et al.*, 2012; Priest *et al.*, 2013; Villalba-Galea, 2014). Relaxation appears to be an intrinsic property of the voltage sensing unit and involves interactions that stabilize the extruded position of the voltage sensor (Villalba-Galea *et al.*, 2008; Haddad & Blunck, 2011). Such stabilization increases the energetic cost of voltage sensor return, shifting the voltage-dependence to more hyperpolarized potentials, separating it from that of voltage sensor activation. Our findings suggest that external protons destabilize the relaxed state of the voltage sensor catalyzing voltage sensor return and thus pore closure.

To test this we constructed a kinetic model using IonChannelLab (Santiago-Castillo *et al.*, 2010) to describe voltage sensor gating transitions between resting, activated and relaxed states (Figure 4.8A). The Markov state model in Figure 4.8A is a simplified form of a previous model used to describe hERG gating (Piper *et al.*, 2003), and considers transitions of the voltage sensor domain alone in an attempt to model the voltage sensor behaviour observed in our study. As in the original model (Piper *et al.*, 2003), the scheme in Figure 4.8A includes two independent conformational changes in each subunit of the tetramer (S0-S1 and S1-S2) that are voltage-dependent followed by a concerted transition to the activated state (A). Forward rates were calculated as $\alpha = \alpha o * \exp(z\alpha * VF/RT)$, and reverse rates were calculated as $\beta = \beta o * \exp(z\beta * VF/RT)$. As described previously (Piper *et al.*, 2003), it was necessary to include a positive cooperativity factor in the rates to recapitulate the fast and slow phases of gating current observed experimentally (see also Table 4-4). The scheme in Figure 4.8A also includes a

voltage sensor transition into the relaxed state with the intent to simulate mode-shift behaviour of the voltage sensor. The term, zα, in the forward rate was set to zero, consistent with previous reports that entry into the relaxed state is voltage-independent (Villalba-Galea *et al.*, 2008). Thus transition into the relaxed state is modelled as being time-dependent with a forward rate constrained by previous measurements of the kinetics of entry of the voltage sensor into the relaxed state (Thouta *et al.*, 2017). The backward rate for the transition out of the relaxed state is termed de-relaxation, consistent with a previous description in *Shaker* channels (Priest *et al.*, 2013).

Figure 4.8A shows simulated on-gating currents produced by the model. These simulations demonstrate that the model is capable of recapitulating the main features of hERG on-gating currents recorded experimentally, including the prominent fast and slow phases of charge movement, as well as both the voltage-dependence of on-gating charge movement and the separation of the voltage-dependence of the off-gating current that we describe as mode-shift behaviour. To model voltage sensor gating behaviour at pH 6.5, we simply adjusted the backward rate for the relaxation transition, such that de-relaxation was accelerated (Table 4-4). Manipulating this rate in this way reproduced the effects of acidic pH on voltage sensor gating that we observed experimentally. There was little effect on on-gating behaviour, but off-gating was accelerated and there was a pronounced right-shift of the voltage-dependence of off-gating charge movement that resulted in reduction of mode-shift behaviour. While this may not be a unique solution and the slope factors of the model output are somewhat steeper, the model is able to emulate the observed voltage sensor behaviour and supports our conclusion that external protons destabilize the relaxed state of the voltage sensor leading to accelerated charge return.

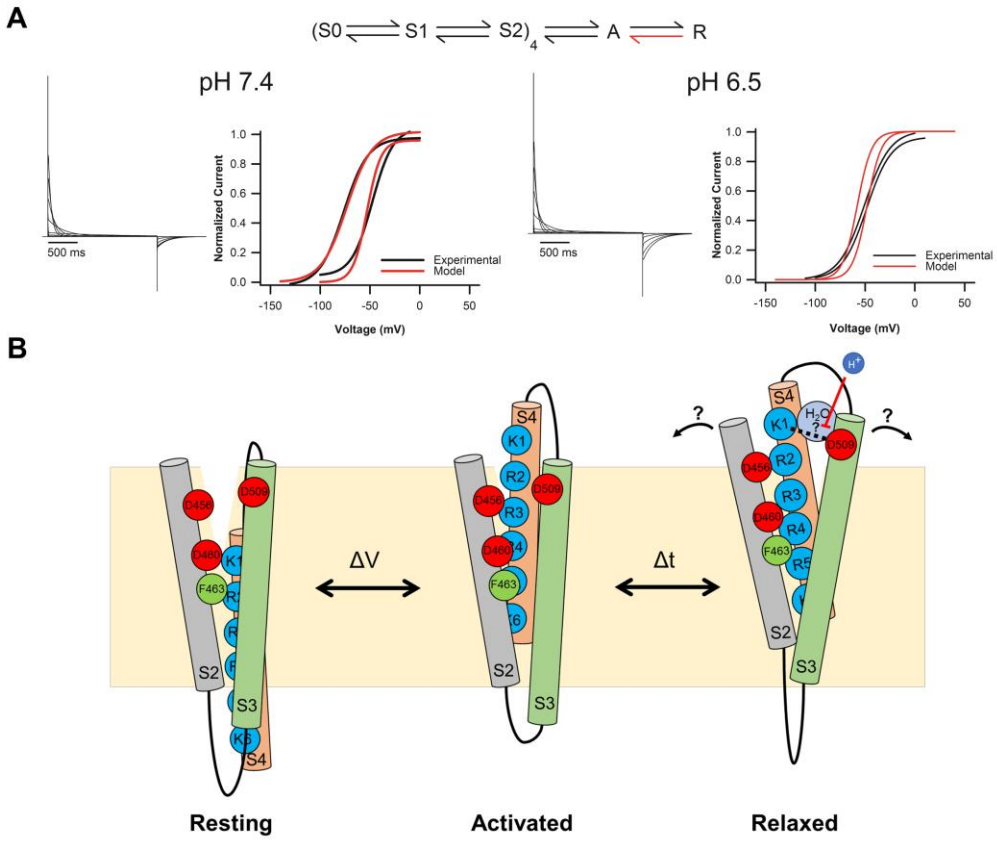

Figure 4.8 - Model of hERG voltage sensor relaxation.

A., Markov gating scheme used to model hERG voltage sensor gating at pH 7.4 and pH 6.5 (*top*). Details are provided in the test and transition rates are described in Table 4-4. The transition highlighted red represents that which was modified to simulate voltage sensor behaviour at pH 6.5. Simulated on-gating currents using the model along with predicted on- and off-gating currents are shown at *lower, left* for pH 7.4 and at *lower, right* for pH 6.5. Boltzmann fits yielded $V_{1/2}$ values of -52.8 mV and -73.0 mV for the Q_{on}-V and Q_{off}-V, respectively at pH 7.4 (mode-shift = 20.2 mV). At pH 6.5, equivalent values -47.9 mV and -54.7 mV (mode-shift = 6.8 mV). The salient features of gating currents at pH 6.5 could be modelled by accelerating the rate of de-relaxation. **B.,** Cartoon representation of proposed reconfigurations of S2, S3 and S4 voltage sensor transmembrane domains in the resting, activated and relaxed state. K1 and K6 refer to K525 and K538, respectively. R1-R5 describe R528-R537. Putative reconfigurations associated with entry into the relaxed state are shown, which may involve stabilizing interactions of D509 with outer S4 positive charges either directly, or via a water molecule network. Neutralization of D509, or external protonation is predicted to destabilize these interactions and consequently the relaxed state.

4.5.3 Site and mechanism of action of external protons

Numerous previous studies have attempted to define the site and mechanism of action of protons that determines the pH-induced acceleration of deactivation gating in hERG channels (Bérubé *et al.*, 1999; Bett & Rasmusson, 2003; Liu *et al.*, 2003; Zhang *et al.*, 2005; Piper *et al.*, 2008). We demonstrate in Figures 4.3 and 4.4 that protons specifically reduce the energetics of voltage sensor return, suggesting that the relaxed state of the voltage sensor is destabilized. Since protons are applied externally, these findings imply that the destabilization of the relaxed state is mediated by an external site that is associated with the voltage sensing unit. Previously, we, and others, have shown that more extreme acidification than used in the present study right-shifts the voltage-dependence of voltage sensor activation via protonation of acidic residues, D456, D460 and D509, in S2 and S3 (Kazmierczak *et al.*, 2013; Shi *et al.*, 2014). Cations, such as Ca^{2+}, Cd^{2+}, Mg^{2+}, Zn^{2+}, also coordinate with these sites, which form a discrete binding pocket (Ho *et al.*, 1998; Anumonwo *et al.*, 1999; Johnson *et al.*, 2001; Fernandez *et al.*, 2005; Abbruzzese *et al.*, 2010; Kazmierczak *et al.*, 2013; Shi *et al.*, 2014). Of the acidic charges forming the S2-S3 binding pocket, D509 was shown to have the greatest influence on the ability of protons to shift the voltage-dependence of hERG channel activation gating (Shi *et al.*, 2014), and therefore we focused attention on this site in the present study. The data in Figure 4.5 suggest that protonation at D509 modifies the stability of the relaxed state of the voltage sensor, since neutralization of this site largely abolished mode-shift of the voltage sensor by shifting the voltage-dependence of voltage sensor return. This destabilization of the relaxed voltage sensor is associated with accelerated closure of the pore gate as evidenced by the rapid ionic current deactivation (Figure 4.6), consistent with our conclusion that the stability of the relaxed voltage sensor contributes to hERG deactivation kinetics. We interpret these findings to suggest that titration of the native charge at D509 by external protons destabilizes the relaxed state of the voltage sensor, decreasing the energy barrier for deactivation and accelerating deactivation kinetics. Figure 4.8B shows a cartoon representation of how this might occur. This model, which depicts the hERG S2, S3 and S4 helices with putative interactions associated with transitions between resting, activated and relaxed states, is based upon a number of findings. The external acidic residues in S2 and S3 (D456, D460, D509) have previously been reported to be involved in stabilizing ionic interactions with S4 gating charges (Papazian *et al.*, 1995; Liu *et al.*, 2003; Zhang *et al.*, 2005; Piper *et al.*, 2008). For

example, double mutant cyclic analysis has shown energetic coupling between R531 and D456, D460, and D509, as well as D411 and D466, through a cooperative electrostatic interaction mechanism (Piper *et al.*, 2008), and accessibility studies have revealed that D460 and D509 increase the stability of the activated state (Liu *et al.*, 2003). For this reason the activated voltage sensing unit is depicted with R531 (R3) in close proximity with D456, D460 and D509, which themselves are closely positioned to form the cation binding pocket as shown in previous functional studies (Kazmierczak *et al.*, 2013; Shi *et al.*, 2014). In the model, K525 (K1) moves upon activation from a lipid embedded location to become exposed to the extracellular environment consistent with accessibility studies (Elliott *et al.*, 2009), and is in close proximity with the gating charge transfer centre residue, F463, with which it has been shown to form functional interactions that stabilize the resting state (Cheng *et al.*, 2013). Activation of the voltage sensing unit presumably involves S4 charges shuttling through the F463 gating charge transfer centre as has been suggested in *Shaker* (Tao *et al.*, 2010) with R537 (R5) and K538 (K6) aligning closely with F463 in the activated state, consistent with evidence suggesting functional interactions between the innermost basic charges and the phenylalanine that stabilize the activated state (Cheng *et al.*, 2013). Importantly, D509 occupies a position that is readily accessible to extracellular aqueous solvent as shown previously (Liu *et al.*, 2003). The model in Figure 4.8B also includes possible time-dependent, voltage-independent, transitions associated with stabilization of the voltage sensing unit into the relaxed state. Reconfigurations during this gating step are likely to be subtle given that they are not associated with charge translocation across the membrane and are not readily observable as environmental change in the report from fluorophores attached at the top of S4. We propose that relaxation in hERG channels could involve a widening of the cleft between the outer ends of the S2, S3 and S4 helices that either stabilizes interactions between D509 and S4 basic charges, such as R528 (R2), or enables D509 to form H-bonds or electrostatic interactions with water molecules within the water-filled crevice. In the latter case, this could establish a network of interactions that then bridge the acidic residue with positive residues in S4, similar to that described for external acidic charges in the Hv1 proton channel (Ramsey *et al.*, 2010; Rosa *et al.*, 2018). This possibility is consistent with the observation that the presence of water molecules in an aqueous extracellular crevice at the outer end of S4 influences the stability of the activated voltage sensor via interactions with S4 positive charges (Bezanilla, 2000; Swartz, 2008; Ramsey *et al.*, 2010; Islas, 2016). In the model, stabilization of these salt-bridge interactions or water molecule networks contributes to the

stability of the activated state of the hERG voltage sensor and precipitates entry of the sensor into the relaxed state. In this scenario, destabilization of these interactions by neutralization of D509, or by titration of the charge with external acidification, would disrupt this extracellular electrostatic network to destabilize the activated voltage sensor reducing the energetic barrier for its return to the resting state. Since only fractional charge return, perhaps a single S4 in the tetramer, appears to be required to close the pore gate (Thouta *et al.*, 2017) similar to that suggested in *Shaker* channels (Gagnon & Bezanilla, 2009), this would result in accelerated channel deactivation. This model thus establishes a working hypothesis of the mechanism underlying relaxation of the voltage sensor in hERG channels and how voltage sensor gating is influenced by external protons.

Refinement of high resolution structures of the hERG voltage sensor would contribute to confirming this working model, since the current cryo-EM structure (Wang & MacKinnon, 2017) possesses a disordered upper S3 helical structure that introduces uncertainty as to the position of D509. This could indicate that the upper S3 helix is highly dynamic, thus reducing the resolution, or alternatively that the resolved S3 structure is in some way perturbed, for example, has become partially unwound due to denaturing purification conditions. Further structural refinement may also aid our description of D509 as a proton sensor. For example, while the *pKa* for the side chain of D509 in free solution is 3.71, it is conceivable that the local environment may modify the *pKa* of D509, allowing protonation of the side chain at pH 6.5. Although extracellular histidine residues are the most likely candidates as proton sensors (*pKa* = 6.0), a previous study showed that mutation of the five histidine residues that are accessible to the extracellular environment to glutamine did not reduce the proton-induced acceleration of deactivation (Van Slyke *et al.*, 2012). We used ROSETTA to predict the *pKa* of the D509 side chain based on the cryo-EM hERG structure (Wang & MacKinnon, 2017) to evaluate whether the *pKa* might be influenced by the surrounding environment. However, this approach predicted values equivalent to an aspartate in free solution and is likely limited by the fact that D509 is located in a highly dynamic, or less well-ordered region in the available structures. Further structural information that includes, for example, D509 contributing to a cation binding pocket constructed by D456, D460 and D509 as has been shown previously in functional studies (Fernandez *et al.*, 2005; Kazmierczak *et al.*, 2013), may influence the predicted *pKa* of the aspartate due to tighter packing of the residue than is evident in the available cryo-EM structure. Such information could provide valuable insight to the role of D509 in stabilization of voltage sensor relaxation in hERG channels.

4.5.4 The stability of the relaxed state modulates deactivation kinetics in hERG channels

It is interesting to note that the *pKa* for the effect of external protons on deactivation gating (pH 7.0) that is mediated through D509 (Figure 4.2) is different to that which we reported previously for the acidic pH-induced shift in the voltage-dependence of activation (pH 5.4) that is mediated by the same site (Shi *et al.*, 2014). That D509 mediates both entry into the activated state and the stability of the relaxed state is, however, consistent with our conclusion that titration of D509 influences charge-charge interactions within the voltage sensing unit that are important for S4 gating. The differing pH-dependence suggests a greater sensitivity of the relaxed state to the charge on D509. This may be because the pH-sensitivity of the voltage-dependence of activation involves a complex interplay and coordination between D456, D460 and D509 in the cation binding pocket as channels transition into the open state (Piper *et al.*, 2008). Therefore, a higher degree of protonation at multiple sites may be required to alter the activation transition pathway (*pKa* = 5.4). This would support the observation that D509, together with coordination of D456 and D460, is involved in the activation gating of hERG channels (Shi *et al.*, 2014). In contrast, protonation of D509 alone was sufficient to destabilize the relaxed conformation of the voltage sensor. One explanation for this may be that relaxation occurs from the activated state when the stabilizing ionic interactions within the voltage sensing unit are exposed to the extracellular milieu and may be more readily protonated. Alternatively, it may be that the interaction(s) involving D509 are important when the voltage sensor is in the fully activated and/or relaxed state, and that D456, and D460 are important during the intermediate transitions along the activation pathway.

We propose that return of the voltage sensor from the relaxed state, i.e. de-relaxation, acts functionally as a “master-switch”, a previously used term (Liu *et al.*, 2003), that regulates deactivation gating. In this way, de-relaxation is the limiting step that allows return of the fraction of charge required to close the pore gate. We propose that mutations within the voltage sensing unit may accelerate deactivation gating by modifying the stability of the relaxed state of the voltage sensor, disrupting the extracellular water molecule network or salt bridge formations between S4 charges and their counter charges within the voltage sensing unit, or by modifying the electric field within which these interactions take place.

4.5.5 Destabilization of the relaxed state by external protons compromises hERG protective currents in response to premature stimulations

We show in Figure 4.7 that external protons alter the transient current passed by hERG channels in response to brief premature stimulations applied early in the refractory period. The transient repolarizing current through hERG channels that are still open due to slow deactivation is thought to contribute to the refractory period after an action potential by suppressing premature depolarization due to ectopic stimuli (Smith *et al.*, 1996; Yu Lu *et al.*, 2001; Perry *et al.*, 2016). As such, the transient hERG current has been suggested to suppress arrhythmias induced by afterdepolarizations (Yu Lu *et al.*, 2001; Du *et al.*, 2010). Given our observations that acidic pH accelerates hERG channel deactivation by destabilizing the relaxed state of the voltage sensor, we tested the hypothesis that extracellular acidic pH, e.g. pH 6.5, which may be encountered during myocardial ischemia (Yan & Kléber, 1992; Carmeliet *et al.*, 1999), might increase arrhythmogenesis by suppressing the protective current. Figure 4.7B shows that acidic pH reduced the peak protective current by 40 % and shifted the timing of the peak protective current to occur 20 ms earlier during repolarization. Markedly, acidic pH also hastened the decay of the repolarizing current with increasing coupling interval, suppressing the protective current at all diastolic intervals tested. These findings are consistent with in silico modelling studies, which predict decreased protective hERG current during early refractory (Du *et al.*, 2010) and strongly indicate that acidic pH reduces the protective current, which may increase the risk of early or delayed afterdepolarizations activity leading to ventricular arrhythmia.

4.5.6 An activator compound that slows deactivation kinetics rescues hERG protective currents

Since their initial discovery (Kang *et al.*, 2005), small molecule activators of hERG channels have received significant interest as potential therapeutics for the management of LQT syndrome type 2, which is caused by hERG channel dysfunction. An increasing number of hERG activator compounds have since been described and characterization of their action has resulted in the broad classification of activators into Type I (e.g. RPR260243), which slow deactivation (Perry *et al.*, 2010), and Type II (e.g. PD118057, NS1643), which attenuate inactivation by either shifting the voltage-dependence of

inactivation to more depolarized potential or slowing the onset of inactivation (Zhou, 2005; Xu *et al.*, 2008; Perry *et al.*, 2009; Su *et al.*, 2009). Other activators, that fall outside of this categorization, e.g. Mallotoxin, promote activation as their primary action (Zeng *et al.*, 2006; Vandenberg *et al.*, 2012). We reasoned that the suppression of protective hERG currents in response to premature stimulations caused by proton-induced destabilization of the relaxed voltage sensor and the consequent accelerated deactivation, might be rescued by the action of a Type I activator, such as RPR260243. We show in Figure 4.7A that by slowing deactivation gating, 10 μM RPR260243 provides robust enhancement of protective currents previously suppressed by acidic pH. This was evident as an enhanced peak protective current, as well as a dramatic enhancement of the protective current at longer diastolic intervals. These findings suggest that targeted slowing of hERG channel deactivation may offer a therapeutic avenue for enhancement of hERG channel function in LQTS2 and protection against arrhythmias. This is intuitive for LQTS2 cases caused by mutations that accelerate deactivation, e.g. R56Q (Chen *et al.*, 1999), but may have more broad applicability, since numerous LQTS2-associated trafficking deficient hERG mutations were recently shown to reduce the protective current once the trafficking issue was resolved (Perry *et al.*, 2016). Furthermore, this approach may mitigate some of the risk of hERG activator compounds by providing targeted enhancement of WT and mutant channel function in early refractory without significant shortening the action potential, as is often seen with Type II activators that modify inactivation gating. Further study in translational models could reveal the benefits of such a strategy to manage arrhythmia risk in LQTS2.

4.6 Supplementary Material

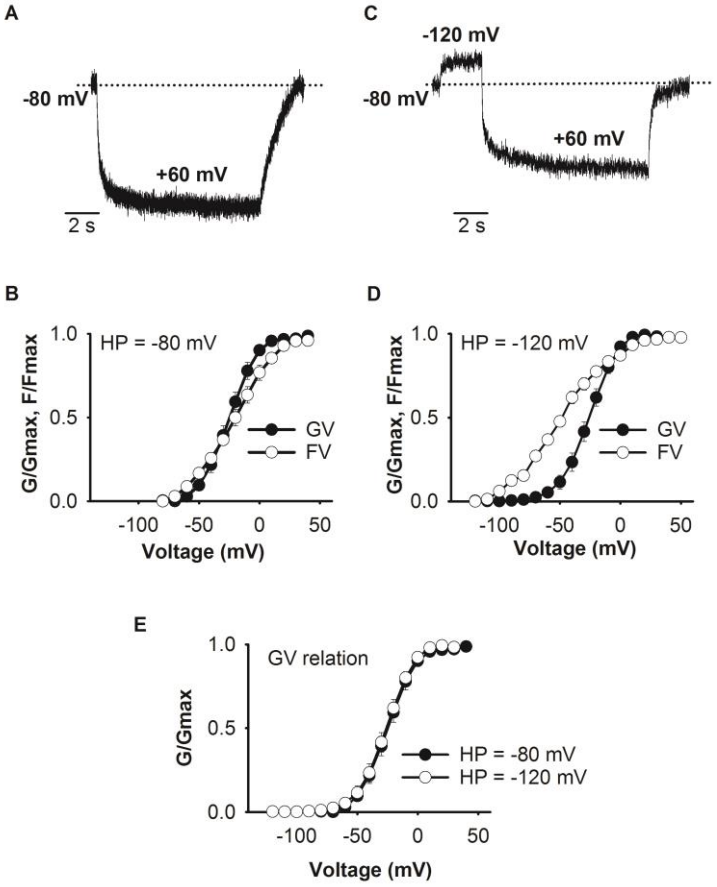

Figure S 4.1 - Use of a hyperpolarized holding potential allows capture of the full F-V relationship from TMRM labelling of L520C.

A., C. Typical fluorescence measurements recorded from TMRM attached at L520C in response to an 8 s depolarizing step to +60 mV from a holding potential (HP) of -80 mV (A), or following a 500 ms pre-pulse to -120 mV (C). **B., D.** F-V and G-V relationships recorded from data collected with a HP of -80 mV (B), or a pre-pulse to -120 mV (D). Boltzmann fits of the data from a HP of -80 mV yielded $V_{1/2}$ values for the F-V of -20.8 ± 0.6 (n = 4) mV and -29.5 mV ± 3.4 (n = 5) for the G-V. Following a pre-pulse to -120 mV, the $V_{1/2}$ of the F-V relationship was -44.9 ± 1.0 (n = 5) compared with -25.8 ± 2.1 (n = 2) for the G-V relationship. **E.** Holding potential had no effect on the G-V relationship. The -120 mV HP shifted the F-V relationship by -24 mV compared with a HP of -80 mV, and this precedes the G-V relationship by 19 mV, consistent with gating current measurements. Dotted line represent baseline.

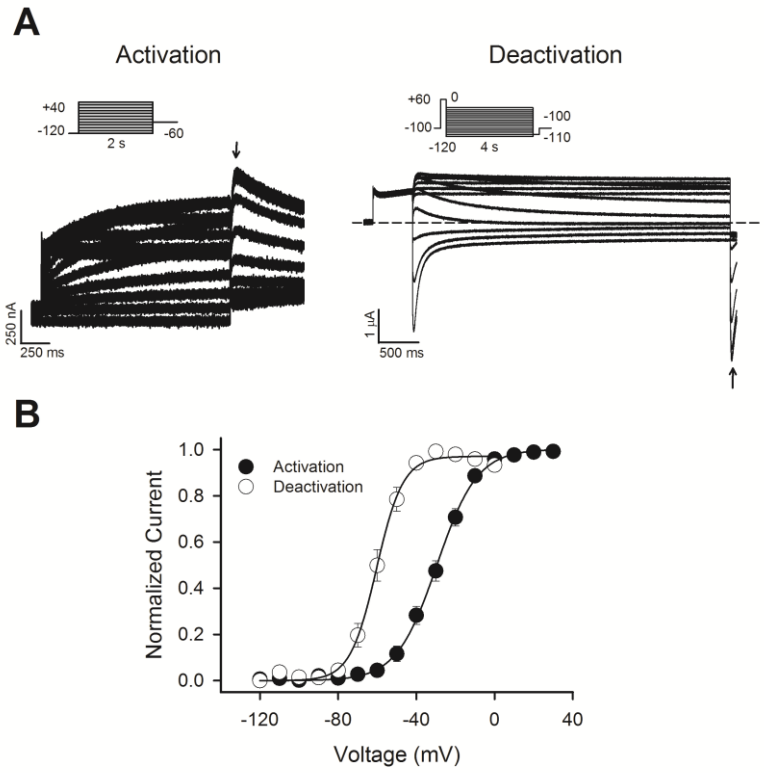

Figure S 4.2 - Ionic recordings of voltage-dependence of activation and deactivation in hERG L520C C-less construct.

A. Typical ionic recordings of activation and deactivation recorded with voltage protocol shown (inset) of hERG L520C C-less with 2 s activation duration and 4 s deactivation duration, consistent with durations measured in gating currents and fluorescence (Figure 3 and 4). Dotted line represents baseline and arrow marks where the ionic current measurements were made. **B.** Plot of the voltage-dependence of activation and deactivation fitted to a Boltzmann function. Activation $V_{1/2}$ and slope is -29.3 ± 1.8 mV and 10.2 ± 0.4 (n = 5), respectively. Deactivation $V_{1/2}$ and slope is -60.1 ± 2.0 and 6.6 ± 0.2 (n = 5).

Table S 4-1: Effect of holding potential on fluorescence-voltage and conductance-voltage relationship Boltzmann fit parameters.

	Activation G-V ***$V_{1/2}$ (mV)***	***k***	**F_{on}-V** ***$V_{1/2}$ (mV)***	***k***
L520C				
HP = -80 mV	-29.5 ± 3.4 (5)	14.0 ± 0.6	-20.8 ± 0.6 (4)	16.8 ± 0.5
HP = -120 mV	-25.8 ± 2.1 (2)	10.8 ± 0.2	-44.9 ± 1.0 (5)	22.3 ± 0.8

Data expressed in mean ± SEM, number of cells in parentheses

Chapter 5. Acidosis delays repolarization in optically mapped adult zebrafish whole hearts as a result of hERG channel inhibition

5.1 Overview

In the previous two chapters, I have presented data which indicate the site and mechanism responsible for the proton-induced shift in the voltage-dependence of activation and the acceleration of deactivation. Both of these effects of protons might be expected to cause a reduction in the overall hERG current and lead to a prolongation of the action potential and potentially arrhythmogenicity. Consistent with this, we have shown in Chapter 4 (Figure 4.7), that acidic pH reduces the hERG channel protective current passed in response to a premature stimulus, which mimics the occurrence of early afterdepolarizations (EADs) and delay afterdepolarizations (DAD). This is in close agreement with a previous report (Du *et al.*, 2010), and suggests that the hERG inhibition may be pro-arrhythmogenic. Du and colleagues incorporated the pH-induced reduction in hERG conductance, right-shift in voltage-dependence of activation and acceleration of deactivation and modeled the consequence of acidosis using the ten Tusscher *et al*. human ventricular cell model. The ten Tusscher *et al* cell model encapsulates major ion channel and transporter currents to simulate a human ventricular action potential (ten Tusscher, 2003). *In silico* experiments by Du et al predicted a lower peak repolarization current, which led to a slight prolongation of the APD_{90} by 9 ms. Next, they subjected the model to a paired stimuli experiment where a suprathreshold stimuli was applied to elicit a normal initiation of the AP, followed by application of a second, subthreshold, stimuli to simulate a premature stimulus such as that of a DAD. The model showed that at pH 7.4 the second stimulus did not elicit an action potential, however the same stimulus intensity initiated an action potential at pH 6.3 (Du *et al.*, 2010). The *in silico* data suggest that acidosis impairs the protective role of the hERG channel and increases the susceptibility of the cell to initiation of an AP by a premature stimulus, which supports the notion that acidosis is pro-arrhythmogenic (Du *et al.*, 2010). However, there are caveats to using the ten Tusscher model. One is that the experimental data used to constrain the model were collected from HEK, CHO, and/or *Xenopus* oocytes often at room temperature, but not from human cardiomyocytes at 37 ºC (ten Tusscher, 2003). Secondly, the I_{Kr} conductance is modeled to be considerably smaller compare to that of I_{Ks} current, placing relatively little

weight on I_{Kr} conductance. For example, setting the I_{Kr} conductance, in the model, to zero only prolongs the APD by ~50 ms whereas homozygous disruptions of hERG function is embryonic lethal. This may explain the small 9 ms prolongation of the ventricular APD observed at pH 6.3 in the model (Du *et al.*, 2010). Thirdly, the ten Tusscher is a mathematical model. Therefore, in this chapter, I used the zebrafish whole heart model to assess, experimentally, the pro-arrhythmogenic nature of external acidosis. As discussed in the introduction (Section 1.6), zebrafish hearts present a promising model to study electrophysiology due to their similarities to human cardiology. Combined with optical mapping techniques, which track the fluorescence of voltage-sensitive dyes, this allows us to capture the electrical activity of the whole heart organ to provide translational studies.

5.2 Introduction

The human *ether-à-go-go* related gene (hERG) channel conducts the rapid component of the delayed rectifier potassium (I_{kr}) current that contributes to the repolarization phase of the cardiac action potential. Mutations or drugs that cause a loss-of-function in hERG channels, reduce the repolarizing current, which leads to a prolongation of the action potential (AP) duration and can lead to congenital or acquired forms of long QT syndrome type 2 (LQT2). LQT2 can degenerate into Torsades de Pointes, a polymorphic ventricular tachycardia and ventricular fibrillation (Weiss *et al.*, 2010). The unique gating of the hERG channel underlies its important functional role in the cardiac AP. During depolarization the hERG channel activates slowly and rapidly inactivates, passing a small repolarizing current during the early phases of the AP. Following repolarization, the hERG channel rapidly recovers from inactivation and deactivates slowly, leading to a robust repolarizing current that returns the membrane back to rest (Sanguinetti *et al.*, 1995). Slow deactivation properties may also allow the hERG channel to continue passing repolarizing current during the resting phase of the AP. This is evident from experiments measuring hERG current in response to paired action potential waveform voltage-clamps, which show that hERG channels pass robust repolarizing current in response to a premature depolarizing stimulus. When applied at increasing coupling intervals following an action potential, these premature stimuli, which mimics that of EADs and DADs, produce transient hERG currents that initially increase with coupling interval to reach a peak protective current, and then decrease with further increases in the coupling interval. The increase in the transient hERG current follows the

time course of recovery from inactivation while the slow decrease in the current with increasing coupling interval follows the time course of slow deactivation. These observations suggest that hERG channels exhibit a protective role against afterdepolarizations; however, this has not been directly tested experimentally (Yu Lu *et al.*, 2001; Du *et al.*, 2010).

Myocardial ischemia is caused by a reduction of blood flow to cardiac muscle due to blockage in the arteries and leads to oxygen starvation. Prolonged ischemia can lead to irreversible damage of the heart leading to myocardial infarction. Myocardial infarction is a common coronary artery disease that affects over 3 million people worldwide. One of the major consequences of myocardial ischemia is extracellular acidosis, which is well recognized to inhibit the function of many ion channels, such as Nav1.5 (Jones *et al.*, 2011), Cav1.2 (Krafte & Kass, 1988), and hERG (Anumonwo *et al.*, 1999; Bérubé *et al.*, 1999; Jiang *et al.*, 1999; Terai *et al.*, 2000; Bett & Rasmusson, 2003; Du *et al.*, 2010, 2011*a*; Zhou & Bett, 2010; Van Slyke *et al.*, 2012; Shi *et al.*, 2014), and may provide a pro-arrhythmic substrate during ischemia. Extracellular acidosis has numerous effects on hERG channel gating processes such as reducing maximum conductance (Jo *et al.*, 1999; Van Slyke *et al.*, 2012), inducing a depolarized-shift in the voltage-dependence of activation (Jiang *et al.*, 1999; Bett & Rasmusson, 2003; Shi *et al.*, 2014), slowing activation (Zhou & Bett, 2010), and accelerating deactivation (Anumonwo *et al.*, 1999; Jiang *et al.*, 1999; Bett & Rasmusson, 2003). These effects would be predicted to lead to a reduction in the hERG repolarizing current and prolong the AP duration. It was observed in isolated rabbit hearts that following the onset of ischemia, the ventricular action potential exhibits an initial prolongation of the AP duration followed by a subsequent shortening (Bethell *et al.*, 1998). The shortening of the APD is thought to be a primary determinant of arrhythmogenesis during ischemia (Janse & Wit, 1989), and is likely due to a combination of accumulation of K^+ ions in the extracellular space (Carmeliet *et al.*, 1999), and increasing efflux of K^+ via activation of K_{ATP} channels due to a drop in the $[ATP]_i$ during ischemia (Noma, 1983). The significance of the brief initial prolongation of the APD has been given less attention. The increased APD has been suggested to be a result of acidosis (Watanabe *et al.*, 1997), and may be due to inhibition of I_{to}, however this has not been directly measured (Verkerk *et al.*, 1996). Interestingly, the biphasic change in the timing of repolarization was observed in a clinical study in 74 patients (Kenigsberg *et al.*, 2007). Following balloon inflation to occlude blood flow, which mimics ischemia, 100% of

the subjects showed acute (within the first 1 min of ischemia) prolongation of the Q-T interval, a measure of APD repolarization timing. Moreover, these effects on repolarization were observed to be readily reversible. These findings suggest that the initial APD prolongation caused by ischeia is due to reduced repolarization, which may be pro-arrhythmogenic (Kenigsberg *et al.*, 2007). Futhermore, the rapid onset and recovery of repolarization changes are consistent with effects mediated by changes in extracelllar pH, which is known to fall rapidly during ischemia. Given that external acidosis reduces hERG channel function and leads to a prolongation of the cardiac AP, we hypothesized that the initial prolongation of the Q-T interval (delayed repolarization), may be the result of reduction in hERG channel current. This would lead to increased susceptibility to EADs and DADs, which can trigger arrhythmias.

Zebrafish (*Danio rerio*) are ectothermic tropical fresh water teleosts, which have emerged as a popular cost-effective model to study human cardiology. This is in part due to the similarities in the electrical activity in the zebrafish heart compared to that of human. The adult zebrafish intrinsic heart rate is 120-180 beats per minute (bpm) (Nemtsas *et al.*, 2010), similar to that of human of 60-100. At 28 ºC the Q-T interval in zebrafish hearts is around 200-290 ms, which is also similar to that of human of 300-450 ms (Leong *et al.*, 2010*a*; Poon & Brand, 2013; Lin *et al.*, 2014). Zebrafish ventricular APD_{90} (APD at 90% repolarization) at 28 ºC is approximately 132 ms, which is shorter than that of human (242 ms), but much longer than that of mouse (82 ms) (Nemtsas *et al.*, 2010). Most importantly, the major repolarizing current in the zebrafish ventricular AP is the I_{kr} current, conducted by zERG channels, with little contribution from I_{ks} (Nemtsas *et al.*, 2010). This makes zebrafish hearts a particularly good model to study the impacts of altered hERG function on cardiac repolarization. In this study, we used optical mapping to observe zebrafish action potential changes in intact ex vivo whole hearts when subjected to acute external acidosis. Our optical mapping takes advantage of the voltage-sensitivity of the fluorescence emission of lipophilic dye, RH 237. RH 237 is excited by a 530 nm light source and emits at 710 nm. Changes in membrane voltage induce a rapid conformational change to the dye and cause a blue shift in the emission spectrum that results in a decrease in the fluorescence intensity proportional to the voltage change. Using the fluorescence emission changes of RH 237 to report electrical activity in the heart, we observed robust intrinsic ventricular APs that displayed rate dependent shortening. Upon application of acute external acidosis, we observed prolongation of the action potential

duration, consistent with a reduction in the repolarization current. The acidosis-induced prolongation of the AP was readily reversible with a rapid onset and recovery suggesting an extracellular effect and was greatly attenuated in the presence of the hERG specific blocker, dofetilide, suggesting that the majority of the acidosis-induced prolongation in the zebrafish AP is due to an impairment of the zERG current. These changes in zERG function as a result of acute acidosis resulted in increased arrhythmogenicity. Triangulation (APD_{30} – APD_{90}), which strongly associates with development of ventricular tachyarrhythmia (Milberg *et al.*, 2007) was increased at pH 6.5. Acute external acidosis also reduced rate adaptation of the zebrafish AP by flattening the restitution curve, which strongly suggests that the effect of acidosis on zERG channels is pro-arrhythmogenic.

5.3 Material and Methods

5.3.1 Zebrafish husbandry

Adult zebrafish (*Danio rerio*) were purchased from a local supplier and housed at 28 ºC, in accordance with the principles established by the Canadian Council on Animal Care and approved by the Simon Fraser University Animal Care Committee. Zebrafish were fed daily with processed food.

5.3.2 Heart Isolation and reagents

Mature zebrafish (~40 mm in length) were euthanized in an ice bath followed by decapitation. Hearts were extracted and isolated as described previously (Lin *et al.*, 2015) at room temperature in calcium Tyrode's solution (containing (in mM): 117 NaCl, 5.7 KCl, 4.4 $NaHCO_3$, 1.5 NaH_2PO_4-H_2O, 1.7 $MgCl_2$, 10 Na-HEPES, 5 glucose, 5 creatine, 5 Na-pyruvic acid, 1.8 $CaCl_2$, titrated to pH 7.3 with HCl, and vacuum filtered. Following isolation, hearts were cannulated on an 8 mm 34-gauge ultrafine cannula (World Precision Instruments, Sarasota, FL) by inserting the cannula through the bulbus arteriosus and into the ventricle and securing the heart to the cannula by a surgical knot.

10 mM blebbistatin (Sigma-Aldrich, Oakville, ON, Canada) and RH 237 (Life Technologies, Burlington, ON, Canada) stocks were made by diluting with DMSO and were kept at 4 ºC in the dark. These reagents were diluted in calcium Tyrode's solution to a final working concentration of 10 µM for both blebbistatin and RH 237. Cannulated hearts

were first labeled with 10 µM RH 237 for 30 min at room temperature, and then with 10 µM blebbistatin for 1h prior to recording.

5.3.3 Optical Mapping

Cannulated hearts were suspended in a custom-built imaging chamber containing 1.75 ml calcium Tyrode's solution supplemented with 10 µM blebbistatin to ensure motion suppression as previously described (Lin *et al.*, 2015). A Peltier device (HP-199-1.4-0.8P, TE Technology, Traverse City, MI) was used to maintain the temperature of the imaging chamber. A PID temperature controller (TC-36-25 RS232; TE Technology, Traverse City, MI) was implemented to compare the command temperature with the temperature in the imaging chamber and rapidly adjust the size and direction of a DC current into the Peltier device until the desired temperature is reached in the imaging chamber (Lin *et al.*, 2015). All experiments were conducted with the imaging chamber controlled recorded at 28 ºC.

Excitation of RH 237 labeled hearts was achieved by a 350 mW 530 nm LED module (Thorlabs) through a 630 nm long-pass dichroic mirror (XF2021, 630 DRLP, Omega Optical, Brattleboro, VT). The fluorescence emission was collected by reflection from the 630 nm long-pass dichroic and filtered through a 700 nm long-pass filter (Omega 700LP). Fluorescence emission decreased in intensity with increasing membrane depolarization, thus producing a voltage-dependent emission signal. The fluorescence signal was imaged by a GE680 CCD camera (Allied Vision Technologies, Burnaby, BC, Canada) with a maxmimum acquisition rate of 205 frames per second (fps). Prior to experiments, RH 237 labeling was assessed in each heart to ensure adequate loading by directly measuring the RH 237 intensity and hearts were re-labeled if necessary. At the same time, the base line intrinsic heart rate was assessed. Field stimulation was applied using a pair of 1.0 mm Tungston electrodes, one on each side of the heart inserted and fixed in the imaging chamber. The large diameter of the electrode ensured that the whole zebrafish heart was subjected to a uniform electrical field. Custom software allowed adjustment of the voltage stimulus intensity, timing, and duration along with acquisition of RH 237 fluorescence emission. The 1.75 ml of pH 7.3 Ca^{2+} Tyrode solution was replaced by pH 6.5 Ca^{2+} Tyrode solution in the imaging chamber via the suction/injection port of the chamber to rapidly alter the pH. Dofetilide was made in Ca^{2+} Tyrode solution and added into the imaging chamber to achieve 250 nM in 1.75 mL of Ca^{2+} Tyrode solution via the injection port.

To measure the electrical restitution curve (ERC) in the zebrafish optical mapping set up, we designed a variable rate stimulation protocol that commands the firing of a series of stimuli at a given voltage with decreasing beat-to-beat interval or increasing heart rate from 60 bpm up to 300 bpm (Figure 5.5A). Each interval is repeated twice to allow accommodation of APD. The voltage of this stimuli was adjusted to ensure that every stimulus initiated a firing of the action potential at pH 7.4. This protocol aims to simulate a progressive increase in heart rate, by decreasing the beat-to-beat interval.

5.3.3.1 Data Analysis

Data were analyzed by custom-built software in the IDL environment (Exelis Visual Information Solutions, McLean, VA). A region of interest (ROI) was manually selected outlining the atrium and/or the ventricle, which yields an ensemble of action potential (AP) cycles within a 2000 frame acquisition window (9.75 s) recorded at a frame rate per second (fps) of 205. Individual AP cycles within an ensemble are peak detected automatically and averaged spatially, and temporally to increase signal-to-noise ratio to yield a single, averaged representative AP. Spatial averaging takes the average of all the pixels within the area of the ROI per recording. Large ROI that covers majority of the atria and ventricle allows spatial averaging of larger number of pixels, reducing the noise and increasing the voltage intensity. This yields a smoother and less noisy AP signal. Temporal averaging first detects the peak of each individual AP within an ensemble, followed by normalizing the voltage signal of all the individual AP to 1, then lastly aligning the peaks (Lin *et al.*, 2014). Baseline normalization was applied to control for photobleaching during the acquisition. This is possible due to the robust voltage signal that RH 237 produces during depolarization. To increase accuracy and reduce noise in the averaged, representative AP, the recording window was adjusted to capture an ensemble of at least 8-10 AP cycles. In some cases where the intrinsic heart rate was low, 4000 acquisition frames were used (~19 s) to ensure at least 8-10 AP cycles were recorded. The software measures the number of frames for the voltage signal to drop from peak to 30%, 50%, 75%, and 90% and this was used to calculate the APD_{30}, APD_{50}, APD_{75}, and APD_{90}. From here, triangulation can be calculated as the difference between APD_{30} and APD_{90} at pH 7.4 and compare it with pH 6.5. The same approach was used to determine the APD in the variable rate stimulation protocol at each interval. Statistical comparisons between means were conducted using a two-tailed Student's t-test, with $P < 0.05$ taken as an indicator for statistical significance.

5.4 Results

5.4.1 External acidosis prolonged the action potential duration in adult zebrafish hearts.

The first goal was to characterize the effect of external acidosis on action potentials recorded from the zebrafish whole hearts labeled with RH 237. Figure 5.1A shows typical labeling intensity of RH 237 in the zebrafish heart. The red regions represent strong labeling of RH 237 whereas blue regions represent weaker labeling. The ROIs were manually drawn to encompass both the atrial and the ventricular regions. Setting ROIs in this way yields ensembles of AP cycles such as those shown in Figure 5.1B, where the orange is the signal from the atria and the brown is the ventricle. The patch of high intensity RH 237 labeling in the ventricle give rise to a robust and low noise ventricular AP signal. The atrial AP signal has a lower signal-to-noise ratio compared to that of ventricular AP, because strong atrial labeling can be difficult to achieve due to the lack of rigid structure of the zebrafish atria and weaker labeling can lead to a more noisy signal. At pH 7.4 the intrinsic pacing of the atria and ventricle AP were uniform and exhibited an atrial-ventricular delay (AV delay) (Figure 5.1C), that resembles the AV delay in humans. This AV delay represents the conduction of the electrical signal from the atrial tissue via the AV node to the triggering of the AP in the ventricle.

At pH 6.5, there were dramatic changes in the AP in both the atria and the ventricle recoded (Figure 5.1B). Firstly, the intrinsic pacing was slowed indicating that the heart rate significantly dropped. Second, the pacing became irregular and exhibited formation of doublets. Lastly, the atrial and ventricular AP was prolonged, with significant prolongation observed in the ventricle as observed in Figure 5.1C. Interestingly, the AV delay remained similar to that at pH 7.4. The prolongation of the atrial and ventricular AP, which is more pronounced in the ventricle where I_{Kr} is the predominant repolarization current, is consistent with our hypothesis that the external acidosis inhibits the zERG potassium channel in the zebrafish ventricle.

We explored this further by observing the extent of prolongation of the ventricular APD at different time intervals following the application of acidosis. Figure 5.1D shows average representative ventricular APs constructed from ensembles of AP cycles recorded at pH 6.5 with increasing incubation time. Within the first minute of incubation at

pH 6.5, the ventricular APD was significantly prolonged from 131 ± 8.5 ms at pH 7.4 to 197 ± 10.8 ms (*P* = 0.02, n = 3). After 10 mins, the ventricular APD prolongation saturated at 218 ± 9.8 ms (n = 3) with no further prolongation at 20 mins (APD was 229 ms) (Figure 5.1E). These data suggest that the onset for the effect of external acidosis on APD is rapid and likely indicates an extracellular effect since internal pH is unlikely to be altered within the first minute.

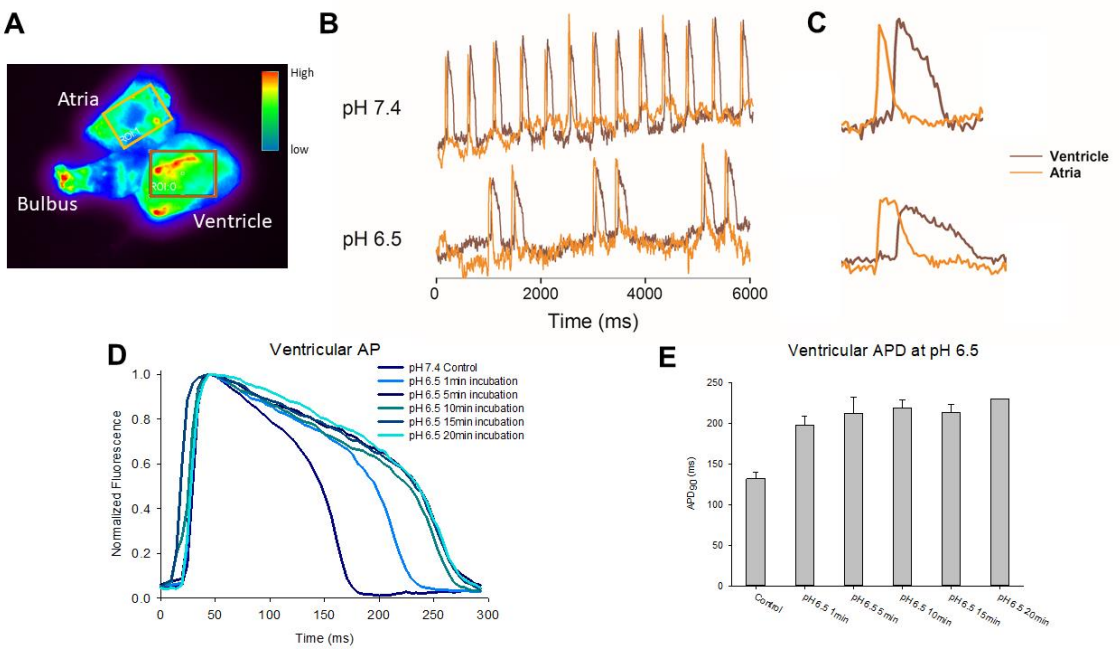

Figure 5.1 - External acidosis prolonged the ventricular AP.

A. RH 237 labeling of the zebrafish whole heart. Red regions represent high intensity of RH 237 signal while blue regions represent low intensity. ROIs were manually drawn and included the atria and ventricle to yield the ensemble of AP cycles in **B,** acquired with 1500 frames at 205 fps**.** At pH 6.5, the heart rate slowed, doublets formed and the atria and ventricle APD was prolonged. **C.** Individual atrial and ventricular AP was compared at pH 7.4 and 6.5 taken from measurements in B. At low pH both atrial and ventricular Aps were prolonged, but the AV delay was not different from that at pH 7.4. **D, E.** Averaged representative ventricular APs at various incubation durations with pH 6.5. The prolongation of the ventricular APD at pH 6.5 occurs within 1 min and saturates at 5-10 mins with no further prolongation at 20 min (n = 3). This suggests a rapid, and likely an extracellular effect.

5.4.2 The effect of acidosis on the ventricular APD is acute and extracellular.

Kenigsberg et al found that within the first minute of onset of ischemia (induced by elective percutaneous coronary balloon angioplasty procedure), all 74 patients showed prolongation of the QT interval (Kenigsberg *et al.*, 2007). This rapid prolongation of the QT interval coincides well with our observed rapid onset of the effect of external acidosis on the zebrafish ventricular APD. Since functional studies have shown that inhibition of the repolarization current is by extracellular acidosis and not intracellular acidosis, we focused attention on the first minute of the onset of acidosis to assess whether inhibition of repolarization is the major contributor.

In Figure 5.2A, we exposed the zebrafish hearts to acidosis (pH 6.5) for 1 min and 5 mins and measured the ventricular AP. Within the first minute, the intrinsic heart rate remained unchanged from that at pH 7.4, with slowing occurring only after 5 mins. This suggests that acidosis-induced slowing of the heart rate occurs more slowly than the effect on APD and may involve the acidification of internal pH. Slowed pacing and the doublet formation observed in Figure 5.1B suggests that pacemaking at the sino-atrial node (SAN) may be inhibited by more prolonged exposure to external acidosis. Functional studies have shown that HCN2 channels are inhibited by internal, but not external acidosis (Zong *et al.*, 2001). This would suggest that after 5-10 min incubation at external pH 6.5, the internal pH in the SAN may have become acidic. During the first minute of external acidosis, however, heart rate did not change and the biggest change was the prolongation of the ventricular APD, which was readily reversible (Figure 2.5B). Figure 5.2C shows a plot of the APD at different repolarization phases (APD_{30}, APD_{50}, APD_{75}, and APD_{90}) at pH 7.4 and at 1 min following acidosis. External acidosis prolonged APD_{30} by 21.1 ± 8.6 ms (from 47.6 ± 7 ms to 68.7 ± 5 ms (P = 0.0003)), APD_{50} by 44.6 ± 14.8 ms (from 109.9 ± 7 ms to 154.5 ± 13 ms (P = 0.002)), APD_{75} by 49.3 ± 13.4 ms (from 130.3 ± 6 ms to 179.6 ± 12 ms (P = 0.002)), and APD_{90} by 65.2 ± 13.9 ms (from 148.8 ± 5 ms to 214.0 ± 13 ms (P = 0.004, n = 5). P-values were calculated by two-ways ANOVA with the Tukey HSD test, where the mean APD_{30}, APD_{50}, APD_{75}, and APD_{90} (n = 5) were compared at pH 7.4 to that at pH 6.5. All of these effects were readily reversed following restoration of pH 7.4. These data show that external acidosis prolonged all phases of repolarization within 1 min, but that the largest prolongation was observed at APD_{75} and APD_{90}. This finding suggests an inhibition of the latter phase of repolarization, consistent with an effect on zERG channel.

The difference in the acidosis-induced prolongation of APD_{30} and APD_{90} indicates an increase in AP triangulation (repolarization time between APD_{30} and APD_{90}). An increase in triangulation, especially a prolongation of the late phase of repolarization, has been shown to strongly associate with development of TdP (Hondeghem *et al.*, 2001*a*, 2001*b*), because the prolongation of the late phase of repolarization increases the susceptibility of generating EADs from reactivating calcium and/or sodium channels. Figure 5.3A shows an averaged, representative AP at pH 7.4 and pH 6.5 (*top*), and a box plot of the APD_{30} and APD_{90} for pH 7.4 and pH 6.5 (*left* and *right*, respectively). The difference between the APD_{30} and APD_{90} (APD_{90} – APD_{30}) at each pH is plotted in Figure 5.3B. At pH 7.4, the triangulation (APD_{90} - APD_{30}) was 101.2 ± 7.6 ms, and this was significantly increased to 145.4 ± 8.6 ms at pH 6.5 (P = 0.02, calculated from paired two-tailed Student's t-test comparing the mean triangulation at pH 7.4 and pH 6.5). These data show that there is a significant increase in triangulation of 44.1 ± 11 ms induced by 1 min incubation at pH 6.5 (Figure 5.3B).

The increase in triangulation suggests that the major contributor to the acidosis-induced prolongation of the ventricular APD is a reduction in repolarization, which in zebrafish, is driven by the I_{Kr} current. Furthermore, the rapid onset of prolongation of the ventricular APD at pH 6.5, which can be rapidly reversed upon wash off (Figure 5.2B), provides strong evidence for an extracellular effect, which is consistent with biophysical studies showing that acidosis-induced inhibition of hERG channels is mediated by extracellular rather than intracellular protons (Ho *et al.*, 1998; Jo *et al.*, 1999; Vereecke & Carmeliet, 2000; Bett & Rasmusson, 2003; Van Slyke *et al.*, 2012; Shi *et al.*, 2014).

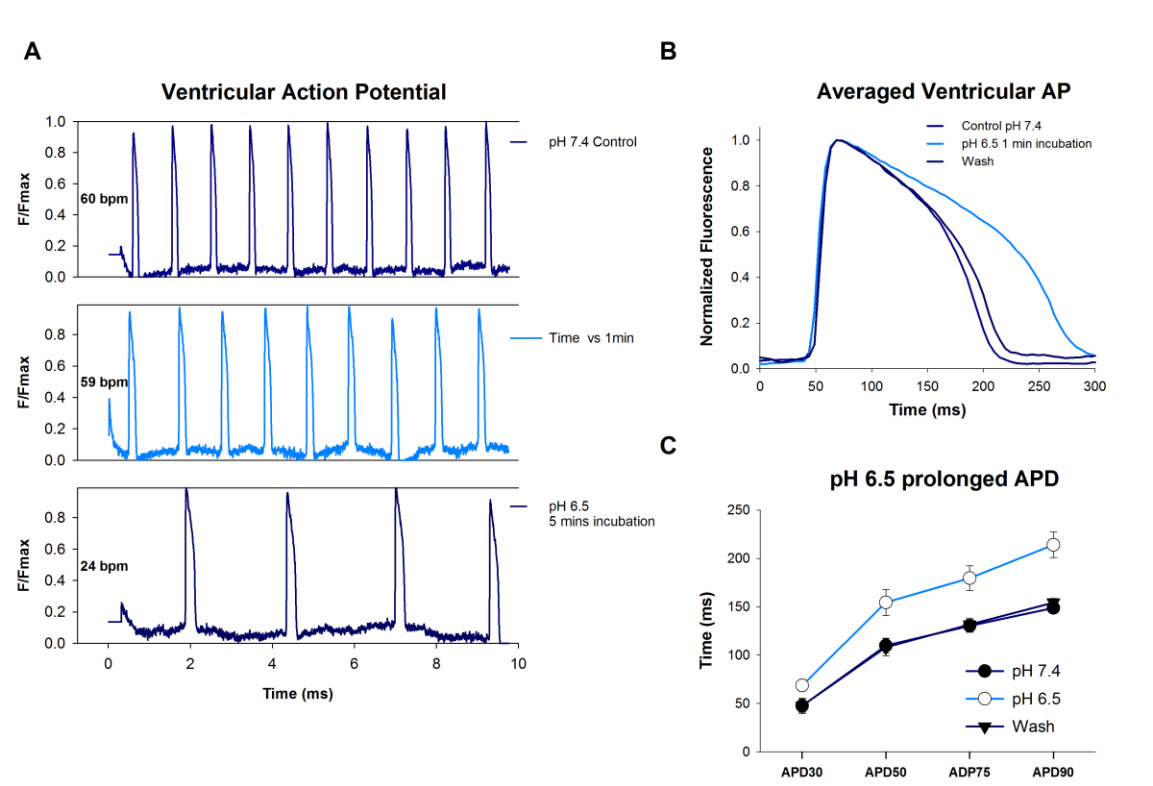

Figure 5.2 - External acidosis acts extracellularly to prolong the ventricular AP.

A. Representative recordings of an ensemble of AP cycles acquired at 2000 frames with 205 fps. With 1 min incubation at pH 6.5, there was little change in the heart rate, while incubation at 5 mins at pH 6.5 drastically reduced the heart rate to 24 bpm (from 60 bpm at pH 7.4). **B.** Plot of the averaged, representative ventricular AP that shows the rapid onset and washoff of the change in APD with pH 6.5, strongly suggesting an extracellular effect. **C.** Plot of the ventricular APD at various phases of repolarization at pH 7.4, incubated within the first minute at pH 6.5, and during washoff. The prolongation of APD_{30} was 21.1 ± 8.6 ms from 47.6 ± 7 ms to 68.7 ± 5 ms (P = 0.0003), APD_{50} was 44.6 ± 14.8 ms from 109.9 ± 7 ms to 154.5 ± 13 ms (P = 0.002), APD_{75} was 49.3 ± 13.4 ms from 130.3 ± 6 ms to 179.6 ± 12 ms (P = 0.002), and APD_{90} was 65.2 ± 13.9 ms from 148.8 ± 5 ms to 214.0 ± 13 ms (P = 0.004) (n = 5, paired). The largest prolongation was seen at APD_{75} and APD_{90}, which suggests that majority of the prolongation by external acidosis was by inhibition of the I_{Kr} current.

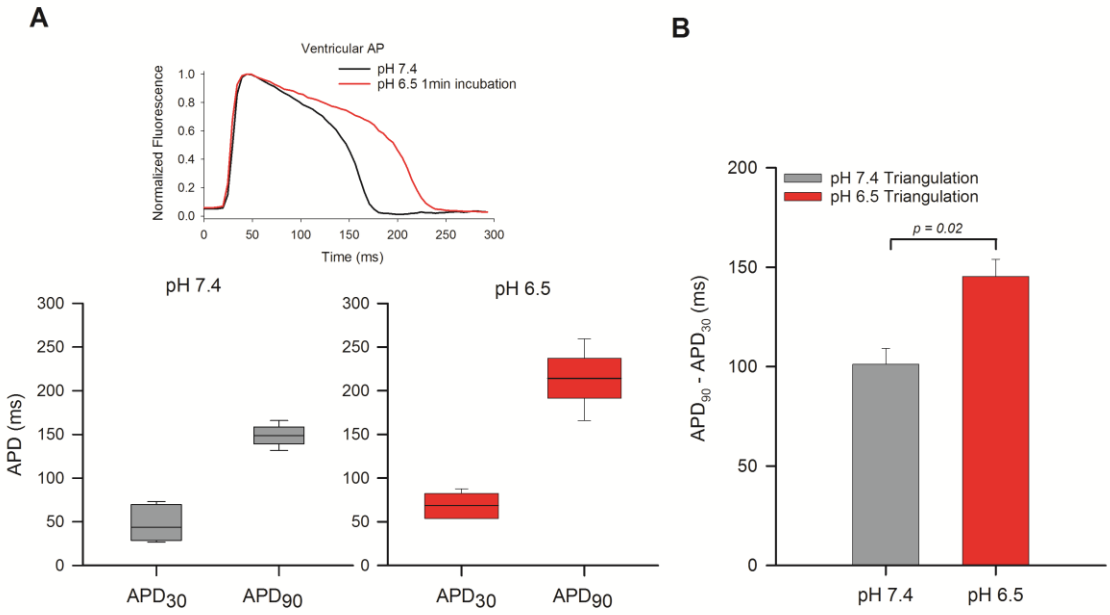

Figure 5.3 - Acidosis increases triangulation of the ventricular AP.

A. Typical average ventricular APs recorded at pH 7.4 and following 1 min application of pH 6.5 solution. Box plots of the APD_{30} and APD_{90} at pH 7.4 and pH 6.5 showing the maximum, upper quartile, medium, lower quartile, and minimum. 1 min of incubation at pH 6.5 prolonged the ventricular action potential at all phases of repolarization, however, the prolongation was greater at APD_{90} than at APD_{30}. At pH 7.4 APD_{30} was 47.6 ± 7 ms, and APD_{90} was 148.8 ± 5 ms. At pH 6.5 the APD_{30} was 68.7 ± 5 ms, and APD_{90} was 214.0 ± 13 ms (n = 5, paired two-tailed Student's t-test). **B.** At pH 6.5, AP triangulation was increased by 44.1 ± 11 ms. AP triangulation is calculated as APD_{90} - APD_{30}. Increase in triangulation is a strong proarrhythmogenic marker for increase susceptibility to Torsades de Pointes (Hondeghem *et al.*, 2001*a*, 2001*b*; Milberg *et al.*, 2007).

5.4.3 The presence of dofetilide greatly reduced the prolongation of the ventricular APD by external acidosis.

To further test the idea that the prolongation of the APD induced by external acidosis is due to an inhibition of the I_{Kr} current, conducted by zERG potassium channels, we analyzed the pH-induced prolongation in the presence of an I_{Kr} specific blocker, dofetilide. Dofetilide is a well-known high affinity open channel blocker of the hERG potassium channel (Ficker 1998, Synder 1996). Here, our aim was to use dofetilide to block available zERG channels and reduce the repolarizing I_{kr} current. If external acidosis exerts its effect via zERG channels there would be reduced prolongation of the ventricular APD as most of the zERG channels are blocked. However, on the contrary, if external acidosis mainly affects other ion channels, then an additive effect where additional prolongation of the APD would be expected.

The first experiment was to assess the effect of dofetilide alone. Figure 5.4A shows representative ventricular APs from hearts during control (pH 7.4) conditions and following incubation with 250 nM dofetilide for varying durations. Figure 5.4B plots the prolongation of the ventricular APD in response to incubation of dofetilide at different phases of repolarization (APD_{30}, APD_{50}, APD_{75}, and APD_{90}). 250 nM dofetilide prolonged the ventricular APD at all phases of repolarization and the effect saturated at 30-45 mins incubation.

Having established that selective block of zERG channels by dofetilide prolongs the zebrafish ventricular APD, for the next set of experiments zebrafish hearts were first incubated with 250 nM dofetilide for 60 min to ensure steady-state dofetilide effect, and then the extracellular pH was changed to pH 6.5. Figure 5.4C shows representative ventricular APs recorded during such an experiment. The 60 min incubation with dofetilide prolonged the APD, as expected. However, changing the extracellular solution to pH 6.5 in the presence of dofetilide only caused a small further prolongation of the APD. Figure 5.4D shows a closer examination of the APD prolongation at various phases of repolarization in the presence of dofetilide. For all phases of repolarization, dofetilide caused a significant prolongation of the ventricular APD ($P < 0.05$). *P*-values were calculated by two-way ANOVA Tukey HSD post hoc test. However, more prolongation is seen at APD_{50}, APD_{75}, and APD_{90} compared to that of APD_{30}. Interestingly, in the presence of dofetilide, changing the extracellular solution to pH 6.5 showed no further prolongation

of the APD in all phases of repolarization ($P > 0.05$, two-way ANOVA Tukey HSD). Figure 5.4E compares the percentage of ventricular APD prolongation by pH 6.5 in the absence and presence of 250 nM dofetilide. The prolongation of the APD by pH 6.5 is dramatically reduced in the presence of dofetilide at all phases of repolarization. The percentage of APD prolongation was reduced from 21.1% to 1% at APD_{30}, from 44.5% to 14.7% at APD_{50}, from 49.3% to 17.8% at APD_{75}, and from 65.3% to 2.4% at APD_{90} (n = 5). These results strongly suggest a competitive effect between dofetilide and protons and that both prolong the APD in zebrafish whole hearts by inhibition of the zERG potassium channel.

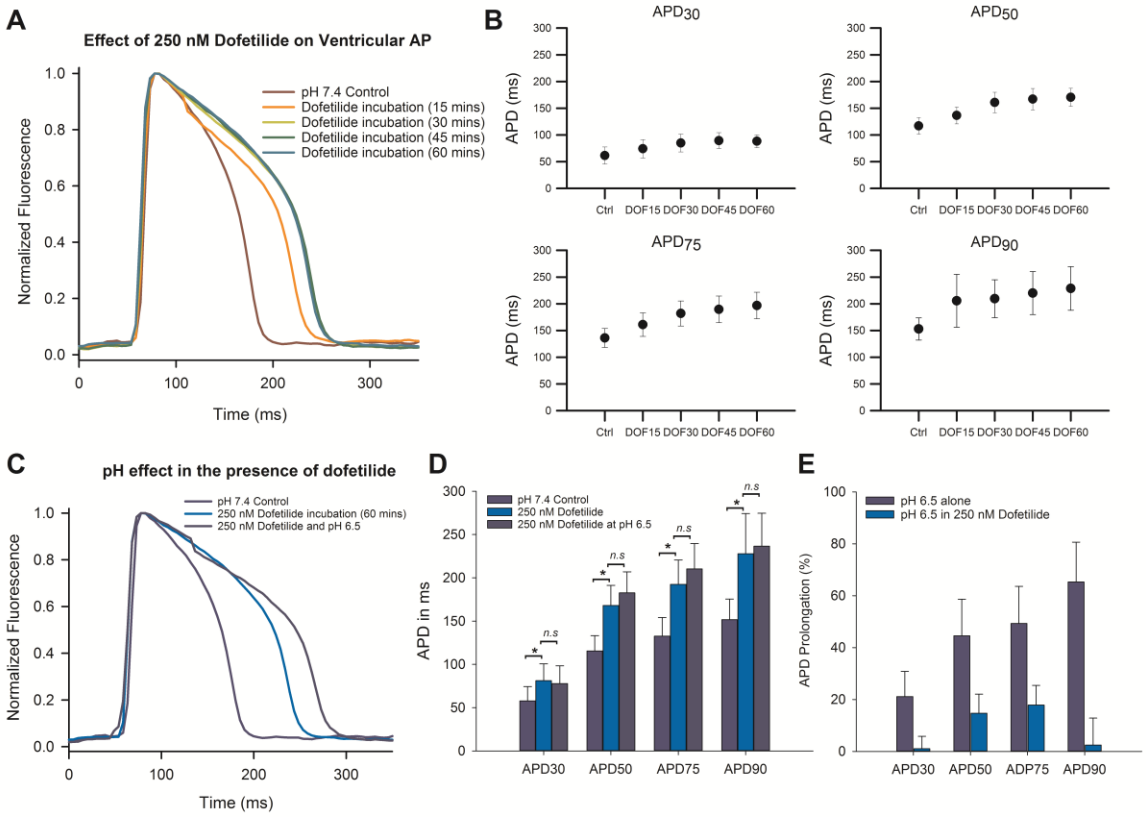

Figure 5.4 – Dofetilide block of I_{Kr} attenuates the effect of external acidosis in the ventricular APD.

A. Averaged, representative ventricular APs recorded from hearts in the absence and presence of 250 nM dofetilide. The prolongation of the APD by dofetilide saturated between 30-45 minutes of incubations. Dofetilide prolonged the APD at all phases of repolarization with increased incubation time plotted in **B. C.** Averaged, representative ventricular APs in the absence of dofetilide, with dofetilide at pH 7.4 and pH 6.5 following dofetilide block. Acidosis produces only a modest further prolongation of the APD in the presence of zERG block by dofetilide. **D**. Plot of APD prolongation by dofetilide and pH 6.5 in the presence of dofetilide at various phases of repolarization showing that dofetilide alone significantly prolonged the APD ($P < 0.05$, indicated by the asterisks), while there is no significant further prolongation by pH 6.5 ($P > 0.05$, indicated by the *n.s*). **E.** Plot of the comparison in the percentage of APD prolongation between pH 6.5 alone, and pH 6.5 in the presence of dofetilide. At APD_{30}, the % of APD prolongation was reduced from 21.1% to 1%, at APD_{50}, it was reduced from 44.5% to 14.7%, at APD_{75}, it was reduced from 49.3% to 17.8%, and at APD_{90}, it was reduced from 65.3% to 2.4% (n = 5). These data suggest that external dofetilide and external acidosis both prolong the action potential by inhibiting the I_{Kr} current.

5.4.4 External acidosis flattened the slope of the electrical restitution curve

The external acidosis-induced prolongation of the APD and increase in AP triangulation both suggest a strong association of acute acidosis during the early phase of ischemia with arrhythmogenesis. To further assess potential arrhythmogenesis with external acidosis, we measured the electrical restitution curve (ERC). The ERC is a plot of the change in APD in response to increasing rate and describes the time course and recovery of ion channel currents underlying the AP. APD is rate-dependent and shortens as the rate is increased. This shortening of the APD is a result of incomplete recovery of a combination of ionic currents underlying a normal AP. As the rate increases, Na^+ influx is increased as a result of fast onset and fast inactivation of Na^+ channels, and the increasing $[Na^+]_i$ leads to activation of the electrogenic Na^+/K^+ pump that will drive three Na^+ out for two K^+ in, thus generating an outward current that hyperpolarizes the cell and shortens repolarization (Carmeliet, 2004). When the rate is enhanced, insufficient removal of Ca^{2+} also leads to an accumulation of $[Ca^{2+}]_i$ that inactivates L-type calcium channels and reduces the duration of the plateau phase, shortening the APD (Carmeliet, 2004). In addition, with an increasing rate, I_{Kr} currents remains robust and accumulates with, which further shortens the APD (Carmeliet, 2004). Thus, the slope of the restitution curve indicates a complex combination of the kinetics of recovery from inactivation of sodium, calcium, and potassium ion channels (FRANZ, 2003). Overall, an inability of cardiac tissue to adapt to rate increases by appropriately shortening the APD has been shown to be highly proarrhythmogenic (R.W.Kurz *et al.*, 1993; Kurz *et al.*, 1994).

To construct the ERC in the zebrafish optical mapping set up, we designed a variable rate stimulation protocol that could command the firing of a series of stimuli of a given voltage at decreasing beat-to-beat intervals i.e, increasing heart rate from 60 bpm up to 300 bpm. The voltage of this stimuli was adjusted to ensure that each stimulus initiated firing of an action potential at pH 7.4. This protocol aims to simulate a progressive increase in heart rate, by decreasing the beat-to-beat interval. Figure 5.5A shows typical ventricular APs recorded using this protocol. The beat-to-beat interval is then plotted against the APD_{75} (Figure 5.5B) and APD_{90} (Figure 5.5C) change to yield the electrical restitution curve. At pH 7.4, every stimulus was able to initiate an action potential and the progressive shortening of the APD indicates the adaptability of the heart to increasing heart rate. At pH 6.5 with 1 min incubation time, there was significant prolongation of the

action potential and the APD ceased to change with increase in heart rate, remaining constant regardless of the stimulation frequency. Figure 5.5B,C shows that the slope of the ERC is flattened (slope < 1), measured at APD_{75} and APD_{90}, within 1 min of incubation in pH 6.5. This suggests that 1 min of acute acidosis greatly attenuated the rate adaptation of the zebrafish ventricular APD, flattening the slope of the ERC, and increasing susceptibility to tachyarrhythmias (FRANZ, 2003).

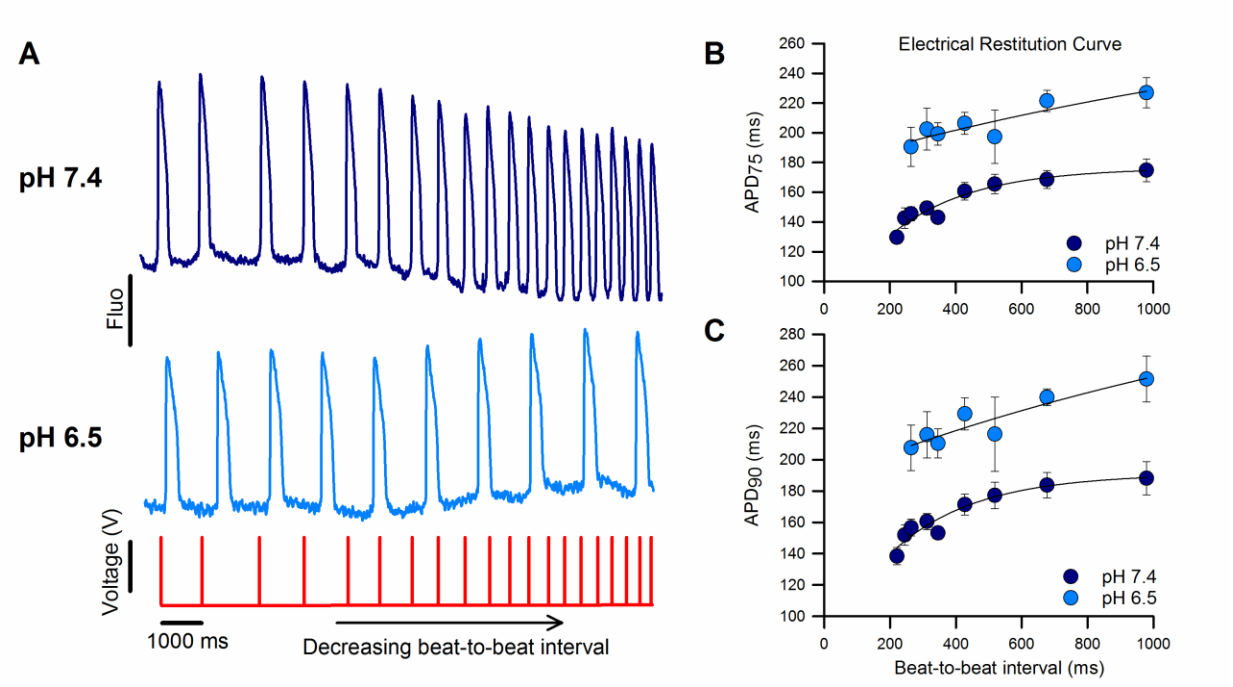

Figure 5.5 - External acidosis flattened the electrical restitution curve (ERC) and is pro-arrhythmogenic.

A. Typical ensemble of AP cycles subjected to a series of stimuli with decreasing beat-to-beat interval (increasing heart rate) from 60 bpm to 300 bpm. At pH 7.4 every stimulus initiated the action potential and the APD shortens as the heart adapts to the increasing stimulation rate. At pH 6.5, the APD is prolonged, and there is an attenuated rate adaptation. **B. C.** Plot of the beat-to-beat interval against APD_{75} (B) and APD_{90} (C). At pH 7.4 the steep slope indicates rapid changes in the APD to accommodate an increase in heart rate, but at pH 6.5, the APD largely remained the same with minimum shortening, which leads to a flattening of the slope of the ERC. This flattening of the slope is a strong predictor for generation of tachyarrhythmia which can lead to ventricular fibrillation.

5.5 Discussion

Here, we have reported the first observations of the effect of external acidosis on the ventricular AP of the zebrafish whole heart and assessed the pro-arrhythmogenic nature of external acidosis using the optical mapping technique. Zebrafish hearts present a promising model to study cardiac electrophysiology due to the similarities in the electrical activity compared with human hearts. Of particular interest for our studies is the observation that the I_{Kr} current is the dominant repolarization current in the zebrafish ventricle (Nemtsas *et al.*, 2010), which enables us to investigate the consequences of modulation of hERG channel behaviour by external acidosis in a whole heart model.

5.5.1 Prolongation of the ventricular action potential by acute external acidosis is an extracellular effect.

External acidosis has been shown to reduce hERG potassium channels, which conducts the I_{Kr} current (Ho *et al.*, 1998; Jo *et al.*, 1999; Van Slyke *et al.*, 2012). *In silico* modeling has shown that inhibition of hERG conductance by external acidosis may lead to a prolongation of the action potential duration and could be pro-arrhythmogenic (Du *et al.*, 2010). Here, we have shown experimentally, using zebrafish as a whole heart translational model, that acute acidosis prolongs the ventricular APD. This is consistent with studies in ferret hearts that showed prolongation of the APD with early acidosis (Bethell *et al.*, 1998). We used pH 6.5 to mimic the local pathophysiological pH change during the onset of ischemia. In papillary muscles in the rabbit heart, following the onset of ischemia, the local extracellular pH was reported to be as low as pH 6.1 (Yan & Kléber, 1992). Application of external solution at pH 6.5 induced continued prolongation of the APD, which reached steady-state after 15-30 mins incubation. During these longer incubations, acidosis also reduced the heart rate and caused irregular heart rhythm in the form of doublets. The mechanism underlying the slowing of heart rate and the doublet formation in the heart rhythm is not clear (Figure 5.1A). During the experiments, development of doublets in heart rhythm were highly variable between hearts, whereas prolongation of the APD and slowing of heart rate was robust and consistently observed. Since the AV delay was still preserved even in the irregular events, the alterations in the AV node function is unlikely to be the underlying cause (Figure 5.1C). Prolonged exposure to pH 6.5 may have changed the intracellular pH that could inhibit the pacemaker current in the SAN of the zebrafish atrial.

The main focus of our studies was the first minute of exposure to acidosis since this allows us to isolate the effects of extracellular pH changes without significant changes to intracellular pH, and because delayed repolarization was observed in a clinical study within 42 s of induced ischemia (Kenigsberg *et al.*, 2007) and in ferret hearts within the first 3 min of ischemia (Bethell *et al.*, 1998). This prolongation of the QT interval or ventricular APD appears to coincide well with the timing of the development of extracellular acidosis, we hypothesized that extracellular acidosis is a major contributor to the prolongation of the APD. Figure 5.2 demonstrates that within the first minute of exposure to pH 6.5 the zebrafish ventricular APD was markedly prolonged with little effect on the heart rate or rhythm (Figure 5.2A). This prolongation was rapidly washed off with pH 7.4 solution. This rapid onset and recovery is strong evidence that supports an extracellular effect.

We attempted to assess whether the intracellular pH did in fact remain unchanged within the first minute of extracellular acidosis using an optical method. We chose to measure the emission spectra of seminaphthorhodafluor-4F 5-(and-6) carboxylic acid (SNARF-4F), a cell-permeant ratiometric pH fluorescence dye that is excited by a 525 nm light source and emits two emission peaks at wavelengths 560 nm and 630 nm. The emission peak intensity changes ratiometrically depending on the pH of the environment. At pH 8.0, for example, SNARF-4F will show a large emission peak at 630 nm and a small peak at 560 nm, yielding a large ratio. Conversely, at pH 6.0, the emission peaks of 630 nm and 560 nm are similar, yielding a small ratio. By using the ratio between the two peaks, we can determine the pH of the environment of SNARF-4F. Since SNARF-4F has a pKa of 6.4, it is well suited for the pH range we were interested in. We used the acetoxymethyl ester (AM-ester) form of SNARF-4F to introduce the dye into the cell. Once inside the cytoplasm, the ester group is targeted for esterification and the dye is retained inside the cytoplasm. Previously, SNARF-4F have been successfully labeled in single cardiomyocytes or monolayers where fewer cells were used to label. Here, we attempted to label an entire organ. In order to change the intracellular pH of the heart, we perfused the zebrafish hearts with a nigericin solution, titrated to a given pH. Nigericin is an antiporter of K^+ and H^+. It acts as an ionophore that transport H^+ across the membrane to equilibrate the intracellular pH with that of the extracellular solution. Unfortunately, fluorescence emission captured at the 560 nm and 630 nm peaks showed a large drop in signals over time, and similarly the ratio between the peaks either decreased overtime, or

remained unchanged regardless of intracellular pH change, despite numerous attempts (n = 34, data not shown). This drop in fluorescence signal may be due to wash off, or insufficient labeling. Major limitations in our system could be the accessibility, and concentration of the SNARF-4F dye. It is possible that scaling up to the whole organ labeling may require an insurmountable concentration of the SNARF-4F dye. Despite this method being unsuccessful, it is highly unlikely that there are changes to the intracellular pH following the first minute of the extracellular acidosis exposure in our experiments. For example, in rabbit heart papillary muscles, the intracellular pH remained unchanged during the first 5 minutes of ischemia while extracellular pH dramatically decreased, but after 5 mins the intracellular pH decreased markedly (Yan & Kléber, 1992).

5.5.2 External acidosis increased AP triangulation, which is a strong predictor for Torsade de Pointes.

From Figure 5.2 it can be seen that the upstroke velocity of the ventricular AP was unaffected by external acidosis, which suggests that there is little effect on activation of I_{Na} current in the zebrafish ventricle. Instead, the majority of the effect of external acidosis was on the repolarization producing prolongation of the APD at all phases (i.e, APD_{30}, APD_{50}, APD_{75}, and APD_{90}). Indeed, external acidosis have been shown to destabilize the slow-activated state of Nav1.5 channels leading to an elevation in persistent I_{Na} current (Jones *et al.*, 2011), which may contribute to the prolongation of the APD observed. However, the largest effect of acute external acidosis was on the late phase repolarization, in particular APD_{90}, where the predominant current is I_{Kr}. This is consistent with functional studies showing that external acidosis inhibits hERG channels current (Ho *et al.*, 1998; Jo *et al.*, 1999; Jiang *et al.*, 1999; Du *et al.*, 2010; Van Slyke *et al.*, 2012; Shi *et al.*, 2014).

The differential prolongation of early (APD_{30}) and late phase (APD_{90}) of repolarization, induced by external acidosis, resulted in a significant increase in the triangulation compare to that at pH 7.4. Triangulation is defined as the repolarization time from APD_{30} to APD_{90} (Hondeghem *et al.*, 2001*a*, 2001*b*). Increased triangulation is strongly associated with, and is a predictor of, tachyarrhythmias, such as Torsades de Pointes (TdP). A study done in rabbit hearts looked at the effect of quinolones and showed that the antibiotics significantly prolonged myocardial repolarization. However, the hearts that developed EADs and TdP were those that had both an increase in dispersion of repolarization, which is defined as the difference between the longest and shortest

repolarization times, and increase in triangulation of the action potential (Milberg *et al.*, 2007). Another study observed the cardiac electrophysiological effects of 702 class 2 antiarrhythmic drugs which block hERG channels in 1071 rabbit hearts. They measured the instability of APD, triangulation, and induction of ectopic beats (Hondeghem *et al.*, 2001*a*). In 59 hearts that exhibited prolongation of the APD coupled with increase in triangulation, polymorphic ventricular tachycardia was observed. In contrary, in 19 hearts that showed the same prolongation of APD but no increase in APD triangulation, no arrhythmia was observed (Hondeghem *et al.*, 2001*a*). These studies are consistent with the idea that acute external acidosis is proarrhythmogenic, because protons not only prolongs the APD, but also increase the triangulation of the ventricular AP. This would be expected to increase the susceptibility of the heart to develop TdP caused by prolongation of the latter repolarization phases increasing the susceptibility to EADs and DADs in the zebrafish heart during acute acidosis following the early onset of ischemia.

5.5.3 Dofetilide and external acidosis compete for block of I_{Kr} current.

In order to provide further evidence that APD prolongation induced by acute external acidosis is caused by inhibition of I_{Kr} current, we used dofetilide (a potent and specific open channel blocker of the hERG potassium channel) to reduce the available I_{Kr} current in the zebrafish ventricle and observed whether acidosis could further prolong the APD. We showed that 250 nM dofetilide significantly prolonged the ventricular APD, in particular the APD_{50}, APD_{75}, and APD_{90} compared to that of APD_{30}, by specifically blocking the I_{Kr} current. In the presence of dofetilide, pH 6.5 induced markedly less change in the ventricular APD across all phases of repolarization (APD_{30}, APD_{50}, APD_{75}, and APD_{90}) (Figure 5.4D). These data suggest that both dofetilide and pH 6.5 causes a prolongation of the action potential by blocking the I_{Kr} current as a shared mechanism. It is intriguing that 250 nM dofetilide, which is around the IC_{50} in the zebrafish ventricle (data not shown), largely abolished the effect of external acidosis, rather than reducing the effect by ~50%. A possible explanation is that since pH 6.5 is at the pKa for the acceleration of deactivation on the hERG channels, this may not be a saturating pH. The observed effect seen here reflect a complex interaction between protons and dofetilide to reduce I_{Kr} current. An alternative experiment to further validate that prolongation of the APD by external acidosis is due to block of I_{Kr} current may be to use a hERG specific activator, such as RPR260243,

to rescue the I_{Kr} current at pH 6.5, which would be expected to shorten the APD back to that observed at pH 7.4.

5.5.4 The slope of the electrical restitution curve as a predictor of arrhythmia.

The slope of the ERC is an important predictor for arrhythmogenesis, with both a steep slope (slope > 1), and a shallow slope (slope < 1) indicated as a precursor to cardiac arrhythmia (FRANZ, 2003). A steep slope leads to very rapid changes in APD with small changes in heart rate, which amplifies APD alternans and is a strong predictor of ventricular fibrillation (FRANZ, 2003). It is this initial steep portion of the restitution curve that establishes what has been described as the “vulnerable window” of the heart (FRANZ, 2003). It is within this “vulnerable window” that EADs and DADs may arise that can lead to vulnerability to tachyarrhythmia. Indeed, novel antiarrhythmic drugs often aim to flatten the slope of the ERC as an arrhythmia protection mechanism (Weiss *et al.*, 1999). However, diseased hearts often show flattening of the ERC slope rather than steepening. In isolated rabbit hearts, reduction of coronary blood flow produced a dramatic flattening of the ventricular ERC within 5 min. This ischemia-induced flattening of the ERC slope was accompanied by sensitivity to APD alternans, and tachyarrhythmias were easily induced, or occurred spontaneously (R.W.Kurz *et al.*, 1993). Following prolonged ischemia (> 6 mins), where irreversible ischemic damage occurred, the ERC slope was so flattened as to become horizontal. In this case, the APD remained constant regardless of cycle length, which reflects severe disruption of ion channel recovery kinetics (R.W.Kurz *et al.*, 1993). This was also seen in human action potential recordings during myocardial ischemia (Taggart *et al.*, 1986; John *et al.*, 1991). One of the more important reasons that a flattened ERC slope is proarrhythmogenic is that the heart is unable to rapidly adapt and change the APD following increases in heart rate. Physiologically, the APD rapidly changes and adapts to the change in the heart rate, which indicates a fine balance in the ion channel recovery kinetics underlying these APD changes. Here, we designed a stimulation protocol in the optical mapping set-up to experimentally measure the ERC of the zebrafish ventricle at pH 7.4 and pH 6.5. At pH 7.4 (Figure 5.5B), the heart rapidly adapts and the APD shortened in response to increasing heart rate from 60 bpm to 300 bpm. In contrast, 1 min application of pH 6.5 largely flattened the ERC slope, and the APD remained relatively unchanged regardless of the heart rate. This is consistent with observations seen in ischemic-induced rabbit hearts and suggests that prolongation of the

APD alters ion channel recovery kinetics (Kurz *et al.*, 1994). The inability to change APD to adapt the changes in rate at pH 6.5 is likely to be highly proarrhythmogenic. For instance, at high heart rates the inability to shorten the APD and return the cell back to rest would be expected to cause an increased susceptibility to EADs and DADs, which can lead to premature initiation of an ectopic action potential that degenerates into ventricular tachyarrhythmia.

In summary, we have shown that acute acidosis (1 min) prolonged the ventricular AP by inhibiting the I_{Kr} current as the major underlying cause. Due to this, the late phase of repolarization (APD_{90}) is prolonged more than the early phase (APD_{30}), thus leading to an increased in the triangulation, which is a strong predictor for TdP. In addition, acute acidosis markedly flattened the ERC, and impaired the APD rate adaptation with increasing rate, which may increase susceptibility to EADs and DADs.

5.5.5 Limitations

One of the major limitations to our study is the genetic background of the zebrafish used in the experiments reported. From the protocol approved by the Simon Fraser University Animal Care Committee, the zebrafish used were purchased from a local supplier and therefore the genetic background of the purchased zebrafish is unknown. This can provide a challenge if a zebrafish carries a mutation that may potentially confound our observed results. One zebrafish may be more susceptible to lower heart rates, doublet formation, and prolongation of the APD compared to another. In our experiments, some variation of phenotypic development amongst hearts when subjected to longer incubation time at pH 6.5 was observed, however within the first minute at pH 6.5, all zebrafish hearts tested showed very similar phenotypic behavior: a prolongation of the ventricular APD, and no changes in the heart rate or rhythm. Future studies will benefit from a recently established zebrafish housing facility, in which the WT strain (AB) zebrafish are being bred. Tail-clip procedures are being implemented to ensure that the genetic background of all generations of zebrafish in the housing facility are known.

Another limitation lies within the genome of the zebrafish. Zebrafish have gone through multiple whole genome duplications and this provides a challenge in comparing the orthologs between human and zebrafish. Previously, a number of studies were conducted on zebrafish *zerg-2* which is the human orthologue of *KCNH2*. However,

Kcnh6a is by far the most prevalent transcript in the zebrafish heart and exhibits human *KCNH2*-like gating properties and pharmacology. Due to this, the external acidosis prolongation of the ventricular APD in this study is likely from an inhibition of the KCNH6a channels in the zebrafish heart.

Chapter 6. General Discussion and Future Directions

In my thesis I have proposed a site and mechanism of action for the extracellular proton-induced shift of the voltage-dependence of activation and the acceleration of deactivation in the hERG potassium channel. Understanding how external protons act on the hERG channel has provided valuable mechanistic insight into the normal regulation of hERG channel gating. I then translated these functional studies to the zebrafish heart model and demonstrated that, at the whole organ level, the arrhythmogenicity of acute acidosis is largely mediated by the inhibition of zERG function. This last chapter will discuss more of the findings in the previous chapters in a broader scope and considers future directions.

6.1 hERG activation gating

6.1.1 Modulation of hERG activation by external protons

The slow activation, coupled with fast inactivation, of hERG channel gating is unique amongst Kv channels and is important in suppressing hERG current during the early phases of the cardiac action potential. Gating current measurements show that one of the reasons for slow activation of hERG channels is due to differences in the movement of the voltage sensor during activation compared to that of the archetypal *Shaker* channel. First of all, hERG channels pass fewer elemental charges during activation (~8-9 e_o) compared to that of *Shaker* (~12-14 e_o), suggesting that the voltage sensor movement may be limited in the hERG channel (Zhang *et al.*, 2005). Second, kinetic measurement of gating charge movement showed a slower on gating charge movement compared to that of *Shaker* (Piper *et al.*, 2003). Lastly, the outermost charge on the S4 voltage sensor of hERG channels is a lysine instead of an arginine, as it is in *Shaker*-like channels. Mutagenesis studies have shown that this lysine is critical in hERG activation and that even a charge conserving mutation (K525R) did not exhibit WT-like activation suggesting the importance of the side chain at this position (Subbiah *et al.*, 2004). The basic residues in the S4 segment of the hERG channel play a crucial role in the activation gating. Charge reversal mutations and cysteine substitutions of the basic residues in the S4 have differential effects on the hERG channel activation gating. K525D, for example shift the G-

V of activation to the left suggesting destabilization of the closed state (Zhang *et al.*, 2005). On the other hand, R531D, and R534D shift the G-V of activation to the right suggesting that the open state is destabilized (Zhang *et al.*, 2005). R528D, and R537D did not affect the G-V of activation, but R528D dramatically slowed deactivation (Zhang *et al.*, 2005). Due to these differential effects, interactions that stabilize these basic residues are likely to be important in the normal activation gating. Disruption of these interactions by external protons, for example, can dramatically alter normal channel activation and be pro-arrhythmogenic.

Acidic residues in the neighbouring S1-S3 transmembrane segments (D411 in the S1, D456, D460, and D466 in the S2, and D501, and D509 in the S3), are critical in providing the stabilizing interactions, in the form of ionic pairings, with the basic residues in the S4 to facilitate normal hERG activation gating. These ionic pairings are thought to stabilize the S4 voltage sensor as it translocates outwards. Several studies suggest that the S4 moves in a helical motion and interacts with the acidic residues in a ratchet-like fashion (Schönherr *et al.*, 2002; Lecar *et al.*, 2003). Protonation of the acidic residues by extracellular protons may act to impair this ratchet-like motion leading to slower activation kinetics, which has been suggested to be a modulation of the voltage-insensitive transition by external protons (Zhou & Bett, 2010).

6.1.2 Extracellular protons altered the voltage-dependence of hERG activation by protonating D456, D460, and D509

D456, and D460 in the S2, and D509 in the S3 transmembrane segment of the hERG channel, which form a metal cation binding pocket, are critical in the regulation of hERG channel activation gating. Double mutant cycle analysis was used to assess the interactions of these three acidic residues with basic residues in the S4. This is a method use to quantify the coupling of the mutant effects on channel function. The effects of each mutation are calculated based on the free energy of channel activation. If the effects of two mutations on channel activation are not additive (> 3 kcal/mol), the two mutation sites may be coupled, while if the effects are additive (< 1 kcal/mol) then they are not coupled (Zhang *et al.*, 2005). From this analysis, it was shown that D456R – K525D and D456R – R528D are coupled during activation (Zhang *et al.*, 2005). In the hERG open-state cryo-EM structure, D456 and D460 interact closely with R528 and R531, respectively, consistent with stabilization of the open state (Wang & MacKinnon, 2017). Replacing the

aspartic acid residues with alanine caused a right-shift in the voltage-dependence of activation suggesting that all three residues are involved in stabilization of the open state (Figure 3.2), which is in agreement with several previous reports (Liu *et al.*, 2003; Fernandez *et al.*, 2005; Zhang *et al.*, 2005).

These specific ionic pairings within the metal cation binding pocket are very sensitive to disruption by extracellular factors such as divalent cations. Cd^{2+}, Ca^{2+}, and Mg^{2+}, have all been shown to right-shift the voltage dependence of activation by coordinating within this pocket and destabilizing the open state (Paquette *et al.*, 1998; Ho *et al.*, 1998; Jo *et al.*, 1999; Fernandez *et al.*, 2005; Kazmierczak *et al.*, 2013). One study aimed to assess the accessibility of the acidic residues to extracellular side chain modifications by methanethiosulfonate (MTS) reagent (Liu *et al.*, 2003). Acidic residues were mutated to cysteine, and those that are accessible to modification by MTS exhibited drastic reduction in hERG channel current (Liu *et al.*, 2003). From this the authors revealed that D411 (located at the bottom of S1) and D466 (located at the bottom of S2) are both accessible by MTS (Liu *et al.*, 2003). This suggests that there is a water-filled crevice that penetrates deep into the bottom of S1 and S2 (Liu *et al.*, 2003). A proline at position 507 (in the S3) may cause a kink in the S3 which would open up a wide crevice at the top portion between S2 and S3 (Liu *et al.*, 2003). This proposed structural configuration may explain the readiness of cations, and potentially protons, to access the acidic residues within the S2 and S3 transmembrane domains. Detailed molecular mapping of the metal cation binding pocket using Cd^{2+} showed that Cd^{2+} interacts specifically with D456, D460, and D509. Neutralization of all three acidic residues abolished the Cd^{2+} effect on activation. Cd^{2+} is commonly coordinated in a tetrahedral arrangement where three of the interactions come from D456, D460, and D509, and the fourth interaction may be formed with a water molecule within the crevice (Fernandez *et al.*, 2005). We observed in Chapter 3 that external protons also right-shift the voltage dependence of activation similar to that of Cd^{2+} with a pKa of 5.5, and the proton-induced shift of activation was dramatically reduced in the presence of 0.1 mM of Cd^{2+} suggesting competitive binding (Shi *et al.*, 2014). The mutagenic study in Figure 3.3 indicates that the pH-dependent shift of the voltage-dependence of activation involves D456 and D460 acting in concert with D509, and the triple mutant construct, D456A/D460A/D509A, completely abolished the pH-dependent shift in G-V of activation (Shi *et al.*, 2014). Figure 6.1 shows a cartoon representation of the proposed transition of the S4 voltage sensor from the resting to the

activated state following membrane depolarization. During the resting state, K1 (K525) is in close proximity to the gating charge transfer centre (F463) as our lab has shown previously (Cheng *et al.*, 2013). As the S4 translocate outwards, stabilization of the activated state is provided by the coordinated action of D456, and D460 in concert with D509 as suggested in Section 3.4.3. I propose that protons can access and protonate the acidic residues, D456, D460, and D509 of the metal cation binding pocket in the water-filled crevice to disrupt ionic pairings with the basic residues in the S4 that would otherwise stabilize the open state. In my thesis, I also propose that this water-filled crevice is not only important for regulating activation but also for regulating the slow deactivation gating of the hERG channel, albeit with a different *pKa* (Chapter 5).

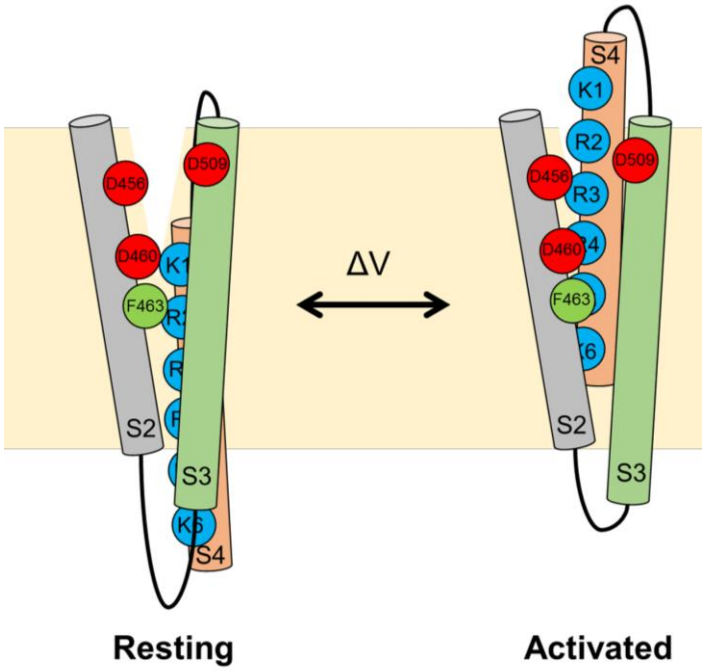

Figure 6.1 - Cartoon representation of the resting to activated state of the hERG voltage sensor.

Proposed cartoon representation of the hERG S4 voltage sensor transitioning from the resting state to the activated state. At the resting state, K1 (K525, blue) is in close proximity to the gating charge transfer centre (F463, green), and D460. As the S4 translocate outwards following membrane depolarization, the stabilizing interactions are facilitated by D456, D460, and D509 forming ionic pairings with R2 (R528), R3 (R531), and R4 (R534).

6.2 hERG deactivation gating

6.2.1 Modulation of slow hERG deactivation

The slow deactivation gating of hERG channels is another unique and important feature that facilitates the conduction of the resurgent repolarizing current necessary to return the membrane to rest. In addition, slow deactivation may allow hERG current to pass after the cardiac AP during early refractory period. This large protective current may act to protect against premature stimuli such as EADs or DADs that may initiate a premature AP and increase arrhythmogenicity. Indeed, *in silico* experiments suggest that reducing this protective current may increase susceptibility of the cell to premature initiation of an AP by a simulated DAD. Interestingly, a cluster of eight long-QT syndrome-associated mutations, located on the PAS domain of the hERG channel (F29L, N33T, G53R, R56Q, C66G, H70R, A78P, and L86R), were all found to exhibit an acceleration of the deactivation rate that reduces hERG current (Chen *et al.*, 1999). This precipitated a series of studies to investigate the regulation of slow deactivation in hERG channels, such as what are the domains involved, what are interacting partners, and what residues are involved in the interactions. This work has revealed a complex interplay between multiple cytoplasmic domains that play an essential role in the regulation of slow deactivation. However, the exact mechanism that regulates slow deactivation is still unclear.

One of the first studies showed that deletion of the PAS domain dramatically accelerated the deactivation rate, suggesting that the entire domain is essential in slow deactivation (Sanguinetti *et al.*, 1996; Schönherr & Heinemann, 1996; Wang *et al.*, 1998). It was later discovered that point mutations in the PAS domain also show rapid acceleration of deactivation kinetics, in particular, the first 19 amino acids of the N-terminus called the N-cap (Chen *et al.*, 1999; Gustina & Trudeau, 2009). Forster resonance energy transfer experiments showed that the PAS domain is in close proximity to the channel near the plasma membrane (Gustina & Trudeau, 2009), suggesting that the PAS domain interacts directly with other parts of the cytoplasmic domains to regulate slow deactivation. One suggested interaction partner is the S4-S5 linker. Cysteine residues introduced at V3 in the N-terminus and Y542 in the S4-S5 linker were close enough to be crosslinked suggesting that the N-cap is in close proximity to the S4-S5 linker (de la Peña *et al.*, 2011). Mutations in the S4-S5 linker also exhibit fast deactivation kinetics, similar to that of point mutations in the N-terminus (Wang *et al.*, 1998). However,

the C-terminus also appears to play a critical role in the regulation of slow deactivation. In the hERG channel, deletion of the cNBHD accelerated the deactivation kinetics, similar to that of deletion of the N-terminus region (Gustina & Trudeau, 2011). A protein interaction assay fusing the PAS domain to GST, and a FLAG tag to the cNBHD region (hERG 666-872 flag) showed that a cNBHD-containing protein 666-872 was only detected when the PAS domain was present suggesting a direct and specific interaction (Gustina & Trudeau, 2011). Another study used a lysine mutation scan along the surface residues of the cNBHD of hERG and found a patch of conserved hydrophobic residues, which when mutated to lysine accelerated deactivation (Al-Owais *et al.*, 2009). A similar approach with the PAS-domain also revealed a patch of hydrophobic residues in this domain (Cabral *et al.*, 1998). These hydrophobic patches on the cNBHD and PAS-domain may be the docking sites for their interactions, and they may dock near the S4-S5 linker to alter channel deactivation by altering the coupling between the voltage sensor with the pore. Consistent with this, fluorescence and ionic measurements of mode-shift in N-terminus deleted constructs showed that the fluorescence mode-shift of the voltage sensor remained similar to that of WT, but the ionic mode-shift was dramatically reduced, suggesting that the N-terminus deleted mutation caused a decoupling of the voltage sensor to the pore (Tan *et al.*, 2012).

To add another layer of complexity to the regulation of slow deactivation, mutations of any of the six acidic residues within the S1, S2, and S3 transmembrane domains also accelerated deactivation kinetics, regardless of cysteine or alanine substitutions (Liu *et al.*, 2003; Fernandez *et al.*, 2005; Shi *et al.*, 2014). A proposed mechanism of a “master-switch” that exists to keep hERG deactivation slow, which when turned off would produce fast deactivation was proposed (Liu *et al.*, 2003). It was suggested that all of the acidic residues in S2 and S3 may need to be present to participate to keep the “master-switch” on (Liu *et al.*, 2003). This could conceivably involve ionic pairings with the basic residues in the S4 which stabilize the voltage sensor. In Chapter 4 (Figure 4.5), I showed that D509 is a critical site that stabilizes the relaxed conformation of the voltage sensor, limiting the return of the voltage sensor and contributing to the slow deactivation kinetics. This return from the relaxed state of the voltage sensor may slow the closing of the pore via the S4-S5 linker and the intracellular PAS domain and cNBHD, effectively acting as a “master-switch” to control hERG deactivation.

6.2.2 Slow hERG deactivation as a result of voltage sensor relaxation

Recently, it was shown that the hERG channel exhibits mode-shift behavior, where there is a marked separation between the voltage-dependence of activation and deactivation. This is thought to be due to a process known as voltage sensor relaxation, where membrane depolarization activates the voltage sensor, but prolonged depolarization relaxes the voltage sensor to a more stable conformation, termed the relaxed state. Returning the voltage sensor from this relaxed state requires more energy, thus leading to a left-shift in the voltage-dependence of deactivation (Tan *et al.*, 2012). This mode-shift phenomenon is seen in many other channels such as *Shaker* (Lacroix *et al.*, 2011; Haddad & Blunck, 2011; Labro *et al.*, 2012; Priest *et al.*, 2013), Kv1.2 (Labro *et al.*, 2012), HCN (Männikkö *et al.*, 2005), NaChBac (Kuzmenkin *et al.*, 2004) and a voltage-sensor related protein *Ci*-VSP (Villalba-Galea *et al.*, 2008) and is therefore thought to be an intrinsic property of the voltage sensor. Recent studies suggest that voltage sensor relaxation contributes to slow deactivation in the hERG channels (Tan *et al.*, 2012; Goodchild & Fedida, 2014; Thouta *et al.*, 2017), where prolonged depolarization not only left-shifts the voltage-dependence of deactivation, but also slows the deactivation kinetics (Thouta *et al.*, 2017). Here, I used extracellular protons as a tool and compared the *pKa* of the proton-induced acceleration of deactivation kinetics with that of the loss of mode-shift (Figure 4.2C,F). The similarities in the *pKa* (*pKa* ~7) suggest that both effects may be shared by the same mechanism of action, and that the loss of mode-shift may be a consequence of the faster deactivation kinetics.

In Chapter 4, I have discovered a potential site underlying the mechanism for the pH-induced acceleration of deactivation. External protons accelerated deactivation by destabilizing the relaxed state of the voltage sensor, right shifting the voltage sensor return, leading to a loss of the voltage sensor mode-shift (Figure 4.4). Neutralization of D509 abolished the fluorescence measurement of voltage sensor mode-shift, very similar to the effect induced by external protons (Figure 4.5). I propose that extracellular protons protonate the D509 acidic residue and set in motion the fast deactivation kinetics by disrupting the ionic pairing with the basic residues in the S4, or with a network of water within the water-filled crevice. In this way, extracellular protons accelerate the deactivation rate by destabilizing the relaxed voltage sensor without altering the intracellular coupling mechanism. This would suggest that extracellular stabilization of the voltage sensor, as well as intracellular coupling between the voltage sensor and the pore involving the PAS-

domain, S4-S5 linker, and cNBHD are all critical components regulating the slow deactivation gating of the hERG channels. Disruption of any of these components set in motion the fast deactivation kinetics that can be highly pro-arrhythmogenic. Here, I have shown that D509 is a key residue that mediates both the pH-induced shift in the voltage-dependence of activation (Figure 3.2), and the pH-induced acceleration of deactivation (Figure 4.5), however with different *pKa* (5.6 and 7, respectively). As mentioned in Chapter 4, the differing pH-sensitivity may reflect on a complex coordination from D456 and D460 with D509, during the activation pathway that stabilizes the activated voltage sensor, resulting in a lower *pKa* for protons-induced shift in voltage-dependence of activation. In the relaxed state, however, D509 appears to face the extracellular milieu (Wang & MacKinnon, 2017) and may be coordinated by other factors such as water molecules that altered the pH-sensitivity to stabilize the relaxed state of the voltage sensor to regulate deactivation (Figure 4.8).

It is interesting to consider, therefore, that slowing deactivation in hERG channels may provide a therapeutic target to rescue or enhance I_{Kr} current. In Figure 4.7, I have shown that RPR260243, an activator that primarily slows hERG deactivation, can restore the peak protective current at pH 6.5 and potentially rescue the protective nature of the I_{Kr} current to antagonize against premature stimulus such as EADs or DADs. Indeed, stabilization of the voltage sensor in the relaxed state may also be a potential target for compounds. The target site could potentially be the extracellularly accessible water-filled crevice between the S2/S3 and S4 domain and the cation binding pocket. Since voltage sensor relaxation contributes to the slow deactivation gating, compounds that stabilize interactions between the acidic residues and basic residues in the voltage sensor in the relaxed state may slow down deactivation gating and enhance the I_{Kr} current. This may be useful, for example, to rescue long QT syndrome type 2 mutations such as R56Q, where deactivation kinetics are accelerated. By using a compound to stabilize the voltage sensor in the relaxed state in R56Q mutant channels, the deactivation kinetics may be rescued to restore WT-like gating.

6.3 Using a translational model to assess arrhythmogenicity

In Chapter 3, and 4, I have used biophysical techniques, TEVC, VCF, and COVC, to investigate the site and mechanism underlying the effect of external protons on hERG

channel activation and deactivation gating. These disruptions in hERG channel gating may have critical consequences on cardiac rhythm during myocardial ischemia where external acidification is one of the hallmarks. The optical mapping system is a powerful imaging screening tool due to its ability to rapidly measure robust voltage signals in whole ex vivo hearts with the ease of changing extracellular conditions. Optical mapping can be performed not only on zebrafish hearts, but on other cell types such as rabbit hearts, and human induced pluripotent stem cell-derived cardiomyocytes (iPSC-CM). The field stimulation capability can enable us to subject the heart to programmed premature stimuli, mimicking that of EADs or DADs to assess markers for arrhythmogenesis subjected to application of drugs, or low pH. In Chapter 5, I used the zebrafish whole heart model to translate the knowledge gained from functional studies to assess the arrhythmogenicity induced at low external pH at a whole organ level. We showed that acute extracellular acidosis prolonged the ventricular action potential and increased the triangulation of the ventricular AP, which is a strong predictor for Torsades de Pointes (Figure 5.3). Other evidence that this acute acidosis may be arrhythmogenic is from the flattening of the electrical restitution curve (Figure 5.5), in which the heart was unable to change the ventricular APD to adapt to the increasing heart rate. This can lead to increased susceptibility to induced or spontaneous tachyarrhythmias. One possible explanation may be that the flattening of the restitution curve increases the “vulnerable window” and this is expected to increase susceptibility of the heart to APD alternans and arrhythmia. This is consistent with the observation in rabbit hearts where the ERC was markedly flattened within 5 minutes of ischemia (Kurz *et al.*, 1994).

Kenigsberg et al showed that all the patients subjected to balloon inflation technique, to simulate an ischemic event, exhibited an initial prolongation of the QT-interval within the first minute. The onset of this prolongation of the QT-interval coincide well with the fast onset of external acidosis within the early phase of ischemia and the prolongation of the QT-interval may suggest an impaired repolarization due to reduction in I_{Kr} current. Here, using the zebrafish heart model, I demonstrated that acute external acidosis prolonged the action potential duration by mostly impairing the repolarization phase due to the inhibitory effect of external acidosis on the ERG channel. This may contribute to the prolongation of the Q-T interval seen clinically. Although the arrhythmogenicity of the clinical prolongation of QT-interval during ischemia remains untested, acute external acidosis does dramatically prolong the ventricular APD, increase

the triangulation and flatten the electrical restitution curve in the zebrafish heart model, all of which suggest that external acidification is highly arrhythmogenic. In Chapter 3 and 4, I have shown that the mechanism for the pH-induced shift in voltage-dependence of activation and acceleration of deactivation, that contribute to the inhibition of hERG channel at low external pH, has a *pKa* of 5.6 and 7, respectively. These data suggest that during acute external acidosis to pH 6.5, tested in the zebrafish whole heart model in Chapter 5, there is minimal effect on the zERG channel voltage-dependence of activation (Figure 3.1), and maximum conductance (Bett & Rasmusson, 2003; Van Slyke *et al.*, 2012), but significant acceleration of deactivation kinetics and reduction in mode-shift (Figure 4.2). Taken together, the APD changes and arrhythmogenesis observed at pH_o 6.5 in the zebrafish heart is predominantly due to an acceleration of zERG channel deactivation kinetics by destabilization of the relaxed state of the voltage sensor as the underlying mechanism.

6.4 Final summary and future directions

In this thesis, I have identified a site and mechanism for the proton-induced right-shift of the voltage-dependence of hERG channel activation (Chapter 3). I have shown that the divalent cation, Cd^{2+}, can dramatically reduce the proton-induced shift of activation and found that both Cd^{2+} and protons share a similar site to induce the right-shift in the voltage dependence of activation. I postulate that this occurs by disruption of ionic pairing between acidic residues within the cation binding pocket and basic residues in the S4. Using neutralization mutations of residues forming the cation binding pocket, I have shown that the proton-induced shift in activation is due to protonation of residues D456 and D460 acting in concert, along with D509. Neutralization of the entire cation binding pocket completely abolished the proton-induced shift in activation.

Next, I have identified a site and mechanism for the proton-induced acceleration of hERG channel deactivation (Chapter 4). I have shown that the extent of the proton-induced reduction of ionic mode-shift and the acceleration of deactivation kinetics share a similar *pKa*, consistent with the idea that these two effects are correlated. I used a combination of voltage clamp fluorimetry and gating current measurements to assess voltage sensor mode-shift with near steady-state durations that would push the channels to the relaxed state. I found that at pH 6.5, the voltage sensor mode-shift was markedly reduced, and this reduction is mainly due to a right-shift in the voltage-dependence of

voltage sensor return with only a small change in voltage sensor activation. These data suggest that the relaxed state of the voltage sensor is destabilized by external protons. I have also identified that D509 is a critical site that mediates the stabilization of the relaxed state of the voltage sensor. Neutralization of D509 abolished the voltage sensor mode-shift measured by fluorescence, mimicking the reduction at pH 6.5. Lastly, I have demonstrated that the accelerated deactivation leads to a dramatic reduction in the peak protective current elicited by a premature stimulus which may be highly pro-arrhythmogenic. By using a small molecule activator (RPR260243) to slow down deactivation, the peak protective current can be rescued at pH 6.5, which may present a potential therapeutic approach to rescue loss of function.

The proton-induced shift in the voltage-dependence of activation and the acceleration of deactivation both cause an overall reduction in the hERG current that may be pro-arrhythmogenic. I used optical mapping of zebrafish whole hearts as a translational model to assess AP characteristics and potential for arrhythmogenicity during acute acidosis. I have shown that acute acidosis markedly prolonged the ventricular APD during the late phase of repolarization leading to an increase in AP triangulation, which is a strong predictor of susceptibility to tachyarrhythmias. The proton-induced prolongation of the APD was abolished in the presence of a hERG specific blocker, dofetilide, suggesting that the majority of the prolongation of the ventricular APD by low pH is due to an inhibition of I_{Kr} current, conducted by zERG. Finally, I have used a variable rate stimulation protocol to measure the electrical restitution at low pH and found that the slope of the electrical restitution curve is flattened, suggesting that the APD adaptation to increasing heart rate is severely disrupted. Both the increase in triangulation and the flattened slope of the electrical restitution curve are markers for increased susceptibility to cardiac arrhythmias.

In the future there are several exciting projects to follow up. An immediate project is to assess whether during acute acidosis the zebrafish heart shows increased susceptibility to premature firing of an action potential. This would require designing a stimulation protocol where we first initiate firing of a series of suprathreshold stimuli to pace the zebrafish heart at a known frequency (S1), then follow immediately with a single subthreshold stimuli (S2) to mimic that of an EAD/DAD. We would expect to see that at pH 7.4 the subthreshold S2 stimulus will not initiate an AP firing, however, during acute acidosis, due to the impairment of the ERG channel and reduction in the protective current, the same subthreshold S2 stimulus will fire an AP. This will provide further evidence to

suggest that acute acidosis is arrhythmogenic and likely due to an impairment of the protective current conducted by ERG channels. Another project is to use CRISPR genome editing technology to engineer long QT syndrome type 2 causing mutations such as R56Q, which primarily accelerates deactivation, into zebrafish and assess the arrhythmogenesis of the mutation. At the same time, activators can be screened to assess their ability to rescue the effect and potentially reduce arrhythmogenesis. There could also be projects investigating the effects of low pH in iPSC-CM and observe the changes in APD, triangulation, and susceptibility to arrhythmia by premature stimuli. Finally, CRISPR genome editing technology can also be used to create mutant cardiomyocytes in a similar fashion to that for zebrafish to assess the arrhythmogenicity, and screen for activators that would rescue the mutant cells. Although this is not a whole organ model, it is a human model which would provide much more relevant and valuable insights to our understanding of arrhythmogenesis.

Taken together, the data presented in my thesis provide fundamental insights into how hERG channel activation and deactivation are regulated using protons as a tool. My studies also uncover sites and mechanisms for the proton-induced changes in hERG channel gating, which identify potential therapeutic targets to modify and rescue hERG loss of function. Finally, my studies demonstrate that acute extracellular acidosis during the early phase of myocardial ischemia is arrhythmogenic as a direct result of inhibition of hERG channel function and that activator compounds that modify hERG gating may have value as potential therapies.

References

Abbruzzese J, Sachse FB, Tristani-Firouzi M & Sanguinetti MC (2010). Modification of hERG1 channel gating by Cd^{2+}. *J Gen Physiol* **136,** 203–224.

Adaixo R, Harley CA, Castro-Rodrigues AF & Morais-Cabral JH (2013). Structural Properties of PAS Domains from the KCNH Potassium Channels ed. Zhang Z. *PLoS One* **8,** e59265.

Aggarwal SK & MacKinnon R (1996). Contribution of the S4 segment to gating charge in the Shaker K^+ channel. *Neuron* **16,** 1169–1177.

Ahern CA & Horn R (2005). Focused electric field across the voltage sensor of potassium channels. *Neuron* **48,** 25–29.

Al-Owais M, Bracey K & Wray D (2009). Role of intracellular domains in the function of the herg potassium channel. *Eur Biophys J* **38,** 569–576.

Anderson SE, Cala PM, Steenbergen C, London RE & Murphy E (1991). Effects of hypoxia and acidification on myocardial Na and Ca. Role of Na-H and Na-Ca exchange. *Ann N Y Acad Sci* **639,** 453–455.

Antzelevitch C & Burashnikov A (2011). Overview of Basic Mechanisms of Cardiac Arrhythmia. *Card Electrophysiol Clin* **3,** 23–45.

Anumonwo JMB, Horta J, Delmar M, Taffet SM & Jalife J (1999). Proton and zinc effects on HERG currents. *Biophys J* **77,** 282–298.

Arnaout R, Ferrer T, Huisken J, Spitzer K, Stainier DYR, Tristani-Firouzi M & Chi NC (2007). Zebrafish model for human long QT syndrome. *Proc Natl Acad Sci U S A* **104,** 11316–11321.

Baartscheer A, Schumacher CA & Fiolet JWT (1997). Small changes of cytosolic sodium in rat ventricular myocytes measured with SBFI in emission ratio mode. *J Mol Cell Cardiol* **29,** 3375–3383.

Bakkers J (2011). Zebrafish as a model to study cardiac development and human cardiac disease. *Cardiovasc Res* **91,** 279–288.

Bers DM (2002). Cardiac excitation-contraction coupling. *Nature* **415,** 198–205.

Bers DM & Despa S (2009). Na^+ transport in cardiac myocytes; Implications for excitation-contraction coupling. *IUBMB Life* **61,** 215–221.

Bérubé J, Chahine M & Daleau P (1999). Modulation of HERG potassium channel properties by external pH. *Pflugers Arch Eur J Physiol* **438,** 419–422.

Bethell HW, Vandenberg JI, Smith GA & Grace AA (1998). Changes in ventricular repolarization during acidosis and low-flow ischemia. *Am J Physiol* **275,** H551–H561.

Bett GCL & Rasmusson RL (2003). Functionally-distinct proton-binding in HERG suggests the presence of two binding sites. *Cell Biochem Biophys* **39,** 183–193.

Bezanilla F (2000). The voltage sensor in voltage-dependent ion channels. *Physiol Rev* **80,** 555–592.

Bezanilla F, Perozo E, Papazian D & Stefani E (1991). Molecular basis of gating charge immobilization in Shaker potassium channels. *Science (80-)* **254,** 679–683.

Blaustein MP & Lederer WJ (1999). Sodium/calcium exchange: its physiological implications. *Physiol Rev* **79,** 763–854.

Blunck R & Batulan Z (2012). Mechanism of electromechanical coupling in voltage-gated potassium channels. *Front Pharmacol* **3 SEP,** 1–16.

Brelidze TI, Carlson AE, Sankaran B & Zagotta WN (2012). Structure of the carboxy-terminal region of a KCNH channel. *Nature* **481,** 530–533.

Brelidze TI, Gianulis EC, DiMaio F, Trudeau MC & Zagotta WN (2013). Structure of the C-terminal region of an ERG channel and functional implications. *Proc Natl Acad Sci* **110,** 11648–11653.

Bruening-Wright A & Larsson HP (2007). Slow Conformational Changes of the Voltage Sensor during the Mode Shift in Hyperpolarization-Activated Cyclic-Nucleotide-Gated Channels. *J Neurosci* **27,** 270–278.

Brum G, Ríos E & Stéfani E (1988). Effects of extracellular calcium on calcium movements of excitation-contraction coupling in frog skeletal muscle fibres. *J Physiol* **398,** 441–473.

Brum G, Stefani E & Rios E (1987). Simultaneous measurements of Ca^{2+} currents and intracellular Ca^{2+} concentrations in single skeletal muscle fibers of the frog. *Can J Physiol Pharmacol* **65,** 681–685.

Cabral JHM, Lee A, Cohen SL, Chait BT, Li M & Mackinnon R (1998). Crystal Structure and Functional Analysis of the HERG Potassium Channel N Terminus. *Cell* **95,** 649–655.

Carmeliet E et al. (1999). Cardiac ionic currents and acute ischemia: from channels to arrhythmias. *Physiol Rev* **79,** 917–1017.

Carmeliet E (2004). Intracellular Ca^{2+} concentration and rate adaptation of the cardiac action potential. *Cell Calcium* **35,** 557–573.

Cha A & Bezanilla F (1997). Characterizing voltage-dependent conformational changes in the Shaker K^+ channel with fluorescence. *Neuron* **19,** 1127–1140.

Cha A & Bezanilla F (1998). Structural Implications of Fluorescence Quenching in the *Shaker* K^+ Channel. *J Gen Physiol* **112,** 391–408.

Chen J, Zou A, Splawski I, Keating MT & Sanguinetti MC (1999). Long QT syndrome-

associated mutations in the Per-Arnt-Sim (PAS) domain of HERG potassium channels accelerate channel deactivation. *J Biol Chem* **274,** 10113–10118.

Chen XH, Bezprozvanny I & Tsien RW (1996). Molecular basis of proton block of L-type Ca^{2+} channels. *J Gen Physiol* **108,** 363–374.

Cheng H, Smith GL, Orchard CH & Hancox JC (2009). Acidosis inhibits spontaneous activity and membrane currents in myocytes isolated from the rabbit atrioventricular node. *J Mol Cell Cardiol* **46,** 75–85.

Cheng YM, Hull CM, Niven CM, Qi J, Allard CR & Claydon TW (2013). Functional interactions of voltage sensor charges with an S2 hydrophobic plug in hERG channels. *J Gen Physiol* **142,** 289–303.

Clarke K, Stewart LC, Neubauer S, Balschi JA, Smith TW, Ingwall JS, Nédélec J -F, Humphrey SM, Kléber AG & Springer CS (1993). Extracellular volume and transsarcolemmal proton movement during ischemia and reperfusion: A31P NMR spectroscopic study of the isovolumic rat heart. *NMR Biomed* **6,** 278–286.

Claydon TW, Boyett MR, Sivaprasadarao a & Orchard CH (2002). Two pore residues mediate acidosis-induced enhancement of C-type inactivation of the Kv1.4 K(+) channel. *Am J Physiol Cell Physiol* **283,** C1114-21.

Claydon TW, Boyett MR, Sivaprasadarao A, Ishii K, Owen JM, O'Beirne HA, Leach R, Komukai K & Orchard CH (2000). Inhibition of the K^+ channel Kv1.4 by acidosis: Protonation of an extracellular histidine slows the recovery from N-type inactivation. *J Physiol* **526,** 253–264.

Claydon TW & Fedida D (2007). Voltage clamp fluorimetry studies of mammalian voltage-gated K^+ channel gating. *Biochem Soc Trans* **35,** 1080–1082.

Curran ME, Splawski I, Timothy KW, Vincen GM, Green ED & Keating MT (1995). A molecular basis for cardiac arrhythmia: HERG mutations cause long QT syndrome. *Cell* **80,** 795–803.

Dong D-L, Li Z, Wang H-Z, Du Z-M, Song W-H & Yang B-F (2004). Acidification alters antiarrhythmic drug blockade of the ether-a-go-go-related Gene (HERG) Channels. *Basic Clin Pharmacol Toxicol* **94,** 209–212.

Doyle DA, Cabral JM, Pfuetzner RA, Kuo A, Gulbis JM, Cohen SL, Chait BT & MacKinnon R (1998). The structure of the potassium channel: Molecular basis of K^+ conduction and selectivity. *Science (80-)* **280,** 69–77.

Du CY, Adeniran I, Cheng H, Zhang YH, El Harchi A, McPate MJ, Zhang H, Orchard CH & Hancox JC (2010). Acidosis Impairs the Protective Role of hERG K^+ Channels Against Premature Stimulation. *J Cardiovasc Electrophysiol* **21,** 1160–1169.

Du CY, El Harchi A, McPate MJ, Orchard CH & Hancox JC (2011*a*). Enhanced inhibitory effect of acidosis on hERG potassium channels that incorporate the hERG1b isoform. *Biochem Biophys Res Commun* **405,** 222–227.

Du CY, El Harchi A, Zhang YH, Orchard CH & Hancox JC (2011*b*). Pharmacological inhibition of the hERG potassium channel is modulated by extracellular but not intracellular acidosis. *J Cardiovasc Electrophysiol* **22,** 1163–1170.

Ehrenstein G (2001). Surface Charge. *Biophys Textb Online*.

Elinder F, Männikkö R, Pandey S & Larsson HP (2006). Mode shifts in the voltage gating of the mouse and human HCN2 and HCN4 channels. *J Physiol* **575,** 417–431.

Elliott DJS, Dondas NY, Munsey TS & Sivaprasadarao A (2009). Movement of the s4 segment in the herg potassium channel during membrane depolarization. *Mol Membr Biol* **26,** 435–447.

Es-Salah-Lamoureux Z, Fougere R, Xiong PY, Robertson GA & Fedida D (2010). Fluorescence-tracking of activation gating in human ERG channels reveals rapid S4 movement and slow pore opening ed. Nitabach MN. *PLoS One* **5,** e10876.

Fernández-Trillo J, Barros F, Machín A, Carretero L, Domínguez P & de la Peña P (2011). Molecular determinants of interactions between the N-terminal domain and the transmembrane core that modulate hERG K^+ channel gating ed. Attali B. *PLoS One* **6,** e24674.

Fernandez D, Ghanta A, Kinard KI & Sanguinetti MS (2005). Molecular mapping of a site Cd^{2+}-induced modification of human ether-à-go-go-related gene (hERG) channel activation. *J Physiol* **567,** 737–755.

Ferrer T, Rupp J, Piper DR & Tristani-Firouzi M (2006). The S4-S5 linker directly couples voltage sensor movement to the activation gate in the human ether-a-go-go-related gene (hERG) K^+ channel. *J Biol Chem* **281,** 12858–12864.

Firek L & Weingart R (1995). Modification of gap junction conductance by divalent cations and protons in neonatal rat heart cells. *J Mol Cell Cardiol* **27,** 1633–1643.

Frankenhaeuser B & Hodgkin AL (1957). Frankenhaeuser, Hodgkin - 1957 - The action of calcium on the electrical properties of squid axons(2).pdf. *J Physiol* **137,** 8–244.

FRANZ MR (2003). The Electrical Restitution Curve Revisited:. Steep or Flat Slope-Which is Better? *J Cardiovasc Electrophysiol* **14,** S140–S147.

Gagnon DG & Bezanilla F (2009). A single charged voltage sensor is capable of gating the *Shaker* K^+ channel. *J Gen Physiol* **133,** 467–483.

Gilbert DL & Ehrenstein G (1969). Effect of Divalent Cations on Potassium Conductance of Squid Axons: Determination of Surface Charge. *Biophys J* **9,** 447–463.

Glitsch HG & Tappe A (1995). Change of Na^+ pump current reversal potential in sheep cardiac Purkinje cells with varying free energy of ATP hydrolysis. *J Physiol* **484 (Pt 3,** 605–616.

Goldin AL (1991). Chapter 25 Expression of Ion Channels by Injection of mRNA into Xenopus Oocytes. *Methods Cell Biol* **36,** 487–509.

Gong Q, Anderson CL, January CT & Zhou Z (2002). Role of glycosylation in cell surface expression and stability of HERG potassium channels. *Am J Physiol Heart Circ Physiol* **283,** H77-84.

Goodchild SJ & Fedida D (2014). Gating charge movement precedes ionic current activation in hERG channels. *Channels* **8,** 84–89.

Goodchild SJ, Macdonald LC & Fedida D (2015). Sequence of gating charge movement and pore gating in hERG activation and deactivation pathways. *Biophys J* **108,** 1435–1447.

Gustina AS & Trudeau MC (2009). A recombinant N-terminal domain fully restores deactivation gating in N-truncated and long QT syndrome mutant hERG potassium channels. *Proc Natl Acad Sci U S A* **106,** 13082–13087.

Gustina AS & Trudeau MC (2011). hERG potassium channel gating is mediated by N- and C-terminal region interactions. *J Gen Physiol* **137,** 315–325.

Gustina AS & Trudeau MC (2012). HERG potassium channel regulation by the N-terminal eag domain. *Cell Signal* **24,** 1592–1598.

Gutman GA, Chandy KG, Grissmer S, Lazdunski M, McKinnon D, Pardo LA, Robertson GA, Rudy B, Sanguinetti MC, Stühmer W & Wang X (2005). International Union of Pharmacology. LIII. Nomenclature and molecular relationships of voltage-gated potassium channels. *Pharmacol Rev* **57,** 473–508.

Haddad G a & Blunck R (2011). Mode shift of the voltage sensors in Shaker K^+ channels is caused by energetic coupling to the pore domain. *J Gen Physiol* **137,** 455–472.

Haitin Y, Carlson AE & Zagotta WN (2013). The structural mechanism of KCNH-channel regulation by the eag domain. *Nature* **501,** 444–448.

Hardman RM, Stansfeld PJ, Dalibalta S, Sutcliffe MJ & Mitcheson JS (2007). Activation gating of hERG potassium channels: S6 glycines are not required as gating hinges. *J Biol Chem* **282,** 31972–31981.

Harris TK & Turner GJ (2002). Structural basis of perturbed pKa values of catalytic groups in enzyme active sites. *IUBMB Life* **53,** 85–98.

Hassel D, Scholz EP, Trano N, Friedrich O, Just S, Meder B, Weiss DL, Zitron E, Marquart S, Vogel B, Karle CA, Seemann G, Fishman MC, Katus HA & Rottbauer W (2008). Deficient zebrafish ether-à-go-go-related gene channel gating causes short-QT syndrome in zebrafish reggae mutants. *Circulation* **117,** 866–875.

Hassinen M, Haverinen J, Hardy ME, Shiels HA & Vornanen M (2015). Inward rectifier potassium current (IK1) and Kir2 composition of the zebrafish (Danio rerio) heart. *Pflugers Arch* **467,** 2437–2446.

Heasman J (2002). Morpholino oligos: making sense of antisense? *Dev Biol* **243,** 209–214.

Henke G, Maier G, Wallisch S, Boehmer C & Lang F (2004). Regulation of the voltage gated K^+ channel Kv1.3 by the ubiquitin ligase Nedd4-2 and the serum and glucocorticoid inducible kinase SGK1. *J Cell Physiol* **199,** 194–199.

Hille B (2001). Hille 2001 (Ion channels of excitable membranes).pdf. 1–37.

Ho WK, Kim I, Lee CO & Earm YE (1998). Voltage-dependent blockade of HERG channels expressed in Xenopus oocytes by external Ca^{2+} and Mg^{2+}. *J Physiol* **507,** 631–638.

Hoekstra M, Mummery CL, Wilde AAM, Bezzina CR & Verkerk AO (2012). Induced pluripotent stem cell derived cardiomyocytes as models for cardiac arrhythmias. *Front Physiol* **3,** 1–14.

Hondeghem LM, Carlsson L & Duker G (2001*a*). Instability and Triangulation of the Action Potential Predict Serious Proarrhythmia, but Action Potential Duration Prolongation Is Antiarrhythmic. *Circulation* **103,** 2004–2013.

Hondeghem LM, Dujardin K & De Clerck F (2001*b*). Phase 2 prolongation, in the absence of instability and triangulation, antagonizes class III proarrhythmia. *Cardiovasc Res* **50,** 345–353.

Hoshi T & Armstrong CM (2012). Initial steps in the opening of a Shaker potassium channel. *Proc Natl Acad Sci* **109,** 12800–12804.

Hoshi T & Armstrong CM (2013). C-type inactivation of voltage-gated K^+ channels: pore constriction or dilation? *J Gen Physiol* **141,** 151–160.

Hoshi T, Zagotta WN & Aldrich RW (1990). Biophysical and molecular mechanisms of Shaker potassium channel inactivation. *Science* **250,** 533–538.

Hoshi T, Zagotta WN & Aldrich RW (1991). Two types of inactivation in Shaker K^+ channels: effects of alterations in the carboxy-terminal region. *Neuron* **7,** 547–556.

Hoshi T, Zagotta WN & Aldrich RW (1994). Shaker potassium channel gating. I: Transitions near the open state. *J Gen Physiol* **103,** 249–278.

Hu N, Yost HJ & Clark EB (2001). Cardiac morphology and blood pressure in the adult zebrafish. *Anat Rec* **264,** 1–12.

Hull CM, Sokolov S, Van Slyke AC & Claydon TW (2014). Regional flexibility in the S4–S5 linker regulates hERG channel closed-state stabilization. *Pflugers Arch Eur J Physiol* **466,** 1911–1919.

Hwang WY, Fu Y, Reyon D, Maeder ML, Tsai SQ, Sander JD, Peterson RT, Yeh J-RJ & Joung JK (2013). Efficient genome editing in zebrafish using a CRISPR-Cas system. *Nat Biotechnol* **31,** 227–229.

Islas LD (2016). Functional diversity of potassium channel voltage-sensing domains. *Channels* **10,** 202–213.

Ismailov II & Benos DJ (1995). Effects of phosphorylation on ion channel function. *Kidney Int* **48,** 1167–1179.

Ito H, Vereecke J & Carmeliet E (1992). Intracellular protons inhibit inward rectifier K^+ channel of guinea-pig ventricular cell membrane. *Pflügers Arch Eur J Physiol* **422,** 280–286.

Janse MJ & Wit AL (1989). Electrophysiological mechanisms of ventricular arrhythmias resulting from myocardial ischemia and infarction. *Physiol Rev* **69,** 1049–1169.

Jasti J, Furukawa H, Gonzales EB & Gouaux E (2007). Structure of acid-sensing ion channel 1 at 1.9 Å resolution and low pH. *Nature* **449,** 316–323.

Jiang M, Dun W & Tseng GN (1999). Mechanism for the effects of extracellular acidification on HERG-channel function. *Am J Physiol* **277,** H1283-92.

Jo SH, Youm JB, Kim I, Lee CO, Earm YE & Ho WK (1999). Blockade of HERG channels expressed in Xenopus oocytes by external H^+. *Pflugers Arch Eur J Physiol* **438,** 23–29.

John RM, Taggart PI, Sutton PM, Costa DC, Ell PJ & Swanton H (1991). Endocardial monophasic action potential recordings for the detection of myocardial ischemia in man: a study using atrial pacing stress and myocardial perfusion scintigraphy. *Am Heart J* **122,** 1599–1609.

Johnson JP, Balser JR & Bennett PB (1999*a*). Enhancement of HERG K^+ currents by Cd^{2+} destabilization of the inactivated state. *Biophys J* **77,** 2534–2541.

Johnson JP, Balser JR & Bennett PB (2001). A novel extracellular calcium sensing mechanism in voltage-gated potassium ion channels. *J Neurosci* **21,** 4143–4153.

Johnson JP, Mullins FM & Bennett PB (1999*b*). Human ether-à-go-go-related gene K^+ channel gating probed with extracellular Ca^{2+}. Evidence for two distinct voltage sensors. *J Gen Physiol* **113,** 565–580.

Jones DK, Liu F, Vaidyanathan R, Eckhardt LL, Trudeau MC & Robertson GA (2014). hERG 1b is critical for human cardiac repolarization. *Proc Natl Acad Sci* **111,** 18073–18077.

Jones DK, Peters CH, Tolhurst SA, Claydon TW & Ruben PC (2011). Extracellular proton modulation of the cardiac voltage-gated sodium channel, NaV1.5. *Biophys J* **101,** 2147–2156.

Kameyama M, Kakei M, Sato R, Shibasaki T, Matsuda H & Irisawa H (1984). Intracellular Na^+ activates a K^+ channel in mammalian cardiac cells. *Nature* **309,** 354–356.

Kang J, Chen X, Wang H, Ji J, Cheng H, Incardona J, Reynolds W, Viviani F, Tabart M & Rampe D (2005). Discovery of a Small Molecule Activator of the Human. *Mol Pharmacol* **67,** 827–836.

Kaplan P, Hendrikx M, Mattheussen M, Mubagwa K & Flameng W (1992). Effect of ischemia and reperfusion on sarcoplasmic reticulum calcium uptake. *Circ Res* **71,** 1123–1130.

Kaplan WD & Trout WE (1969). The behavior of four neurological mutants of Drosophila. *Genetics* **61,** 399–409.

Karmazyn M, Gan XT, Humphreys RA, Yoshida H & Kusumoto K (1999). The myocardial Na^+-H^+ exchange: structure, regulation, and its role in heart disease. *Circ Res* **85,** 777–786.

Kazmierczak M, Zhang X, Chen B, Mulkey DK, Shi Y, Wagner PG, Pivaroff-Ward K, Sassic JK, Bayliss DA & Jegla T (2013). External pH modulates EAG superfamily K^+ channels through EAG-specific acidic residues in the voltage sensor. *J Gen Physiol* **141,** 721–735.

Kehl SJ, Eduljee C, Kwan DCH, Zhang S & Fedida D (2002). Molecular determinants of the inhibition of human Kv1.5 potassium currents by external protons and Zn^{2+}. *J Physiol* **541,** 9–24.

Kenigsberg DN, Khanal S, Kowalski M & Krishnan SC (2007). Prolongation of the QTc Interval Is Seen Uniformly During Early Transmural Ischemia. *J Am Coll Cardiol* **49,** 1299–1305.

Khan A, Kyle JW, Hanck DA, Lipkind GM & Fozzard HA (2006). Isoform-dependent interaction of voltage-gated sodium channels with protons. *J Physiol* **576,** 493–501.

Kléber AG (2000). ST-segment elevation in the electrocardiogram: a sign of myocardial ischemia. *Cardiovasc Res* **45,** 111–118.

Korn SJ & Trapani JG (2005). Potassium channels. *IEEE Trans Nanobioscience* **4,** 21–33.

Krafte DS & Kass RS (1988). Hydrogen ion modulation of Ca channel current in cardiac ventricular cells. Evidence for multiple mechanisms. *J Gen Physiol* **91,** 641–657.

Kurz RW, Ren XL & Franz MR (1994). Dispersion and delay of electrical restitution in the globally ischaemic heart. *Eur Heart J* **15,** 547–554.

Kuzmenkin A, Bezanilla F & Correa AM (2004). Gating of the Bacterial Sodium Channel, NaChBac. *J Gen Physiol* **124,** 349–356.

de la Peña P, Alonso-Ron C, Machín A, Fernández-Trillo J, Carretero L, Domínguez P & Barros F (2011). Demonstration of physical proximity between the N terminus and the S4-S5 linker of the human ether-a-go-go-related gene (hERG) potassium channel. *J Biol Chem* **286,** 19065–19075.

de la Peña P, Domínguez P & Barros F (2018). Gating mechanism of Kv11.1 (hERG) K^+ channels without covalent connection between voltage sensor and pore domains. *Pflugers Arch* **470,** 517–536.

de la Peña P, Machín A, Fernández-Trillo J, Domínguez P & Barros F (2013). Mapping of interactions between the N- and C-termini and the channel core in HERG K^+ channels. *Biochem J* **451,** 463–474.

de la Peña P, Machín A, Fernández-Trillo J, Domínguez P & Barros F (2015). Interactions between the N-terminal tail and the gating machinery of hERG K^+ channels both in closed and open/inactive states. *Pflugers Arch Eur J Physiol* **467,** 1747–1756.

Labro AJ, Lacroix JJ, Villalba-Galea CA, Snyders DJ & Bezanilla F (2012). Molecular mechanism for depolarization-induced modulation of Kv channel closure. *J Gen Physiol* **140,** 481–493.

Labro AJ & Snyders DJ (2012). Being flexible: The voltage-controllable activation gate of Kv channels. *Front Pharmacol* **3 SEP,** 1–12.

Lacroix JJ, Labro AJ & Bezanilla F (2011). Properties of deactivation gating currents in Shaker channels. *Biophys J* **100,** L28–L30.

Langheinrich U, Vacun G & Wagner T (2003). Zebrafish embryos express an orthologue of HERG and are sensitive toward a range of QT-prolonging drugs inducing severe arrhythmia. *Toxicol Appl Pharmacol* **193,** 370–382.

Lecar H, Larsson HP & Grabe M (2003). Electrostatic Model of S4 Motion in Voltage-Gated Ion Channels. *Biophys J* **85,** 2854–2864.

Leem CH, Lagadic-Gossmann D & Vaughan-Jones RD (1999). Characterization of intracellular pH regulation in the guinea-pig ventricular myocyte. *J Physiol* **517,** 159–180.

Leong IUS, Skinner JR, Shelling AN & Love DR (2010*a*). Zebrafish as a model for long QT syndrome: the evidence and the means of manipulating zebrafish gene expression. *Acta Physiol (Oxf)* **199,** 257–276.

Leong IUS, Skinner JR, Shelling AN & Love DR (2010*b*). Identification and expression analysis of kcnh2 genes in the zebrafish. *Biochem Biophys Res Commun* **396,** 817–824.

Lin C, Cvetanovic I, Ke X, Ranade V & Somberg J (2005*a*). A mechanism for the potential proarrhythmic effect of acidosis, bradycardia, and hypokalemia on the blockade of human ether-a-go-go-related gene (HERG) channels. *Am J Ther* **12,** 328–336.

Lin C, Ke X, Cvetanovic I, Ranade V & Somberg J (2005*b*). The influence of extracellular acidosis on the effect of IKr blockers. *J Cardiovasc Pharmacol Ther* **10,** 67–76.

Lin E, Craig C, Lamothe M, Sarunic M V., Beg MF & Tibbits GF (2015). Construction and use of a zebrafish heart voltage and calcium optical mapping system, with integrated electrocardiogram and programmable electrical stimulation. *Am J Physiol - Regul Integr Comp Physiol* **308,** R755–R768.

Lin E, Ribeiro A, Ding W, Hove-Madsen L, Sarunic M V., Beg MF & Tibbits GF (2014). Optical mapping of the electrical activity of isolated adult zebrafish hearts: acute effects of temperature. *AJP Regul Integr Comp Physiol* **306,** R823–R836.

Lin MCA & Papazian DM (2007). Differences between ion binding to eag and herg voltage sensors contribute to differential regulation of activation and deactivation gating. *Channels* **1,** 429–437.

Liu J, Zhang M, Jiang M & Tseng G-N (2003). Negative Charges in the Transmembrane Domains of the HERG K Channel Are Involved in the Activation- and Deactivation-gating Processes. *J Gen Physiol* **121,** 599–614.

Long SB (2005). Voltage Sensor of Kv1.2: Structural Basis of Electromechanical Coupling. *Science (80-)* **309,** 903–908.

Long SB, Campbell EB & Mackinnon R (2005). Crystal structure of a mammalian voltage-dependent Shaker family K^+ channel. *Science* **309,** 897–903.

Long SB, Tao X, Campbell EB & MacKinnon R (2007). Atomic structure of a voltage-dependent K^+ channel in a lipid membrane-like environment. *Nature* **450,** 376–382.

López-Barneo J, Hoshi T, Heinemann SH & Aldrich RW (1993). Effects of external cations and mutations in the pore region on C-type inactivation of Shaker potassium channels. *Receptors Channels* **1,** 61–71.

Lörinczi É, Gómez-Posada JC, De La Peña P, Tomczak AP, Fernández-Trillo J, Leipscher U, Stühmer W, Barros F & Pardo LA (2015). Voltage-dependent gating of KCNH potassium channels lacking a covalent link between voltage-sensing and pore domains. *Nat Commun* **6,** 6672.

Lu HR, Vlaminckx E, Hermans AN, Rohrbacher J, Van Ammel K, Towart R, Pugsley M & Gallacher DJ (2008). Predicting drug-induced changes in QT interval and arrhythmias: QT-shortening drugs point to gaps in the ICHS7B Guidelines. *Br J Pharmacol* **154,** 1427–1438.

Lu Z, Klem AM & Ramu Y (2002). Coupling between voltage sensors and activation gate in voltage-gated K^+ channels. *J Gen Physiol* **120,** 663–676.

MacKinnon R & Yellen G (1990). Mutations affecting TEA blockade and ion permeation in voltage-activated K^+ channels. *Science* **250,** 276–279.

Männikkö R, Pandey S, Larsson HP & Elinder F (2005). Hysteresis in the Voltage Dependence of HCN Channels. *J Gen Physiol* **125,** 305–326.

Mannuzzu LM, Moronne MM & Isacoff EY (1996). Direct physical measure of conformational rearrangement underlying potassium channel gating. *Science (80-)* **271,** 373.

Marques-Carvalho MJ, Sahoo N, Muskett FW, Vieira-Pires RS, Gabant G, Cadene M, Schönherr R & Morais-Cabral JH (2012). Structural, biochemical, and functional characterization of the cyclic nucleotide binding homology domain from the mouse

EAG1 potassium channel. *J Mol Biol* **423,** 34–46.

Milan DJ, Peterson TA, Ruskin JN, Peterson RT & MacRae CA (2003). Drugs that induce repolarization abnormalities cause bradycardia in zebrafish. *Circulation* **107,** 1355–1358.

Milberg P, Hilker E, Ramtin S, Cakir Y, Stypmann J, Engelen MA, Mönnig G, Osada N, Breithardt G, Haverkamp W & Eckardt L (2007). Proarrhythmia as a class effect of quinolones: Increased dispersion of repolarization and triangulation of action potential predict torsades de pointes. *J Cardiovasc Electrophysiol* **18,** 647–654.

Mitcheson JS, Chen J, Lin M, Culberson C & Sanguinetti MC (2000). A structural basis for drug-induced long QT syndrome. *Proc Natl Acad Sci* **97,** 12329–12333.

Muskett FW, Thouta S, Thomson SJ, Bowen A, Stansfeld PJ & Mitcheson JS (2011). Mechanistic insight into human ether-à-go-go-related gene (hERG) K^+ channel deactivation gating from the solution structure of the EAG domain. *J Biol Chem* **286,** 6184–6191.

Nakajima T, Furukawa T, Tanaka T, Katayama Y, Nagai R, Nakamura Y & Hiraoka M (1998). Novel mechanism of HERG current suppression in LQT2: shift in voltage dependence of HERG inactivation. *Circ Res* **83,** 415–422.

Nemtsas P, Wettwer E, Christ T, Weidinger G & Ravens U (2010). Adult zebrafish heart as a model for human heart? An electrophysiological study. *J Mol Cell Cardiol* **48,** 161–171.

Ng CA, Hunter MJ, Perry MD, Mobli M, Ke Y, Kuchel PW, King GF, Stock D & Vandenberg JI (2011). The N-terminal tail of hERG contains an amphipathic α-helix that regulates channel deactivation ed. Uversky VN. *PLoS One* **6,** e16191.

Ng CA, Perry MD, Tan PS, Hill AP, Kuchel PW & Vandenberg JI (2012). The S4-S5 linker acts as a signal integrator for hERG K^+ channel activation and deactivation gating ed. Attali B. *PLoS One* **7,** e31640.

Ng CA, Phan K, Hill AP, Vandenberg JI & Perry MD (2014). Multiple interactions between cytoplasmic domains regulate slow deactivation of Kv11.1 channels. *J Biol Chem* **289,** 25822–25832.

Nichols CG, Ripoll C & Lederer WJ (1991). ATP-Sensitive potassium channel modulation of the guinea pig ventricular action potential and contraction. *Circ Res* **68,** 280–287.

Noble D & Tsien RW (1969). Outward membrane currents activated in the plateau range of potentials in cardiac Purkinje fibres. *J Physiol* **200,** 205–231.

Noma A (1983). ATP-regulated K^+ channels in cardiac muscle. *Nature* **305,** 147–148.

Orchard CH & Cingolani HE (1994). Acidosis and arrhythmias in cardiac muscle. *Cardiovasc Res* **28,** 1312–1319.

Papazian DM, Shao XM, Seoh SA, Mock AF, Huang Y & Wainstock DH (1995). Electrostatic interactions of S4 voltage sensor in shaker K^+ channel. *Neuron* **14,** 1293–1301.

Paquette T, Clay JR, Ogbaghebriel A & Shrier A (1998). Effects of divalent cations on the E-4031-sensitive repolarization current, I(Kr), in rabbit ventricular myocytes. *Biophys J* **74,** 1278–1285.

Peretz A, Schottelndreier H, Aharon-Shamgar L Ben & Attali B (2002). Modulation of homomeric and heteromeric kcnq1 channels by external acidification. *J Physiol* **545,** 751–766.

Pérez-Cornejo P (1999). H^+ ion modulation of C-type inactivation of Shaker K^+ channels. *Pflugers Arch Eur J Physiol* **437,** 865–870.

Perry M, Sachse FB, Abbruzzese J & Sanguinetti MC (2009). PD-118057 contacts the pore helix of hERG1 channels to attenuate inactivation and enhance K^+ conductance. *Proc Natl Acad Sci U S A* **106,** 20075–20080.

Perry M, Sanguinetti M & Mitcheson J (2010). Revealing the structural basis of action of hERG potassium channel activators and blockers. *J Physiol* **588,** 3157–3167.

Perry M & Sanguinetti MC (2008). A single amino acid difference between ether-a-go-go- related gene channel subtypes determines differential sensitivity to a small molecule activator. *Mol Pharmacol* **73,** 1044–1051.

Perry MD, Ng CA, Phan K, David E, Steer K, Hunter MJ, Mann SA, Imtiaz M, Hill AP, Ke Y & Vandenberg JI (2016). Rescue of protein expression defects may not be enough to abolish the pro-arrhythmic phenotype of long QT type 2 mutations. *J Physiol* **594,** 4031–4049.

Piper DR, Hinz WA, Tallurri CK, Sanguinetti MC & Tristani-Firouzi M (2005). Regional specificity of human ether-a-go-go-related gene channel activation and inactivation gating. *J Biol Chem* **280,** 7206–7217.

Piper DR, Rupp J, Sachse FB, Sanguinetti MC & Tristani-Firouzi M (2008). Cooperative interactions between R531 and acidic residues in the voltage sensing module of hERG1 channels. *Cell Physiol Biochem* **21,** 37–46.

Piper DR, Varghese A, Sanguinetti MC & Tristani-Firouzi M (2003). Gating currents associated with intramembrane charge displacement in HERG potassium channels. *Proc Natl Acad Sci* **100,** 10534–10539.

Poon KL & Brand T (2013). The zebrafish model system in cardiovascular research: A tiny fish with mighty prospects. *Glob Cardiol Sci Pract* **2013,** 4.

Priest MF, Lacroix JJ, Villalba-Galea CA & Bezanilla F (2013). S3-s4 linker length modulates the relaxed state of a Voltage-gated potassium channel. *Biophys J* **105,** 2312–2322.

Prod'hom B, Pietrobon D & Hess P (1989). Interactions of protons with single open L-

type calcium channels. Location of protonation site and dependence of proton-induced current fluctuations on concentration and species of permeant ion. *J Gen Physiol* **94,** 23–42.

R.W.Kurz, R.Mohabir, X.L.Ren & M.R.Franz (1993). Ischaemia induced alternans of action potential duration in the intact-heart:dependence on coronary flow, preload and cycle length. *Eur Heart J* **14,** 1410–1420.

Ramsey IS, Mokrab Y, Carvacho I, Sands ZA, Sansom MSP & Clapham DE (2010). An aqueous H^+ permeation pathway in the voltage-gated proton channel Hv1. *Nat Struct Mol Biol* **17,** 869–875.

Rasmusson RL, Morales MJ, Wang S, Liu S, Campbell DL, Brahmajothi M V & Strauss HC (1998). Inactivation of voltage-gated cardiac K^+ channels. *Circ Res* **82,** 739–750. Available at: http://www.ncbi.nlm.nih.gov/pubmed/9562433.

Root MJ & MacKinnon R (1994). Two identical noninteracting sites in an ion channel revealed by proton transfer. *Science* **265,** 1852–1856.

Rosa VD La, Bennett AL & Ramsey IS (2018). Coupling between an electrostatic network and the Zn^{2+} binding site modulates Hv1 activation. *J Gen Physiol*1–19.

Rulíšek L & Vondrášek J (1998). Coordination geometries of selected transition metal ions (Co^{2+}, Ni^{2+}, Cu^{2+}, Zn^{2+}, Cd^{2+}, and Hg^{2+}) in metalloproteins. *J Inorg Biochem* **71,** 115–127.

Sanguinetti MC, Curran ME, Spector PS & Keating MT (1996). Spectrum of HERG K^+-channel dysfunction in an inherited cardiac arrhythmia. *Proc Natl Acad Sci* **93,** 2208–2212.

Sanguinetti MC, Jiang C, Curran ME & Keating MT (1995). A mechanistic link between an inherited and an acquird cardiac arrthytmia: HERG encodes the IKr potassium channel. *Cell* **81,** 299–307.

Sanguinetti MC & Jurkiewicz NK (1990). Two components of cardiac delayed rectifier K^+ current. Differential sensitivity to block by class III antiarrhythmic agents. *J Gen Physiol* **96,** 195–215.

Sanguinetti MC & Tristani-Firouzi M (2006). hERG potassium channels and cardiac arrhythmia. *Nature* **440,** 463–469.

Sanguinetti MC & Xu QP (1999). Mutations of the S4-S5 linker alter activation properties of HERG potassium channels expressed in Xenopus oocytes. *J Physiol* **514,** 667–675.

Santiago-Castillo JA De, Covarrubias M, Sánchez-Rodríguez JE, Perez-Cornejo P & Arreola J (2010). Simulating complex ion channel kinetics with IonChannelLab. *Channels (Austin)* **4,** 422–428.

Scholz EP, Niemer N, Hassel D, Zitron E, Bürgers HF, Bloehs R, Seyler C, Scherer D, Thomas D, Kathöfer S, Katus HA, Rottbauer WA & Karle CA (2009). Biophysical

properties of zebrafish ether-à-go-go related gene potassium channels. *Biochem Biophys Res Commun* **381,** 159–164.

Schönherr R & Heinemann SH (1996). Molecular determinants for activation and inactivation of HERG, a human inward rectifier potassium channel. *J Physiol* **493,** 635–642.

Schönherr R, Mannuzzu LM, Isacoff EY & Heinemann SH (2002). Conformational switch between slow and fast gating modes: allosteric regulation of voltage sensor mobility in the EAG K^+ channel. *Neuron* **35,** 935–949.

Schwartz PJ, Ackerman MJ, George AL & Wilde AAM (2013). Impact of Genetics on the Clinical Management of Channelopathies. *J Am Coll Cardiol* **62,** 169–180.

Schwartz PJ, Crotti L & Insolia R (2012). Long-QT Syndrome: From Genetics to Management. *Circ Arrhythmia Electrophysiol* **5,** 868–877.

Seoh S-A, Sigg D, Papazian DM & Bezanilla F (1996). Voltage-Sensing Residues in the S2 and S4 Segments of the Shaker K^+ Channel. *Neuron* **16,** 1159–1167.

Shi YP, Cheng YM, Van Slyke AC & Claydon TW (2014). External protons destabilize the activated voltage sensor in hERG channels. *Eur Biophys J* **43,** 59–69.

Silverman WR, Roux B & Papazian DM (2003). Structural basis of two-stage voltage-dependent activation in K^+ channels. *Proc Natl Acad Sci U S A* **100,** 2935–2940.

Silverman WR, Tang CY, Mock a F, Huh KB & Papazian DM (2000). Mg^{2+} modulates voltage-dependent activation in ether-à-go-go potassium channels by binding between transmembrane segments S2 and S3. *J Gen Physiol* **116,** 663–678.

Van Slyke AC, Cheng YM, Mafi P, Allard CR, Hull CM, Shi YP & Claydon TW (2012). Proton block of the pore underlies the inhibition of hERG cardiac K^+ channels during acidosis. *Am J Physiol Physiol* **302,** C1797–C1806.

Van Slyke AC, Rezazadeh S, Snopkowski M, Shi P, Allard CR & Claydon TW (2010). Mutations within the S4–S5 Linker Alter Voltage Sensor Constraints in hERG K^+ Channels. *Biophys J* **99,** 2841–2852.

Smith PL, Baukrowitz T & Yellen G (1996). The inward rectification mechanism of the HERG cardiac potassium channel. *Nature* **379,** 833–836.

Smith PL & Yellen G (2002). Fast and slow voltage sensor movements in HERG potassium channels. *J Gen Physiol* **119,** 275–293.

Spector PS (1996). Fast inactivation causes rectification of the IKr channel. *J Gen Physiol* **107,** 611–619.

Sroubek J, Krishnan Y & McDonald T V. (2013). Sequence and structure-specific elements of HERG mRNA determine channel synthesis and trafficking efficiency. *FASEB J* **27,** 3039–3053.

Starace DM & Bezanilla F (2004). A proton pore in a potassium channel voltage sensor reveals a focused electric field. *Nature* **427,** 548–553.

Starkus JG, Varga Z, Schönherr R & Heinemann SH (2003). Mechanisms of the inhibition of Shaker potassium channels by protons. *Pflugers Arch* **447,** 44–54.

Steidl J V. & Yool AJ (1999). Differential sensitivity of voltage-gated potassium channels Kv1.5 and Kv1.2 to acidic pH and molecular identification of pH sensor. *Mol Pharmacol* **55,** 812–820.

Stengl M, Carmeliet E, Mubagwa K & Flameng W (1998). Modulation of transient outward current by extracellular protons and Cd^{2+} in rat and human ventricular myocytes. *J Physiol* **511,** 827–836.

Su Z, Limberis J, Souers A, Kym P, Mikhail A, Houseman K, Diaz G, Liu X, Martin RL, Cox BF & Gintant GA (2009). Electrophysiologic characterization of a novel hERG channel activator. *Biochem Pharmacol* **77,** 1383–1390.

Subbiah RN, Clarke CE, Smith DJ, Zhao J, Campbell TJ & Vandenberg JI (2004). Molecular basis of slow activation of the human *ether-á-go-go* related gene potassium channel. *J Physiol* **558,** 417–431.

Swartz KJ (2008). Sensing voltage across lipid membranes. *Nature* **456,** 891–897.

Swift LM, Asfour H, Posnack NG, Arutunyan A, Kay MW & Sarvazyan N (2012). Properties of blebbistatin for cardiac optical mapping and other imaging applications. *Pflugers Arch Eur J Physiol* **464,** 503–512.

Taggart P, Sutton P, Runnalls M, O'Brien W, Donaldson R, Hayward R, Swanton H, Emanuel R & Treasure T (1986). Use of monophasic action potential recordings during routine coronary-artery bypass surgery as an index of localised myocardial ischaemia. *Lancet (London, England)* **1,** 1462–1465.

Tan PS, Perry MD, Ng CA, Vandenberg JI & Hill AP (2012). Voltage-sensing domain mode shift is coupled to the activation gate by the N-terminal tail of hERG channels. *J Gen Physiol* **140,** 293–306.

Tao X, Lee A, Limapichat W, Dougherty DA & MacKinnon R (2010). A Gating Charge Transfer Center in Voltage Sensors. *Science (80-)* **328,** 67–73.

Terai T, Furukawa T, Katayama Y & Hiraoka M (2000). Effects of external acidosis on HERG current expressed in Xenopus oocytes. *J Mol Cell Cardiol* **32,** 11–21.

Thouta S, Hull CM, Shi YP, Sergeev V, Young J, Cheng YM & Claydon TW (2017). Stabilization of the Activated hERG Channel Voltage Sensor by Depolarization Involves the S4-S5 Linker. *Biophys J* **112,** 300–312.

Thouta S, Sokolov S, Abe Y, Clark SJ, Cheng YM & Claydon TW (2014). Proline scan of the hERG channel S6 helix reveals the location of the intracellular pore gate. *Biophys J* **106,** 1057–1069.

Trudeau M, Warmke J, Ganetzky B & Robertson G (1995). HERG, a human inward rectifier in the voltage-gated potassium channel family. *Science (80-)* **269,** 92–95.

ten Tusscher KHWJ (2003). A model for human ventricular tissue. *AJP Hear Circ Physiol* **286,** H1573–H1589.

Vandenberg JI, Perry MD, Perrin MJ, Mann SA, Ke Y & Hill AP (2012). hERG K^+ Channels: Structure, Function, and Clinical Significance. *Physiol Rev* **92,** 1393–1478.

Vaughan-Jones RD, Spitzer KW & Swietach P (2009). Intracellular pH regulation in heart. *J Mol Cell Cardiol* **46,** 318–331.

Vereecke J & Carmeliet E (2000). The effect of external pH on the delayed rectifying K^+ current in cardiac ventricular myocytes. *Pflügers Arch - Eur J Physiol* **439,** 739–751.

Verkerk AO, Veldkamp MW, van Ginneken AC & Bouman LN (1996). Biphasic response of action potential duration to metabolic inhibition in rabbit and human ventricular myocytes: role of transient outward current and ATP-regulated potassium current. *J Mol Cell Cardiol* **28,** 2443–2456.

Villalba-Galea CA (2014). Hv1 proton channel opening is preceded by a voltage-independent transition. *Biophys J* **107,** 1564–1572.

Villalba-Galea CA, Sandtner W, Starace DM & Bezanilla F (2008). S4-based voltage sensors have three major conformations. *Proc Natl Acad Sci* **105,** 17600–17607.

Vornanen M & Hassinen M (2016). Zebrafish heart as a model for human cardiac electrophysiology. *Channels* **10,** 101–110.

Wang DT, Hill AP, Mann S a, Tan PS & Vandenberg JI (2011). Mapping the sequence of conformational changes underlying selectivity filter gating in the Kv11.1 potassium channel. *Nat Struct Mol Biol* **18,** 35–41.

Wang J, Myers CD & Robertson GA (2000). Dynamic control of deactivation gating by a soluble amino-terminal domain in HERG K^+ channels. *J Gen Physiol* **115,** 749–758.

Wang J, Trudeau MC, Zappia AM & Robertson GA (1998). Regulation of deactivation by an amino terminal domain in human ether-à-go-go-related gene potassium channels. *J Gen Physiol* **112,** 637–647.

Wang S, Liu S, Morales MJ, Strauss HC & Rasmusson RL (1997). A quantitative analysis of the activation and inactivation kinetics of HERG expressed in Xenopus oocytes. *J Physiol* **502,** 45–60.

Wang W & MacKinnon R (2017). Cryo-EM Structure of the Open Human Ether-à-go-go-Related K+Channel hERG. *Cell* **169,** 422–430.e10.

Warmke JW & Ganetzky B (1994). A family of potassium channel genes related to eag in Drosophila and mammals. *Proc Natl Acad Sci U S A* **91,** 3438–3442.

Watanabe I, Kanda A, Engle CL & Gettes LS (1997). Comparison of the effects of regional ischemia and hyperkalemia on the membrane action potentials of the in situ pig heart. Experimental Cardiology Group, University of North Carolina at Chapel Hill. *J Cardiovasc Electrophysiol* **8,** 1229–1236.

Watanabe I, Zhu J, Recio-Pinto E & Thornhill WB (2004). Glycosylation affects the protein stability and cell surface expression of Kv1.4 but Not Kv1.1 potassium channels. A pore region determinant dictates the effect of glycosylation on trafficking. *J Biol Chem* **279,** 8879–8885.

Weiss JN, Garfinkel A, Karagueuzian HS, Chen P-S & Qu Z (2010). Early afterdepolarizations and cardiac arrhythmias. *Hear Rhythm* **7,** 1891–1899.

Weiss JN, Garfinkel A, Karagueuzian HS, Qu Z & Chen PS (1999). Chaos and the transition to ventricular fibrillation: a new approach to antiarrhythmic drug evaluation. *Circulation* **99,** 2819–2826.

Whicher JR & MacKinnon R (2016). Structure of the voltage-gated K^+ channel Eag1 reveals an alternative voltage sensing mechanism. *Science* **353,** 664–669.

Woods IG, Kelly PD, Chu F, Ngo-Hazelett P, Yan YL, Huang H, Postlethwait JH & Talbot WS (2000). A comparative map of the zebrafish genome. *Genome Res* **10,** 1903–1914.

Wu W, Gardner A & Sanguinetti MC (2015). Concatenated hERG1 tetramers reveal stoichiometry of altered channel gating by RPR-260243. *Mol Pharmacol* **87,** 401–409.

Xiao Y-F, Chandler N, Dobrzynski H, Richardson ES, Tenbroek EM, Wilhelm JJ, Sharma V, Varghese A, Boyett MR, Iaizzo PA & Sigg DC (2010). Hysteresis in human HCN4 channels: A crucial feature potentially affecting sinoatrial node pacemaking. *Sheng Li Xue Bao* **62,** 1–13.

Xu X, Recanatini M, Roberti M & Tseng G-N (2008). Probing the Binding Sites and Mechanisms of Action of Two Human Ether-a-go-go-Related Gene Channel Activators, 1,3-bis-(2-Hydroxy-5-trifluoromethyl-phenyl)-urea (NS1643) and 2-[2-(3,4-Dichloro-phenyl)-2,3-dihydro-1H-isoindol-5-ylamino]-nicotinic acid (PD3. *Mol Pharmacol* **73,** 1709–1721.

Yakovchuk P, Protozanova E & Frank-Kamenetskii MD (2006). Base-stacking and base-pairing contributions into thermal stability of the DNA double helix. *Nucleic Acids Res* **34,** 564–574.

Yan GX & Kléber a G (1992). Changes in extracellular and intracellular pH in ischemic rabbit papillary muscle. *Circ Res* **71,** 460–470.

Yu Lu M, Mahaut-Smith P, Varghese A, Huang CLH, Kemp PR & Vandenberg JI (2001). Effects of premature stimulation on HERG K^+ channels. *J Physiol* **537,** 843–851.

Zagotta W, Hoshi T & Aldrich R (1990). Restoration of inactivation in mutants of Shaker potassium channels by a peptide derived from ShB. *Science (80-)* **250,** 568–571.

Zeng H, Lozinskaya IM, Lin Z, Willette RN, Brooks DP & Xu X (2006). Mallotoxin Is a Novel Human. *Pharmacology* **319,** 957–962.

Zhang JF & Siegelbaum SA (1991). Effects of external protons on single cardiac sodium channels from guinea pig ventricular myocytes. *J Gen Physiol* **98,** 1065–1083.

Zhang M, Liu J, Jiang M, Wu DM, Sonawane K, Guy HR & Tseng GN (2005). Interactions between charged residues in the transmembrane segments of the voltage-sensing domain in the hERG channel. *J Membr Biol* **207,** 169–181.

Zhang M, Liu J & Tseng G-N (2004). Gating Charges in the Activation and Inactivation Processes of the hERG Channel. *J Gen Physiol* **124,** 703–718.

Zhang S, Kwan DCH, Fedida D & Kehl SJ (2001). External K^+ relieves the block but not the gating shift caused by Zn^{2+} in human Kv1.5 potassium channels. *J Physiol* **532,** 349–358.

Zhang X, Bursulaya B, Lee CC, Chen B, Pivaroff K & Jegla T (2009). Divalent cations slow activation of EAG family K^+ channels through direct binding to S4. *Biophys J* **97,** 110–120.

Zhao Y, Goldschen-Ohm MP, Morais-Cabral JH, Chanda B & Robertson GA (2017). The intrinsically liganded cyclic nucleotide-binding homology domain promotes KCNH channel activation. *J Gen Physiol* **149,** 249–260.

Zhou J (2005). Novel Potent hERG Potassium Channel Enhancers And Their In Vitro Antiarrhythmic Activity. *Mol Pharmacol* **68,** 876–884.

Zhou Q & Bett GCL (2010). Regulation of the voltage-insensitive step of HERG activation by extracellular pH. *Am J Physiol Circ Physiol* **298,** H1710–H1718.

Zong X, Stieber J, Ludwig A, Hofmann F & Biel M (2001). A single histidine residue determines the pH sensitivity of the pacemaker channel HCN2. *J Biol Chem* **276,** 6313–6319.